

T451

Tropical Mesoscale Convective Systems and Associated Energetics : Observational and Modeling Studies

S. ABHILASH

Thesis submitted in partial fulfillment of the requirements
for the degree of

DOCTOR OF PHILOSOPHY
in
ATMOSPHERIC SCIENCE



Department of Atmospheric Sciences
COCHIN UNIVERSITY OF SCIENCE AND TECHNOLOGY
COCHIN, INDIA

December 2007

DECLARATION

I declare that the work presented in this thesis entitled *Tropical Mesoscale Convective Systems and Associated Energetics : Observational and Modeling Studies* is a genuine record of research work carried out by me and no part has been submitted to any University or Institution for the award of any degree or diploma.



Cochin
December 27, 2007

S. Abhilash
Research Student



COCHIN UNIVERSITY OF SCIENCE AND TECHNOLOGY
DEPARTMENT OF ATMOSPHERIC SCIENCES

Lakeside Campus, Fine Arts Avenue, Cochin - 682 016, India.

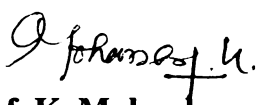
Dr. K. Mohankumar M.Sc., Ph.D.
Dean, Faculty of Marine Sciences &
Hon. Director, Centre for Space Research

CERTIFICATE

This is to certify that the research work presented in this thesis *Tropical Mesoscale Convective Systems and Associated Energetics : Observational and Modeling Studies* is the original work done by Mr. S. Abhilash under my guidance and has not been submitted for the award of any degree or diploma by any other University or Institution.

Certified that Mr S. Abhilash has passed the Ph.D qualifying examination conducted by the Cochin University of Science and Technology in September, 2006.

Cochin
December 27, 2007


Prof. K. Mohankumar
Supervising Guide

ACKNOWLEDGMENTS

I am thankful to Prof. K. Mohankumar, Dean, Faculty of Marine Sciences for help and guidance during my research work. I thank him for providing me an opportunity to do research under his supervision. His constant encouragement, support and positive mind could help me in undertaking this observational and modeling work.

I would like to thank Dr. C. A. Babu, Head, Department of Atmospheric Sciences for providing necessary facilities to carry out this work. I am thankful to all my teachers.

While working in the field of tropical convection, many people helped to ensure successful data collection. Special thanks must go to Dr. V. K. Anadan, Scientist, NARL, Gadanki, who showed me many of the technical aspects of VHF and UHF radars. Dr. R. Suresh, Director, Cyclone Detection Radar Center, IMD, Chennai was not only an inspiration in the field of radar meteorology, but also greatly helped in data analysis. Thanks must also go to Dr. S. B. Thampi, Director, Cyclone Detection Radar Center, IMD, Chennai for teaching me fundamentals of the DWR system at Chennai and providing DWR data when necessary. Many other people and groups provided valuable discussions and assistance during this research period.

I would like to thank Dr. A. K. Bohra, Head, NCMRWF, Noida for providing necessary computer facilities to carry out the modeling part of the thesis. I would like to thank Dr. Someshwar Das, Scientist, NCMRWF, Noida for providing guidance during the course work at NCMRWF. His unlimited enthusiasm and energy level for his work were also a great source of inspiration for me during this period. Special thanks must also go to Dr. John. P. George, Scientist, NCMRWF, Noida for providing necessary support and guidance in the 3-DVAR system of both MM5 and WRF.

I should thank Dr. D. Praveen Kumar, Scientist, NCMRWF, Noida, for providing valuable suggestions and support. His affection and compassion really helped me during my stay at NCMRWF.

I would like to thank Dr. Bindu G, Principal Investigator, DST-WOSA, for providing the computer system in finalizing the thesis in a nice way.

I am thankful to the office staffs, Ms. Sreedevi, Mr. Yeshodharan, Ms. Merry and Ms. Binimol for their support and cooperation during the Ph.D program.

I would like to thank my roommates Mr. Prasanth and Mr. Sabin for their support and cooperation. I extend my sincere thanks to Mr. Vijayakumar for his assistance during the Ph.D program.

I acknowledge the Council of Scientific and Industrial Research, Govt. of India, for providing financial support in the form of Junior and Senior Research Fellow.

I would never have made it without the love, affection, and inspiration I got from my family members. I wish to express my deep sense of affection to my Achan, Amma and my cousin brother Kamji. I would like to thank Dhanya, whose encouragement, in particular over the last few months helped me to focus on this and finish this work. I thank all my friends and well wishers for their help at various stages of my study.

Finally, I remember the omnipresent God, who made this endeavor meaningful.

S ABHILASH

CONTENTS

Title Page	i
Declaration	iii
Certificate	iv
Acknowledgments	v
Table of Contents	vii
List of Figures	xii
List of Tables	xix
Preface	1
1 Introduction	5
1.1 Relevance of the Study	5
1.2 Mesoscale Meteorology and Convective Systems	6
1.2.1 Mesoscale preconditioning and triggering processes	8
1.2.2 Classification of clouds	9
1.2.3 Life cycle of cumulonimbus clouds	13
1.2.4 Classification of cumulonimbus clouds	15
1.2.5 Organization of cumulonimbus clouds	17
1.3 Field Campaigns on Severe Storms	19
1.3.1 International field experiments	22
1.3.2 Thunderstorm studies in India	23
1.4 Scope of the Thesis	25
2 Radar Remote Sensing and System Description	27
2.1 Introduction	27
2.2 Radar Meteorology	28
2.2.1 Propagation of electromagnetic waves	30

2.2.2	Refractive index of air and refractivity	31
2.2.3	Radar equation	33
2.2.4	Scattering theory	35
2.2.5	Turbulent scattering or Bragg scattering	37
2.2.6	Fresnel reflection and scattering	38
2.2.7	Doppler principles	38
2.3	Doppler Weather Radar	41
2.3.1	Overview of the DWR principles	42
2.3.2	Display of base products	44
2.4	MST Radar Principles	45
2.4.1	Signal detectability	47
2.4.2	Power aperture product and its significance	48
2.5	Configuration of Indian MST radar	48
2.5.1	Antenna array and feeder network	51
2.5.2	High power transmitter system	52
2.5.3	Receiver	53
2.5.4	Exciter and radar controller	53
2.5.5	Data acquisition and signal processing	54
2.5.6	Computation of three components of the wind vector	56
2.6	Description of Gadanki LAMP system	57
3	Radar Observations of the Structure and Evolution of TMCS	61
3.1	Introduction	61
3.2	Storm Classification	63
3.3	VHF Radar Observations of TMCS : Case I	65
3.3.1	Experiment setup	66
3.3.2	Approach	67
3.3.3	Genesis (cumulus) region	68
3.3.4	Mature region	70
3.3.5	Transition region	71
3.3.6	Stratiform region	72
3.3.7	Conceptual model of TMCS	74
3.4	VHF radar observations of Supercell Storm : Case II	74
3.4.1	System evolution and structure	76
3.4.2	Radar reflectivity and spectral width	78
3.4.3	Vertical velocity	81
3.5	Weak Evolving Multicell Storm : Case III	85
3.6	UHF Radar Observations of Precipitating Convection	87
3.6.1	Observations and data description	88
3.6.2	Mean structure of convection	88
3.6.3	Radar reflectivity and Doppler vertical velocity	89
3.6.4	Bright band structure associated with the stratiform region	91

3.7	DWR observations of Convective Systems	96
3.7.1	Evolution and propagation of Nor'Westers	96
3.8	Summary	100
4	Microphysical Structure of Tropical Cloud Clusters	101
4.1	Introduction	101
4.2	Brief description of the modeling system	104
4.2.1	Model horizontal and vertical grid	106
4.2.2	Key features of MM5 modeling system	106
4.2.3	Brief note on cumulus parameterizations	108
4.2.4	Overview of the microphysical processes	109
4.3	Cloud Resolving Scale Simulations	111
4.3.1	Experiment design	112
4.4	Thunderstorm on 06 May 2007 : Case I	114
4.4.1	Simulated radar reflectivity	114
4.4.2	Hydrometeor structure and vertical velocity	116
4.5	Mesoscale Convective System : Case II	120
4.5.1	Hydrometeor structure	122
4.6	Comparison of model simulation with TMI Retrievals	124
4.6.1	Description of the data set	125
4.6.2	Overview of the synoptic condition	127
4.6.3	Experiment design	127
4.6.4	Hydrometeor structure during the initial phase	129
4.6.5	Radar reflectivity structure during the initial phase	135
4.6.6	Hydrometeor structure during the mature phase	136
4.6.7	Radar reflectivity structure during the mature phase	141
4.6.8	Accumulated rainfall	142
4.7	Summary	144
5	Assimilation of Conventional and Satellite Data for simulating TMCS	145
5.1	Introduction	145
5.2	Brief note on Initialization and Data Assimilation	147
5.3	Overview of MM5-3DVAR System	148
5.3.1	Background preprocessing	149
5.3.2	Observation preprocessing and quality control	152
5.3.3	Variational analysis (VAR)	153
5.3.4	Updation of boundary condition	153
5.4	Experiment design	154
5.5	MCS during 05-06 May 2005 : Case I	157
5.5.1	Vorticity	158
5.5.2	Simulated rainfall	159
5.6	MCS during 18-19 April 2006 : Case II	160

5.7	MCS during 06-07 May 2007 : Case III	165
5.8	Forecast verification	167
5.9	Summary	169
6	Signatures of Gravity Waves Associated with Convection	170
6.1	Introduction	170
6.2	TMCS on 21 June 2000	175
6.2.1	Vertical velocity disturbance	175
6.2.2	Spectral characteristics of the wind disturbance	177
6.2.3	Amplitude-height profile	178
6.2.4	Wavelet analysis of the vertical wind	178
6.2.5	Cloud resolving scale simulation	181
6.2.6	Simulated reflectivity	182
6.2.7	Vertical velocity and penetrative convection	183
6.2.8	Cloud liquid water and system evolution	188
6.3	Supercell storm on 17 October 2002	189
6.3.1	Vertical wind disturbance	189
6.3.2	Spectral characteristics of the observed wave event	191
6.3.3	Wavelet analysis of the vertical wind	192
6.3.4	Cloud resolving scale simulation	193
6.3.5	Penetrative convection	194
6.3.6	Cloud liquid water and system evolution	194
6.3.7	Condensational heat and propagation characteristics	197
6.3.8	Spectral characteristics of the simulated wave event	200
6.4	Summary	203
7	Impact of DWR Observations in the Simulation of TMCS	204
7.1	Background and Motivation	204
7.2	Single Doppler Velocity Retrieval Method	205
7.3	Assimilation of Doppler Radar Wind Data	207
7.3.1	Synoptic overview	208
7.3.2	Experiment design	209
7.3.3	Vorticity	213
7.3.4	Simulated rainfall	213
7.3.5	Horizontal and vertical wind fields	217
7.3.6	Composite reflectivity and integrated liquid water	217
7.3.7	Hydrometeor fields	219
7.3.8	Forecast verification	222
7.4	Assimilation of Radar Reflectivity and Radial velocity	224
7.4.1	Brief description of the WRF modeling system	224
7.5	Overview of WRF-3DVAR system	225
7.5.1	Vertical velocity increments	226

7.5.2	Partitioning of the moisture and water hydrometeor increments . . .	226
7.5.3	The observation operators for radial velocity and reflectivity	227
7.6	Synopsis of the cyclonic event Ogni	228
7.6.1	Experiment design	228
7.6.2	Mean sea level pressure	229
7.6.3	Horizontal wind	232
7.6.4	Rainfall	233
7.6.5	Mesoscale organization of clouds	233
7.7	Summary	235
8	Conclusion and Recommendations	237
8.1	Radar Observations of TMCS	237
8.2	CSRM Simulations	240
8.3	Mesoscale Data Assimilation	242
8.4	Future scope	243
	References	245
	List of Publications	262

LIST OF FIGURES

1.1	Scale definitions and processes with characteristic time and horizontal scales (Modified from Orlanski, 1975)	7
1.2	Schematic model of the Life cycle of cumulonimbus clouds (Adapted from Cotton and Anthes, 1989)	14
1.3	Plan view of storm showing radar structure of a unicellular supercell storm (Adapted from Chisholm and Renick, 1972)	16
1.4	Vertical section through a supercell storm (Adapted from Chisholm and Renick, 1972)	17
1.5	Satellite Infra Red image of a MCC (modified from Maddox, 1980)	19
1.6	Global distribution of mesoscale convective complexes (dots) and widespread frequent convection as inferred from outgoing long wave radiation minima (shading) (taken from Laing and Fritsch, 1997)	20
1.7	Percentage of MCSs detected by the TRMM Precipitation Radar (PR) that had extensive ice scattering in the 85-GHz channel of the TRMM Microwave Sensor (taken from Nesbitt et al., 2000)	20
1.8	Annual average lightning flash density (flashes per month) for June, July, and August derived from the TRMM Lightning Image Sensor (taken from Nesbitt et al., 2000)	21
1.9	(a) Annual rainfall and (b) Fraction of the annual rainfall that is stratiform, as determined from the TRMM PR. (Schumacher and Houze, 2003)	21
2.1	Electro magnetic spectrum	31
2.2	Relative contribution of water vapor, dry air and free electron to refractivity	34
2.3	Block diagram of DWR	42
2.4	A typical PPI(Z) and MAX(Z) display of a convective system	45
2.5	Operating principles of VHF radar	46

2.6	Location and topography of Indian MST radar site	49
2.7	Block diagram of MST radar	50
2.8	Flow diagram of signal processing	55
2.9	A typical Doppler spectrum	56
3.1	(a) Contour charts of outgoing long-wave radiation in Wm^{-2} and 200 hPa winds in ms^{-1} and (b) Synoptic charts of geopotential height in gpm and 850 hPa wind in ms^{-1}	66
3.2	Time series of rainfall rate recorded by ORG at the radar site	67
3.3	Time-height intensity plots of (a) Signal-to-Noise Ratio (SNR) in dBZ (b) Doppler width in ms^{-1} and (c) Vertical Velocity in ms^{-1}	68
3.4	Averaged vertical velocity during (a) Initial stage, (b) Mature stage, (c) Transition zone and (d) Stratiform region	69
3.5	Time-height intensity plots of SNR near tropopause during the mature stage (Tropopause break is highlighted as rectangle)	70
3.6	Time-height intensity plots of SNR in the middle troposphere	72
3.7	Conceptual model of TMCS	74
3.8	Same as figure 3.1, but for 17 October 2002	75
3.9	Doppler radar reflectivity, PPI(Z) showing the structure of the convective system	77
3.10	Same as figure 3.2 but for 17-18 October 2002	78
3.11	same as figure 3.3 but for 17-18 October 2002	79
3.12	Time-height intensity plots of SNR in the middle troposphere	80
3.13	Time series of maximum vertical velocity (ms^{-1}) and the corresponding height (km)	83
3.14	Averaged vertical velocity during (a) Mature stage (20:40-21:10 LT) and (b) Dissipating stage (21:20-22:00 LT)	84
3.15	Same as figure 3.3 but for 15 September 2001	86
3.16	Time-height intensity plots of SNR in the middle troposphere	87
3.17	Time series of rainfall from ORG records	89
3.18	Time-height section of SNR in the middle troposphere during precipitating convection	90
3.19	Time-Height section of Doppler Vertical Velocity	91
3.20	Time-Height section of SNR in the lower and middle troposphere	92
3.21	Profiles of Reflectivity and DVV	94
3.22	(a-f) DWR reflectivity, MAX(Z) during 12:10-17:10 UTC on 18 April 2006 showing the Propagation of Nor'Westers	97
3.23	(g-l) DWR reflectivity, MAX(Z) during 18:10-23:10 UTC on 18 April 2006 showing the Propagation of Nor'Westers	98
3.24	Radar reflectivity, MAX(Z) showing the convective and stratiform regions of a squall line system	99

4.1	Flow chart of MM5 modeling system	105
4.2	Domain configuration for the experiments	114
4.3	Schematic picture of microphysical processes involved in the three micro-physical schemes	115
4.4	Simulated radar reflectivity (dBZ) from MM5-WR	116
4.5	Simulated radar reflectivity (dBZ) from MM5-SI	117
4.6	Simulated radar reflectivity (dBZ) from MM5-GSFC	117
4.7	Latitudinal section of CLW (mgm^{-3}), RNW (mgm^{-3}) and total hydrometeor (mgm^{-3}) from MM5-WR (top panel), MM5-SI (middle panel), and MM5-GSFC (lower panel) experiments on 6 May 2007	118
4.8	Radar reflectivity, MAX (Z) from Kolkata Doppler radar at (a) 10:00 and (b) 10:30 UTC on 6 May 2007	120
4.9	3-hourly accumulated rainfall from (a) TRMM-3B42, (b) MM5-WR, (c) MM5-SI and (d) MM5-GSFC in mmhr^{-1}	121
4.10	Latitudinal section of CLW (mgm^{-3}), RNW (mgm^{-3}) and total hydrometeor (mgm^{-3}) from MM5-WR (top panel), MM5-SI (middle panel), and MM5-GSFC (lower panel) experiments 17 October 2002	123
4.11	Three dimensional structure of RNW	124
4.12	Instantaneous rainfall rate (mmhr^{-1}) from (a) TMI and (b) MM5-GSFC during the initial phase of the storm	130
4.13	Longitude-height section of hydrometeors, CLW (mgm^{-3}), RNW (mgm^{-3}), ICE (mgm^{-3}), and SNOW (mgm^{-3}) from TMI (left panel) and MM5-GSFC (right panel) during the initial phase of the storm for box A	131
4.14	Same as figure 4.13, but for box B	132
4.15	Box-averaged vertical profiles of hydrometeors, (a) CLW (mgm^{-3}), (b) RNW (mgm^{-3}), (c) ICE (mgm^{-3}), (d) SNOW (mgm^{-3}) from TMI (solid line) and MM5-GSFC (dashed line) for box A	133
4.16	Same as figure 4.15, but for box B	134
4.17	(a) Attenuation corrected near surface reflectivity (dBZ) from TRMM-PR and (b) composite reflectivity (dBZ) from MM5-GSFC during the initial phase of the storm.	135
4.18	Longitude-height section of radar reflectivity (dBZ) from (a) TRMM-PR and (b) MM5-GSFC during the initial phase of the storm.	137
4.19	Same as figure 4.12, but for during the mature phase of the storm.	137
4.20	Same as figure 4.13, but for box C during the mature phase of the storm.	138
4.21	Same as figure 4.13, but for box D during the mature phase of the storm.	139
4.22	Same as figure 4.15, but for box C	140
4.23	Same as figure 4.15, but for box D	140
4.24	Same as figure 4.17, but during the mature phase of the storm.	141
4.25	Same as figure 4.18, but during the mature phase of the storm.	142

4.26	24-hr accumulated rainfall valid at 00:00 UTC on 27th October from (a) TRMM, (b) MM5-GSFC and valid at 00:00 UTC on 28 October 2005 from (c) TRMM and (d) MM5-GSFC	143
5.1	Flow chart showing the MM5/WRF 3DVAR system for (a) Cold start and (b) Cycling mode	150
5.2	Coverage of (a) SYNOP, (b) TEMP, (c) PILOT and (d) SSM/I observations on a typical day used for the assimilation experiments	155
5.3	Satellite Infra Red images from Kalpana Satellite at (a) 12:00 and (b) 17:00 UTC 5 May, (c) 12:00 and (d) 17:00 UTC 6 May 2005	157
5.4	Reflectivity MAX (Z) in dBZ at (a) 11:48 UTC and (b) 16:48 UTC of 05 May 2005 and (c) 11:08UTC and (d) 14:08 UTC 06 May 2005	158
5.5	Vorticity at 00:00 UTC of 5 May 2005 for (a) MM5-GSFC and (b) MM5-3DVAR experiments	159
5.6	Six hourly accumulated precipitation (cm) from TRMM starting from 00:00 UTC, 5 May 2005	161
5.7	Six hourly accumulated precipitation (cm) from MM5-GSFC experiment based on Initial condition of 00:00 UTC, 5 May 2005	161
5.8	Six hourly accumulated precipitation (cm) from MM5-3DVAR experiment based on Initial condition of 00:00 UTC, 5 May 2005	162
5.9	Radar reflectivity, MAX (Z) during 07:00 to 15:00 UTC on 18 April 2006	163
5.10	Simulated composite reflectivity from the MM5-GSFC and MM5-3DVAR experiments	164
5.11	Latitudinal section of CLW, RNW, ICE, SNOW and GRAUPEL (mgm^{-3}) for (a) MM5-GSFC and (b) MM5-3DVAR experiments	165
5.12	Latitudinal section of Total hydrometeors (mgm^{-3}) for (a) MM5-GSFC and (b) MM5-3DVAR experiments	166
5.13	Simulated CAPE (Jkg^{-1}) from (a) MM5-GSFC and (b) MM5-3DVAR experiments	167
5.14	Equitable threat scores with a threshold of (a) 10 mm and (b) 5 mm for MM5-GSFC and MM5-3DVAR experiments	168
6.1	Time series of vertical velocity in the troposphere and lower stratosphere during 19:35 on 21 June to 01:20 UTC on 22 June 2000	176
6.2	Multi-height normalized spectrum of vertical velocity perturbation in the UT/LS region	177
6.3	Amplitude-height profiles of the two dominant modes of oscillation	179
6.4	(a) Wavelet analysis of the vertical velocity in the lower stratosphere. Local time in ordinate and periods in abscissa. (b) Significance test carried out for the wavelet spectrum	180
6.5	Simulated composite reflectivity in dBZ at (a) 15:00 (b) 16:00 and (c) 17:00 UTC on 21 June 2000	182

6.6	Latitudinal section of the simulated reflectivity at 16:30 UTC on 21 June 2000	183
6.7	Time-space evolution of vertical velocity in ms^{-1} at (a) 3 km, (b) 6 km, (c) 10 km, (d) 13 km and (e) 16 km levels. Solid contours shows upward motion and dashed contours represents downward motion	184
6.8	Simulated thermodynamic profile at the radar site	186
6.9	Time series of Integrated Cloud Liquid Water (ICLW) in cm (green line), Integrated Rain Water (IRNW) in cm (blue line) and vertical velocity at 500 hPa in ms^{-1} (red line)	187
6.10	(a-e) Latitudinal section of potential temperature in $^{\circ}\text{K}$ (blue contours), Vertical Velocity in ms^{-1} (red solid contours represents upward and dashed contours represents downward motion), Cloud Liquid Water in gkg^{-1} (green shades) during 14:00-18:00 UTC at one hour intervals	188
6.11	Time series of vertical velocity in troposphere and lower stratosphere during 20:30 17 October to 00:45 UTC on 18 October 2002	190
6.12	Averaged power spectral density in the UT/LS region	191
6.13	(a) Wavelet analysis of the vertical velocity in the lower stratosphere. Local time in ordinate and periods in abscissa. (b) Significance test carried out for the wavelet spectrum	192
6.14	(a) Simulated composite reflectivity in dBZ and (b) Latitudinal cross-section of simulated radar reflectivity averaged along 1° longitude strip centered at 79°E valid at 17:00 UTC of 17 October, 2002	193
6.15	Time-space evolution of vertical velocity in ms^{-1} at (a) 3 km, (b) 6 km, (c) 10 km, (d) 13 km and (e) 16 km levels. Red shades represent upward and blue shades represent downward motion	195
6.16	Latitudinal section of potential temperature in $^{\circ}\text{K}$ (blue contours), Vertical Velocity in ms^{-1} (red solid contours represents upward and dashed contours represents downward motion), Cloud Liquid Water in gkg^{-1} (green shades) during 15:00 to 18:30 UTC on 17 October 2002 at 30 min intervals	196
6.17	(a-e) Cross section of potential temperature in $^{\circ}\text{K}$ (green contours) along line AB (in figure 6.14 a), Condensational Heat in Khr^{-1} (yellow shades), upward velocity greater than 3ms^{-1} (red solid contour) and downward velocity less than 1.5ms^{-1} (red dashed contour)	198
6.18	Vertical profiles of condensational heat in Khr^{-1} during the initial, mature and dissipating stages of the TMCS	200
6.19	Power spectrum of vertical wind field as a function of (a) Frequency (b) Horizontal wavenumber and (c) Vertical wavenumber	201
7.1	(a) Wind field retrieved from DWR at 1.0 km (b) Wind analysis at 900 hPa interpolated to MM5 domain at 00:00 UTC 5 May 2005	207
7.2	Satellite Infra Red images from Kalpana Satellite at (a) 12:00 and (b) 17:00 UTC 5 May, (c) 12:00 and (d) 17:00 UTC 6 May 2005	209

7.3	Reflectivity MAX (Z) in dBZ at (a) 11:48 UTC (b) 16:48 UTC 05 May 2005 and (c) 11:08 UTC (d) 14:08 UTC 06 May 2005	210
7.4	Domain configuration for MM5-3DVAR experiments	210
7.5	Experiment design for radar data assimilation	212
7.6	Vorticity at 00:00 UTC of 5 May 2005 for the (a) CTRL-GSFC , (b) 3DVAR-NoDWR and (c) 3DVAR-DWR experiments	213
7.7	Six hourly accumulated precipitation (cm) from TRMM during 05-06 May 2005	214
7.8	Six hourly accumulated precipitation (cm) from CTRL-GSFC experiment based on initial condition of 00:00 UTC, 05 May 2005	215
7.9	Six hourly accumulated precipitation (cm) from 3DVAR-NoDWR experiment based on initial condition of 00:00 UTC, 05 May 2005	216
7.10	Six hourly accumulated precipitation (cm) from 3DVAR-DWR experiment based on initial condition of 00:00 UTC, 05 May 2005	216
7.11	Horizontal velocity vector and vertical velocity in cm s^{-1} (shading) at (a) 850 hPa and (b) 700 hPa valid for 18:00 UTC 06 May 2005	218
7.12	Simulated a) Composite reflectivity in dBZ (shading) and surface pressure (dotted contours at 3 hPa intervals) b) vertically integrated liquid water (VIL) in mm and potential temperature (dotted contours at 3°K intervals) from the three experiments valid at 18:00 UTC 06 May 2005 based on initial condition at 00:00UTC 05 May 2005	220
7.13	Latitudinal cross-section of (a) total cloud hydrometeor (mgkg^{-1}) and (b) radar reflectivity averaged along 2° longitude strip centered at 88.0°E for the three experiments valid at 18:00UTC 06May 2005	221
7.14	Time section of (a) cloud water mixing ratio (mgkg^{-1}) and (b) rain water mixing ratio (mgkg^{-1}) averaged over 2° latitude/longitude around Kolkata for the three experiments based on the initial condition at 00:00UTC 05 May 2005.	222
7.15	Equitable threat scores with a threshold of (a) 10 mm and (b) 20 mm for the three experiments	223
7.16	Mean sea level pressure simulated by the WRF-NoDWR experiment (left panel) and WRF-DWR experiment (right panel), valid at 12:00 UTC 28 October (top panel), 12:00 UTC, 29 October (middle panel) and 12:00 UTC, 30 October 2006 (lower panel).	230
7.17	Horizontal wind vectors at 850 hPa simulated by the WRF-NoDWR experiment (left panel) and WRF-DWR experiment (right panel), valid at 12:00 UTC 28 October (top panel), 12:00 UTC, 29 October (middle panel) and 12:00 UTC, 30 October 2006 (lower panel)	231
7.18	Time series of (at 12-hr intervals) of Maximum wind (ms^{-1}) for the WRF-NoDWR , WRF-DWR and from Observed / Estimated	232

7.19	24 -hr accumulated rainfall from forecast valid at (a) 00:00 UTC 29 October and (b) 00:00 UTC 30 October 2006. Left, middle and right panel shows the simulated rainfall from WRF-NoDWR, WRF-DWR and TRMM observations	234
7.20	Latitudinal section of Total Hydrometeor (mgm^{-3}) from (a) WRF-NoDWR and (b) WRF-DWR during the mature phase of the storm	235

LIST OF TABLES

1.1	Mesoscale preconditioning processes for severe weather (Johnson, 1995; Mapes, 1998)	9
1.2	Mesoscale triggering processes for severe weather (Johnson, 1995; Mapes, 1998)	10
1.3	Storm-generated mesoscale effects (Johnson, 1995; Mapes, 1998)	11
1.4	Mesoscale Convective Complex definition (Maddox, 1980)	18
2.1	Characteristic wavelength for radar remote sensing	31
2.2	System specifications of MST radar at Gadanki	51
2.3	System specifications of LAWP at Gadanki	58
3.1	Experiment specification table	64
4.1	Physics options available in MM5 modeling system	107
4.2	Significant microphysical processes involved in the Warm Rain, Simple Ice and GSFC schemes and their abbreviations	113
5.1	Description of data used in the assimilation experiments	156
5.2	Summary of experiments	156
5.3	Contingency table	168
7.1	Cases selected for the assimilation experiment	208
7.2	Summary of experiments	212

PREFACE

Weather in the tropical region is characterized by mesoscale organization of clouds. Precipitating convection over tropical regions is fundamental in regulating the vertical structure of the water vapor and entropy in the lowermost layer of the atmosphere and transporting heat, moisture and momentum to the middle and upper atmosphere. Thus, understanding the dynamic and thermodynamic forces that controls the generation and intensification of convection are very much important. Most of the field experiments on severe storms conducted over tropical Pacific and Atlantic to study the detailed structure and dynamics of thunderstorms and mesoscale cloud clusters. Despite some national efforts, nature of the precipitating cloud system over tropical Indian region is poorly known. This thesis focuses on the observational and modeling studies on Tropical Mesoscale Convective Systems (TMCS) over northeast India around Kolkata during pre-monsoon (March to May) and southeast India around Chennai during monsoon and post-monsoon (June to September and October to November) seasons.

Tropical convection occurs on various spatial and temporal scales. The TMCS are characterized by regions of both convective and stratiform precipitation. As scattering mechanism depends on operating frequency or wavelength of the probing radar, this thesis dis-

cusses the radar observations of the convection and clouds at three frequency bands namely VHF, L band UHF, and S band DWR. Chapter 3 discusses the classification of various forms of convective clouds passing over the radar site using the Time-Height variation of the radar reflectivity and vertical velocity. These data can also be used to classify different characteristic regions of TMCS. The features such as Weak Echo Region (WER) and enhanced reflectivity zone or radar bright bands near the melting layer have also been studied with the aid of these high resolution observations. The variance in the atmospheric refractive index and profiles of radar reflectivity-Doppler vertical velocity pairs has been used to explain the bright band.

The cloud resolving scale models, also known as cloud system resolving models (CSRMs) have resolutions fine enough to represent individual cloud elements and space time domains large enough to encompass many clouds and their life times. Chapter 4 deals with the sensitivity of different single moment bulk microphysical schemes to Quantitative Precipitation Forecasting (QPF) and hydrometeor structure during different phases of the storm life cycle. Sophisticated microphysical scheme with five hydrometeor species such as Goddard Space Flight Centers (GSFC) microphysical scheme simulates the rainfall, reflectivity and hydrometeor structure of the MCS reasonably well. The results from the CRSM simulations have been compared with the hydrometeor profiles retrieved from Tropical Rainfall Measuring Mission (TRMM) Microwave Imager (TMI) retrievals. The amount of hydrometeorological fields retrieved from TMI is slightly less than that simulated by the model.

It is difficult to produce operational forecast of these convective events mostly because the convective elements within these MCS are relatively small and short-lived. Both conventional and satellite observations provide variety of information to be assimilated in the modeling system to reduce the uncertainty in the initial condition. Chapter 5 discusses the impact of the various conventional and satellite observations for the short range prediction

of the convective rainfall and simulation of the cloud structure. The model forecast of precipitation has been verified by calculating the equitable threat scores (ETS) for all the three cases considered and found that assimilation of conventional and satellite observations significantly improves the prediction of intense rainfall associated with TMCS.

Cumulus convection has received a great deal of attention as a possible source mechanism for the generation of Internal Gravity Waves (IGW), especially over tropics where frequency of occurrence of cumulus clouds is more. A need exists to explore the features associated with these convectively generated Gravity waves over tropical Indian region. The vertical wind disturbances and possible signatures of gravity waves associated with tropical convection are reported in chapter 6. The effect of deep convection and vertical wind disturbances in the middle troposphere on the characteristics of gravity waves has been investigated using 53-MHz Indian MST radar data. Wavelet analysis has been performed on the vertical velocity to study the variability of the dominant modes in time. The CRSM simulations of the observed wave suggest that, multiple mechanisms such as thermal forcing due to condensational heat and oscillatory nature of updraft-downdraft pairs reaching as high as tropopause level are equally important for forcing, maintenance and amplification of gravity waves.

Doppler Weather Radar (DWR) observation is an important data source for mesoscale and microscale weather analysis and forecasting. Despite the importance of the DWR data for use in warning the heavy rainfall associated with the convective systems, there remains no effort to include analyzed Doppler radar data in the assimilation cycle of the operational weather prediction models in India. Chapter 7 aims to initialize the storm-scale numerical model using retrieved wind fields from single Doppler radar. In the present chapter, Doppler wind velocities from the Kolkata (22.6°N, 88.4°E) and Chennai (13.0°N, 80.1°E) DWR is assimilated into a mesoscale model (MM5) using three-dimensional variational data assimilation (3-DVAR) system for the prediction of intense convective events occurred over the

radar site. The assimilation of DWR wind observations shows positive impact on the short range QPF associated with TMCS. The assimilation system has been modified further to incorporate the radar reflectivity and radial velocity data to improve the simulation of the microphysical and thermodynamic structure of the convective storms. Preliminary results from the radar reflectivity assimilation have also been included in this chapter.

Chapter 8 presents the major outcome of the study in the form of summary and conclusions. Future scope and recommendation for further research in this field is also suggested.

CHAPTER 1

Introduction

1.1 Relevance of the Study

Weather in the tropical region is characterized by mesoscale organization of clouds (*Houze, 1977; Leary and Houze, 1979; Cotton and Anthes, 1989; Houze, 1993*). Tropical atmospheric deep convection is a critical element in the earth's climate. Severe convective storms over tropics produce torrential rains, severe winds including downbursts and tornadoes, hail, thunder and lightning and majority of snow storms. Vertically developing convective clouds over tropics play an important role in the earth's general circulation, water budget, climate and climate variability. Latent heat released in clouds serves as tropical heat engine that drive the atmospheric circulation (*Webster, 1972*). Precipitating convection over tropical regions is fundamental in regulating earth's hydrological cycle by transporting water vertically and horizontally with a change of phase between vapor, liquid and solid phases, removing water from the atmosphere through precipitation, and shielding the earth's surface from direct solar radiation, thus altering atmospheric evapotranspiration rates.

The vertical redistribution of water vapor by deep convective updrafts is believed to be crucial, but poorly understood, feed back mechanism to global warming (*Lindzen, 1990; Betts, 1990*). Clouds are also a major factor in determining the earth's radiation budget by reflecting incoming solar radiation and absorbing upwelling terrestrial radiation (*Webster and Stephens, 1984; Ramanathan and Collins, 1991; Harrison et al., 1990*). Variations in the coverage of clouds, the height of the clouds, and even the number and sizes of individual cloud particles all have large effects on the radiation budget of the earth. Clouds and precipitation play a key role in the atmospheric chemistry on regional and global scales.

Hence, Precipitating convection over tropical regions is fundamental in regulating the vertical structure of the water vapor and entropy in the lowermost layer of the atmosphere and transporting heat, moisture and momentum to the middle and upper atmosphere. Thus, understanding the dynamic and thermodynamic forces that controls the generation and intensification of convection are very much important. The clouds and precipitation systems are very fascinating and interesting features to study. Atmospheric effects of clouds and precipitation such as rainbow, lightning and organization of cloud clusters and scattering of sunlight are a passion of common man. The knowledge gained from studying them in detail is essential to improve the short range and long range forecasting and gaining a quantitative understanding of atmospheric chemistry, the earth's general circulation, and climate variability.

1.2 Mesoscale Meteorology and Convective Systems

Mesoscale meteorology is concerned with weather systems that have spatial and temporal scales between the domains of macro-meteorology and micro-meteorology. Most of the scale definition is based on geometric scales of atmospheric motion. The macro-meteorology is concerned with weather systems that have spatial and temporal scales be-

tween the domains of macro and micro-meteorology. Generally, macro-meteorology is concerned with weather systems having spatial scales greater than 1000 km and temporal scales on the order of several days or longer. Micro-meteorology is the science dealing with atmospheric dynamics having spatial scales of tens to hundreds of meters and time scales on the order of minutes. Synoptic meteorological processes such as fronts, highs, and lows are associated with wavelengths of greater than 2000 km and normally persist for days to weeks. Hence, mesoscale features range from near synoptic scales down to individual cloud cells (Fujitha, 1963, 1974, 1981; Orlanski, 1975; Ogura, 1963). Figure 1.1 shows the schematic representation of the scale classification and different processes with their characteristic time and horizontal scales.

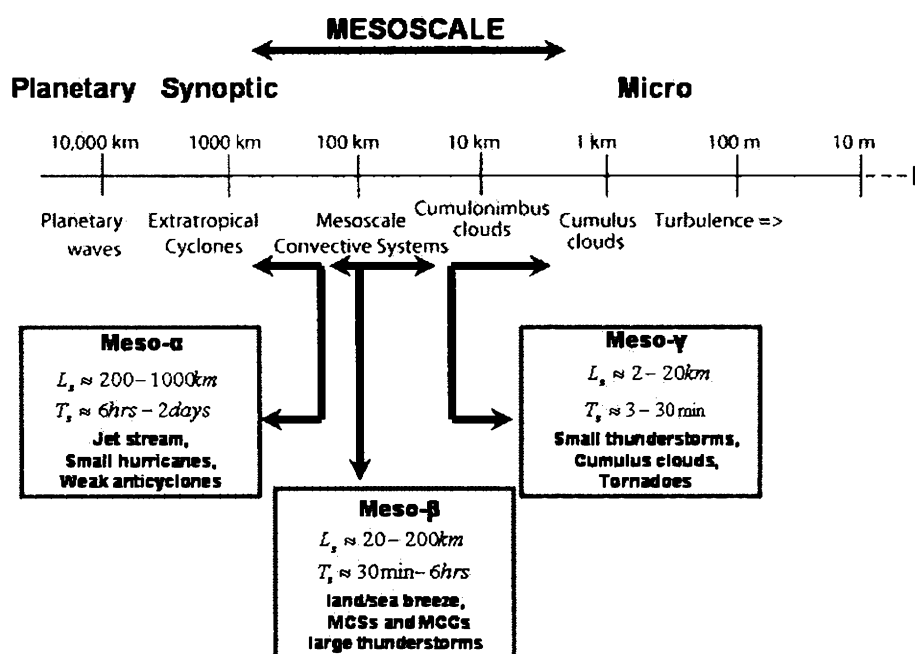


Figure 1.1: Scale definitions and processes with characteristic time and horizontal scales (Modified from Orlanski, 1975)

Based on dynamical considerations, Ooyama (1982) defines the mesoscale flows as those having a horizontal scale between the scale height, H of the atmosphere and Rossby

radius of deformation, $\lambda = \frac{NH}{f}$, where N is the Brunt-Vaisala frequency and f is the Coriolis parameter. By this definition, mesoscale phenomena occur on horizontal scales between ten and several hundred kilometers. This range generally encompasses motions for which both ageostrophic advections and Coriolis effects are important (Emmanuel, 1986). In general, we can apply such a definition; however, strict application is difficult since so many mesoscale phenomena are multiscale. Hence mesoscale systems are further subdivided into three scales: meso- α , meso- β and meso- γ (Orlanski, 1975; Fujitha, 1981).

1.2.1 Mesoscale preconditioning and triggering processes

The genesis, evolution and intensification of MCS depend on mesoscale processes. According to the preconditioning and triggering mechanisms of deep convection, mesoscale processes are again divided. Newton (1963) distinguished factors that precondition (destabilize) the environment (*e.g.* : an approaching upper-level trough, differential horizontal advection, low-level jets) from those that release the instability, such as rapid lifting by fronts, cold domes from thunderstorms, dry lines, and topography. A list of common mesoscale preconditioning processes and presented in table 1.1 (Johnson *et al.*, 1995; Mapes, 1998). The mesoscale processes in table 1.1 have been subdivided into local, advective, and dynamical. If the destabilization occurs rapidly enough, some of these processes may actually trigger convection, thus blurring the distinction between preconditioning and triggering. Specific processes involved in triggering convection are identified and presented table 1.2. As mentioned earlier, some triggering and preconditioning processes are the same. Once initiated, severe storms generate mesoscale phenomena that impact storm evolution as well as the growth of neighboring storms. Storm generated mesoscale processes can have local, advective and dynamical effects. Table 1.3 presents common storm generated mesoscale effects.

Local	<u>Boundary layer processes</u> <i>Deepening the mixed layer, Deepening the moist layer, Nocturnal inversion and low-level jet, Convergence along dryline</i> <u>Terrain effects</u> <i>Creation of convergence, Development of Slop flows, Modification of hodograph</i> <u>Surface effects</u> <i>Evaporation, heating, Surface discontinuities, soil moisture, roughness,</i>
Advective	<u>Differential advection</u> <i>Creation of capping inversion, Destabilization and deep PBL</i> <u>Convergence lines</u> <i>Fronts, Drylines, Sea/land/lake breezes, Mountain/valley breezes,</i> <u>Moisture advection</u> <i>Increase CAPE, lower LFC, Local cumulus moistening,</i>
Dynamic	<u>Secondary circulations</u> <i>Geostrophic adjustment jets, Gravity currents, waves, Localized reduction in CIN, Modification of vertical shear, Cold pool</i> <u>Mesoscale instabilities and Boundary layer processes</u> <i>Horizontal Convective rolls, Inertial oscillation,</i>

Table 1.1: Mesoscale preconditioning processes for severe weather (Johnson, 1995; Mapes, 1998)

1.2.2 Classification of clouds

The clouds can occur at any level of the atmosphere where sufficient moisture present to allow condensation. The classification of clouds discussed here is based on the dynamic rather than the physical appearance of the clouds from the perspective of the ground based observer. The cloud classification given in International Cloud Atlas (World Meteorological Society, 1956) is based on 10 main groups called *genera*, and most of the genera are subdivided into *species*. Each subdivision is based on the shape of the clouds or their internal structure. The species is further subdivided into *varieties*, which define special characteristics of the clouds related to their transparency and the arrangements of the microscopic

Local	<u>Boundary layer circulations</u> <i>Thermals</i> <u>Terrain effects</u> <i>Orographic lifting, Thermal forcing, Obstacle effects</i> <u>Surface effects</u> <i>Sensible/latent heat flux discontinuities</i>
Advective	<u>Convergence lines</u> <i>Cold fronts, Gust fronts, Sea/lake breezes, Drylines</i> <u>Boundary intersections</u> <i>Tripple point, Colliding fronts, sea breezes</i>
Dynamic	<i>Gravity currents, waves</i> <i>Boundary layer horizontal convective rolls</i>

Table 1.2: Mesoscale triggering processes for severe weather (Johnson, 1995; Mapes, 1998)

cloud elements. Based on the level at which the clouds occur, the genera are also divided into high, medium and low level clouds. The definitions of 10 genera are as follows:

Higher level clouds tend to develop at or just above the top part of the troposphere. These clouds can vary in shape and thickness. Sunlight can be observed passing through the higher level clouds most of the time. The amount of light that penetrates depends on the density and thickness of the layers. There are three main types of higher level clouds: *viz.*, cirrus, cirrostratus and cirrocumulus. *Cirrus* clouds are detached clouds in the form of white, delicate filaments, white or mostly white patches, or narrow bands. These clouds have a fibrous (hair-like) appearance, or a silky sheen or both. *Cirrocumulus* are thin white patches, sheets or layers of clouds without shading, composed of very small elements in the form of grains or ripples, merged or separated or more or less regularly arranged. Most of the elements have an apparent width of less than 1° . *Cirrostratus* is transparent, whitish cloud veil of fibrous or smooth appearance, totally or partially covering the sky and generally producing halo phenomena.

Local	<u>Radiation and Microphysics</u> <i>Downdraft, cold pool production, Microburst generation</i> <i>Melting-generated midlevel convergence, Lightning production</i>
Advective	<u>Particle advection and phase changes</u> <i>Downdraft generation and Upscale growth</i> <u>Cold pool processes</u> <i>Cell regeneration, MCS evolution</i> <u>Momentum transport/sloping flows</u> <i>Severe surface winds</i> <u>Vortex tilting/stretching</u> <i>Vertical vorticity generation, supercells, MCS and mesovortices</i>
Dynamic	<u>Gravity currents and waves</u> <i>Impact on cell/MCS growth, Influence on neighboring convection</i> <u>Mesoscale pressure fields</u> <i>Buoyancy contribution, Dynamic contribution</i> <i>storm splitting, propagation, Surface highs, Wake lows</i> <u>Baroclinic vorticity generation</u> <i>Horizontal gust front, Vortex breakdown and Mesocyclone</i>

Table 1.3: Storm-generated mesoscale effects (Johnson, 1995; Mapes, 1998)

Middle level clouds are brighter and less fragmented in appearance due to their distance from the ground and the higher composition of ice crystals. These clouds vary in thickness from relatively flat sheets of cloud to a more cumuliform appearance. They tend to move at lesser speed than the lower level clouds. They move in the direction of the wind at that level which does not necessarily have to be the same as that at the surface. There are two basic types of middle level clouds: altocumulus and altostratus. *Altocumulus* are white or grey or both white and grey, patches, sheets, or layers of clouds, generally with shading, composed of laminae, rounded masses, or rolls, which are sometimes partially fibrous or diffuse and which may or may not be merged, most of the regularly arranged small elements usually have an apparent width of 1-5°. *Altostratus* are greyish or bluish cloud sheets or layer of

stratified, fibrous, or uniform appearance, totally or partially covering the sky, and having parts thin enough to reveal the sun at least dimly, as through ground glass. Altostratus does not produce halo phenomena.

Lower level clouds have ever-changing structure due to turbulent motions. The motion of these clouds follows the direction of the wind in the lower levels. There are five types of lower level clouds: cumulus, cumulonimbus, stratus, stratocumulus and nimbostratus. *Nimbostratus* are grey cloud layer, often dark, the appearance of which is rendered diffuse by more or less continuously falling rain or snow, which in most cases reaches the ground. It is thick enough to completely obscure the sun. *Stratocumulus* are grey or whitish or both, patches, sheets, or layers of clouds which almost always have dark parts, composed of rounded masses, or rolls, which are non-fibrous and which may or may not be merged, most of the regularly arranged small elements have an apparent width of more than 5° . *Stratus* is generally grey clouds with a uniform base, which may produce drizzle, ice prisms, or snow grains. If the sun is visible through the cloud, its outline is clearly discernible. *Cumulus* are detached clouds, generally dense and with sharp outlines developing vertically in the form of rising mounds, domes or towers, of which bulging upper part often resembles a cauliflower. The sunlight part of these clouds are mostly brilliant white, their base is relatively dark and nearly horizontal.

Another vigorous type is clouds with large vertical development. These clouds are named as *Cumulonimbus*. They are heavy, dense clouds with considerable vertical extent, in the form of mountain or huge tower. At least part of their upper portion is usually smooth, fibrous, or striated and is nearly always flattened; this part often spreads out in the shape of an anvil or vast plume. Under the base of these clouds, which is generally very dark, there are frequently low ragged clouds and precipitation, sometimes does not reach the ground.

1.2.3 Life cycle of cumulonimbus clouds

As defined by *Byres and Braham* (1949) and *Browning* (1977), the fundamental building block of cumulonimbus cloud are the *cell*. They identified three stages in the evolution of an ordinary thunderstorm cloud: the *cumulus stage*, *mature stage* and *dissipating stage*. As illustrated in figure 1.2 (a), the *cumulus stage* is characterized by one or more towering cumulus clouds that are fed by moisture convergence in the boundary layer. Strong updrafts prevail during the cumulus stage, penetrative downdrafts near the cloud top and on the downshear flank of the cumuli can occur. The end of the cumulus stage is marked when precipitation forms in the upper portion of the cumuli, but significant precipitation in the subcloud layer is unlikely. The merger of cumulus elements into large-scale convective system characterizes the transition to the *mature stage*. The merger processes is frequently associated with the collision of downdraft induced gust fronts from adjacent cumulus clouds. Thus the onset of precipitation into the subcloud layer is also characteristic of the transition from the cumulus to the mature phase. As illustrated in figure 1.2 (b), both updrafts and downdrafts characterize the mature phase. Divergence of the updraft just below the tropopause results in the formation of the anvil cloud, and a cloud dome is often present. Near the ground, the diverging downdraft air, chilled by evaporation and melting of precipitation, spreads out to form a gust front. Heavy localized rain showers also characterize this stage.

Downdrafts characterize the lower portions during the *dissipating stage* of a cumulonimbus. However local pockets of convective updrafts can remain as shown in figure 1.2 (c), especially in the upper half of the cloud. Entrainment through the sides of the cloud and turbulence also occur. Near the ground, the diverging evaporatively chilled air feeds the gust front, and the front advances far away from the cloud, thus air lifted by the gust front can no longer feed the storm updrafts. Light stratiform precipitation prevails during the dissipating stages.

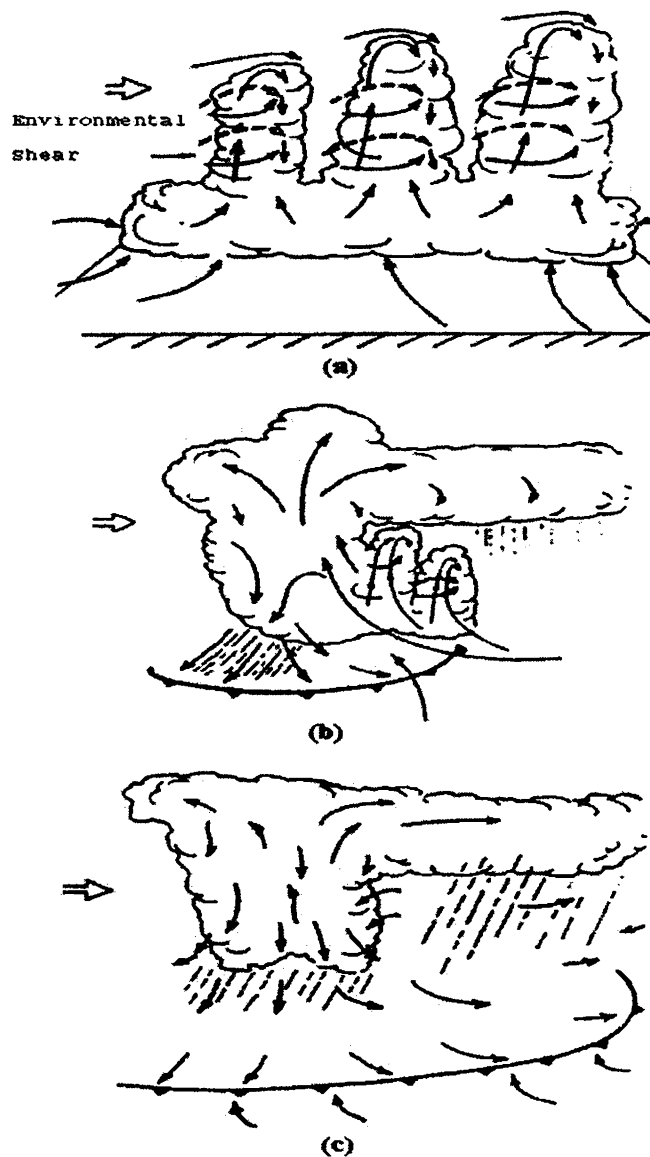


Figure 1.2: Schematic model of the Life cycle of cumulonimbus clouds (Adapted from Cotton and Anthes, 1989)

1.2.4 Classification of cumulonimbus clouds

There have been numerous attempts to classify thunderstorms and cumulonimbus clouds into various storm types (*Browning, 1977; Chisholm and Renick, 1972; Weisman and Klemp, 1984; Foote, 1984*). Based on radar observations, *Browning (1977)* used the label *ordinary* to refer to a thunderstorm that undergoes the three stages in the evolution for a period of 45-60 min and in which mature stage lasts for about 15-30 min. He distinguishes these from a more vigorous type of convection that is often referred to as a *supercell*. Large size and intensity distinguishes supercell storms, where the updraft and downdraft circulations coexist in a nearly steady state form for a periods of 30 min or longer. The features such as rotating updrafts or mesocyclone typically associated with tornado producing storms and their radar echo characteristics can be used to identify quasi-steady supercell storms. Figure 1.3 illustrates the plan view and figure 1.4 shows the vertical cross-section through a supercell storm. The *hook echo* that wraps around a so-called *vault* (*Browning and Ludlam, 1960, 1962*) or *bounded weak-echo region* (BWER) are characteristic features of a supercell storm.

Byres and Braham (1949), Browning (1977), Marwitz (1972), Chisholm and Renick (1972), etc., have identified another form of severe storm called the multicell storm, which as its name implies, typically composed of two to four cells. At any time, some cells may be in the cumulus stage, some in the mature stage, and others in the dissipating stage of the life cycle of a cumulonimbus cell. Multicell thunderstorms are generally less intense than supercell storms. They also exhibits radar features such as *hook echo* and *weak-echo region* (WER), but the WER is not fully bounded in the form of an echo-free vault and the occurrence of BWER is unlikely. *Browning (1977)* distinguished between a typical multicell storm and supercell storm by the visual appearance of the daughter cells. Some scientists argue that a supercell storm is nothing more than a multicell storm in which daughter cells are embedded within the forward overhanging anvil cloud and precipitation. In some cases

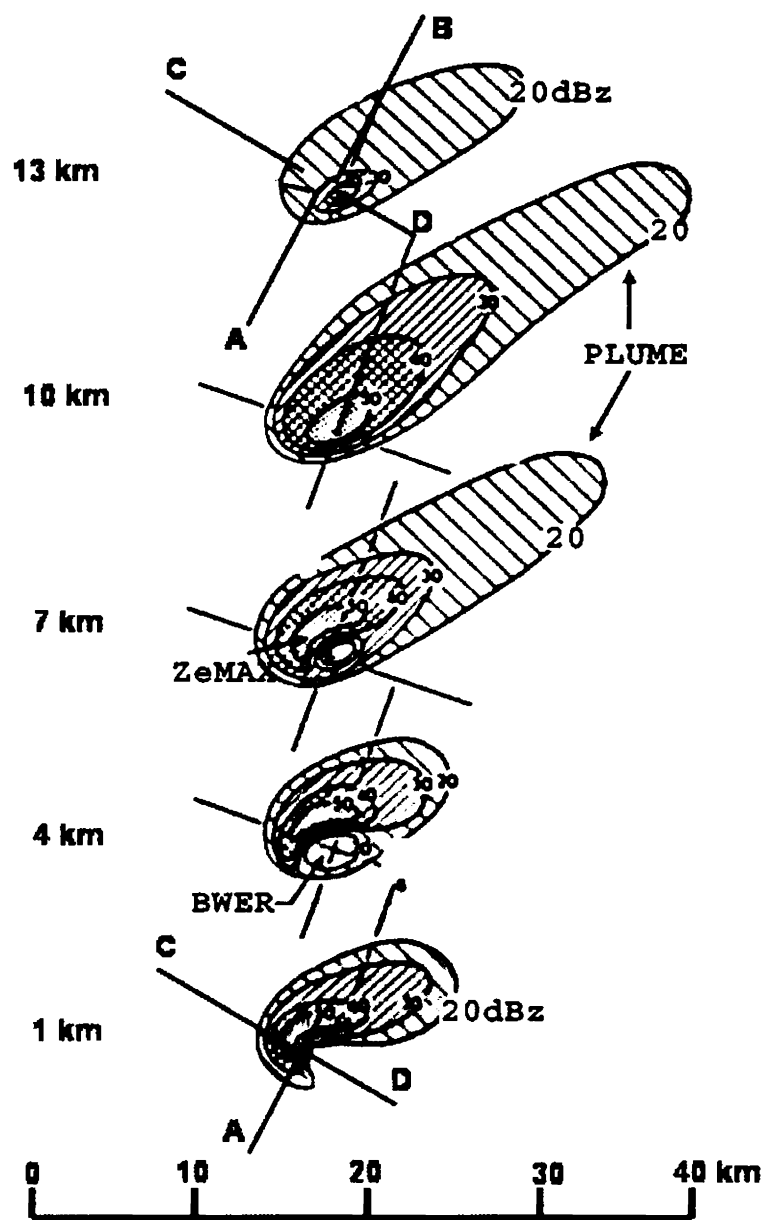


Figure 1.3: Plan view of storm showing radar structure of a unicellular supercell storm (Adapted from Chisholm and Renick, 1972)

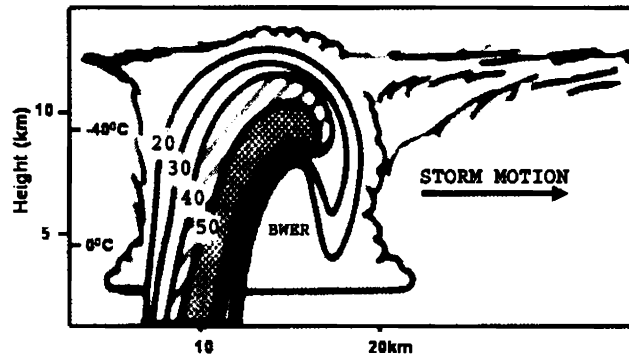


Figure 1.4: Vertical section through a supercell storm (Adapted from Chisholm and Renick, 1972)

multicell storms evolve into supercell storms (*Vasiloff et al.*, 1986; *Knupp and Cotton*, 1982). Moreover, there is some evidence of a continuum of storm types, ranging from the lesser organized multicell storms, to organized multicell storms, to steady supercell storm (*Foote and Wade*, 1982).

1.2.5 Organization of cumulonimbus clouds

Occasionally thunderstorms organize into clusters of cumulonimbi called Mesoscale Convective Systems (MCSs) that have maximum dimensions of 100 km or more and are often marked by an extensive middle to upper tropospheric stratiform-anvil cloud of several hundred kilometers in horizontal dimension. The cloud systems typically have lifetimes of 6 to 12 hours and on some occasions, the stratiform-anvil portion of the system can survive for several days. *McBride and Gray* (1980) found that the dominant forcing of such systems in the western Pacific and eastern Atlantic oceans is the convergence associated with the Intertropical Convergence Zone (ITCZ). The regional circulation such as land and sea breezes can also be a source of sustained large-scale mesoscale systems forced by convergence (*Houze*, 1981; *Houze et al.*, 1981). *McBride and Gray* (1980) determined that

easterly waves in the tropics are an important forcing mechanism of MCSs but not as important as large-scale convergence in the ITCZ.

More circular MCS as viewed from satellites are referred to as Mesoscale Convective Complexes (MCCs) in the midlatitudes and Tropical Cloud Clusters (TCC) in tropics. *Maddox* (1980) studied the detailed organizational characteristics of MCCs over midlatitudes based on satellite Infra-Red (IR) measurements and their characteristics are listed in table 1.4. Figure 1.5 shows the satellite IR image of MCCs. The MCSs occurring over tropical region are called Tropical Mesoscale Convective Systems (TMCSs) and are broadly classified as tropical squall clusters and tropical non-squall clusters.

Size:	(A) Cloud shield with IR temperature $\leq -32^{\circ}\text{C}$, must have an area $\geq 100,000 \text{ km}^2$ (B) Interior cold cloud region with temperature $\leq -52^{\circ}\text{C}$, must have an area $\geq 50,000 \text{ km}^2$
Initiate:	Size definitions A and B are first satisfied
Duration:	Size definitions A and B must be met for a period $\geq 6 \text{ h}$
Maximum	Continuous cold cloud shield (IR temperature $\leq -32^{\circ}\text{C}$)
Extent:	reaches maximum size
Shape:	Eccentricity (minor axis/major axis) ≥ 0.7 at time of maximum extent
Terminate:	Size definitions A and B no longer satisfied

Table 1.4: Mesoscale Convective Complex definition (Maddox, 1980)

Using satellite imagery *Laing and Fritsch* (1997) have synthesized the global distribution of MCCs. Figure 1.6 shows global distribution of MCCs as inferred from the outgoing long wave radiation (OLR). These intense systems especially occur over land, where they probably benefit from the greater peak low level buoyancy generated by day time heating. *Nesbitt et al.* (2000) examined the data from passive microwave radiance in 85-GHz

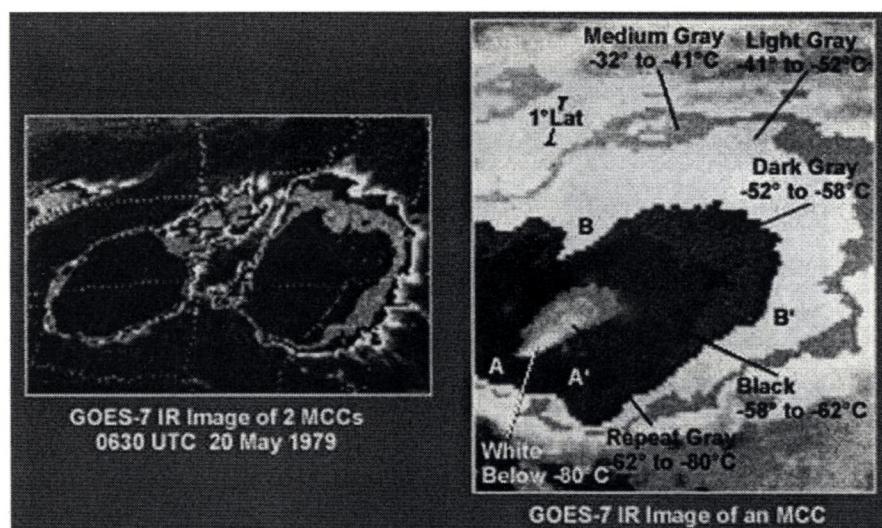


Figure 1.5: Satellite Infra Red image of a MCC (modified from Maddox, 1980)

channel of Tropical Rainfall Measuring Mission (TRMM) Microwave Imager (TMI) in combination with data from the TRMM Precipitation Radar (PR) (Figure 1.7). The tropical continental MCSs identified in this analysis exhibited strong scattering of 85-GHz signal in the locations of most frequent lightning (Figure 1.8). Differences between the land and ocean convection are further evident from TRMM PR data. Figure 1.9 (a) shows the TRMM PR annual mean rainfall, while figure 1.9 (b) shows the fraction of that rainfall characterized as stratiform. The largest stratiform fractions occur over oceanic ITCZ of the Pacific and Atlantic.

1.3 Field Campaigns on Severe Storms

With the fast developments in the information technology and electronics, the remote sensing, data processing, display and transmission of weather data reached a new facet. With the increasing computational power, high resolution numerical studies have been contributed significantly to our understanding of storm organization and life times. Several field cam-

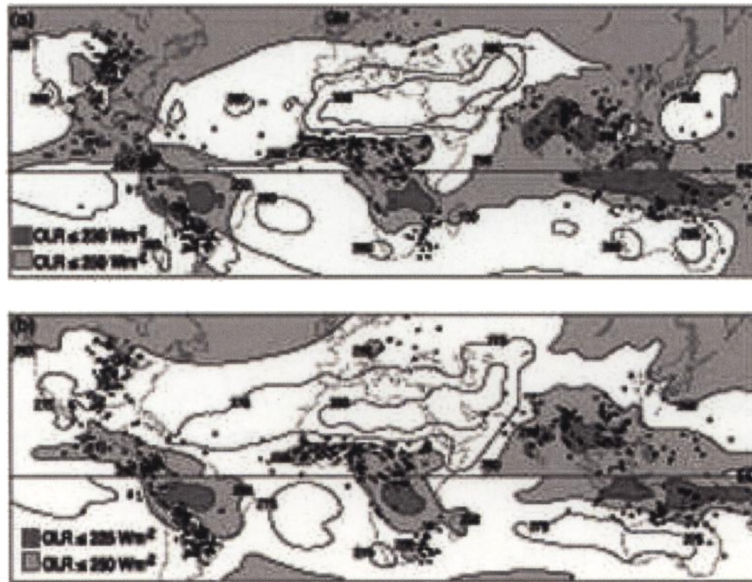


Figure 1.6: Global distribution of mesoscale convective complexes (dots) and widespread frequent convection as inferred from outgoing long wave radiation minima (shading) (taken from Laing and Fritsch, 1997)

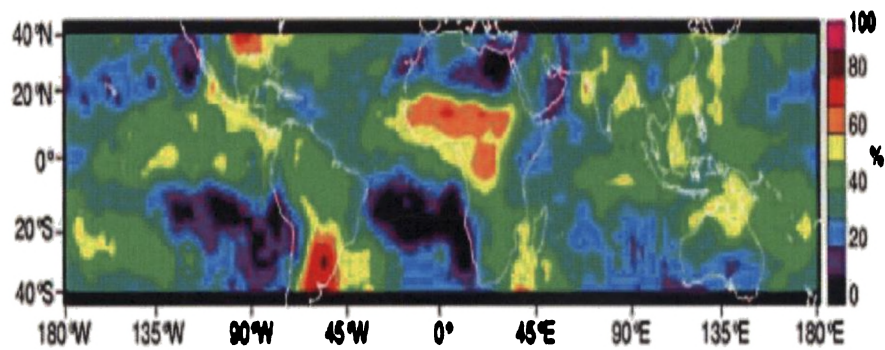


Figure 1.7: Percentage of MCSs detected by the TRMM Precipitation Radar (PR) that had extensive ice scattering in the 85-GHz channel of the TRMM Microwave Sensor (taken from Nesbitt et al., 2000)

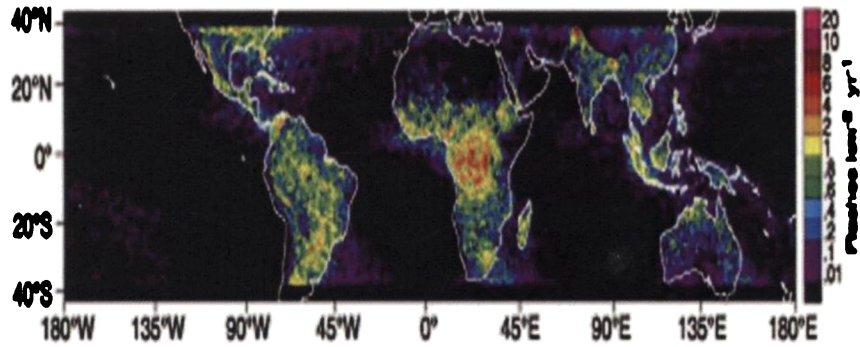


Figure 1.8: Annual average lightning flash density (flashes per month) for June, July, and August derived from the TRMM Lightning Image Sensor (taken from Nesbitt et al., 2000)

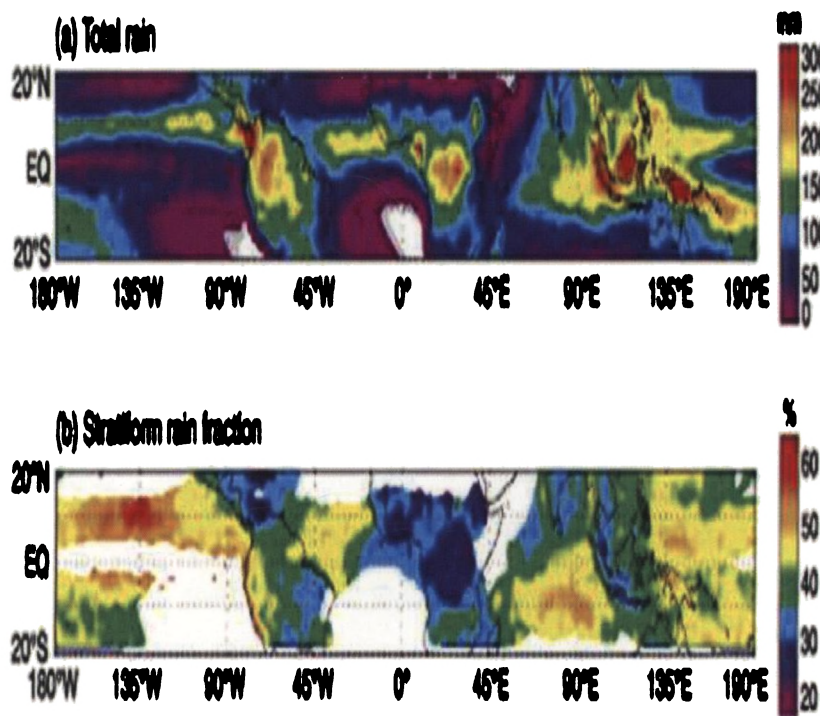


Figure 1.9: (a) Annual rainfall and (b) Fraction of the annual rainfall that is stratiform, as determined from the TRMM PR. (Schumacher and Houze, 2003)

paings have been conducted around the world to study the detailed structure and dynamics of the convective systems. Data derived from these field campaigns can be used to force storm scale or Cloud Resolving Scale models. Much of our understanding on MCSs and MCCs come from field experiments and modeling studies during 1970's and 1980's. Those defining studies were synthesized by *Cotton and Anthes (1989)* and *Houze (1993)*.

1.3.1 International field experiments

Tropical oceanic and land-based convection has been studied in number of international field experiments. The Australian Monsoon Experiment-AMEX (*Holland et al., 1986*) in its second phase provided a comprehensive data set on the same time and space scale as the major weather systems that exist during the Australian monsoon period. AMEX was followed by the Equatorial Mesoscale EXperiment-EMEX (*Webster and Houze, 1991*) conducted during the Southern Hemisphere summer to investigate the mesoscale convective systems in the monsoonal flow north of Australia. Aircraft were used to measure vertical profiles of divergence in convective, transitional and stratiform regions in oceanic cloud clusters. The Down Under Doppler and Electricity Experiment-DUNDEE (*Rutledge et al., 1992*) conducted during the wet season of 1989 near Darwin examined the electrical characteristics of convective clouds and relationships between their electrical and convective states.

The Tropical Ocean-Global Atmosphere Coupled Ocean Atmosphere Response Experiment-TOGA COARE (*Webster and Lukas, 1992*) focused on convection in the western Pacific warm pool and Winter Monsoon Experiment (WMONEX) designed solely to study the MCS characteristics. These experiments have been conducted to study the convective systems over the continents and over the ocean. Field campaigns such as Taiwan Area Mesoscale Experiment (TAMEX), Maritime continental Thunderstorm Experiment (MCTEX) and Thunderstorm Research International Programme (TRIP) also emphasize

the importance of such studies to understand the convective clouds, which have considerable scientific and practical importance. There remains no effort to study the TMCS over Indian subcontinent. Several field experiments have been conducted regionally over USA on thunderstorms. These include the North Illinois Meteorological Research on Downbursts (NIMRD) during the spring and summer of 1978, the Joint Airport Wind Shear (JAWS) project conducted from 15 May to 13 August 1982 in the Denver-Colorado area and the Micro-burst and Severe Thunderstorm (MIST) project in Alabama during the summer of 1986. The Severe Thunderstorm Electrification and Precipitation Study (STEPS) involving both ground and airborne measurements to study the electrical properties of thunderstorms occurring in New Mexico, Florida, Colorado etc.

1.3.2 Thunderstorm studies in India

The main region of high thunderstorm activity in India during the pre-monsoon season (March to May) are northeast India around Indo-Gangetic plain, southwest peninsular India particularly Kerala and northwest India outside Rajasthan. More than 35 thunderstorm days are occurring over these region during the pre-monsoon season. Though there is considerable thunderstorm activity during monsoon season (June to September), frequency is less compared to pre-monsoon season. The southeast coastal stations and southwest peninsular region also receive thunderstorms during post-monsoon season (October-November).

Srinivasan et al. (1973) in their forecasting manual has given a detailed account of severe thunderstorms in India and described several case studies. By reviewing the annual reports of India Meteorological Department (IMD) from 1982-1989, *Nizamudin* (1993) finds that there were 228 hail storm days of moderate to severe intensity. The exhaustive review on tornado occurrence over India reported that about 76 % of the tornadoes in India occur during March to May (*Gupta and Ghosh*, 1980; *Bhattacharya and Banerjee*, 1980; *Mandal*, 1983; *Mukherjee and Bhattacharya*, 1972; *Asnani*, 1985; *Golder et al.*, 2001).

Joseph et al. (1980) made a comprehensive study of 40 cases of Andhi (Dust storms during pre-monsoon season) that occurred at the Delhi airport during 1973-1977, using a transmissometer (to measure the variation of horizontal visibility as the dust wall moved across the airport), a weather radar (to study the movement of associated thunderstorm cloud) and wind, temperature, humidity and pressure measuring instruments.

Radar observations of tornadoes and supercell storms show the appearance of *hook* or *six shape* echoes. *De and Sen* (1961); *De* (1963); *Kulshetha and Jain* (1965); *Kundu and De* (1969); *Mukherjee and Bhattacharya* (1972); *Narayan and Krishnamurthy* (1966) describe studies of thunderstorms of India, particularly of the pre-monsoon season. *Raghavan et al.* (1981); *Jayanti et al.* (1980); *Biswas and Gupta* (1989, 1992) showed that over south Indian stations the tallest thunderstorms occur in the pre-monsoon season and there is a sharp fall in heights after the monsoon sets in. But this is not true for north India (*Kumar*, 1992). *Cornford and Spavins* (1973) in collaboration with IMD conducted extensive observations of thunderstorms over Kolkata region using air-borne radar, cameras and horizon gyroscopes besides the ground based radar of the IMD. They found that pre-monsoon thunderstorms in northeast India extends to 20 km altitude or more and grow at a rate of 6 ms^{-1} . In India, the maximum number of MCSs has occurred over the northeast. *Gambheer and Bhatt* (2000, 2001) have studied the life cycle characteristics and diurnal variation of MCSs over the Indian region.

The eastern and north-eastern part of the country i.e., Gangetic West Bengal, Jharkhand, Orissa, Assam and parts of Bihar gets affected by severe thunderstorms during pre-monsoon months, in particular during April-May. These thunderstorms are locally named as *Kalbaishakhi* which means calamities in the month of Baishakh. These storms are also known as *Nor'Westers* as they move from northwest to southeast. These Norwesters produce heavy rain showers, hail, severe squalls and at times tornadoes (*Choudhari and Chattopadhyay*, 2003). The bases of *Nor'Westers* are low, generally about a kilometer

above ground. A majority of these thunderstorms are accompanied by squalls, the frequency of squalls increasing from northwest to southeast. They do not advance more than 130-160 km into the sea and travel at a speed of 50-60 kmhr⁻¹. *Das et al.* (2006) and *Abhilash et al.* (2007a) simulated the propagation characteristics of rainband associated with *Nor'Wester*s and their microphysical structure.

So far, no comprehensive observational and modeling campaign on severe thunderstorm has been conducted over Indian region. Realizing the importance of improved understanding and prediction of these weather events and their socio-economic impact, Department of Science and Technology (renamed as Ministry of Earth Sciences), Govt. of India planned a national coordinated programme on *Severe Thunderstorm Observation and Regional Modeling (STORM)*. This is a comprehensive observational and modeling effort to be implemented during 2008-2010. Pilot phase of the this experiment has been conducted during 2005-2007 period. The data collected during the pilot phase of the STORM program has also been used in this thesis.

1.4 Scope of the Thesis

Despite some national efforts, nature of the precipitating cloud system over tropical Indian region is poorly known. Many studies have been conducted to understand the dynamical and thermodynamical structure of these severe weather phenomenon, but they are mostly in the form of case studies and are limited due to lack of observations. The microphysical processes leading to the development of these severe storms are also not well understood due to lack of mesoscale observations. The improvements in prediction of these important weather phenomena are also handicapped due to lack of mesoscale observations and insufficient understanding. This thesis focus on the observational and modeling studies on TMCS over northeast India around Kolkata during pre-monsoon (March to May) and southeast

India around Chennai during monsoon and post-monsoon (June to September and October to November) season.

The thesis has three major components:

- *Radar Observations of the TMCS.*
- *Mesoscale / Cloud Resolving Scale modeling.*
- *Assimilation of satellite and DWR observations.*

Thus, the thesis aimed to improve both understanding and prediction of severe convective storms with the following objectives:

- *Classification of the MCS based on radar observations.*
- *To understand the genesis (both the timing and location) and evolution (areal coverage, duration and propagation) of TMCS.*
- *To study the sensitivity of various microphysical schemes in simulating TMCS and microphysical and thermodynamical structure during different phases of the storm.*
- *To study the impact of various conventional and Satellite data in the simulation and short range prediction of TMCS.*
- *To understand different forcing mechanisms responsible for the generation of the spectrum of convectively generated gravity waves and their spectral and spatial structure.*
- *To assimilate the Doppler Weather Radar observations in a mesoscale model for the simulation of the organization and propagation of TMCS.*

CHAPTER 2

Radar Remote Sensing and System Description

2.1 Introduction

Radars have been increasingly used to observe the thunderstorm and MCS at various spatial scales. This chapter focuses on the basic concepts and principles of the two types of the pulsed Doppler radars. Scanning Doppler radars (meteorological radars or Doppler Weather Radars-DWR) can be used to detect the MCS by making use of the enhanced echoes arising from the clouds and hydrometeors associated with such systems. These observations added much to our knowledge and understanding of the thunderstorm structure. *Doviak and Zrnica* (1991) and *Bluestein et al.* (1995) report some radar observations during the passage of the severe and moderate convective events. On the other hand, the clear air Doppler radars (Wind Profiles-WP) is also used to study the effect of convective events on the intensity of the wind field, including the vertical velocity, radar reflectivity and turbulent energy

dissipating rate (*Gage and Balsley, 1978, 1980; Green et al., 1986; Larsen and Rottger, 1987*).

This chapter covers general discussion on the development of the radars, radar operating principles including choice of radar wavelength, scattering mechanisms of electromagnetic waves at different wavelengths, basic components of the radar system, signal processing and parameter estimation. The DWR scans 0-360° azimuth at many elevation angles out a radius of about 400 km depending on the scatters. On the other hand, WP uses fixed beam directions close to vertical and therefore only observes atmospheric properties directly over the radar. The scanning DWR provides good horizontal spatial coverage, whereas the vertically pointing WP provides a higher temporal and vertical spatial resolution view of the atmosphere. Therefore these two systems can complement each other. The WP and DWR used in the present study are 120 km apart and the comparison of precipitating convection observed with these radars are not brought about within this study. However, individual observations of the internal structure of the clouds and convection using VHF (53 MHz), UHF (1357.5 MHz) radar at Gadanki (13.5°N, 79.2°E) and DWR (2.8 GHz) at Chennai (13.0°N, 80.1°E) have been reported.

2.2 Radar Meteorology

The acronym, *RADAR* stands for Radio Detection and Ranging. The term radio is generic and applies to all electromagnetic radiation of frequencies from almost fifteen thousand cycles per seconds to a billion cycles per second. Neither a single state nor a single person is able to say, he is the inventor of the radar method. The radar is a result of an accumulation of many developments and improvements, which scientists of several nations parallelly made share. There are several milestones with the discovery of important basic knowledge and important inventions.

Initially, weather echoes used to be noise or unwanted signal for radar users. Later, through studies of the signal returned by the hydrometeors, much has been achieved in the field of radar meteorology and atmospheric science. It is difficult to trace the origin of the first radar detection of precipitation due to wartime secrecy. However, beginning in July 1940 a 10 cm radar system was operated by the General Electric Cooperation Research Laboratory in Wembley, England, a place where Dr. J. W Ryde was working. There is no documented evidence that this radar detected echoes from precipitation in 1940, but the subsequent work of Ryde published in 1946 to estimate the attenuation and echoing properties of clouds and rain evidenced that this study was undertaken because precipitation echoes were observed. Because, there was concerns on the effect of precipitation echoes on the detection of aircrafts. Thus it seems likely that radar first detected precipitation in the latter half of 1940s. The origin of radar meteorology are hence traced back to this early work of Ryde. A convective storm was tracked in 1941 using 10 cm wavelength radar in England, and multicellular storms were first looked at by *Byres and Braham* (1949), when they studied vertical wind shear and showed that a new cell grew up-shear of an old one. Most early radars were continuous-wave (CW), relying on the interference between the direct signal received from the transmitter and the Doppler-shifted signal from the moving target for detection. A pulsed-Doppler radar was first used to observe precipitation in 1953 at the Cavendish Lab, Cambridge. *Browning and Ludlam* (1962) observed the first supercell in England.

Most of the DWR systems operate near 3GHz (S-band) and few of them operates at slightly higher frequency bands at 6 GHz (C-band) and 10-12 GHz (X-band). The choice of the frequency is mainly a trade off between the attenuation of electromagnetic (E-M) waves in the atmosphere, which increases steeply with frequency and range coverage and portability of the system for a given transmitter power. The Ultra High Frequency (UHF) and Very High Frequency (VHF) radars can detect echoes caused by Bragg scattering from

refractive index fluctuations due to variations in humidity and temperature in both the clear and cloudy atmosphere, and they have now become accepted in the radar meteorology community as a valuable complement to the weather radar measurement techniques that make use of Rayleigh scattering from hydrometeors. The UHF/VHF radar typically operates in the frequency range from the low VHF band (40-50 MHz) to upper UHF band (3 GHz). To distinguish the UHF/VHF radar technique from the conventional weather radar technique, the term *clear air radar* is often used. Since the radars also measure the winds, the term *wind profiler* has gained acceptance with meteorologists.

2.2.1 Propagation of electromagnetic waves

The basic idea behind atmospheric radar is to transmit an E-M wave and to observe the effects the atmosphere has on that wave. As E-M wave passes through the atmosphere, they interact with hydrometeors. Most of the weather radars exploit this property of the E-M wave. Figure 2.1 shows the electromagnetic spectrum, within which microwave region is that used for radar system. Table 2.1 shows the main frequency bands used in radar remote sensing and their characteristic properties.

In free space wave propagates in straight lines because everywhere the dielectric permittivity ϵ_0 and the magnetic permeability μ_0 are constant related to speed of propagation ($c = [\epsilon_0\mu_0]^{-1/2}$). However, atmospheric permittivity ϵ is larger than ϵ_0 and is vertically stratified, therefore micro waves propagates at speed v (lower than c) along curved path and sometimes beam is refracted back to the surface (anomalous propagation). The path of the radar signals depends primarily on the change in height of the atmospheric refractive index, $\epsilon_r = \frac{\epsilon}{\epsilon_0} = n^2$ (since the relative permeability of air μ_r is unity). We need to show, how refractive index is related to pressure, temperature and water vapor. Hence, given a vertical profiles of these meteorological variables, one can determine the distance and strength of the radar signal at a scatterer.

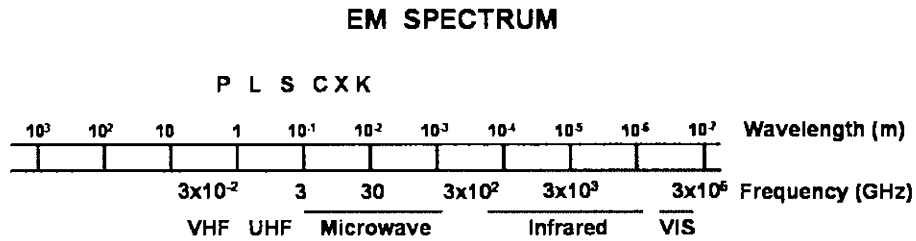


Figure 2.1: Electro magnetic spectrum

FREQUENCY BAND	FREQUENCY (GHz)	WAVELENGTH Range (cm)	METEOROLOGICAL Typical
(VHF)	0.040-0.055	100.0-1000.0	Profile
P(UHF)	0.3-1.0	30.0-100.0	Profile
L	1.0-2.0	15.0-30.0	Profile
S	2.0-4.0	7.5-15.0	10 cm
C	4.0-8.0	4.0-7.5	5 cm
X	8.0-12.5	2.5-4.0	3 cm
K _u	12.5-18.0	1.7-2.4	mm
K	18.0-26.5	1.1-1.7	mm
K _a	26.5-40.0	0.75-1.1	mm

Table 2.1: Characteristic wavelength for radar remote sensing

2.2.2 Refractive index of air and refractivity

The refractive index is proportional to the density of the molecules and their polarization. Molecules that produce their own electric field without external electrical forces are called *polar molecules*. The water vapor molecule is polar. Although, dry air molecules do not possess a permanent dipole moment, they become polarized when an external electric field is imposed on them. Without an external electric field, polar molecules have their dipole moments, randomly oriented due to thermal agitation. External forces can align these molecules so that their dipole fields add constructively to enhance the net electric

force acting on each molecule. Thus electric force acting on each molecule is the sum of external field and that produced by polarized molecules.

According to Lorenz-Lorentz formula, the permittivity of a gas depends only on the number N_v of the molecules and a factor α_T proportional to the molecules level of polarization. For a gas that contains a mixture of molecules,

$$n^2 = 1 + N_v^{(1)}\alpha_T^{(1)} + N_v^{(2)}\alpha_T^{(2)} + \dots \quad (2.1)$$

By assuming the thermal equilibrium and using the Avogadro's law and equation of state,

$$n^2 = 1 + \left[\frac{273}{1013} \right] \frac{N_{v0}}{T} (P_1^{(1)}\alpha_T^{(1)} + P_1^{(2)}\alpha_T^{(2)} + \dots) \quad (2.2)$$

where P_1 is the partial pressure of gas 1 and P_2 is the partial pressure of gas 2,

In the troposphere, we need to consider the effect of dry air as well as water vapor. Hence,

$$n^2 = 1 + \frac{C_d P_d}{T} + \frac{C_{w1} P_w}{T} + \frac{C_{w2} P_w}{T} + \dots \quad (2.3)$$

Where C is constant, P_d and P_w are partial pressure of dry air and water vapor. The last term is the contribution to the refractive index from permanent dipole moment of water vapor molecule.

Since relative permittivity ϵ_r and refractive index n of the atmosphere are near unity at microwave frequencies, it became convenient to introduce another measure of refractive property of the atmosphere, the refractivity, N defined as (*Bean and Dutton, 1964*),

$$N = (n - 1) \times 10^6 \quad (2.4)$$

$$N = \left[\frac{77.6}{T} \right] \left[P + 4810 \frac{e}{T} \right] - \left[40.3 \times 10^6 \frac{N_e}{f_0^2} \right] \quad (2.5)$$

where T is the temperature, e is vapour pressure, N_e number density of free electrons, f_0 is the radar frequency.

Refractive index of the atmosphere differs very little from that of free space. Nevertheless, a change in n in the fifth or sixth significant digit is sufficient to have a measurable effect on electromagnetic wave propagation and scattering. In addition to systematic smooth variations in the atmospheric properties, there are small scale fluctuations in temperature, pressure, humidity and electron content etc; that causes N to have small scale variations. Electromagnetic wave scattering occurs from these refractive index irregularities.

The above equation can be written as,

$$n = 1 + n_1 + n_2 + n_3 \quad (2.6)$$

where, $n_1 = 3.73 \times 10^{-1} \frac{e}{T^2}$, $n_2 = 77.6 \times 10^{-6} \frac{P}{T}$, $n_3 = -40.3 \frac{N_e}{f_0^2}$

The first term is called wet term and is important in the lower troposphere, the second term is called dry term and is favorable in the upper troposphere and lower stratosphere, the last term is called electron density term and is applicable for ionosphere. The estimate of relative contribution of each term is shown in figure 2.2 (*Gage and Balsley, 1980*).

2.2.3 Radar equation

The basic radar equation is a relation between the received backscattered signal level and the radar parameters such as transmit peak power, antenna aperture (or gain), the distance to the scattering target, the scattering parameter of the medium denoted by the scattering cross-section, σ . The classical radar equation for point target can be written as (*Sato, 1989*),

$$P_r = \left[\frac{P_t G_t}{4\pi R^2} \right] \left[\frac{\sigma}{4\pi R^2} \right] A_e \quad (2.7)$$

where P_t is transmitter power radiated by an isotropic antenna into space, R is the distance of the target from the antenna, G_t is the forward gain, A_e is the antenna aperture (area) and P_r is the return signal power at the receiver.

In meteorology, radar targets are distributed in a certain volume and we need to integrate the scattering in the radar illuminated region. In such situation, the scattering is a

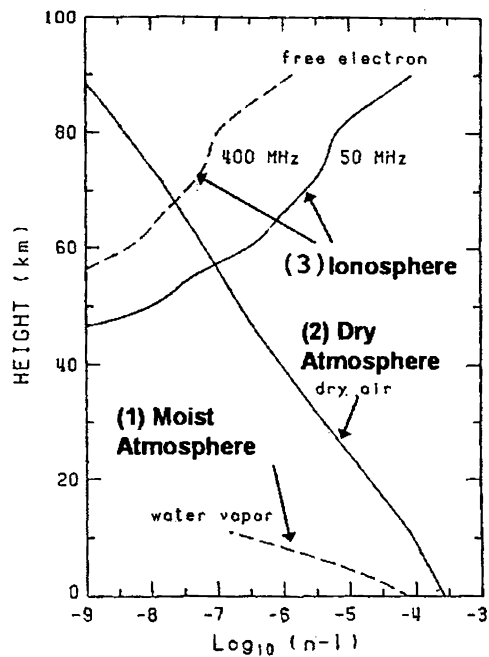


Figure 2.2: Relative contribution of water vapor, dry air and free electron to refractivity

volume phenomenon and hence the atmospheric target is called a volume target. The volume pertinent to the radar is the radar volume composed of the antenna beam spread in two dimensions at the distance R and the radar pulse spread $c\tau$, where c is the velocity of the electromagnetic radiation and τ is the radar transmitter pulse width. In deriving the radar volume at distance R , we tactically assume that all the transmit power is contained in 3db width of the antenna. By assuming a Gaussian beam shape, the radar volume which contains the full power and can be written as (Probert-Jones, 1960),

$$V = \frac{\pi R^2 \theta \phi c \tau}{16 \ln 2} \quad (2.8)$$

where θ and ϕ are the elevation and azimuth beam widths of the antenna.

Therefore, Equation 2.7 becomes,

$$P_r = \frac{P_t A_e^2 \theta \phi c \tau \eta}{\lambda^2 (64 \ln 2) R^2} \quad (2.9)$$

If we consider the transmitter loss (α_t) and receiver loss (α_r), then $L = \alpha_t \alpha_r$ then Equation 2.9 takes the form (Rao, 1990),

$$p_r = \left[\frac{c}{64 \ln 2} \right] \left[\frac{P_t A_e^2 \theta \phi \tau L}{\lambda^2} \right] \left[\frac{\eta}{R^2} \right] \quad (2.10)$$

The first term in Equation 2.10 is known as radar constant, the second term represent the radar parameters and the third term represent the target parameters. The received signal power has to compete with the noise power which would be present at the input to the receiver called the Low Noise Amplifier (LNA). If the background (cosmic) noise temperature at the operating wavelength is T_B and if the LNA noise temperature is T_n , then the equivalent noise temperature at the input to the radar LNA would be $T_{en} = (\alpha_r T_B + T_n)$ and the corresponding noise power P_n is given by $P_n = K T_{en} B$, where K is the Boltzman constant and B is the nose band width. The ratio (P_r/P_n) is the single pulse signal to noise ratio (SNR).

2.2.4 Scattering theory

The amount of energy backscattered from the hydrometeors depends upon the number of particles within the pulse volume of the radar beam, their composition, relative position, shape and orientation. The total backscattered energy is the sum of the energy backscattered by each of the scattering particles. However, the particles do not scatter isotropically and therefore, a backscattering cross-section is defined as the equivalent area required for an isotropic scatter to return to the receiver, the power actually received. The backscattering cross-section for spheres is expressed as,

$$\sigma = \frac{\pi D^2}{4a^2} \left[\sum_{n=1}^{\infty} (n-1)^n (2n+1) (a_n - b_n)^2 \right] \quad (2.11)$$

Where, D is the drop diameter and $a = \frac{\pi D}{\lambda}$ is called the electric size, λ is the wavelength and a_n and b_n are coefficients involving Bessel and Hankel functions which relates the scattering angle, the electric size complex refractive index.

When drop diameter is small compared with the wavelength, the scattering is known as Rayleigh scattering and σ may be simplified as,

$$\sigma = \frac{\lambda^2 a^6}{\pi} \left| \frac{m^2 - 1}{m^2 + 2} \right|^2 \quad (2.12)$$

where m is the complex index of refraction, $n - ik$, where n is the ordinary refractive index and k is an absorption coefficient and $m^2 = \epsilon_r$ is the relative permittivity. Therefore,

$$\sigma = \frac{\pi^5}{\lambda^4} \left| \frac{m^2 - 1}{m^2 + 2} \right|^2 D^6 \quad (2.13)$$

The above equation shows that the scattering cross-section is proportional to the sixth power of the drop diameter. Then the reflectivity,

$$\eta = \frac{1}{\Delta v} \sum_{vol} \sigma_i = \frac{\pi^5}{\lambda^2} K^2 \frac{1}{\Delta v} \sum_{vol} D_i^6 \quad (2.14)$$

where $K = (m^2 - 1)/(m^2 + 2)$.

The use of radar reflectivity η is only valid if the scattering particles are very small compared with the radar wavelength. In the real atmosphere, the particles may not be spheroids as is the case of ice crystals. Hence, a quantity known as effective radar reflectivity η_e is defined (*Atlas et al.*, 1964; *Battan*, 1973) as the summation per unit volume of the sixth power of the diameter of spherical water drops in the Rayleigh scattering region that would back scatter the same power as the measured reflectivity and is measured in dBZ units.

From the early beginning of the use of weather radars, it was noticed that, occasionally echoes occurred from an atmosphere, which do not contain hydrometeors. These echoes being produced by turbulent inhomogeneities in the atmospheric refractive index, provided that the radar is sensitive enough.

The scattering and reflection mechanisms responsible for the clear air radar (VHF/UHF) signal return have been described in detail by *Balsley and Gage* (1980) and *Gage and Balsley* (1980). They are classified generally as: (i) Turbulent scatter, (ii) Fresnel (Partial)

reflection/scatter and (iii) Thermal (incoherent or Thomson) scatter. The first two mechanisms provide coherent scatter which results from macroscopic fluctuations in refractive index associated with turbulence. The third arises from Thomson scatter by free electrons in the ionosphere and the signal return is characterized by statistical fluctuations of electron density due to random thermal motions of the electrons and ions (*Evans, 1975*).

2.2.5 Turbulent scattering or Bragg scattering

The regions of atmospheric refractive index inhomogeneities occur in areas of turbulence, in layers of enhanced stability, in wind shear cells of free convection or in inversion with sharp gradients of temperature and moisture. The scattering mechanism from refractive index inhomogeneities is quite different from that for hydrometeors and is expressed in terms of structure parameter of refractive index (*Ottersten, 1969*);

$$C_n^2 = \left[\frac{\eta}{0.38} \right] \lambda^{1/3} \quad (2.15)$$

and

$$\eta = 0.38 C_n^2 \lambda^{-1/3} \quad (2.16)$$

Where λ is the radar wavelength and η is the reflectivity for backscatter from the refractive index inhomogeneities (*Doviak and Zrnic, 1991*). Hence it is clear from the scattering theory that, scattering mechanism has a strong dependence on the radar wavelength. The reflectivity associated with clear air turbulence scatter (Bragg scatter) has a weak dependence on the wavelength as compared to Rayleigh scattering from precipitation particles. Rayleigh scattering is enhanced at shorter wavelengths compared to Bragg scattering.

According to the theory of radio wave scattering from turbulent fluctuations of refractive index, the radar backscattered signal arises from the spatial Fourier components whose wavelength is equal to one half of the radar wavelength λ_R . In order to have coherent

backscatter, the condition to be satisfied is $\lambda_{min} < \lambda_{R/2} < \lambda_{max}$. Where, λ_{min} and λ_{max} are related to the inner (l_0) and outer (L_0) scale size of turbulence.

2.2.6 Fresnel reflection and scattering

Fresnel (partial) reflection occurs from a sharp gradient in refractive index that is horizontally coherent over a scale greater than Fresnel zone. Radar observations at VHF have shown evidence for the importance of Fresnel reflections from horizontally layered structures in the neutral atmosphere of troposphere and stratosphere (*Gage and Balsley, 1978; Gage et al., 1979; Röttger and Liu, 1978*) and electron density stratifications in the mesosphere (*Fukao et al., 1994*). The power received by the radar due to reflection from a single discontinuity in the radio refractive index is given as (*Friend, 1949*),

$$p_r = \frac{\alpha p_t A_e^2 |\rho|^2}{4\lambda^2 R^2} \quad (2.17)$$

Where, α is the efficiency factor for antenna transmission lines. The partially reflected power is maximum when the radar beam is normal to the extension of the discontinuity. The amplitude reflection coefficient, $|\rho|^2$ cannot be determined uniquely, since it depends strongly on the refractive index profile over a distance of less than the one radar wave length. The general case of partial reflection in which there are many closely spaced layers randomly distributed in height is called Fresnel scatter.

2.2.7 Doppler principles

When the radar target is moving, the returned signal is shifted in frequency compared with the signal that would have been returned from a stationary target. The shift of frequency caused by a moving target is referred to as the doppler shift, f_D of the returned signal, where ignoring the radar losses,

$$f_D = -\frac{2V}{\lambda} \quad (2.18)$$

Where λ is the radar wavelength and V is the radial velocity of the target directed towards (conventionally negative) or away from the radar. Hence the measurement of f_D gives the velocity of the target.

The time of return echo is fixed in the inter pulse period (IPP) between successive pulses. An echo which occur after the transmission of the next pulse known as second time around echoes will give a misleading range. Hence maximum unambiguous range R_{MAX} is defined by the pulse repetition frequency (PRF) of the radar,

$$R_{MAX} = \frac{c}{2PRF} \quad (2.19)$$

In order to measure a frequency fluctuation f , the echo must be sampled at a rate of atleast $2f$. Therefore the maximum Doppler shift frequency f_{MAX} , which can be detected unambiguously, is given by,

$$f_{MAX} = \frac{PRF}{2} \quad (2.20)$$

Then the maximum Doppler velocity, V_{MAX} known as *Nyquist velocity* is given by,

$$V_{MAX} = \pm \frac{PRF\lambda}{4} \quad (2.21)$$

Velocities outside the Nyquist interval of $2V_{MAX}$ are referred to as folded. By combining these two equations yields,

$$V_{MAX} = \frac{c\lambda}{8R_{MAX}} \quad (2.22)$$

Clearly, it is necessary to compromise between V_{MAX} and R_{MAX} . The product of which is a constant $\left(\frac{c\lambda}{8}\right)$. This is widely known as *Doppler dilemma*. The phase detection of the backscattered signal using the transmitted signal as a reference is known as the *bipolar video* or *I (in phase) and Q (quadrature phase)* components of the signal. The radial wind speed (speed of the target), not the direction is therefore contained in either *I* or *Q* component.

$$I_t = \frac{|A|}{\sqrt{2}} u \left[t - \frac{2R}{c} \right] \cos \left[\frac{4\pi R}{\lambda} - \Psi + \Psi_i \right] \quad (2.23)$$

$$Q_t = \frac{|A|}{\sqrt{2}} u \left[t - \frac{2R}{c} \right] \sin \left[\frac{4\pi R}{\lambda} - \Psi + \Psi_i \right] \quad (2.24)$$

Where $2R$ is the total path traversed by the incident and scattered waves; A is the voltage amplitude; c is the speed of light; Ψ_i is the phase shift produced by the scattering target, Ψ is the phase of the transmitted signal, $(n\pi R)/(\lambda + \Psi_i)$ is the phase of the received signal. The sum of I^2 and Q^2 equals the input power $\frac{|A|^2}{2}$ averaged over the cycle of the signal, and I and Q pairs are the time series sample of the Doppler shifted signal.

Fourier analysis of this series gives the power density spectrum or Doppler spectrum, $S(V)$ of the velocities (using the notation of *(Burgess and Ray, 1986)*). The returned power to the radar represents a combined signal from a variety of targets (distributed targets) in the radar pulse volume. The return power is distributed over a range of Doppler velocities. That is, a pulsed Doppler radar detects a spectrum of Doppler shift frequencies. This is known as the Doppler spectrum. Doppler spectrum is a discretized sample between V_{max} and V_{min} . The Doppler Velocity Spectrum (DVS) contains information about the motion of the scatterers as well as the effects of turbulence, shear, and antenna beam width. Total power is the area under the curve (approximated as a Gaussian distribution). Because of the relation of power and reflectivity through the radar equation, the Doppler Velocity Spectrum (DVS) can be thought of as the reflectivity weighted distribution of radial velocities in pulse volume (i.e., radial velocities weighted by D^6). The integral or the area under the spectrum is the reflectivity or zeroth moment of the spectrum, the mean velocity \bar{V} is the first moment of the spectrum and the second moment gives the spectrum width..

$$P = f_0(V) = \int_{-\infty}^{\infty} S(V) dV \quad (2.25)$$

$$\bar{V} = f_1(V) = \frac{1}{P} \int_{-\infty}^{\infty} V S(V) dV \quad (2.26)$$

Higher order moments of the spectrum are given by,

$$f_n(V) = \frac{1}{P} \int_{-\infty}^{\infty} (V - \bar{V})^n S(V) dV \quad (2.27)$$

Where n is the moment of the spectrum. The second moment ($n=2$) is the variance of the spectrum. The spectrum width is determined by a number of factors like, the spread of velocities of the scatterers, the turbulence in the sampling volume including variations in speed for different scatterers, shear of the wind along and across the radar beam and antenna rotation rate.

2.3 Doppler Weather Radar

The DWR consists of a transmitter to generate microwave signal, an antenna to send the signal out to space and to receive energy scattered (echoes) by targets around, a receiver to detect and process the received signals and a display to graphically present the signal in usable form. Magnetrons, Klystrons and traveling wave tubes still continue to be the main powerhouse of the most radars. The antenna collimates the microwave energy into narrow beam while sending it out. Larger the size of the antenna, better the angular resolution. The antenna generally rotates about a vertical axis scanning the atmosphere in azimuth. It is also capable of changing its elevation by rotating about a horizontal axis so that probing of the hemispherical volume of the atmosphere with the radar as the center is possible, according to the scanning strategy decided by the user. Figure 2.3 shows the DWR block diagram. In modern radars the signal processing is done by dedicated computers, they are commonly known as signal processors. The signal processor unit performs analogue to digital conversion, quality assurance and applying various corrections to the data sets in addition to performing complex statistical signal-processing jobs.

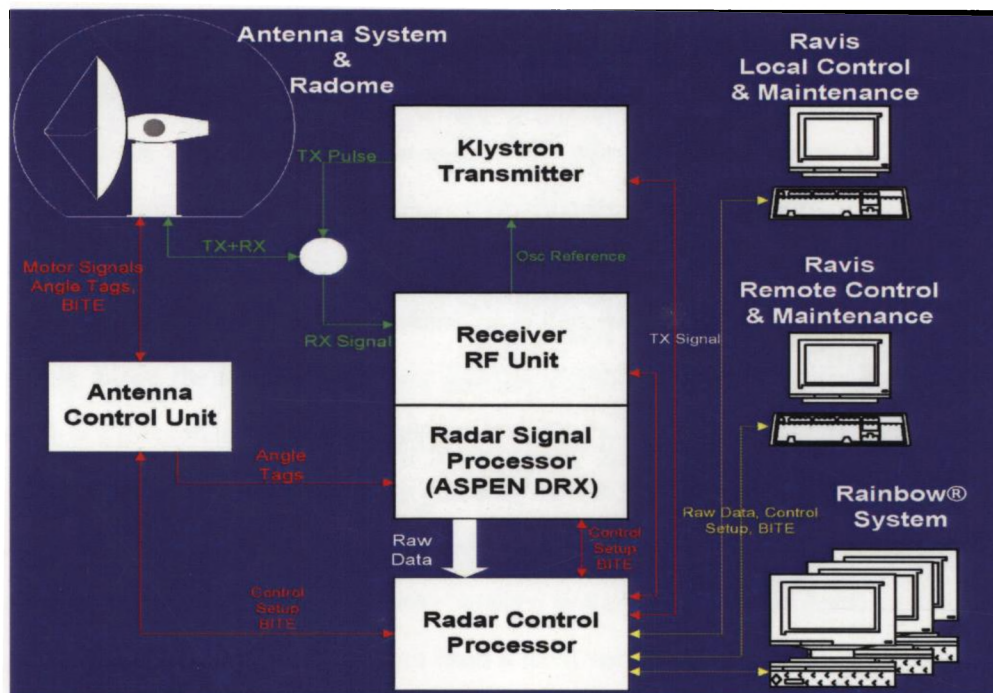


Figure 2.3: Block diagram of DWR

2.3.1 Overview of the DWR principles

Radars used in meteorology are mainly distinguished by their operating frequencies. Widely used frequencies in DWR are X-band (10 GHz, $\lambda=3$ cm), C-band (5 GHz, $\lambda=6$ cm), S-band (3 GHz, $\lambda=10$ cm). X-band radars are mainly used for thunderstorm studies and tracking of airborne balloons for upper air wind computations. S-band radar is used for rainfall measurements and studies of tropical cyclones and similar synoptic scale systems. S-band frequency is more suitable for penetrating deep into intense weather systems without much attenuation, whereas, they are not suitable for cloud physics studies as the reflections are too weak from cloud particles. Moreover, size of the antenna and other system components are much bigger in S-band in comparison to other type of radars. C-band radar is a compromise between X-band and S-band radars. Several X-band and S-band radars

have been installed by India Meteorological Department (IMD) for storm and cyclone detection. Most of these radars are of the type pulsed-monostatic. Based on the capability to measure wind, weather radars can be divided into two types, conventional radar measuring reflectivity alone and modern Doppler radar measuring radial velocity, velocity spectrum and reflectivity. In DWR, the Doppler effect as applicable to microwaves is exploited and in this case both the source and observer are collocated, but the echo-producing target are moving. Since, the forward and return trips are subjected to this effect; the frequency shift, which is a measure of relative velocity, is doubled.

In digital radars the receiver output is monitored at regular but fast intervals of the order of a μs or less, and the instantaneous output power is digitized and used as the representative echo power for the sample volume between that and next sample. Instantaneous power output of the receiver contains return from a fixed volume of the atmosphere called range bin. The bin size is a function of pulse width and antenna beam width. For a nominal $1 \mu s$ pulse and 1° wide beam, the bin size would be $150 \text{ m} \times 1^\circ$. The signal processor would get data samples 150 m wide in space repeated every 150 m , giving a continuous effect. For a maximum range of 300 km , PRF should be less than or equal to 500 and corresponding inter-pulse listening period would be 2 milliseconds. Assuming a scan rate of 3 rpm , scan period for 1° in azimuth would be around 56 milliseconds during which period, returns from nearly 28 pulses would be available for processing. Averaging returns from 28 pulses would improve the quality of the data by filtering out random noise signals. This is known as time averaging.

A series of data points or bins thus obtained by averaging returns during the period between two antenna positions separated by 1° constitute a ray. Data acquisition is done bin-by-bin to form a ray, ray-by-ray to form a slice and slice-by-slice to form a quasi cylindrical volume. As the short pulse is $1 \mu s$, the smallest possible radial resolution is 150 m while the azimuth and elevation resolution vary continuously throughout the ray due to

beam spreading, with range at the rate of about a km for every 60 km. It is meaningless to process the data with range resolution of 150 m when azimuth and elevation resolutions are of the order of 5 to 6 km. In such situations, few range bins are clubbed together and treated as a single data point, this is known as range averaging.

2.3.2 Display of base products

The reflectivity factor (Z), radial velocity (V) and velocity spectrum width (W) are the three base data directly observed/measured by the radar. These data can be displayed in the following formats.

Plan Position Indicator (PPI): The PPI(Z) is quite similar to conventional radar scope display of Z for a given elevation at all azimuth values, with color-coded schemes for display and storage in digital form. This display is possible for all elevations at which data are collected. The PPI(V) gives the radial velocity on a PPI scope. The PPI(W) shows the velocity spectrum width indicating turbulence.

Range Height Indicator (RHI): This is another widely used form of display of base products in the two-dimensional Cartesian coordinate system, having the curvature corrected range as X-axis and height as Y-axis for an elevation scan at fixed azimuth. A similar display with more flexibility of selecting the cut axis is available from a volume scan of a modern DWR, which is generally known as vertical cut.

Constant Altitude PPI (CAPPI): This is a color-coded display for an user defined altitude of any of the Z , V and W in the PPI scope. As such, it displays weather phenomena as occurring over a curved surface parallel to the earth's surface.

Maximum display (MAX) is a display of three partial images into a single imagery. The central image is the PPI displaying the highest value of the parameter chosen for the volume scan. The top portion of the imagery is the north-south view of the highest measured value in Cartesian X-direction. The right side of the image is the highest measured value

in the west-east Cartesian X-direction. Figure 2.4 shows typical PPI(Z) and MAX(Z) from precipitation and cloud observed by DWR at Kolkata at 21:10 UTC of 18 April 2006.

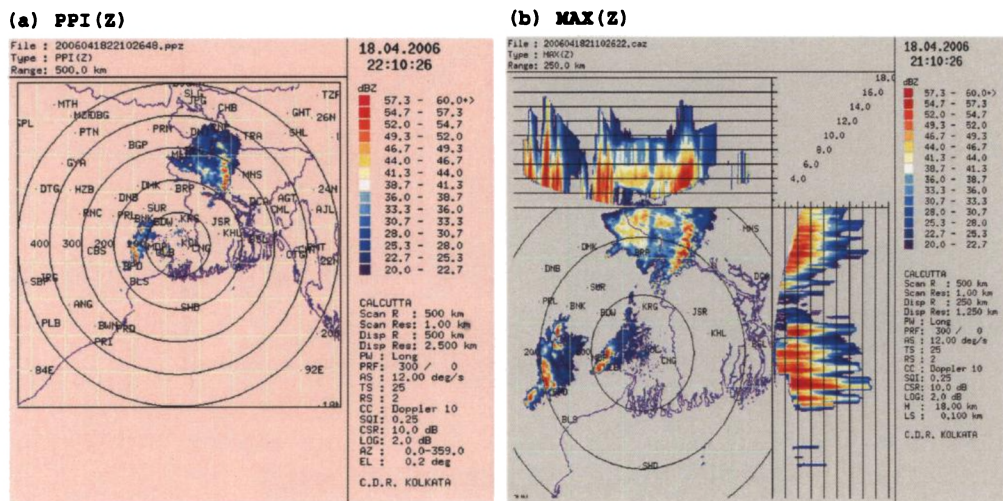


Figure 2.4: A typical PPI(Z) and MAX(Z) display of a convective system

2.4 MST Radar Principles

The Mesosphere Stratosphere Troposphere (MST) radars are used to investigate the atmospheric winds, waves, turbulence and atmospheric stability in the Mesosphere, Stratosphere and Troposphere by using echoes obtained over the height range 1-100 km. Let a pulsed electromagnetic wave of duration (pulse width) Δt is transmitted at time T_1 , the radar pulse reaches the range r_a at time $t_1 = \frac{r_a}{c}$, a target at r_a can scatter or reflect back the radar signal in some direction. A small fraction of the signal received at the receiver at time $t_1 = 2t_1 = 2\frac{r_a}{c}$. Assuming the scatterers fills the radar volume and echoes from range between $r_a - \frac{\Delta r}{2}$ and r_a reaches the radar at time t_1 and those from r_a and $r_a + \frac{\Delta r}{2}$ are received at $t_1 + \Delta t$. The pulse of duration Δt at one time illuminates a volume at r_a extended along a range $\Delta r = c\frac{\Delta t}{2}$. This is the range gate from which the radar echoes are received. The

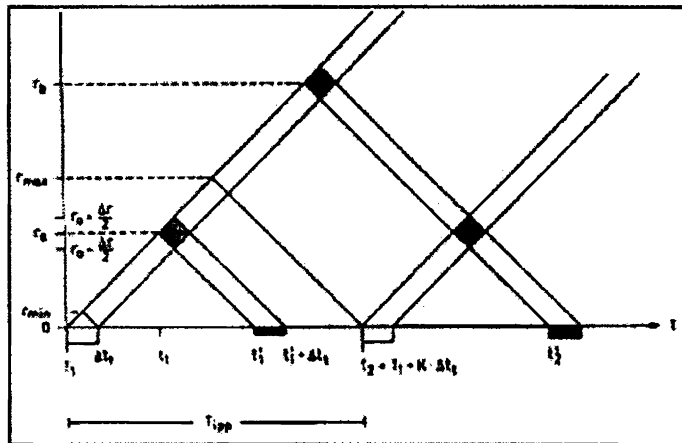


Figure 2.5: Operating principles of VHF radar

ratio of the pulse width to inter pulse period (IPP) is called the duty cycle ($d = \frac{\Delta t}{IPP}$). The transmitted power P_t is the product of the duty cycle and the transmitted pulse peak power P_p .

Normally the PRF kept constant and hence range aliasing may occur. As depicted in figure 2.5, at time t_2 , an echo of pulse T_2 is received from range at r_a and an echo of pulse T_1 is received from range r_b . These echoes returned from separate scatter volume and hence are uncorrelated but still their power accumulates in the same receiver range gates. If no special arrangements (eg: pulse coding and non-periodic IPP) are made, the maximum unambiguous range is $r_{max} = c \frac{T_{IPP}}{2}$. The minimum range r_{min} obviously is given by the pulse duration Δt and some instrumentally entailed transmission time between transmission and reception.

2.4.1 Signal detectability

It can be seen that the reflectivity of turbulent scatter varies with radar frequency as $f_R^{1/3}$ for troposphere and stratosphere (Equation 2.16). Hence, 53 MHz VHF radar with $\lambda \sim 6\text{m}$ is most sensitive to 3m size irregularities in refractive index. *Gossard et al.* (1986) showed that, in order to observe atmospheric turbulence, the clear air sensing radar must have a wavelength greater than $\sim 4.2l_0$. The inner scale l_0 is proportional to the Komolgorov microscale $\eta_0 = (\frac{\nu^3}{\varepsilon})^{1/4}$, where ν is the kinematic viscosity and ε is the eddy dissipation rate. Since ν increases with height, longer wavelength radars are needed to observe turbulence in the middle atmosphere (*Balsley and Gage, 1980*).

Following the Equation 2.10, the single pulse SNR can be written as,

$$\left[\frac{S}{N} \right] = \left[\frac{P_r}{P_n} \right] = \frac{P_t A_e L c \tau \eta}{R^2 (64 \ln 2) K (\alpha_r T_B + T_n) B} \quad (2.28)$$

In practice, one coherently integrates n_c number of radar return pulses at every observed height. The effect of this coherent integration is equivalent to reducing the effective noise band width by n_c . The time series of coherently integrated pulses is normally Fourier transformed to obtain the spectrum of the return signal. A digital Fourier transform operation with P number of coherently integrated pulses (each with n_c coherent integration) is normally performed. The observed signal spectrum has thus a total of P Doppler bins and an atmospheric return signal could lie anywhere among these depending upon the Doppler shift suffered by the return signal corresponding to the mean wind velocity at the height of observation in the atmosphere. The atmospheric signal spectrum has finite width and it may encompass say m number of Doppler bins. The spectral processing can thus improve the detectability of the atmosphere signal by a factor $(\frac{P}{m})$ over and above the improvements obtained by coherent integrations. The detectability $(\frac{S}{N})_d$ can then be written as,

$$\left[\frac{S}{N} \right]_d = \frac{P_t A_e L c \tau}{R^2 (64 \ln 2) K (\alpha_r T_B + T_n) B} \eta \frac{n_c P}{m} \quad (2.29)$$

Equation shows that if the radar parameters are known through design/measurement, and $(\frac{S}{N})_d$ is found out from the spectral domain analysis. The value of η , the radar reflectivity can be estimated at different height in the atmosphere from the corresponding return signal spectrum.

2.4.2 Power aperture product and its significance

The product of peak mean pulse power and its antenna area is defined as the power aperture product. The system sensitivity and high resolution depends upon the average power of the transmitter and the pulse width. A large pulse width is necessary to increase average power to maximize the SNR. But to observe some of the atmospheric phenomena, typical resolution of the order of 150 m corresponding to a pulse width of 1 μ s is required. But the lower pulse width will cause weak return signals from the higher altitudes. So, a large pulse width is needed to probe the higher altitudes. For large pulse widths range resolution is poor. Hence pulse compression techniques are often used to achieve a good height resolution, without compromising large pulse widths. Background noise temperature at 53 MHz (operating frequency for Indian MST radar) is typically 6000 K and thus the receiver performance is almost always limited by cosmic background noise and not the noise figure of LNAs. Typically the power aperture values of the order of 10^8 to 10^{10} Wm^2 are required for successful MST radar campaigns.

2.5 Configuration of Indian MST radar

The MST radar has been established in India as National MST Radar Facility (NMRF) at Gadanki, near temple city of Tirupati (13.5 °N, 79.2 °E) now known as National Atmospheric Research Laboratories (NARL). Figure 2.6 shows the radar location and the topography. The MST radar is comprised of a high resolution two-dimensional phased array, high

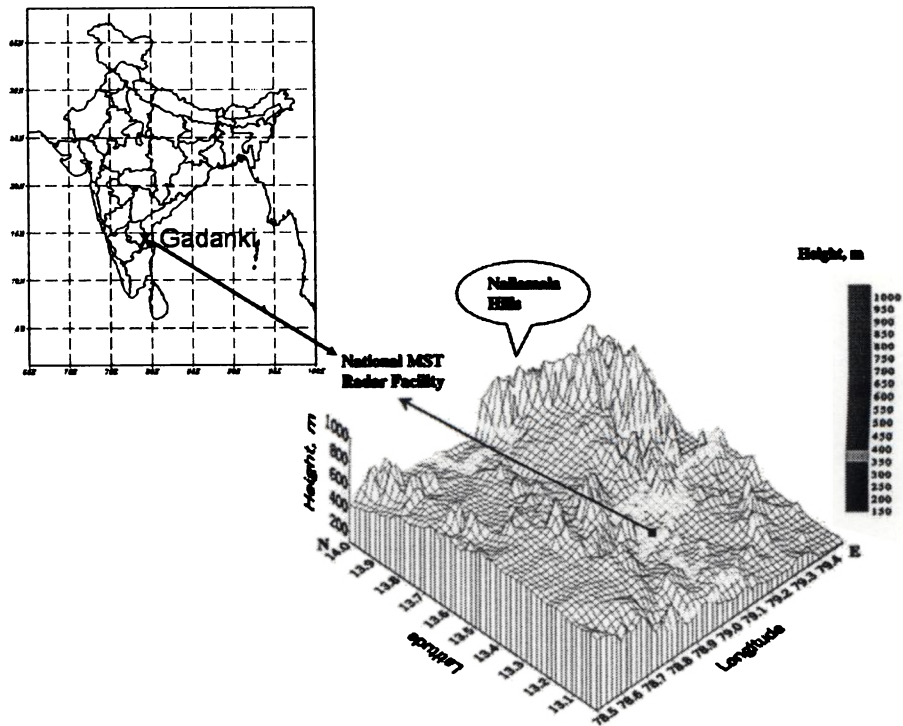


Figure 2.6: Location and topography of Indian MST radar site

power transmitters with appropriate feed network, T/R switches, a phase coherent receiver with quadrature channels, a signal processor consisting of two identical channels of A/D converter, decoder and integrator, a computer interface and a mini/super micro computer with essential peripherals and software support. The Indian MST radar is a highly sensitive, pulse-coded, coherent VHF phased array radar operating at 53 MHz with an average power aperture product of $7 \times 10^8 \text{ W m}^2$. More details can be found from *Rao et al.* (1995). A simplified block diagram of the radar system is shown in Figure 2.7 and system specifications of the radar are presented in Table 2.2.

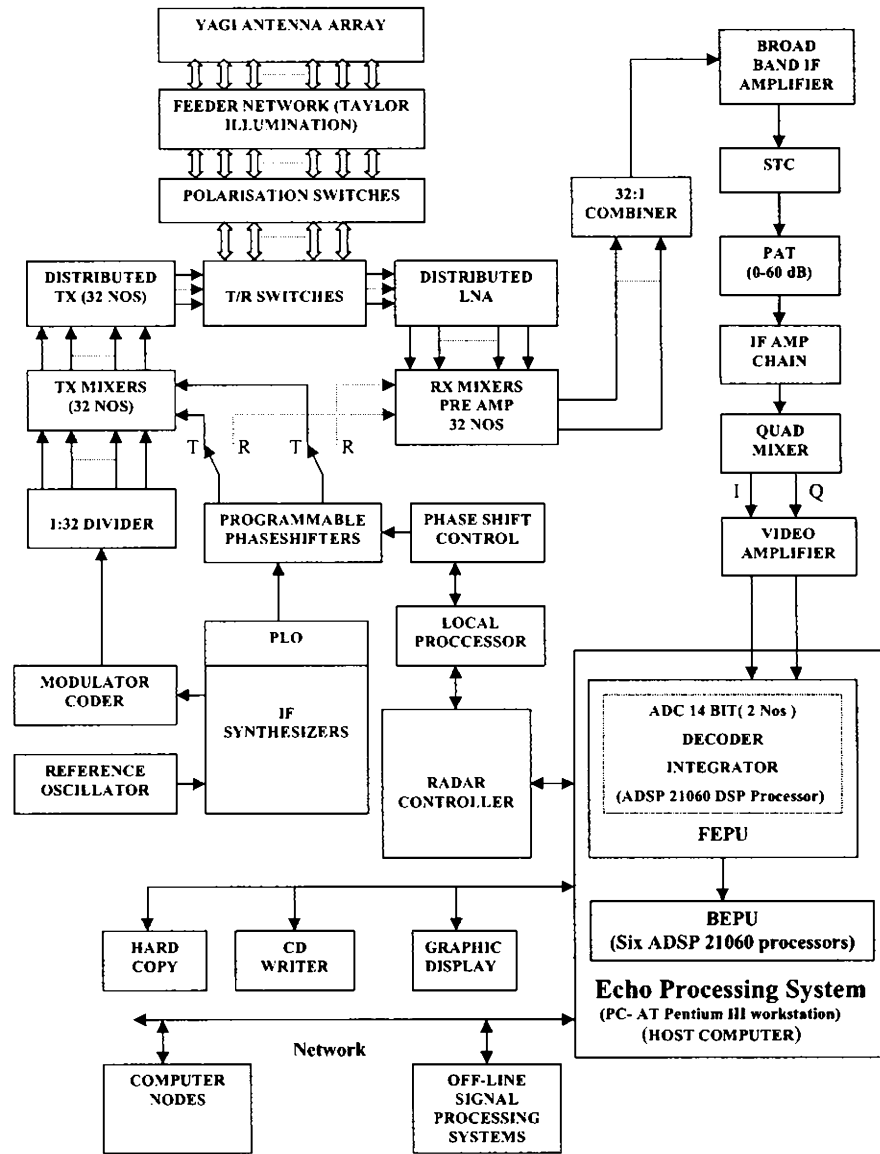


Figure 2.7: Block diagram of MST radar

PARAMETERS	SPECIFICATIONS
Location	Gadanki(13.45°N, 79.18°E)
Frequency	53 MHz
Peak power	2.5 MW
Peak power aperture product	$3 \times 10^{10} W m^2$
Maximum duty ratio	2.5 %
Number of Yagi antennae	1024
Beam width	3°
Angular coverage of beam scans	$\pm 20^\circ$
Pulse width	1 to 64 μs (coded/uncoded)
Pulse repetition frequency	62.5 Hz – 8 kHz
Maximum number of coherent integrations	512
Maximum number of range bins	512
Maximum number of FFT points	1024
Radar controller	IBM PC-AT featuring programmable experiment specification file
Computer system	DSP processors for data acquisition and processing

Table 2.2: System specifications of MST radar at Gadanki

2.5.1 Antenna array and feeder network

To acquire the required power aperture product, a large antenna is required. This can be done by using a phased array antenna. The beam steering is achieved through electronic control of phases at the feed points. The required side lobe levels are realized by using different illumination functions like Taylor illumination function etc. The phased array of the Indian MST radar consists of two orthogonal sets, for each polarization, of 1024 three-element Yagi-Uda antennas arranged in a 32x32 matrix over an area of 130 m x 130 m. The two sets are co-located with pairs of crossed Yagis mounted on the same poles. The intermittent spacing among the elements is selected such that no grating lobes occur. An interantenna spacing of 0.71λ is used in both principal directions that allows a grating

lobe free beam scanning upto an angle of about 24° from the zenith. The desired power distribution across the array is accomplished in one principle directions by the differential powers of the transmitters and other directions by appropriate coupling coefficients of the series feed network (Sarkar *et al.*, 1988). The feeder network consist of high power low loss cables, duplexers, polarization switches, directional couplers etc. The tapering of the antenna illumination is achieved by using directional couplers.

2.5.2 High power transmitter system

Since, MST radar needs a coherence between transmit and receive systems, MOPA (Master Oscillator Power Amplifier) type transmitter is used. The large peak power is achieved using vacuum tubes, power amplifier and solid state drivers. A total transmitter power of 2.5 MW (peak) is provided by 32 transmitters ranging in power from 15 kW to 120 kW, each feeding a sub array of 32 Yagis. This large power is distributed among various elements of the antenna as per the illumination function. The transmitter consists of four stages and associated power monitoring and controlling, and interlock circuits. The amplifier chain consists of a solid state amplifier (SSA), pre-driver (PDR), driver (DDR) and high power amplifier (HPA). The input to the transmitter is a low level (1 mW) pulse-modulated (coded/uncoded) signal at 53 MHz generated by mixer, which receives as inputs a 5 MHz pulse modulated signal and appropriately phase shifted 48 MHz local oscillator (LO) signal. The radar beam can in principle, be positioned at any look angle, but is currently programmed to sequence automatically any combination of 18 look angles over a range of $\pm 20^\circ$ from zenith in the NS and EW planes with a resolution of 1° . It is possible to transmit both coded and uncoded pulses with pulse repetition frequency (PRF) in the range 62.5 Hz to 8 kHz, keeping the duty cycle from exceeding the limit. Both the coded and uncoded pulses can be varied in pulse width from 1 to 32 μs in multiples of two. The coded pulses are either 16 or 32 baud biphas complementary pairs with baud length of 1

μs , providing a range resolution of 150 m. The output to the transmitter is connected to an antenna sub array through a transmit-receive (T/R) duplexer and a polarization selection switch.

2.5.3 Receiver

The front end units of the receiver, consisting of a blanking switch, a LNA, and a mixer-pre amplifier for each of the 32 channels, are located in the four transmitter huts, eight in each of them. The receiver, a conventional super heterodyne system employing highly stable oscillator derived from the same master oscillator feeding the transmitter to ensure phase coherency for extraction of Doppler information. The receiver has a large gain and large dynamic range for signal handling. The complex signal is recovered through I and Q channels whose outputs are converted into digital data using fast ADCs. The quadrature (I and Q) outputs of the receiver are limited to ± 5 volts and given to a pre-processor unit consisting of two identical channels of ADC, decoder and coherent integrator, and a common interface. The ADC is of 12 bit resolution to match the dynamic range of the receiver and of $0.5 \mu\text{s}$ conversion time to meet adequately the requirement of 1 MHz sampling rate. The decoding operation essentially involves cross correlating the incoming data from the ADC with the replica of the transmit code. Coherent integration is a processing step introduced to effect a significant reduction in the volume of the data without compromising in any way the information to be derived from the signal.

2.5.4 Exciter and radar controller

The exciter unit generates all the RF and timing and control signals for various sub-systems of the radar. It comprises a master reference oscillator, a two-channel frequency synchronizer, a phase-locked oscillator, a P-controlled bi-phase coder and a timing signal generator. The radar operates under instruction from IBM PC-AT based radar controller (RC) which

executes an experiment according to the data given in the form of an experiment specification file (ESF). The main function of RC is to set up, control, and synchronize the operations of the various subsystems during the normal operation of the radar. On any experiment, once the radar parameters are specified in the form of ESF, the RC takes over the operation from automatic data acquisition and completes the run without any intervention.

2.5.5 Data acquisition and signal processing

The MST radar data is usually processed in two stages; on line and off-line. Figure 2.8 shows the data processing sequence. The online processing significantly compresses the data volume by time averages and usually produces power spectra and the off-line calculations for parameter extraction (*Farley, 1984*).

The input to the data processing system is the preprocessed data after decoding and coherent integration in the complex format. Coherent integration is the technique that filters much of the wide band noise and reduces the data volume to the signal processor without distorting the information that is contained in the radar returns. The detected quadrature signals are integrated for many pulses over a period in order to increase Signal to Noise Ratio (SNR). This is coherent integration. The complex time series of the samples are subjected to Fast Fourier Transform (FFT) for online computation of the Doppler power spectrum for each range bin of the selected range window. The Doppler spectra are recorded and transmitted for off-line processing. There is a provision, however to record raw data (complex time series samples) directly for any application, if so desired. The off-line data processing for parameterization of the Doppler spectrum is carried out following the method given by *Riddle (1983)*, as suitably modified by *Anandan (1996)*. In this method it defines the number of spectra peaks for the same range gate and tries to extract the best peak, which satisfies the criteria chosen before the estimation. This method involves the following steps. The DC contribution, which is arising either from nonfading clutter or uncancelled system

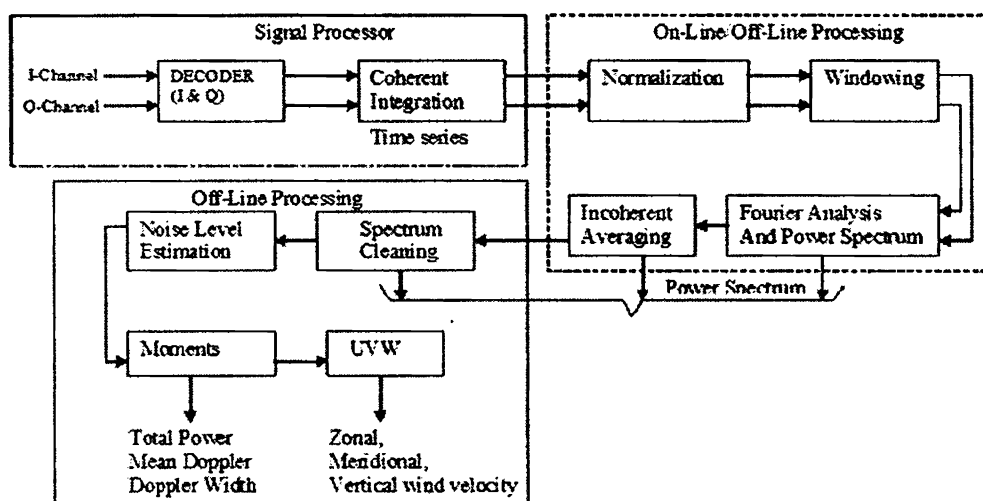


Figure 2.8: Flow diagram of signal processing

biases or both and is eliminated by replacing the spectral point at zero frequency value with the average of two adjacent points (3 point DC removal) or with the four adjacent points (5 point DC removal). The data are further edited to remove if any interference band, that might run through the entire range window and is subtracted out by estimating it in a range bin where it dominates the real signal. After removing the interference from the spectra, suitable incoherent integration can also be done off-line to improve the signal detectability and better estimate of spectral parameters. The spectral parameters viz. total signal power, mean Doppler velocity and velocity variance are obtained from the three lower order moments of the spectrum. A typical spectrum is given in figure 2.9.

The spectrum may contain noise as background and it needs to be removed as a first step to compute the moments. The average noise value for each range bin is estimated following the objective method of *Hilderbrand and Sekhon (1974)*. Now, the median noise level is calculated and subtracted from all the range bins of the spectral frame. For each range bin, the highest peak in the spectrum is recognized as the signal and its spectral window

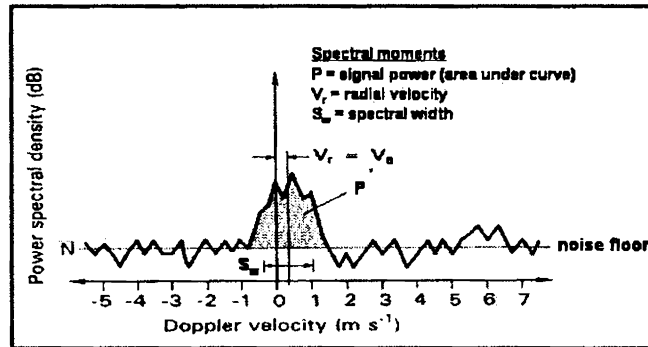


Figure 2.9: A typical Doppler spectrum

is determined by noting all the contiguous points that are above zero level. The three low order (0^{th} , 1^{st} and 2^{nd}) are computed through numerical integration using the expression given by *Woodman* (1985).

2.5.6 Computation of three components of the wind vector

For presenting the observation results in physical parameters, the Doppler frequency and range bin have to be expressed in terms of corresponding radial velocity,

$$V = \frac{cf_d}{2f_c} = \frac{\lambda f_d}{2} \quad (2.30)$$

and vertical height,

$$H = \frac{ct_r \cos \theta}{2} \quad (2.31)$$

Where c is the velocity of light in free space, f_d is the Doppler frequency, f_c is the carrier frequency, λ is the carrier wavelength (here 5.86 m), θ is the beam tilt angle and t_r is range time delay.

After computing the radial velocities for different beam positions, the absolute velocities (UVW) can be calculated. To compute UVW, at least three co-planar beam radial velocity data are required. If higher number of radial velocity data is available, then the

computation will give an optimum result in least square method. The line-of-sight component, V_d of the velocity vector $V = (V_x, V_y, V_z)$ at a given height is expressed as,

$$V_d = V \cdot i = V_x \cos \theta_x + V_y \cos \theta_y + V_z \cos \theta_z \quad (2.32)$$

Where i is the unit vector along the radar beam and X, Y and Z directions are aligned to East-West, North-South and Zenith beam respectively and θ_x , θ_y and θ_z are the angles that the radar beam makes with the X, Y and Z axes. Applying least square method,

$$\varepsilon^2 = [V_x \cos \theta_x + V_y \cos \theta_y + V_z \cos \theta_z - V_{dj}]^2 \quad (2.33)$$

where $V_{dj} = \frac{f_d \lambda}{2}$ and j represents the beam number. To satisfy the minimum residual,

$$\frac{\partial \varepsilon^2}{\partial V_k} = 0, \quad (k = x, y, z) \quad (2.34)$$

$$\begin{bmatrix} V_x \\ V_y \\ V_z \end{bmatrix} = \begin{bmatrix} \cos \theta_{x1} & \cos \theta_{y1} & \cos \theta_{z1} \\ \cos \theta_{x2} & \cos \theta_{y2} & \cos \theta_{z2} \\ \cos \theta_{x3} & \cos \theta_{y3} & \cos \theta_{z3} \end{bmatrix}^{-1} \begin{bmatrix} V_{d1} \\ V_{d2} \\ V_{d3} \end{bmatrix} \quad (2.35)$$

where $V_d = -\frac{f_d \lambda R}{2}$. Thus by solving the above equation, we can derive V_x , V_y and V_z , which corresponds to the zonal (U), meridional (V) and vertical (W) components of the wind velocity.

2.6 Description of Gadanki LAWP system

The UHF radar at Gadanki, known as the Lower Atmospheric Wind Profiler (LAWP), was installed at Gadanki in August 1997, with a major collaboration between the Ministry of Post and Telecommunication (MPT)/Communication Research laboratory (CRL), Japan and the National MST radar facility, India, for detailed investigation of winds, turbulence and precipitating cloud systems in the tropical latitude. UHF radar is a coherent pulsed radar

PARAMETERS		SPECIFICATIONS
Frequency		1357.5 MHz
Maximum bandwidth		2 MHz
Peak power		1 kW
Maximum duty ratio		5%
<u>Antenna</u>		
	Antenna type	phased arrays
	Antenna aperture	3.8 X 3.8 m^2
	Beam width 4°	
	Number of beams for automatic scans	electrical steering three directions
<u>Data processing</u>		
	Pulse width	0.33, 1 and 2 μs
	Inter-pulse period	20-999 μs
	Number of coherent Integrations	1-256
	Number of incoherent	100
	Number of FFT points	64-2048
<u>Height sampling</u>		
	Range gates	1-64
	Beam switching	vertical, north, and east with 150 Zenith angle

Table 2.3: System specifications of LAWP at Gadanki

operating at 1357MHz with effective peak power aperture product of about $1.2 \times 10^4 Wm^2$. The signal wavelength is 0.22m and hence the radar detects the back-scattered echoes from approximately 11cm irregularities. The basic system specifications are given in table 2.3. Detailed Gadanki LAWP description can be found elsewhere (Reddy *et al.*, 2001).

This system uses a phased antenna array for transmission and reception of the signals. The phased antenna array consists of 576 circular microstrip patch antenna elements arranged in a 24 x 24 matrix over an area of 3.8 m x 3.8 m. The total array is organized into four quadrants of 0.715λ spacing, λ being the wavelength at the operating frequency. A

total peak power of 1000 W is delivered to the antenna array by a parallel array of four outputs from Power Amplifier (PA), each feeding 250 W to one quadrant (12 x 12 elements) of the array. The Transmitter (TX) unit, preceded by the PA, generates an output power of 175 W, which is sufficient to drive the PA. The PA generates the required final output power by a division-amplification-combining technique. The output power is fed via the beam changer (BC) switch and hybrid circulator. The power distribution across the array is tapered to obtain better side lobe suppression. The array produces a pattern having a beam width of 4° and a gain of 29 dB. The beam direction can be tilted by 15 degrees towards North and East from the zenith by electrical steering by injecting a progressive phase difference between the successive elements. Phase shifters are used to steer the beam in the North direction. For the East beam required phases are injected through the appropriate lengths of the feeder lines. The same antenna array is used for all the three beams.

The power received by the antenna array from the atmosphere is delivered to the receiver *via* the circulators. The receiver is a phase coherent heterodyne type having a quadrature detector at the final output, and delivering the video outputs to the signal processor. The receiver has an over all gain of 50-120 dB depending upon the gain setting of the Automatic Gain Controller (AGC) amplifier. The dynamic range of the receiver is 66 dB. The quadrature (I and Q) outputs of the receiver are limited to a peak-to-peak voltage of 10 volts and given to the signal processor unit (SPU). The SPU consists of an A/D converter (ADC) and a coherent accumulator. The ADC has 12-bit resolution and samples analogue input at the interval set at the data processing unit (DPU). The SPU performs the coherent accumulation on the ADC output data. The constituted coherent data is then transferred to the DPU for further processing. The DPU performs an FFT' on the received coherent data. The on-line computer displays the frequency spectrum (North, East and Zenith beams), signal strength, wind speed and direction. The data is further processed to compute moments before being transferred to the offline computer *via* Ethernet for archival. Each data file in the

archival corresponds to one cycle and contains parameter file, physical file, spectrum file and moment data file. Finally the data of incoherent, spectral moments and velocity field is archived on magneto-optical disks and eventually transferred to compact disks (CD-ROM). Apart from the online moment estimation facility, an off-line data processing facility similar to VHF radar is available for UHF radar also.

CHAPTER 3

Radar Observations of the Structure and Evolution of TMCS

3.1 Introduction

The passage of a TMCS over a station can be discernable from the leading convective region in which convective clouds prevails, a dissipating region in which stratiform precipitation region exist and a transition region in between, where diminished structure of convection observed. *Churchil and Houze* (1984) investigated the evolution, structure, area coverage and precipitation rates for stratiform and convective regions of a cluster observed during Global Atmospheric Research Programs (GARP) Winter Monsoon Experiment (WMONEX). Radar echoes associated with TMCS show that precipitation divides distinctly into convective and stratiform region (*McAnelly and Cotton*, 1989; *Houze et al.*, 1990). A common feature associated with stratiform region of the TMCS is the radar bright band (BB). The BB is a layer of enhanced radar reflectivity resulting from the difference in

the dielectric factor for ice and water and the aggregation of ice particles as they descend and melt. The bright band height (BBH) is the altitude of maximum radar reflectivity in the BB. The layer over which the transformation from ice to water occurs defines the melting layer. The top of the melting layer is the melting level, also commonly accepted as the 0°C constant-temperature surface (*Glickman, 2000*). Under tropical conditions, the melting level is usually found between 4 and 5 km.

The strength of convective scale updrafts and downdrafts in a TMCS are similar to those in a typical cumulonimbus clouds. Accompanying the convective scale updrafts and downdrafts is a region of weaker upward and downward motions and associated stratiform cloudiness and precipitation (*Houze, 1993, 1997*). *Churchil and Houze (1984)* noted that convective core updraft speed of 17 ms^{-1} were not uncommon in cloud clusters observed in GARPs Atlantic Tropical Experiment (GATE) clusters. Moreover, *Dudhia and Moncrieff (1987)* predicted updraft velocities on the order of 17 ms^{-1} at 10 km height in their 2-D simulation of convective cells observed in the GATE non squall clusters.

The supercell storms are the most researched mesoscale phenomena. Although definition of supercell is not clear cut, *Browning (1977)* was the first to define a supercell storm based on observations. Supercell thunderstorms are the largest, most severe class of thunderstorms. The supercell itself consists of a single massive cell. Because of the powerful updraft, the anvil extends a long distance ahead of a supercell thunderstorm; a dome protrudes above the top. Although the supercells are relatively infrequent, they account for a large percentage of weather related destruction and loss of life. Various sections of a supercell storm consist of different types of precipitation. The severity of the supercell storm is defined by the strength of the updrafts and the intensity of the upper level wind speeds. A supercell storm can be treated as a cumulonimbus cloud with rotating updraft.

It appears that the amount and spatial distribution of precipitation with the convection are vital indicators of the weather phenomena associated with a particular storm. Some

supercell storms produce relatively little precipitation and yet show visual signs of rotation. Such storms are called Low Precipitation supercells. At the other end of the supercell spectrum are the so-called High (Heavy) Precipitation (HP) supercells (*Bluestein et al.*, 1995; *Moller et al.*, 1990). Radar echo characteristics of a supercell storm reveals that these storms are often associated with hook echo that wrap around the so-called vault (*Browning*, 1977; *Lemon*, 1998) or Bounded Weak Echo Region (BWER) (*Chisholm and Renick*, 1972; *Rasmussen et al.*, 2007). An intense precipitation region on the storms rear flank and an overhanging precipitation region on the storms forward flank bound the echo free vault. *Chu and Lin* (1994) first reported the severe depletion of turbulent echo power in a convective system near the melting level using VHF Doppler radar observations. Using beam steering facility of the Indian MST radar, *Kumar et al.* (2005) also reported the occurrence of WER in VHF radar backscattering and found that strong updrafts in the convective systems are mainly responsible for WER.

To investigate these phenomena in more detail, high resolution observations are necessary in both time and space. Unlike the field campaigns, GATE and WMONEX designed solely to study the MCS characteristics, there remains no effort to explore the detailed structure and evolution of TMCS over Indian subcontinent.

3.2 Storm Classification

Vasiloff et al. (1986) proposed a scheme to distinguish between the supercell and multicell storms, that suggest that the difference between successive updraft cells L relative to updraft diameter D can be used to identify storm type. When $L > D$, the storm appears as multicell storms and when $L < D$, they resemble supercell storms. When $L/D < 1$, they suggest that weak evolving multicell storm should prevail in which individual updraft perturbations associated with cells are embedded within a large scale region of background updraft.

Following the method adopted from *Vasiloff et al.* (1986), we use the time-height variation of the radar reflectivity (SNR) and vertical velocity to distinguish the supercell and multicell storm. As the VHF radar probe the atmosphere over a given location, we use the time scale instead of length scale as used in Vasiloff classification. The time difference between updrafts (greater than 3 ms^{-1}), T_{UPLEN} and the duration of updraft, T_{UPDIA} can be used to identify storm type. When $T_{UPLEN} > T_{UPDIA}$, the storm appear as multicell storm and when $T_{UPLEN} \ll T_{UPDIA}$, they resemble supercell storm. When $T_{UPLEN}/T_{UPDIA} < 1$, suggest that weak evolving multicell storm should prevail in which individual updraft perturbations associated with cells are embedded within a large scale region of background updraft. If the duration of the storm from the cumulus to the dissipating stages lasts for 5-6 hours and its mature phase consist of organized vertical motion for a period of 45-60 min can be termed as TMCS. Based on the above criteria, we discuss the evolution and vertical structure of a TMCS and two supercell storm passage over the radar site. The details of experiments are given in table 3.1.

Parameter	Value		
	21 June	17 October	15 September
Pulse width , μs	2	16	16
Inter Pulse Period (IPP), μs	250	1000	1000
Coded/uncoded	Uncoded	Coded	Coded
Range Resolution, m	300	150	150
Coherent integration	512	64	64
No. of FFT points	256	256	256
Beam Position	Zenith	Zenith	Zenith

Table 3.1: Experiment specification table

The wind profilers operating at 53 MHz produce both clear air echoes from Bragg scattering, which arises from turbulent irregularities in refractive index and precipitation

echoes from Rayleigh scattering, since these wavelengths are sensitive to hydrometeors in moderate to heavy precipitation (Carter *et al.*, 1991). It has been observed that the VHF radar echoes from precipitation below melting level is weaker. At radar wavelengths of 6 m, the effects of large hydrometeors associated with thunderstorms did not overwhelm the clear-air component of the radar signal, thereby rendering it possible to identify and remove such effects from the data. The radar returns from the clear air due to Bragg scattering is used for the present study. Any near-zero Doppler shift interference and echoes from Rayleigh scattering have been avoided during spectral moment estimation as suggested by Rao *et al.* (1999).

3.3 VHF Radar Observations of TMCS : Case I

The convective event selected here occurred during 21-22 June, 2000 after the onset of the southwest monsoon. Contour plots of OLR at 0000 UTC shown in figure 3.1 (a) has a low value (less than 170 Wm^{-2}) near the radar site, which confirms the convective nature of the atmosphere and 200 hPa wind is greater than 20 ms^{-1} and is easterlies. Synoptic charts of 1000 hPa geopotential height field and 850 hPa horizontal wind at 0000 UTC shown in the figure 3.1 (b) shows the synoptic condition and mesoscale flow field during the observation period. A trough is observed in the geopotential chart on 21 June 2000 and 850 hPa winds is about 15 ms^{-1} and is the core of Low Level Jet stream (LLJ) observed during the monsoon season. Figure 3.2 shows the time series of rainfall rate recorded at the radar site. The figure clearly shows the contribution of significant amount of rainfall from the stratiform region to the total rainfall associated with TMCS.

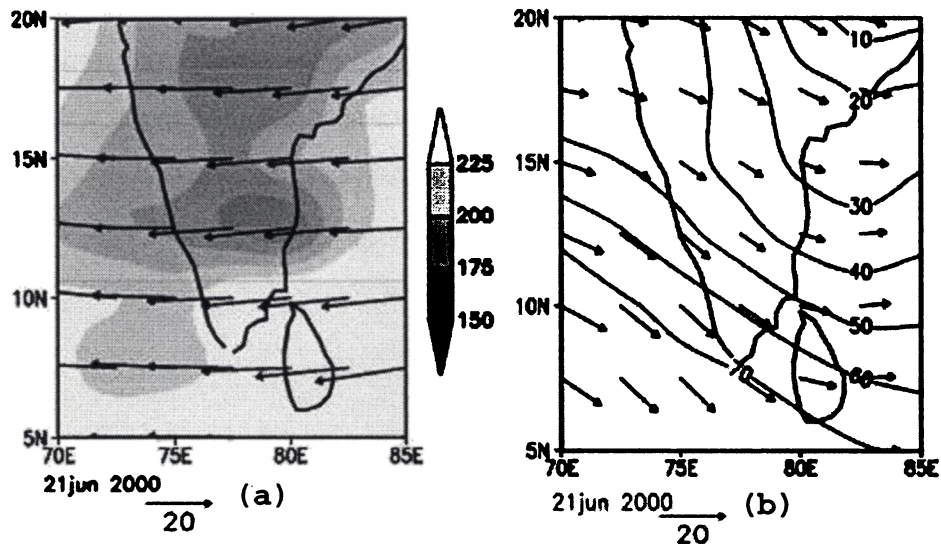


Figure 3.1: (a) Contour charts of outgoing long-wave radiation in Wm^{-2} and 200 hPa winds in ms^{-1} and (b) Synoptic charts of geopotential height in gpm and 850 hPa wind in ms^{-1}

3.3.1 Experiment setup

Continuous convection experiments using VHF Doppler radar for a period of 5-6 hours starting from 19:23 to 01:23 hrs IST (Indian Standard Time = UTC+5:30) during 21-22 June 2000 (monsoon period) have been used to investigate the structure and evolution of TMCS. During the period, radar made observations only with vertical beams, since the convection is much more evident in the vertical wind component. The data provide information about vertical velocity from heights of 1.5 km above the ground at a resolution of 300 m. Some results obtained by the preliminary analysis of the data have already been reported (*Dhaka et al.*, 2002; *Abhilash and Mohankumar*, 2004; *Kumar et al.*, 2005). Detailed analysis of the dynamical and microphysical processes has not yet been done for this case. The evolution and structure of the TMCS have to be investigated with the aid of such data of high quality.

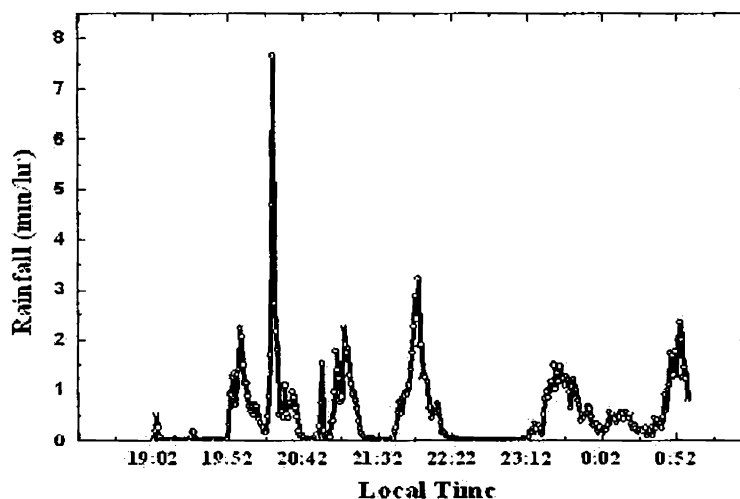


Figure 3.2: Time series of rainfall rate recorded by ORG at the radar site

3.3.2 Approach

At the time of the TMCS passage over the radar site, the main convection band is in its developing or cumulus stage. Figure 3.3 (a, b and c) shows the time-height section of the clear air SNR, Doppler width and intensity of vertical wind disturbances during 21-22 June 2000. The figure clearly shows the evolution of convection occurred over the radar site. As mentioned earlier, the lifecycle of the storm lasts for about 5-6 hours with weak evolving multicellular characteristics. Hence the storm can be termed as TMCS. The figure represents consistency between reflectivity and turbulence in the middle troposphere and associated vertical wind disturbances. The great association of large variance in the spectral width and reflectivity pattern signifies the importance of convection in generating turbulence in the middle troposphere. The radar reflectivity pattern is analyzed in detail to investigate the passage of the TMCS and its structure and evolution. Four distinct echo patterns observed in due course and have been used to separate the four regions of the TMCS, viz the genesis (convective) region, mature region, transition zone and stratiform region. The reflectivity

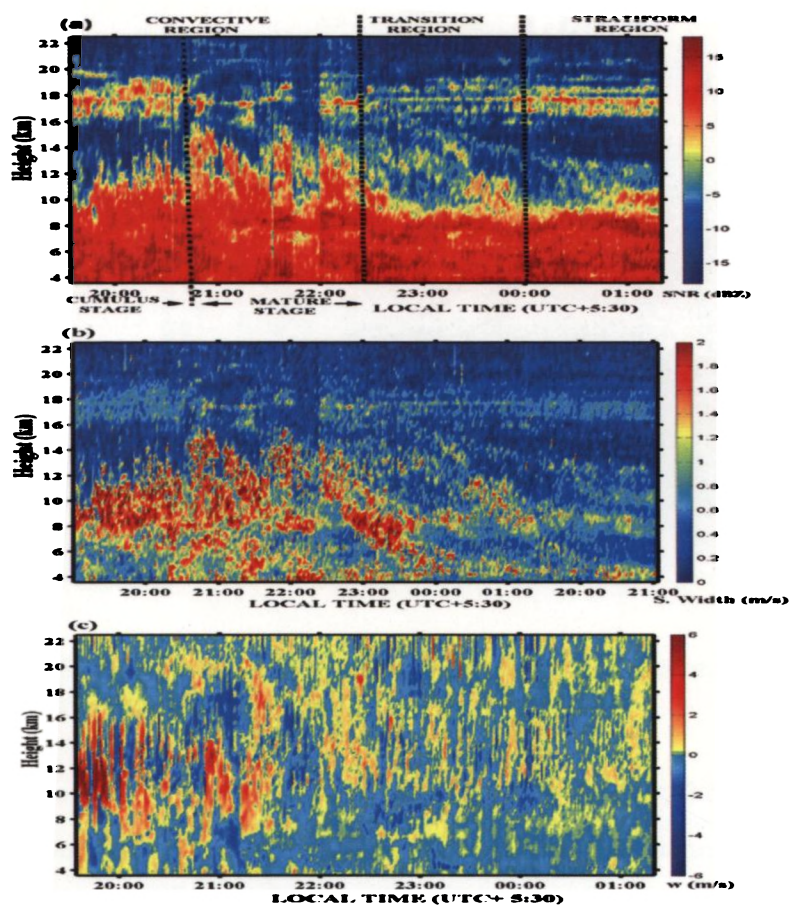


Figure 3.3: Time-height intensity plots of (a) Signal-to-Noise Ratio (SNR) in dBZ (b) Doppler width in ms^{-1} and (c) Vertical Velocity in ms^{-1}

pattern and vertical variation of vertical velocity associated with the four regions have been analyzed to study the characteristics and structure of each region.

3.3.3 Genesis (cumulus) region

The genesis stage is often referred to as the development of cumulus stage. The experiment starts at the time of the overhead passage of the initial phase of the storm. The genesis region was overhead between 19:45 and 20:40 IST. The growth of high reflectivity cores from

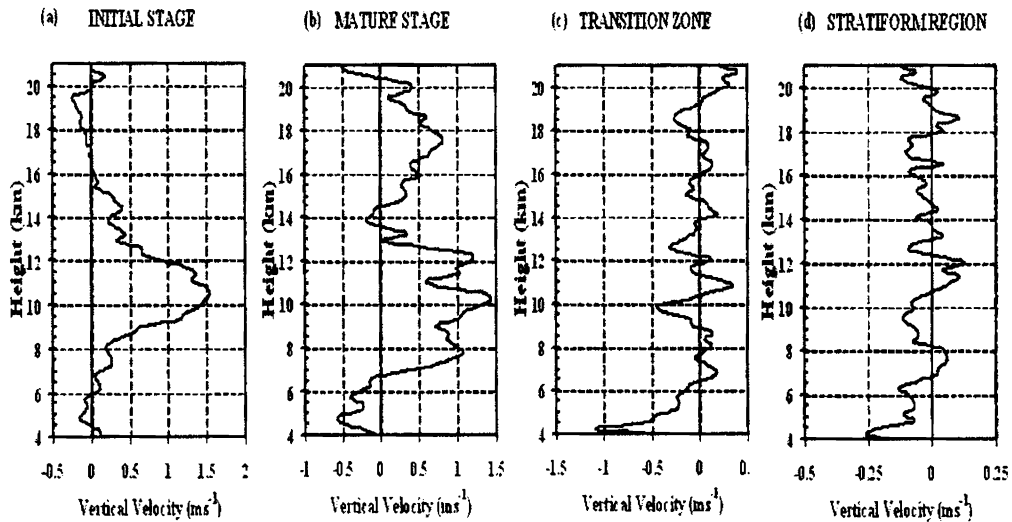


Figure 3.4: Averaged vertical velocity during (a) Initial stage, (b) Mature stage, (c) Transition zone and (d) Stratiform region

the lower troposphere to the middle and upper troposphere (see fig. 3.3 (a)) characterizes the genesis region of the TMCS. During the period, large updrafts of magnitudes $6-8 \text{ ms}^{-1}$ (see fig. 3.3 (c)) initially present in the middle troposphere extends to upper troposphere. The vertical velocity diagnosed separately for each region and presented in figure 3.4. The figure 3.4 (a) represents the average vertical velocity for the genesis region, which include both cumulus scale and mesoscale vertical velocity. Organized vertical motion is observed in the genesis region with mean vertical motion is upward at all levels with peak upward motion occurred near 10 km. Large turbulence in terms of the spectral width is observed in the middle troposphere. The turbulence at this level is generated solely by the inflow of dry environmental air and wind shear in the vicinity of the updraft (*Knupp and Cotton, 1982*).

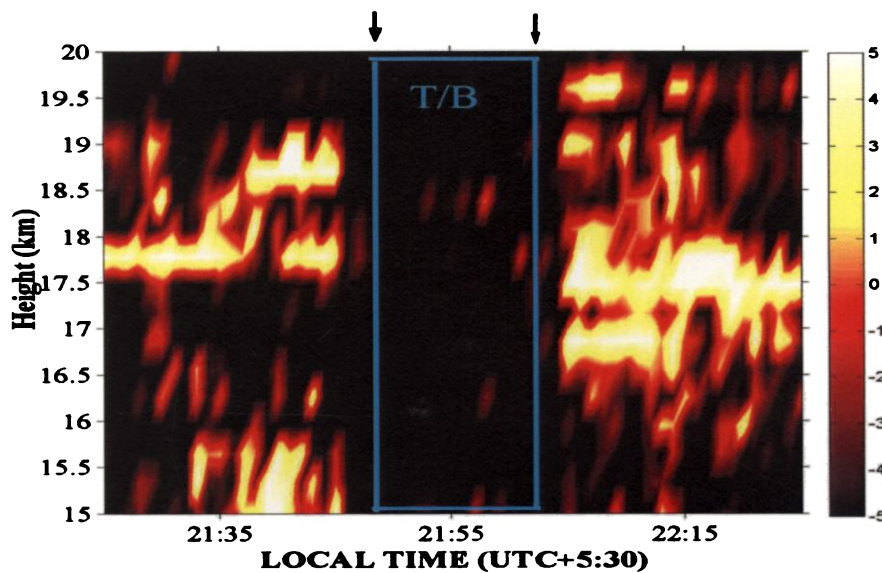


Figure 3.5: Time-height intensity plots of SNR near tropopause during the mature stage (Tropopause break is highlighted as rectangle)

3.3.4 Mature region

The second stage of the development of cloud clusters of TMCS is recognized as the mature stage. The mature stage is characterized by enhancement of reflectivity upto tropopause level (see fig. 3.3 (a)). Figure 3.5 depicts the reflectivity structure near the tropopause during the mature phase of the storm. A noticeable feature from this figure is that the layered structure of high value of reflectivity near tropopause begins to disturbed and the tropopause weakened at the time of system maturity. Figure 3.4 (b) presents the average vertical velocity in the mature region of the system. The mature region exhibits a peak upward motion of 10 ms^{-1} near 12 km. The co-existence of updraft and downdraft demonstrates the mature phase of the storm. Updrafts extend through the depth of the troposphere and even penetrate to lower stratosphere. Convective downdrafts dominate in the lower troposphere. Oscillatory nature of updraft-downdraft pair exists in middle and upper troposphere. Weak downdrafts exist at 14 km, while strong updraft present in the Upper Troposphere and Lower

Stratospheric (UTLS) levels. The weakening of the tropopause together with the penetrating updraft indicates the presence of overshooting convection and possible formation of cloud dome. The weak downdrafts below tropopause signifies the convective outflow or divergence of air and may results in the formation of anvil clouds.

The time evolution of mean vertical motion shows that the level of maximum upward motion near 10 km during the genesis phase ascends to 12 km during the mature phase. This transition corresponds to the greater penetration of convective updrafts resulting in condensation and freezing becomes larger than evaporation. As the maximum updrafts reached 12 km with vigorous updraft speed of 10 ms^{-1} may results in an upward shift of the level of convective heating and mean vertical motion. The additional latent heat released by freezing of the supercooled water drops and vapor deposition growth of ice crystals above freezing level might have contributes to cloud buoyancy and higher updraft speed in the upper troposphere (Cotton, 1972). The low level downdrafts are closely associated with precipitation falling beneath the cloud base. The downdrafts were initiated by precipitation loading and then maintained by evaporation of cloud and precipitation (Barnes and Garstang, 1982; Johnson and Nicholls, 1983).

3.3.5 Transition region

Following the mature region is a region of weaker updraft and downdraft motion and characterizes a well marked transition region. During the transition phase, the reflectivity starts diminishing and confined in the lower levels and layered structure near tropopause moving back to the stable atmospheric condition. Intense downdrafts present in the lower troposphere. However, a local pocket of updraft remains in the middle and upper troposphere. Time evolution of vertical velocity shows that, the convective downdraft dominates the storm and the process of decay of the storm into a stratiform rain region has begun.

3.3.6 Stratiform region

Another important region associated with TMCS is the trailing stratiform region. More than 40 % of the total rainfall associated with TMCS is occurred during the passage of the stratiform region (see fig 3.2). The stratiform region is marked by only weak vertical motion and weakening of echoes. Figure 3.4 (d) shows the average vertical motion in the stratiform region. The vertical motion is relatively small with maximum amplitudes less than 1 ms^{-1} . Furthermore, it is clear in this figure that the convective downdrafts are essentially present in the middle and lower troposphere and is marked as the decaying phase of the storm. However, these observations indicate that mesoscale upward and downward motions are associated with stratiform precipitation. The observed low-level downdraft is considerably more intense, presumably because of water loading and melting and evaporation of falling rain. A well defined radar bright band (BB) is typical of stratiform precipitation (Houze,

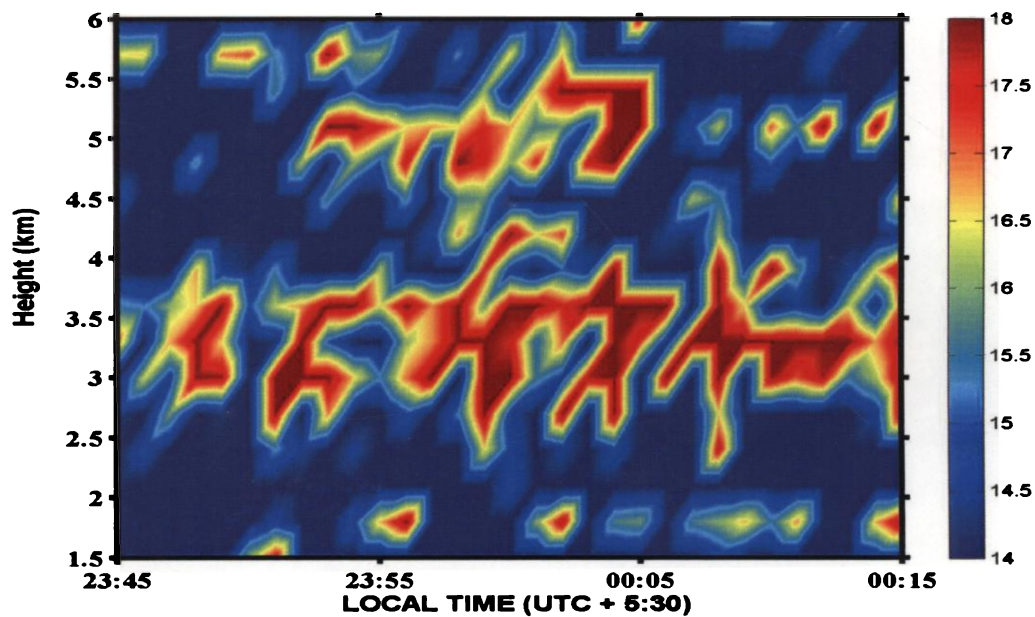


Figure 3.6: Time-height intensity plots of SNR in the middle troposphere

1993). Figure 3.6 depicts the clear air radar reflectivity structure in the stratiform region of the convective system. As evident from the figure, two enhanced reflectivity zone (ERZ) is observed, one near 5.0 km and other near 3.5 km. Here we use the term ERZ instead of BB to avoid the confusion on the scattering mechanism for hydrometeors and clear air. The term bright band is used to represent increase of radar reflectivity as falling snow melts near the melting level. Following *Chu and Lin (1994)*, the occurrence of double ERZ can be explained using the variance of the atmospheric refractive index as,

$$\begin{aligned} \langle \Delta n^2 \rangle \times 10^{12} = & A \langle \Delta q^2 \rangle + B \langle \Delta T^2 \rangle - C \langle \Delta T \Delta q \rangle + \\ & D \langle \Delta P \Delta q \rangle + E \langle \Delta P^2 \rangle - F \langle \Delta T \Delta P \rangle \end{aligned} \quad (3.1)$$

The coefficients A, B, C, D, E and F are determined from Chennai (13.0°N, 80.1°E) radiosonde data and the above equation is written in the order of usual decrease of importance of each term.

Figure 3.4 (d) shows average vertical velocity in the stratiform region. The greater downdraft speed below the melting level is attributed to the precipitation drag and melting of snow. Chilling and moistening of downdraft air below 0°C caused by melting and evaporation results in the negative correlation between temperature and humidity. This consecutively produces the first BB/ERZ near melting level. Echo intensity is maximum at ERZ level and falls sharply. Below the melting layer, the large aggregates of melted particles survive evaporation and reaches well below the melting level. At still warmer temperatures, these aggregates melt fully and break up into small drops. Obviously entrainment of warm dry air into the downdraft air in the subcloud layer evaporates the cloud particles and thereby increases the humidity and subsequent reduction in temperature. Evaporative cooling results in the negative correlation of temperature and humidity and is supposed to be the cause of second ERZ near 3.5 km.

3.3.7 Conceptual model of TMCS

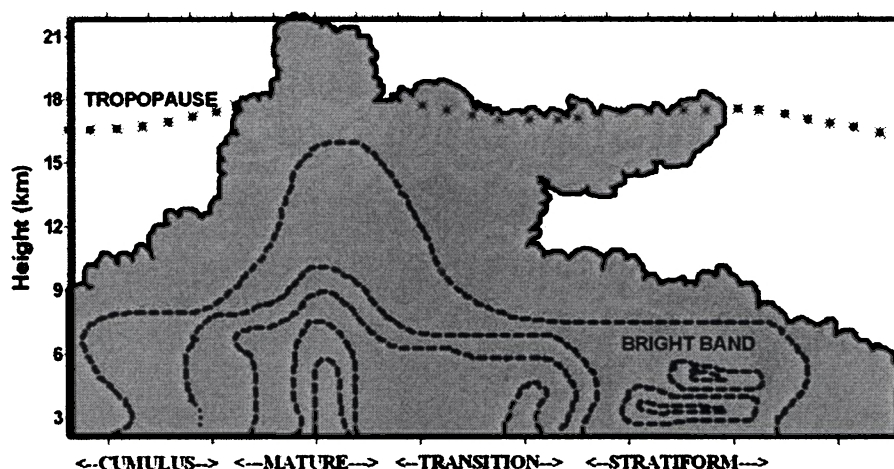


Figure 3.7: Conceptual model of TMCS

The analysis of the convection event provides the conceptual model of the TMCS based on the vertical variation of radar reflectivity and vertical velocity. The conceptual model is shown in figure 3.7. The figure shows the leading cumulus region followed by a mature region in which overshooting convection and formation of cloud dome present. The trailing stratiform region consists of anvil and ERZ or BB. A transition region is typical of TMCS with less intense convection between the mature and stratiform region.

3.4 VHF radar observations of Supercell Storm : Case II

Frequency of occurrence of convective clouds over the radar site is more during October-November (post monsoon or northeast monsoon) season. Contour plots of OLR at 12:00 UTC shown in figure 3.8 (a) has a low value (less than 170 Wm^{-2}) near the radar site, which confirms the convective nature of the atmosphere. Easterly winds of magnitude greater than

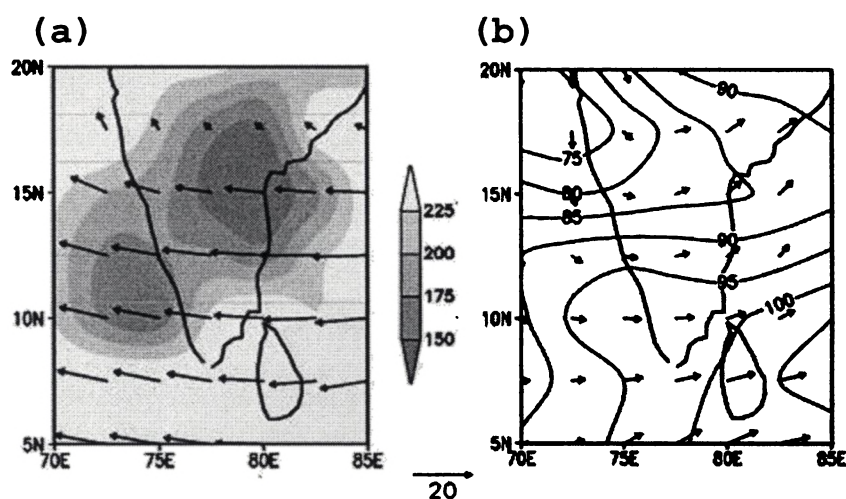


Figure 3.8: Same as figure 3.1, but for 17 October 2002

10 ms^{-1} present at 200 hPa. Synoptic charts of 1000 hPa geopotential height field and 850 hPa horizontal winds at 12:00 UTC shown in the figure 3.8 (b) depict mesoscale flow field during the observation period. A trough is seen in the geopotential field and westerly winds of magnitude less than 10 ms^{-1} is noted on 17th October 2002. Strong westerly winds in the lower level and easterlies in the upper level are observed.

The high sampling rate of the wind profiler provided excellent resolution of vertical air motion within a supercell storm. During the campaign period, the profiler was operated with vertical incidence beam. Continuous convection experiments using VHF Doppler radar for a period of 5-6 hours starting from 17 October, 20:30 to 18 October 2002, 00:40 hrs LT have been used to investigate the structure and evolution of supercell storm. The experimental specifications used for the present observations are given in table 3.2. During the period, radar made observations only with vertical beams, since the convection is much more evident in the vertical wind component and time resolution is 52 seconds. In the present study, relatively small horizontal wind speed (< 15) is seen in the troposphere throughout the

observation period. Influences of horizontal motion on vertical velocity measurements are relatively small. The system described herein was sampled during the mature to dissipating stages of the convective activity.

3.4.1 System evolution and structure

Figure 3.9 shows the Plan Position Indicator (PPI (Z)) diagrams of base radar reflectivity at 0.5 °elevation scan from the Doppler Weather Radar at Sriharikota (13.7 °N, 80.2 °E), India. The maximum range of the radar is 150 km. The MST radar site at Gadanki is marked as cross and the storm is indicated as circle. Figure 3.9 (a)-(g) presents the larger, more mesoscale structure of the storm during the system life time. Figure 3.9 (a) presents the initial or cumulus stage, (b)-(d) shows the mature phase and (e)-(g) represents the dissipating stage of the supercell storm. Obviously, the mature phase of the storm last for more than 40 minutes and covers an area of 40 km².

At the time of the supercell propagation over the Gadanki MST radar site, the main convection band is in its developing or cumulus stage. Figure 3.10 shows the surface rainfall during 20:20-01:00 hrs LT on 17th -18th October 2002. As evident from the time series of rainfall data collected from optical rain gauge, large amount of rainfall is produced between 20:40 and 21:15 hrs LT. This period is manifested as the mature stage of the system. Peak rainfall of 97 mmhr⁻¹ is observed during the period. Thereby the system can be termed as HP supercell (*Moller et al.*, 1990). The observation starts just before the system reaches its mature stage. Consequently, the system evolution during the mature and dissipating stages of the system has been studied by analyzing the VHF radar reflectivity, spectral width and vertical velocity.

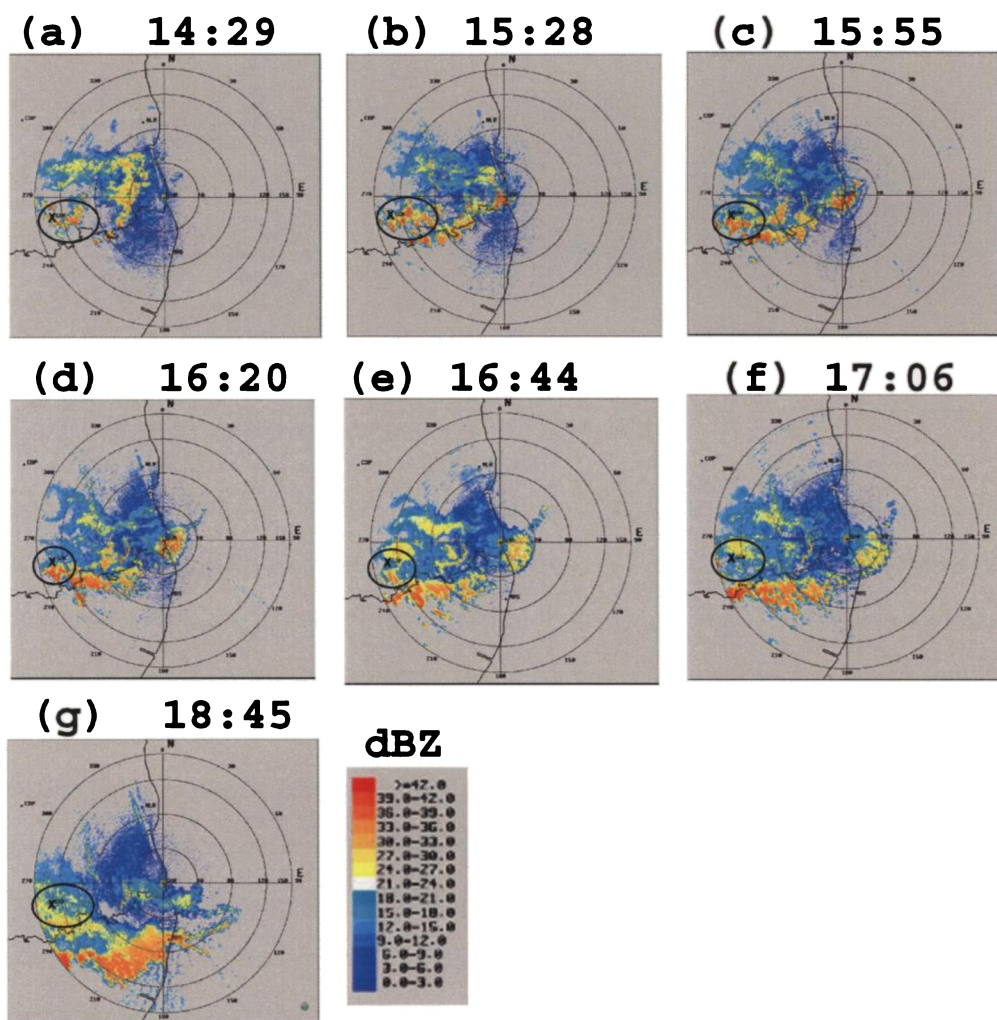


Figure 3.9: Doppler radar reflectivity, PPI(Z) showing the structure of the convective system

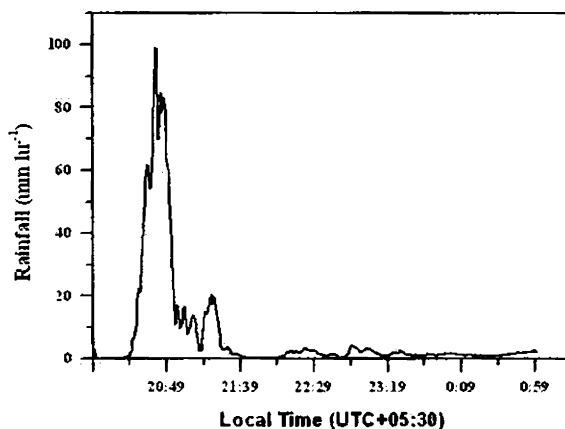


Figure 3.10: Same as figure 3.2 but for 17-18 October 2002

3.4.2 Radar reflectivity and spectral width

Figure 3.11 (a, b and c) shows the time-height section of the clear air signal-to-noise ratio (SNR), Doppler width and vertical velocity during 17 -18 October 2002. The figure clearly shows the evolution of convection occurred over the radar site. The observations starts at the end of the initial or cumulus stage and is marked as *A* in figure 3.11 which is followed by two distinct echo patterns. They have been used to separate the two phases, *viz.*, the mature phase marked as *B* in which enhancement of SNR in the entire troposphere and the dissipating stage marked as *C* wherein SNR suddenly diminished in the upper troposphere. Large SNR values are mostly confined in the lower troposphere. In agreement with the rainfall data, the mature phase of the storm lasts for more than 45 min. After 21:30 hrs LT, the storm begins to dissipate. Following our criteria used to distinguish the storm, T_{UPLEN} is small as compared to T_{UPDIA} and the entire life cycle of the storm lasts for about 3-4 hours. Hence this storm can be termed as supercell storm. As evident from the radar reflectivity pattern, the present supercell storm exhibits single cell characteristics. The figure 3.11 represents consistency between reflectivity and turbulence in the middle troposphere

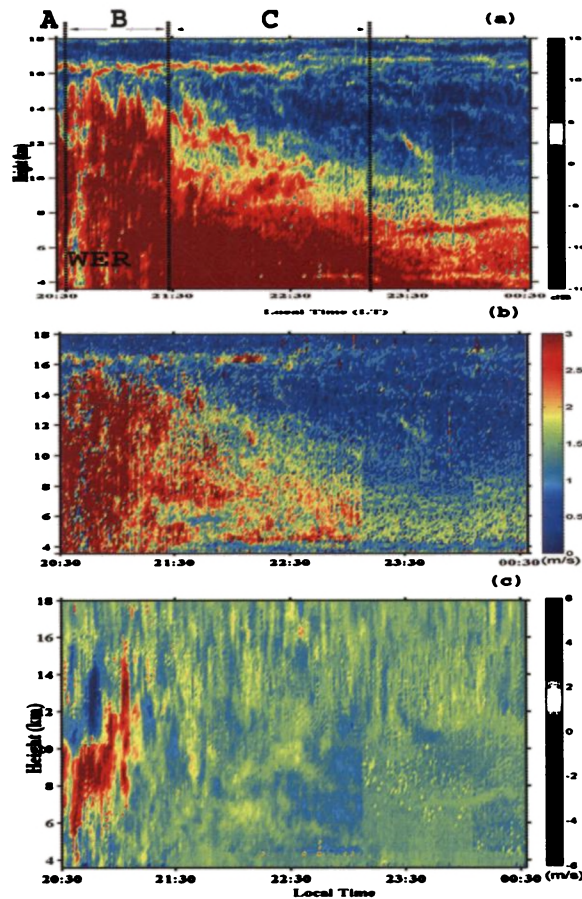


Figure 3.11: same as figure 3.3 but for 17-18 October 2002

and associated vertical wind disturbances. The great association of large variance in the spectral width and reflectivity pattern signifies the importance of convection in generating turbulence in the middle troposphere.

The reflectivity structure in figure 3.12 shows severe depletion of radar reflectivity above and below the melting level (near 4.5km), which is often referred to as weak echo region (WER). As there are no temperature observations available at Gadanki, the melting level is derived from the radiosonde observations at Chennai (13.0 °N, 80.1 °E), southeast of the radar site. The mature stage of the supercell is evident when WER is detected. *Chu*

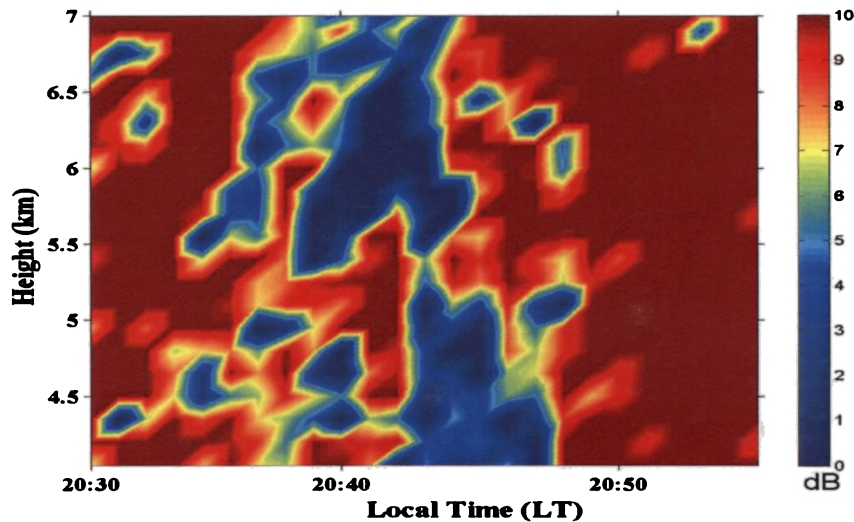


Figure 3.12: Time-height intensity plots of SNR in the middle troposphere

and Lin (1994) reported severe depletion of the turbulent echo power below the melting layer using VHF radar. As evident from the enhanced turbulence in the middle troposphere (see fig. 3.11 (b)) which is a sign of vigorous mixing in the cumulus stage and leads to the variability of vertical velocity structure (fig 3.11 (c)). The thermodynamic properties of updraft at any level in the cloud should be a mixture of properties of air entering cloud base and air entered into the updraft at all levels below that level. Hence the observed structure of the WER can be better explained by the cloud base and lateral entrainment (Abhilash and Mohankumar, 2007).

The occurrence of WER can be explained using variance of atmospheric refractive index given by equation 3.1. The weak echo region (fig. 3.12) is not found at the level of maximum updraft velocity, instead found in the height range (4-6 km) where strong gradient of vertical velocity exist (see fig.3.11(c)). Weisman and Klemp (1984) have also found in their numerical experiments that the bounded WER resides on the gradient of strong updrafts. The reduction in the echo power would be the result of two processes, such as

(1) the plumes of dry environmental air engulfed into the cloud through lateral entrainment might cause the evaporation of cloudy air and thereby chilling the cloudy air resulting in penetrating downdrafts and (2) the cool dry air entering below the updraft core through cloud base entrainment mixes with saturated cloudy air dries out the cloudy environment accompanied by the reduction in the temperature results in the positive co-variance between the temperature and humidity. The figure 3.11(c) shows that the vertical motion in the region of observed weak echo is downward. Both the processes lead to the positive co-variance between the temperature and humidity and reduce the variance in humidity across the cloud, which in turn generate weak echo power. The reflectivity structure in figure 3.12 shows that the WER initially seen at upper levels descends to lower levels as the system passes through the radar site. This signifies the occurrence of overhanging precipitation and bounded WER. As the reflectivity in the WER slopes towards the forward flank of the system, which indicate rear to forward flank jet associated with the supercell storm.

3.4.3 Vertical velocity

During the period, large updrafts of magnitudes $6-8 \text{ ms}^{-1}$ (see fig. 3.11(c)) initially present in the lower and middle troposphere extends to upper troposphere. The time evolution of the mean vertical motion shows that the level of maximum upward motion in the lower troposphere during the cumulus phase ascends to 10-14 km during the mature phase. This transition corresponds to the greater penetration of convective updrafts resulting in condensation and freezing exceeds evaporation. Updrafts extend through the depth of the troposphere and even penetrate to lower stratosphere. As the maximum updrafts reached 12 km with intense vertical wind speed of magnitude greater than 10 ms^{-1} may results in an upward shift of the level of convective heating and mean vertical motion.

Chaboureau et al. (2007) investigated the time evolution of the vertical velocity maximum associated with an observed deep tropical convective system with overshooting up-

drafts during Tropical Convection, Cirrus and Nitrogen Oxides (TROCCINO) campaign near the State of Sao Paulo, Brazil. The Cloud Resolving Scale simulation of this event has been performed using the anelastic non-hydrostatic mesoscale model, Meso-NH. The case was simulated with quadruply nested domains with explicit convection. The microphysical scheme includes three water phases with five hydrometeorological species. They obtained a maximum vertical velocity of 76 ms^{-1} . Such dramatic values have been reported for mid-latitude deep convective events with different convective available potential energy (CAPE) amounts. The 2-D simulations under tropical conditions by *Robinson and Sherwood (2006)* also obtained a maximum vertical velocity of 55 ms^{-1} with a CAPE value of 3520 Jkg^{-1} . Their numerical simulation shows that, the maximum vertical velocity increases with increasing CAPE amounts. *Wang (2003)* carried out the numerical simulation of the observed supercell storm that passed through the center of the Cooperative Convective Precipitation Experiment (CCOPE). The storm and its environment were intensively observed with a combination of seven Doppler radars, seven research aircrafts, six rawinsondes and 123 surface recording stations. The storm evolved under large vertical wind shear between lower and mid-levels with a massive CAPE of 3312 Jkg^{-1} . The numerical simulation has been performed using a three-dimensional, quasi-compressible, time-dependent, non-hydrostatic, primitive equation cloud model, Wisconsin Dynamical/Microphysical Model (WISCDYMM). The microphysics are parameterized by bulk method with six water substances. Their numerical simulation captures the observed Bounded Weak Echo Region (BWER) and maximum vertical velocities of 60 ms^{-1} .

Severe midlatitude cumulonimbi over land exhibits the largest updraft speeds that exceeds 40 ms^{-1} (*Miller et al., 1988*), while in a disturbed tropical environment, *Lemon and Zipser (1980)* diagnosed updraft speed of excess of 14 ms^{-1} . Also, the width of updrafts varies from about 2 km to 10 km. One of the limitations of VHF radar is that, which uses vertically pointing beams that can scan only those regions of the storm that passes over

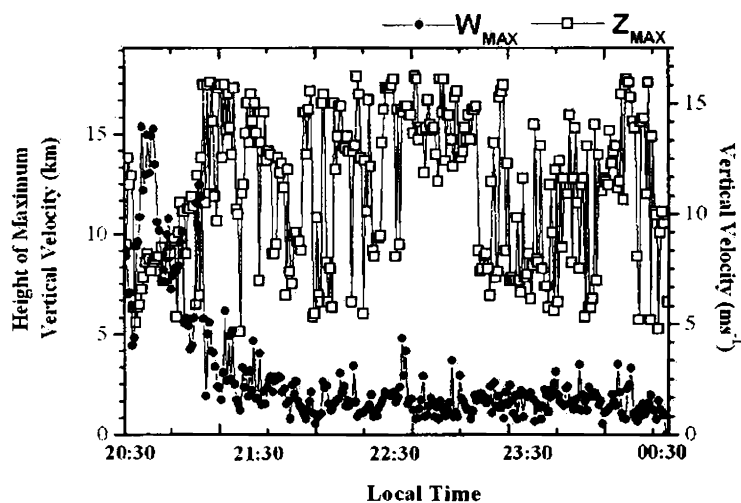


Figure 3.13: Time series of maximum vertical velocity (ms^{-1}) and the corresponding height (km)

the radar site. Hence it is possible to occur maximum updrafts cores somewhere else in the storm, which may not pass through the radar site. However, figure 3.13 shows the maximum updraft speed and corresponding height. During the mature phase of the storm, the maximum updraft speed of 14 ms^{-1} is found between 12-14 km.

The vertical velocity diagnosed separately for each region and presented in figure 3.14. In estimating the time-height composite, we assume that the basic kinematic structure of the storm was not rapidly evolving. Composite analysis was able to resolve the mesoscale flow through the convective region but not the structure of the individual convective cells. The figure 3.14 (a) represents the average vertical velocity during the mature phase, which includes both cumulus scale and mesoscale vertical velocity. Organized vertical motion is observed in the mature phase with mean vertical motion is upward in the middle and upper troposphere with peak upward motion occurred near 10 km. The co-existence of updraft and downdraft demonstrates the mature phase of the storm. Convective downdrafts dominate in the lower troposphere. Oscillatory nature of updraft-downdraft pair exists in

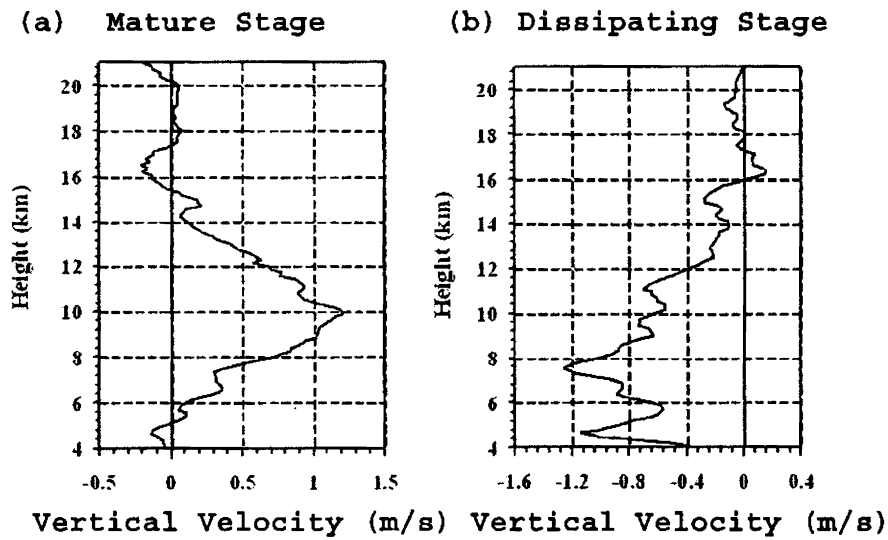


Figure 3.14: Averaged vertical velocity during (a) Mature stage (20:40-21:10 LT) and (b) Dissipating stage (21:20-22:00 LT)

middle and upper troposphere. A weak downward motion exists near the tropopause level.

The additional latent heat released by freezing of the supercooled water drops and vapor deposition growth of ice crystals above freezing level might have contributed to cloud buoyancy and higher updraft speed in the middle and upper troposphere (*Cotton, 1972; Cotton and Anthes, 1989*). The low level downdrafts are closely associated with precipitation falling beneath the cloud base. The downdrafts were initiated by precipitation loading and then maintained by evaporation of cloud and precipitation (*Barnes and Garstang, 1982; Johnson and Nicholls, 1983*). As suggested by *Fritsch (1975)* and *Fritsch and Chapell (1980)*, the upper level subsidence may be due to the dynamic response of the convective updrafts ascent to heights exceeding (overshooting) the parcel equilibrium or interact with stable ambient flow.

The dissipating phase is marked by only weak vertical motion and weakening of echoes. Figure 3.14 (b) shows the average vertical motion during the dissipating phase of the storm.

The vertical motion is relatively small with maximum amplitudes less than 1 ms^{-1} . Consistent with earlier observational studies, it is clear in this figure that deep subsidence found throughout the depth of the troposphere. The maximum downward motion is seen in the middle troposphere ($\sim 7 \text{ km}$) and a secondary maximum found in the lower troposphere ($\sim 4.5 \text{ km}$). Downward motion linked with rearward propagation of hydrometeors outweighed the associated upward motion of the dissipating updrafts. Averaging over a period of time, net subsidence resulted in the middle and upper troposphere. The observed low-level downdraft near the melting level is presumably because of water loading and melting and evaporation of falling rain. *Leary and Houze (1979)* found that cooling associated with melting could be an important factor in driving negatively buoyant mesoscale downdrafts.

3.5 Weak Evolving Multicell Storm : Case III

Figure 3.15 (a, b and c) presents the time-height variation of the SNR, Doppler width and Vertical velocity on 15 September, 2001. Based on the criteria, $T_{UPLEN}/T_{UPDIA} < 1$ and the storm can be grouped as weak evolving multicell storm. The enhancement of high value of radar reflectivity (see fig 3.15 (a)) from the lower troposphere to the upper troposphere upto tropopause level is observed three times during the observation period. The height variations of vertical velocity (fig. 3.15 (c)) also agree with the radar reflectivity pattern. Three vertical velocity cores also suggest the passage of a multicell storm. As these vertical velocity cores are not separated by a large distance, this storm is termed as a weak evolving multicell storm. The great association of radar reflectivity, Doppler width and vertical velocity suggest that storm lasts for about 2 hours. Figure 3.16 shows the zoomed picture of the radar reflectivity (SNR) in the middle troposphere. The figure clearly shows the occurrence of a WER during 16:05 and 16:30 LT. This analysis suggests that the storm also exhibits supercell structure and the entire convective system can be classified as a weak

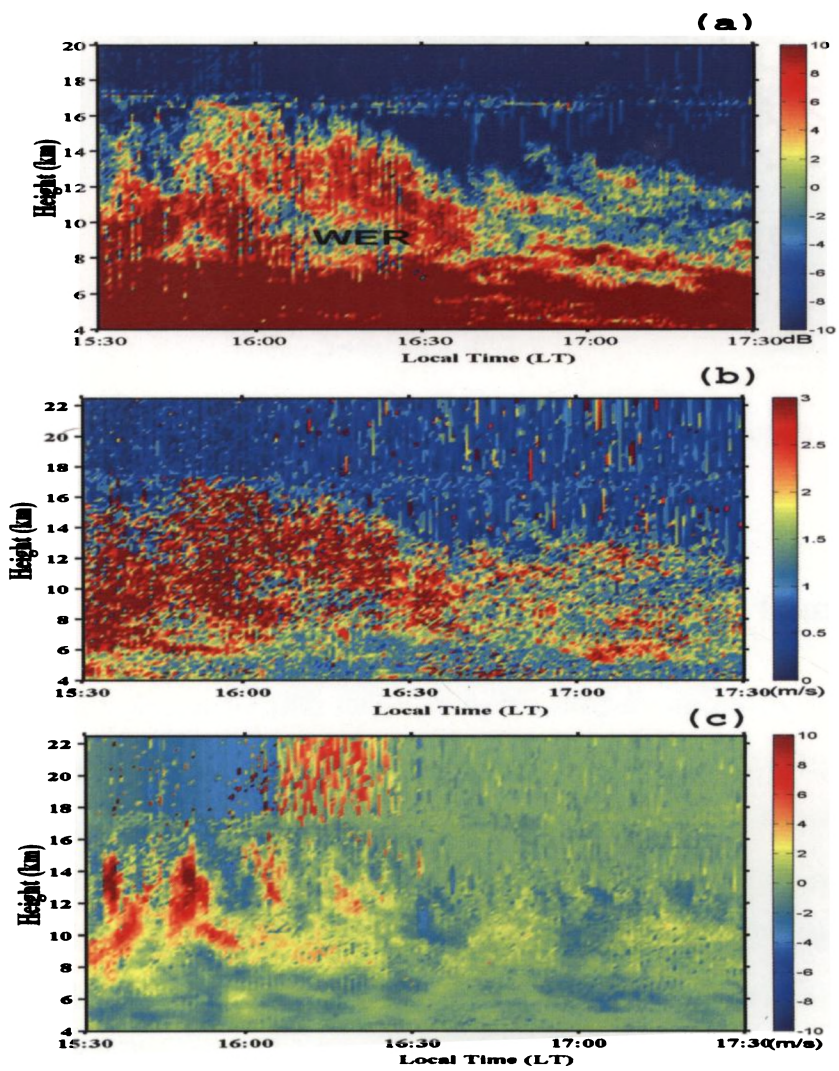


Figure 3.15: Same as figure 3.3 but for 15 September 2001

evolving multicell storm with supercell characteristics.

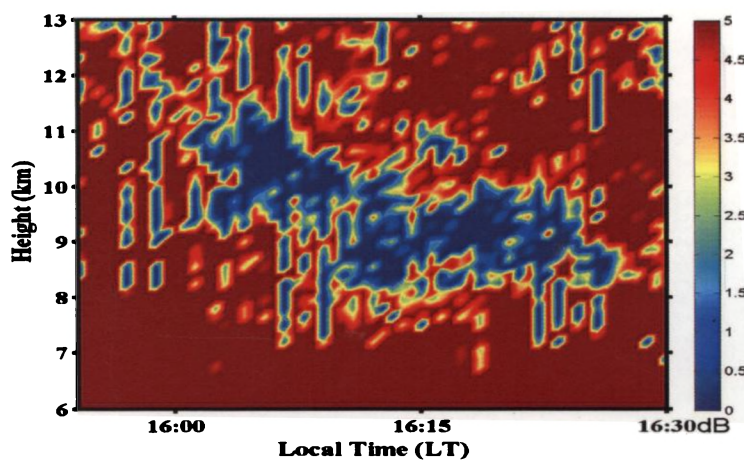


Figure 3.16: Time-height intensity plots of SNR in the middle troposphere

3.6 UHF Radar Observations of Precipitating Convection

Wind profilers operating at 1.3 GHz range are widely used for understanding the lower atmospheric dynamics and precipitating cloud systems (*Martner et al.*, 1993; *Hashiguchi et al.*, 1996; *Engelbart et al.*, 1996; *Yeung*, 1998; *Hadi*, 2000; *Reddy et al.*, 2001). Due to the sensitivity of the frequency band on the hydrometeors, UHF radars are a versatile tool for studying precipitating convection (*Currier et al.*, 1992; *Rogers et al.*, 1993; *Williams et al.*, 1995; *Ecklund et al.*, 1995; *Atlas et al.*, 1999; *Tokay*, 1999; *Williams et al.*, 2000). Most of the wind profiler studies have been conducted in the Pacific Ocean. A need exist to study the vertical structure of the precipitating clouds occurring over Indian region. *Reddy et al.* (2001) already reported some initial results of the convective boundary layer and BB structure using Gadanki-LAWP during monsoon season. Dynamic and microphysical characteristics of the lower atmosphere during precipitating convection have been presented here.

3.6.1 Observations and data description

The Gadanki (13.5°N, 79.2°E) Lower Atmosphere Wind Profiler (LAWP) is L-band pulsed, coherent phased array UHF Radar operating at 1.3 GHz with an effective peak power aperture product of $1.2 \times 10^4 Wm^2$. This wind profiler, which performs well in the tropical environments capable of providing continuous high resolution (time and height) winds in the lower atmosphere. To investigate the characteristics of the lower atmosphere and vertical structure of the precipitating cloud system, reflectivity, Doppler velocity and spectrum width derived from the vertically pointing beam are calculated and presented here. The rainfall data collected from the Optical Rain Gauge (ORG) records at Gadanki radar site has been used to study the distribution of precipitation associated with the convective system.

3.6.2 Mean structure of convection

In the present study, diurnal observations on 17 July 1999 have been selected. Figure 3.17 shows the distribution of rain rate collected from the ORG data at the radar site on 17 July. It is evident from the time series record, that the rainfall is generally produced from propagating cloud systems. On 17 July, the rainfall is distributed over a period of 4-5 hours and most of rainfall occurred in the evening hours. This is unique feature of the precipitating convection observed over the radar site during monsoon season. On 17 July, the rain is produced from the overhead passage of quasi-stationary propagating TMCS. The radar reflectivity structure in terms of signal to noise ratio is analyzed in detail to delineate the structure of the different regions of precipitating cloud systems that is typical to TMCS.

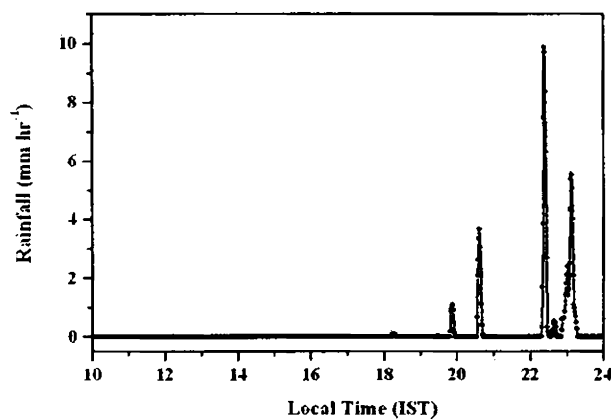


Figure 3.17: Time series of rainfall from ORG records

3.6.3 Radar reflectivity and Doppler vertical velocity

In order to investigate the characteristics of the occurrence of the convective, transition and stratiform precipitation of the tropical cloud clusters, round the clock observations using UHF radar has been used. Vertical beam data has been used to study the vertical structure of the precipitating cloud systems. However, mesoscale convective system signatures can be seen in the ORG time series plot, the cloud classification is based on the vertical structure of the radar reflectivity pattern.

The Doppler spectra are the power weighted distributions of the radial velocities of the scatterers within the radar resolution volume. The shape of the Doppler spectra is characterized by the first three spectral moment information about the hydrometeors in the precipitating cloud systems. The moments yield the reflectivity of the hydrometeors, the reflectivity-weighted fall speed of the hydrometeors and the variance of the hydrometeor fall speeds within in the observing volume. The echoes in the negative side of the Doppler spectrum are due to hydrometeors. The occurrence of the diurnal cycle of the precipitating cloud systems over Gadanki is possibly caused by diurnal convective boundary layer

process established by the monsoon thermal circulations (Reddy *et al.*, 2001).

Figure 3.18 shows the time height section of the hydrometeor reflectivity during the precipitating convection. As Gadanki-LAWP is sensitive to hydrometeors as well as fluctuations in the refractive index in the clear air, both precipitating and non-precipitating regions of the cloud systems can be observed. Three distinct structure of reflectivity is present during the observation period and is used to distinguish three regions of the TMCS *viz.*, convective, transition and stratiform regions. During the passage of the convective region, large value of reflectivity initially found in the lower troposphere reaches to the middle and upper troposphere. Therefore, during the passage of the convective clouds, intense reflectivity is detected at the whole sampling height range. As evident from the rainfall record, precipitation starts after 20:10 hrs local time. Hence the observed reflectivity may be associated with clear air portion of the convective region. The enhanced value of the reflectivity in the lower and middle troposphere is due to the convective turrets carrying large amount of water vapor from the lower troposphere to the middle and upper troposphere.

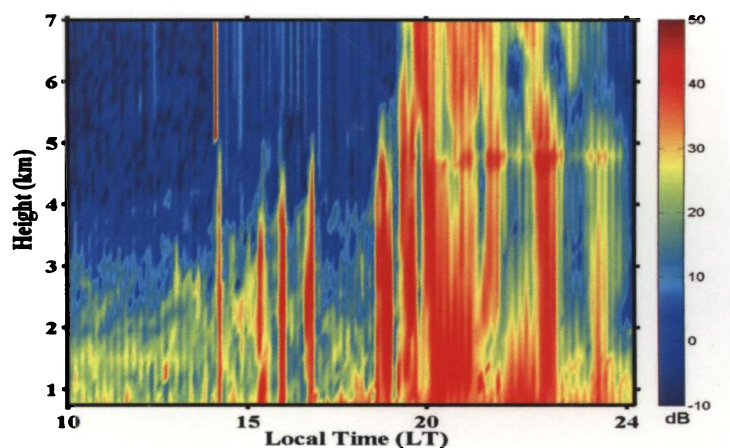


Figure 3.18: Time-height section of SNR in the middle troposphere during precipitating convection

Figure 3.19 shows the Doppler vertical velocity (DVV) during the observation period. The passage of the convective region is associated with large updrafts of magnitude greater

than 5 ms^{-1} . The radar reflectivity and Doppler velocity are found to be smaller during the transition period compared to the convective region. Transition region lasts for about one hour and corresponds to 20:10-21:00 hrs LT. During the late night hours and early morning hours, the mesoscale cloud system is dominated by stratiform clouds. The stratiform region lasts for about two hours and associated with large hydrometeor reflectivity below 6 km. As evident from the time series rainfall data (fig 3.17), the high reflectivities are due to hydrometeors. The large downward DVV below 5 km shows the increased fall speed of raindrops below the melting level (near 5 km). The characteristics of the stratiform region and occurrence of enhanced hydrometeor reflectivity near the melting level are examined separately in next section.

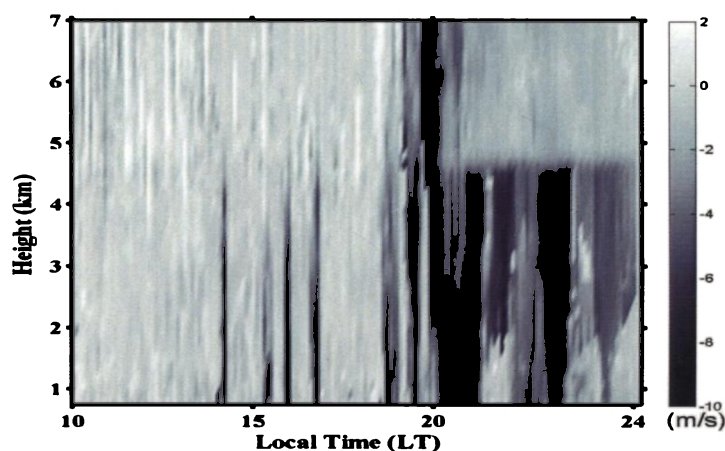


Figure 3.19: Time-Height section of Doppler Vertical Velocity

3.6.4 Bright band structure associated with the stratiform region

Another important region associated with a TMCS is the trailing stratiform region. The stratiform region is marked by weakening of echoes. A well defined radar bright band is typical of stratiform precipitation (*Houze, 1993*). Figure 3.20 shows the zoomed reflectivity

structure to delineate the three characteristic regions of TMCS. The cloud classification is shown on the top of the panel and C, T and S indicate the convective, transition and stratiform regions respectively of the precipitating cloud systems. Here the focus will be on the stratiform region together with the enhancement of reflectivity near the melting level. The bright band structure is evident from the height distribution of precipitation backscatter, which is an indication of cold precipitation process responsible for the formation of raindrops below melting layer in the stratiform region of TMCS.

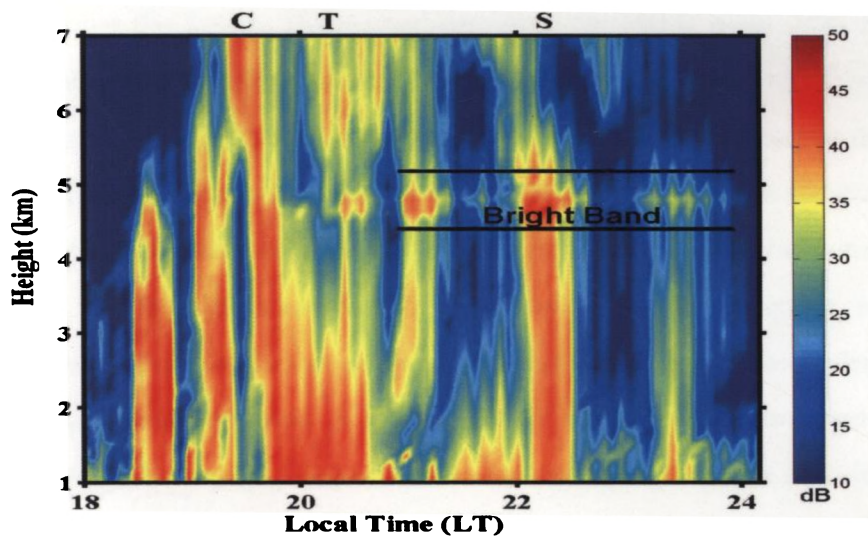


Figure 3.20: Time-Height section of SNR in the lower and middle troposphere

The criteria used for the detection of BB and BBH are based on the method proposed by *White et al.* (2002). Since, the BB coincides with an often sharp radar reflectivity enhancement, one choice for BBH detection would be to search only radar reflectivity profile for this enhancement. *Burrows* (2001) has proposed a method to find the BBH from the volumetric radar reflectivity using scanning Doppler radar measurements from Next Generation Weather Radar (NEXRAD). *Fabry and Zawadski* (1995) used vertically pointing X-band radar for BBH detection. They use only reflectivity profiles for BBH detection.

The potential risk of using only radar reflectivity for BBH detection is that, depending on the radar wavelength, reflectivity enhancement can result from features other than BB. This includes clear-air turbulence, the boundary layer top, and clouds as well as forms of stationary and intermittent clutter targets (*White et al.*, 1996).

The method proposed by *White et al.* (2002) uses both radar reflectivity and DVV profiles to detect the bottom portion of the BB, where the vertical gradients of the radar reflectivity and DVV are negatively correlated. The BBH height is assigned as the height of peak reflectivity above this feature. This method adds some confidence in the BBH detection. This technique can be used for any atmospheric profiling Doppler radars with an operating frequency that is sensitive to hydrometeors but does not suffer severe attenuation in rainfall. The method is also applicable to radars operating in the frequency range of 400-4000 MHz.

Figure 3.21 shows the vertical profiles of radar reflectivity and DVV obtained in rain containing a BB. In precipitation, the DVV provides a reflectivity weighted, integrated estimate of the fall velocity for the particles distributed within the radar scattering volume during the radar sampling period. A vertical gradient in the DVV is associated with the BB because the fall velocity generally increases as the snowflakes melt into rain, which decreases the drag and increases the density. In rain, the radar reflectivity factor and DVV are usually positively correlated, because the large drops fall faster and increase the radar reflectivity factor, which is proportional to the sixth power of the drop diameter. The SNR computed from the Doppler radar spectrum is directly proportional to radar reflectivity. Hence we can use SNR in place of radar reflectivity.

The upper portion of the BB results as snow or ice particles fall through the melting level and obtain wet surfaces as they begin to melt. This process makes the particles sticky and aggregation leads to larger particles. Some aggregation may occur above the melting level as well. As shown in the figure 3.21, the SNR increases and is positively correlated with the DVV in the upper portion of the BB partly because of the increasing particle

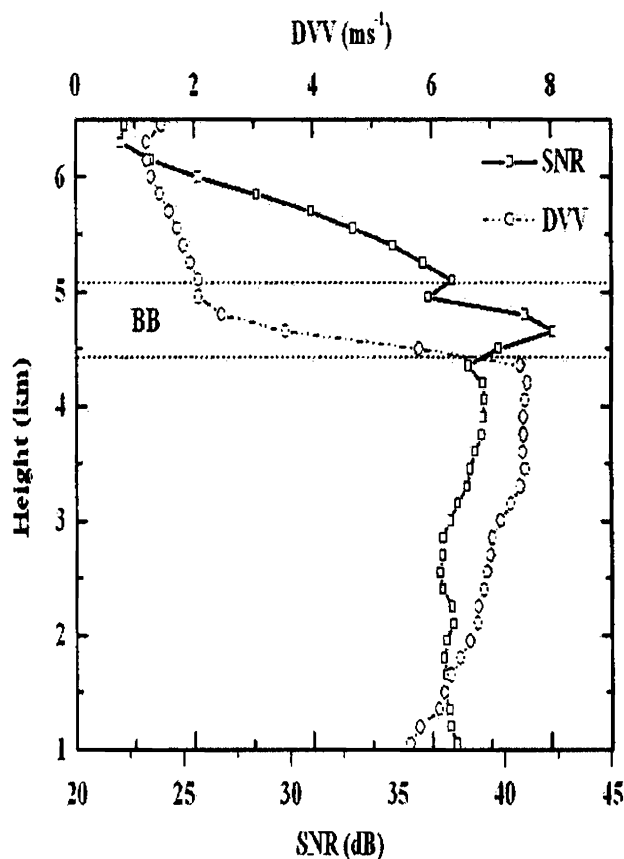


Figure 3.21: Profiles of Reflectivity and DVV

size. However, the SNR increases primarily because the dielectric constant for water is greater than for ice (*Battan, 1973*). Echo intensity is maximum at BBH level and falls sharply. As the particles undergoes further melting, their density increases, which leads to larger fall velocities. Hydrodynamically, unstable drops break up into smaller drops. This aggregation-break up process has traditionally been used to explain the BB intensity.

However, there is still much debate as to whether this effect is important. *Fabry and Zawadski (1995)* conclude that shape effect contribute more strongly to the BB formation at drizzle rates, whereas density effects are more important at stratiform rain rates. The

SNR decreases and is negatively correlated with DVV in the lower portion of the BB. Even though, the particles are smaller, their fall velocities increase. The inertia effect also contributes to the large fall velocities. The greater fall velocity of the raindrops formed from melted snow flakes causes a divergence in particle concentration below melting level, further contributing to the reduction in radar reflectivity in the lower portion of the BB.

The SNR-DVV pair is used to detect the BB structure. If an increase of SNR value of greater than 2.5 dB and a decrease of DVV of 1.5 ms^{-1} over a height of 300 m (two range gates for the radar used in this study), the profile pair is determined to contain a BB as long as DVV is greater than 0.8 ms^{-1} and SNR values greater than 30 dB at each of the altitude bounds. Below the melting level, the large aggregates of melted particles survive evaporation. The BBH is lower than the melting level. This result is due to the fact that snow can exist several hundred meters below the melting level because of the time required at temperatures above freezing to melt the snow. The distance that snow falls below the melting level depends on the physical properties of the snow particles (shape, size and density) as well as the temperature and humidity profiles, the ambient vertical velocity and precipitation rate. The snow level is defined as the lowest level in the atmosphere where snow or ice completely changes to rain. At still warmer temperatures, these aggregates melt fully and break up into small drops. Obviously entrainment of warm dry air into the downdraft air in the subcloud layer evaporates the cloud particles and thereby decreases the reflectivity below the BB. Hence, the decrease in fall speed below 4 km (fig 3.21) is likely due to the evaporation, droplet breakup and decreased Doppler velocity with increasing density.

3.7 DWR observations of Convective Systems

Scanning weather radar is used widely for routine monitoring of precipitating systems. A pulsed Doppler radar determines the reflectivity and velocity of the scatterers in a volume by producing conical scans. In this section, PPI(Z) and MAX(Z) display of the radar reflectivity of convective invent has been used to investigate the areal coverage, duration, propagation and structure of convective storms. Out of several convective events investigated, we discuss a single typical case of a Nor'westers on 18 April 2006. This convective storm usually formed over Gangetic west Bengal and adjoining region during pre-monsoon season. Occasionally, these convective storms exhibit squall line characteristics with leading convective and trailing stratiform region.

3.7.1 Evolution and propagation of Nor'Westers

Figure 3.22 and 3.23 shows MAX (Z) picture of the life cycle and evolution of a Nor'westers during 12:10-23:20 UTC of 18 April 2006. A convective cell labeled as **A** begins to develop at the western sector of the radar domain at 13:10 UTC. At 15:10 UTC, a cloud system entered into the domain from extreme northwest and is marked as **B**. These two well separated cells propagated southeastwards. At 17:10 UTC, the convective cell, **B** exhibit a multicellular structure and the cells are clustered together to form a squall line. At 19:10 UTC, cloud clusters in the squall line system, **B** well organized and propagated eastwards. By this time, cell **A** reaches its dissipating phase.

At 20:10 UTC, along with the squall line system, **B** a new cell **D** appeared over the western sector of the domain and cell **C** separated from the squall line system. At 22:10 UTC, these two cells **C** and **D** joined together to form a new convection center marked as **DC**, and which reaches towards its decaying phase. At the same period, the squall line cluster, **B** reached extreme eastern sector of the domain and propagated out of the radar

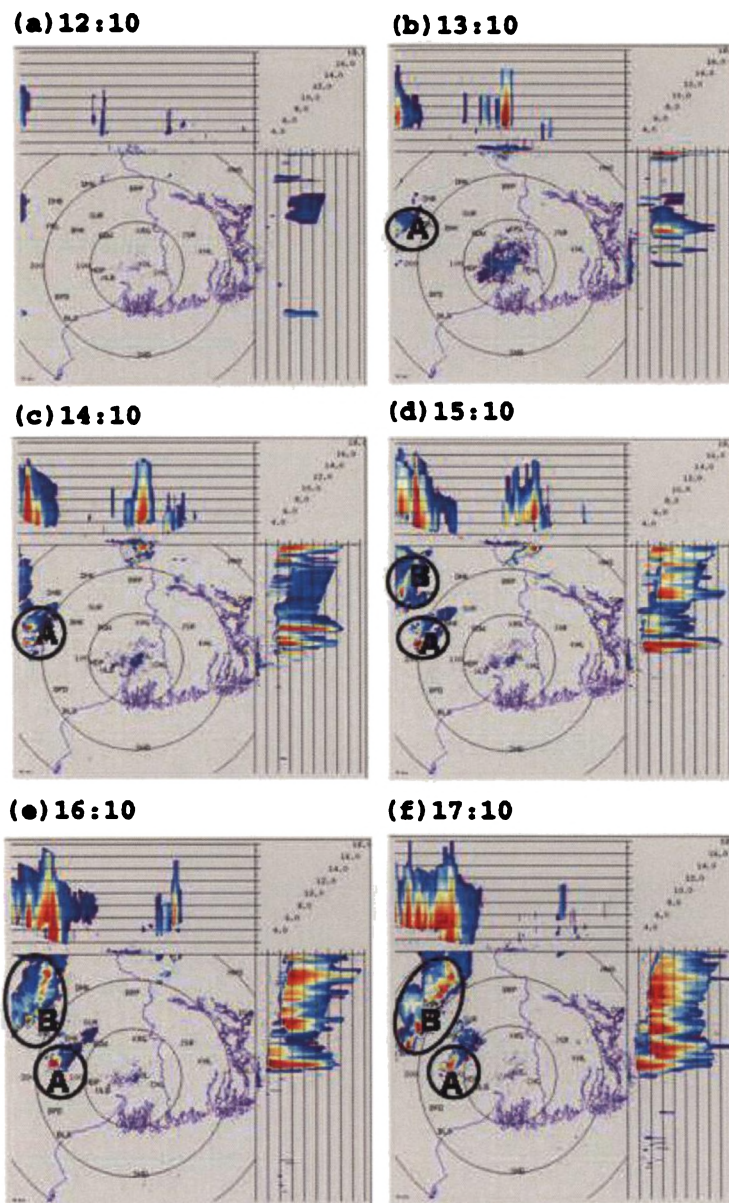


Figure 3.22: (a-f) DWR reflectivity, MAX(Z) during 12:10-17:10 UTC on 18 April 2006 showing the Propagation of Nor' Westers

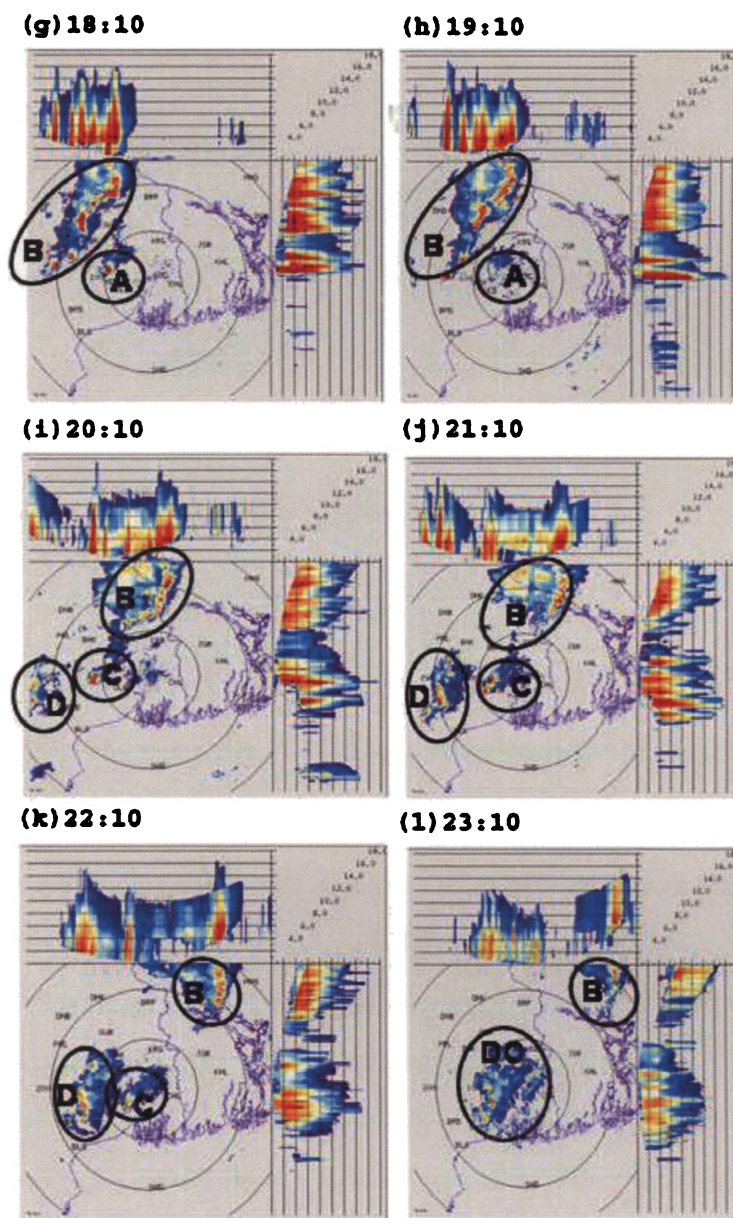
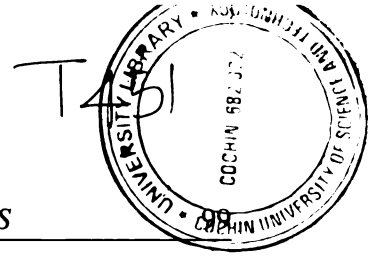


Figure 3.23: (g-l) DWR reflectivity, MAX(Z) during 18:10-23:10 UTC on 18 April 2006 showing the Propagation of Nor'Wester



Chapter 3: Radar Observations of the Structure and Evolution of TMCS

field of view. As evident from the time-sequence analysis of the radar picture, the squall line cluster lasts for more than 8-10 hours. This type of analysis brings out the capability of DWR to study the evolution and structure of TMCS.

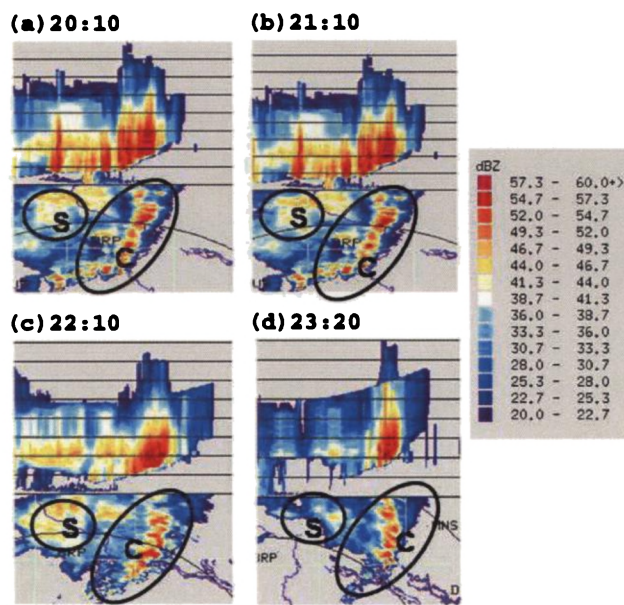


Figure 3.24: Radar reflectivity, MAX(Z) showing the convective and stratiform regions of a squall line system

Following the method proposed by *Steiner et al.* (1995) for the weather radar classification of the convective storms, we classified the characteristic regions of the TMCS into convective and stratiform region. The convective region is marked as C, which shows reflectivity values greater than 45 dBZ, and the reflectivity less than 45 dBZ is marked as stratiform region. Figure 3.24 shows the zoomed image of the squall line marked as B in figure 3.23. The squall line showed a well defined leading edge and propagated eastwards with the environmental wind. Behind the convective elements, C shown by the areas of higher reflectivity, a stratiform region, S of lower and more uniform reflectivity is observed.

3.8 Summary

The structure and evolution of cloud clusters have been examined at three different frequency bands using VHF, UHF and Doppler Weather radars. The height-time sections of several convective systems are studied to explore their reflectivity, turbulence and vertical velocity structure. The time-height variation of SNR and vertical velocity and the duration and intensity of the updraft cores have been used to classify the storm into multicell and supercell. The characteristic features associated with different phases of the storm life cycle such as cumulus, mature and dissipating stages have been examined in detail. The observed radar features such as ERZ/BB and WER have been used to study the dynamical and microphysical characteristics of the stratiform region of the TMCS and convective region of the supercell storm. Composite profiles of vertical velocity of each region have also been obtained for the convective, transition and stratiform regions. The time-height variation of SNR and DVV profiles has been used to explain the dynamical and microphysical processes near BB in UHF frequency. The evolution, areal extent and propagation characteristics of the Norwesters has also been examined using the PPI(Z) and MAX(Z) images from DWR observations.

CHAPTER 4

Microphysical Structure of Tropical Cloud Clusters

4.1 Introduction

It is evident that water substance can take variety of forms in a cloud. The various forms of water and ice co-exist and interact within the overall cloud ensemble. Cloud microphysics is an important area of study in atmospheric science that impacts our lives in so many ways, serving the central role in the atmospheric water cycle. Cloud microphysical models are used in a variety of research areas such as advertent and inadvertent weather modification, atmospheric electrification and lightening, atmospheric chemistry and air quality monitoring, developing improved remote sensing techniques from radars, lidars, profilers and satellites, involving large portion of the electro magnetic spectrum, numerical weather prediction of tropical and midlatitude systems, hurricanes, severe and non-severe local storms,

squall lines and other mesoscale convective systems and long-range prediction from global models, which focus primarily on the accurate representation of cloud-radiation interaction.

Obviously, it is the overall properties of the cloud ensemble that is of primary interest in cloud dynamics. At the same time, it is also impossible to ignore the microphysical processes, which is important for the overall behavior of the clouds. Numerical models require accurate representation of cloud microphysical behavior and it is convenient to group the various forms of water substance in a cloud into several broad categories of water substances viz., water vapor, cloud liquid water, precipitation water (include drizzle drops and rain drops), cloud ice, precipitable ice (include snow, graupel and hail) (Houze, 1993). The evolution of a cloud can be characterized in terms of fields of mixing ratios of all water substances. Hence total hydrometeor content inside a cloud can be divided into cloud liquid water, rain water, cloud ice, snow and graupel. Mesoscale and cloud resolving scale models needs accurate representation of the mixing ratios of each categories. Commonly used microphysical schemes use prognostic equations for the prediction of this five cloud microphysical variables and interaction among different categories of water substances. The total water substance in a parcel of air is given by the sum of the water contained in each of the categories. Vertical distributions of the particle density of these species are important in formulating and testing sophisticated microphysical schemes.

Two and three dimensional modeling of cloud and convection has its root in 1960s. Ever since, cloud models are used to study the bulk properties and internal structure of clouds. These cloud models were also used to quantify the effects of wind shear on deep convection, squall lines and mid-latitude thunderstorms which are associated with tornado genesis (Ogura and Takahashi, 1973; Orville and Kopp, 1977; Klemp and Wilhelmson, 1978). Cloud resolving scale models (CRM) are used to study the collective effects of convection on large scale environment (Arakawa and Schubert, 1974; Cotton *et al.*, 1982; Tao and Simpson, 1984a; Tao *et al.*, 1987b; Redelsperger and Lafore, 1988). The main

objective was to improve the cumulus parameterization schemes based on the knowledge gained from CRM. The CRM can also be used to study multi-scale processes, effect of microphysical processes on cloud formation and evolution, effects of stratiform rainfall and its relationship with deep convective rainfall, cloud-chemistry interaction and surface processes (Grabowski *et al.*, 1996; Xu and Randall, 1996; Lin and Arakawa, 1997; Wu *et al.*, 1999; Tao *et al.*, 1999).

The cloud resolving scale models also known as cloud system resolving models (CSRMs) have resolutions fine enough to represent individual cloud elements and space time domains large enough to encompass many clouds and their life times (Cotton *et al.*, 1982; Tao and Simpson, 1984a; Tao *et al.*, 1987b; Redelsperger and Lafore, 1988). These models can be used to identify possible deficiencies in the parameterizations of physical processes in climate models. Such models are driven by observations of large-scale weather system. One method to achieve this objective is to utilize field observations to initialize, force, and evaluate CSRMs (Moncrieff *et al.*, 1997). The cloud resolving scale models have been successfully used to simulate the local severe storms (Doswell, 2002; Cotton and Anthes, 1989; Cotton, 2003). Cloud-resolving models have successfully simulate atmospheric thermodynamic profiles, cloud properties, and precipitation in the tropics during the Global Atmospheric Research Program (GARP)-Atlantic Tropical Experiment (GATE) (Xu and Randall, 1996; Grabowski *et al.*, 1996) and Tropical Ocean Global Atmosphere Coupled Ocean Atmosphere Response Experiment (TOGA-COARE) (Wu *et al.*, 1999; Liu *et al.*, 2001). Wu *et al.* (1999) conducted sensitivity experiments with two dimensional cloud resolving models and showed the sensitivity of the radiative flux, cloud radiative forcing and albedo to the effective radius of ice particles. They improved the simulations of cloud and radiative forcing by modifying the ice-microphysical parameterization scheme.

Tao *et al.* (1987a) investigated the impact of ice-microphysical processes and large scale

vertical velocity on the structure of a GATE squall line using a time-dependent, nonhydrostatic model. Their simulation results showed that the total ice content in the convective and stratiform regions is reduced by only 15% when large scale vertical velocity is reduced by 40% at middle and upper levels. The development of the transition zone minimum and secondary maxima of radar reflectivity in squall lines with trailing stratiform precipitation and horizontal distribution of precipitation behind the convective line could be determined by the vertical distribution of the amount of ice detrained from convective cells (*Smull and Houze, 1987; Biggerstaff, 1993*).

Cloud resolving mesoscale models using bulk microphysics parameterization have been used to simulate single cloud, cloud ensembles, sea breezes, severe storms, and synoptic and tropical storms. Accurate representation of moisture and microphysical processes in numerical weather prediction (NWP) model is a very challenging problem, and it is essential for good quantitative precipitation forecast (QPF). The sensitivity of different microphysical schemes to QPF and hydrometeor structure has been investigated in the present chapter.

4.2 Brief description of the modeling system

The fifth-generation Pennsylvania State University National Center for Atmospheric Research (PSU-NCAR) mesoscale model (MM5) version 3.5.6 has been employed in this study. The MM5 model is a three-dimensional, limited-area, primitive equation, nested-grid model with a terrain following vertical coordinate.

The MM5 modeling system consists of several dependent programs. The flow chart of the complete modeling systems are depicted in schematically in figure 4.1 , which shows the order of the programs, the flow of data and their primary functions. The terrestrial and isobaric meteorological data are horizontally interpolated (programs *TERRAIN* and

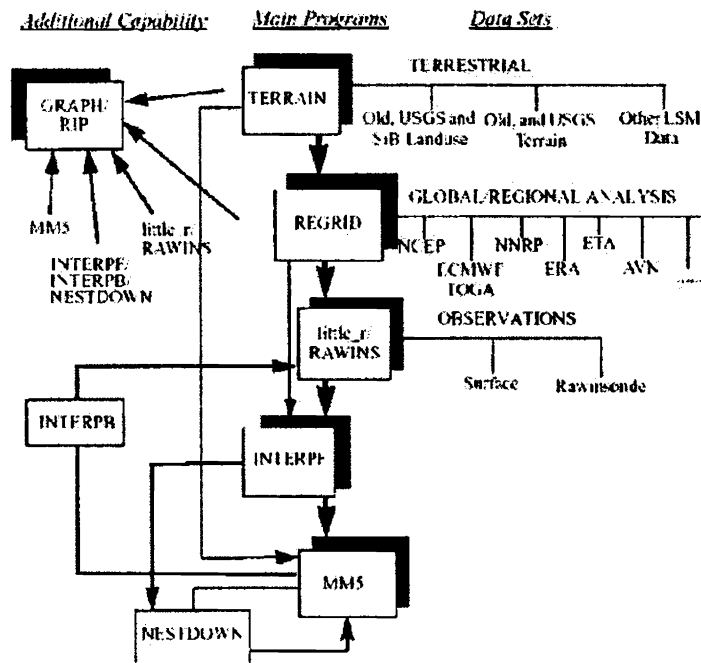


Figure 4.1: Flow chart of MM5 modeling system

REGRID) from a latitude-longitude grid to a mesoscale, regular domain on either a Mercator, Lambert Conformal, or Polar Stereographic projection. Since the interpolation of the meteorological data does not necessarily provide much mesoscale detail, the interpolated data may be enhanced (program *LITTLE_R/RAWINS*) with observations from the standard network of surface and rawinsonde stations using a successive-scan Cressman or multiquadratic technique. Program *INTERPF* then performs the vertical interpolation from pressure levels to the σ -coordinate of the MM5 model. *MM5* is the central weather prediction part of the modeling system and which requires initial and boundary condition files for integration. Alternatively, program *3D-VAR* may be used to ingest data on model σ -levels. After a MM5 model integration, program *INTERPB* can be used to interpolate

data from σ -levels back to pressure levels, while program *NESTDOWN* can be used to interpolate model level data to a finer grid to prepare for a new model integration. Graphic programs (*GrADS*, *RIP* and *GRAPH*) may be used to view modeling system output.

4.2.1 Model horizontal and vertical grid

The modeling systems usually gets and analyze its data on pressure levels and these data are interpolated to models vertical coordinate before being input to the main program, MM5. The vertical coordinate is terrain following meaning that the lower grid levels follow the terrain while upper surface is flat. Intermediate levels progressively flatten as the pressure decreases towards the chosen top pressure. A dimensionless quantity is used to define the model levels,

$$\sigma = \frac{(P_0 - P_t)}{(P_{s0} - P_t)} \quad (4.1)$$

Where P_0 is the reference state pressure, P_t is the specified top pressure and P_{s0} is the reference state surface pressure.

The horizontal grid has an Arakawa-Lamb B-staggering of the velocity variables with respect to scalars. The scalars (temperature (T), specific humidity (q), etc) are defined at the center of the grid square while the eastward (u) and northward (v) velocity components are co-located at the corners. All the above variables are defined at the middle of each model vertical layer, referred to as half levels and the vertical velocity is carried at the full levels.

4.2.2 Key features of MM5 modeling system

The most useful feature of the MM5 model is its flexibility in the sense that many options are user specified. The model can be used in various applications by simply setting these parameters to appropriate values. These include number of nests, type of convection, Planetary Boundary Layer (PBL), radiation parameterization schemes and many other op-

tions. Sub-grid scale processes that has scales below the grid length such as turbulence, convection, radiation and PBL processes influences the large scale and mesoscale weather systems. Hence the collective effects of these processes need to be calculated from information available on grid-scale. Introducing the statistical effects of these processes as additional source or sink terms in the prediction equation for large scale dependent variable is called parameterization. Another advantage of the modeling system is that it is a state-of-art model and has undergone continuous development and well documented. The final version of the model is version 3.7.1. A detailed description of the model and derivation of basic equations can be found from *Dudhia (1993)*, *Grell (1993)* and *Grell et al. (1994)*. The MM5 modeling system can be used for a broad spectrum of theoretical and real-time studies, including applications of both predictive simulation and four dimensional data applications to monsoons, hurricanes and typhoons. On a smaller *meso* – β and *meso* – γ scales (2-200 km), MM5 can be used for studies involving mesoscale convective systems, fronts, land-sea breezes, mountain-valley circulation and urban heat-islands. Various physics options available in MM5 is listed in table 4.1.

Microphysics	Stable Precipitation, Warm rain, Simple ice, Mixed Phase GSFC, Reisner-2, Schultz
PBL	Bulk PBL, Blackadar PBL, Burk-Thompson, Eta PBL, MRF PBL, Pleim-Chang PBL, Gayno-Seaman PBL
Cumulus	Anthes-Kuo, Grell, Arakawa-Schubert, Fritsch-Chappell Kain-Fritsch, Betts-Miller, Kain-Fritsch-2
Radiation	Simple cooling, Cloud radiation, CCM2 radiation, RRTM longwave
Soil	Balckadar, Five-layer soil model, Noah LSM, Pleim-Xiu LSM

Table 4.1: Physics options available in MM5 modeling system

4.2.3 Brief note on cumulus parameterizations

Numerical weather prediction models with large grid spacing do not explicitly resolve and predict convection on the space and time scales where they occur. Hence the effects of convection on the resolvable scales of the model must be parameterized. When deep convection occurs in the atmosphere, it strongly affects the meso and large scale dynamics. Since, cumulus parameterization is an attempt to represent the collective effect of cumulus clouds without predicting individual clouds, it is a closure problem in which we must seek a limited number of equations to represent these effects. The closure assumption is the crux of any cumulus parameterization and should address questions such as how the model will produce clouds and convection and which tendencies will be fed back to the large scale as a result of convection. The initiation, timing, location and intensity of the convection depends on the convective instability in the atmosphere at a grid point, the existence of low-level or vertically integrated mass or moisture convergence and the rate of destabilization by the environment. The convective activity collectively modify the large-scale temperature and moisture fields through detrainment and storm-induced subsidence in the surrounding environment. Detrainment creates large scale cooling and moistening, while the local subsidence creates large scale drying and warming.

Based on the approaches in which a particular parameterization scheme determines the new vertical distribution of heating, cooling, moistening or drying, the cumulus parameterization schemes are broadly classified as adjustment schemes and mass flux schemes. In adjustment schemes, some approaches simply nudge each grid point vertical profiles towards an empirical reference profile, while the others make the profile as a function of the difference between the moist adiabats inside the parameterized clouds and environment. The mass flux approaches are more sophisticated and also they obtain the heating profiles from the amount of the compensating subsidence between the clouds and often account for the effects of downdrafts on the large scale environment as well.

The choice of the cumulus parameterization is based on the scale size of process of interest and grid size of the domain. Usually cumulus parameterization is switched off on grid size less than 5-10 km. The model changes the profiles of environmental temperature and moisture as a result of convective process. This is a complex process and as this convective feed back affects other processes in the model that also be parameterized well. For example, if the model does a poor job of parameterizing boundary layer physics, the resulting convection forecast will also be poor, even if the convective parameterization was perfect.

It is important to realize that the same scheme used in two different models will likely produce different results due to the way in which the scheme interacts with other components of each individual model. It is difficult to make general statements about the quality of one convective parameterization scheme versus other. Based on the closure assumption, the Grell scheme is found to be suitable for grid spacing between 10-30 km. Grell (GL) scheme is based on rate of destabilization or quasi-equilibrium assumption. This is the single cloud version of the Arakawa-Schubert scheme in which updraft and downdraft fluxes and compensating motion determining the heating and moistening profile. This scheme is useful for smaller grid sizes (10-30 km) and tends to allow a balance between the resolved scale rainfall and convective rainfall. Shear effects on precipitation efficiency are also considered (*Grell et al., 1994*). We use Grell cumulus parameterization scheme in the entire thesis.

4.2.4 Overview of the microphysical processes

Among the most popular and least computationally expensive approaches are bulk microphysical parameterizations. These schemes calculate the mixing ratios of liquid and/or ice. Many bulk schemes are based on *Kessler (1969)* autoconversion parameterization, accord-

ing to which the rate of rain water production by cloud droplet collisions is proportional to cloud water content (CWC) and does not depend on the width of the droplet spectrum.

The bulk microphysics developed at the South Dakota School of Mines and Technology (SDSMT) have served as the building blocks for most of the microphysical schemes currently available in the MM5 model and its successor, Weather Research and Forecasting (WRF) model. These schemes are composed of a system of prognostic equations for temperature (or its equivalent), water vapor mixing ratio, and mixing ratios of one or more species of condensate in the form of small (non-precipitating) cloud droplets, small (non-precipitating) ice crystals, (precipitating) raindrops, and larger (precipitating) ice particles. The first two species are treated assuming a monodisperse distribution (i.e., they have the same size), which is approximately consistent with observations of narrow droplet spectra in clouds. The last two precipitating species are assumed to have an exponential distribution based on observed spectra (*Marshall and Palmer, 1948*). As a result, only a limited number of integral parameters are required to describe cloud microphysical processes. These include either the time evolution of mass content (single-moment schemes) or the mass contents and the mean number concentrations (double-moment schemes). The relatively small number of integral parameters makes the bulk parameterization computationally efficient.

In response to the diabatic cooling and moistening from ascent, cloud droplets (cloud water) form by condensation. Small ice crystals (cloud ice) are initiated by one or more modes of ice nucleation, and subsequently grow in size by vapor deposition. Small ice crystals also form through various means of fracturing or break up of larger ice particles. Rain is initiated either by the self collection of small cloud droplets into small drizzle size droplets ($80 - 100\mu m$) or by melting of ice falling below the $0^{\circ}C$ level. Rain can also grow by continuous collection of smaller cloud droplets as they fall through the air. Precipitating ice particles forms because of depositional growth of small ice particles to larger sizes,

self-collection (aggregation) of small ice crystals, riming of cloud water into falling ice particles, and freezing of rain drops carried above the 0°C level in strong updrafts.

The sensitivity of single moment bulk microphysical scheme, namely warm rain, simple ice and Goddard microphysical scheme is discussed in this section. In Warm Rain scheme cloud and rain water fields predicts explicitly with microphysical processes. No ice phase processes considered in this scheme. The Simple Ice scheme adds ice phase above the melting level without adding memory. This scheme does not consider supercooled water and treat immediate melting of snow below the melting level. The Goddard Microphysical (GSFC) scheme adds supercooled water above the melting level and slow melting of snow below the melting level and memory adds for cloud ice and snow. The scheme includes additional equation for graupel prediction (*Lin et al.*, 1983; *Tao et al.*, 1987a; *Tao and Simpson*, 1984b).

4.3 Cloud Resolving Scale Simulations

Despite many improvements in numerical weather prediction systems and further refinement of the grid resolution, prediction of precipitation skill has not improved to a satisfactory level during the past decades (*Ebert et al.*, 2003). Precipitation constitutes the end of a long processes chain in the atmosphere ranging from ascending air motion, nucleation and evolution of hydrometeors. For successful precipitation forecast, the entire processes chain has to be adequately described. Deep convection is one kind of precipitation with particularly bad precipitation skill. Here the problem arise due to a grid resolution too coarse in NWP models even in limited area models to resolve the convection explicitly and due to a rather rudimentary description of cloud microphysical processes. The former can be circumvented by diminishing the grid intervals and time steps accordingly, the latter require more fundamental consideration and process formulations. In this section, the sensitivity of

the microphysical schemes to the initiation, evolution, duration, areal extent and structure of the TMCS has been investigated by considering real cases and conditions.

4.3.1 Experiment design

The PSU-NCAR model MM5 (*Grell et al.*, 1994) is used to simulate the convection events. The figure 4.2 shows the domain configuration, which include three nested domains at 45, 15 and 5 km resolutions. The simulation is carried for 24 h. The initial and boundary conditions are taken from NCEP-FNL global analysis at $1.0^0 \times 1.0^0$ horizontal resolution. Following physics options are used for the simulations. The cumulus parameterization scheme uses Grell scheme (*Grell*, 1993) except for the innermost domain, where convective processes were resolved explicitly, the MRF-PBL scheme (*Hong and Pan*, 1996) and atmospheric radiation scheme of Dudhia (*Dudhia*, 1993). The cumulus parameterization is switched off in the inner most domain. By keeping all the above physics options same, three experiments have been carried out to study the sensitivity of single-moment bulk microphysical parameterization schemes in the MM5 modeling system. The first experiment (*MM5-WR*) uses warm rain processes, simple ice scheme is used in the second experiment (*MM5-SI*) and third experiment *MM5-GSFC* uses GSFC scheme. Due to computational costs, only conventional one moment microphysical schemes will be used for operational precipitation forecasts.

The microphysical processes and their complex interaction through the corresponding mixing ratios of each species in the warm rain, simple ice and GSFC microphysical schemes respectively are listed in table 4.2 and figure 4.3 shows the schematic representation. The prognostic equation for RNW (Q_R) in warm rain processes can be represented as,

$$\frac{\partial Q_R}{\partial t} = -P_S + P_{RAUT} + P_{RACW} + P_{RCCW} - P_{REVP} \quad (4.2)$$

No	Description of the microphysical processes	Abbreviation	WR	SI	GSFC
1	Accretion of CLW by SNOW	PSACW			✓
2	Accretion of CLW by RNW	PRACW	✓	✓	✓
3	Autoconversion of CLW by RNW	PRAUT	✓	✓	✓
4	Collection of cloud ICE by RNW	PRCCI	✓	✓	✓
5	Collection of CLW by GRAUPEL	PGCCW			✓
6	Collection of CLW by SNOW	PSCCW			✓
7	Collection of CLW by RNW	PRCCW	✓	✓	✓
8	Collection of RNW by GRAUPEL	PGCRW			✓
9	Collection of RNW by SNOW	PSCRW			✓
10	Collection of SNOW by RNW	PRCSN			✓
11	Condensation	PCOND		✓	✓
12	Conversion from SNOW to GRAUPEL	PGCNS			✓
13	Conversion from cloud ICE to GRAUPEL	PGCNI		✓	
14	Conversion from cloud ICE to SNOW	PSCNI		✓	✓
15	Deposition of cloud ICE	PIDEP		✓	✓
16	Deposition of GRAUPEL	PGDEP			✓
17	Deposition of SNOW	PSDEP		✓	✓
18	Evaporation of RNW	PREVP	✓	✓	✓
19	Evaporation of melting GRAUPEL	PGMLTE			✓
20	Evaporation of melting SNOW	PSMLTE			
21	Evaporation of CLW	PCEVP	✓	✓	✓
22	Freezing of CLW	PIFZC			✓
23	Freezing of RNW by collection with ICE	PSIACR		✓	
24	Freezing of RNW to GRAUPEL	PGFZR			✓
25	Ice multiplication processes	PISPLS			✓
26	Melting of GRAUPEL	PGMLT			✓
27	Melting of SNOW	PSMLT			✓
28	Melting of ICE	PIMLT			✓
29	Sublimation of cloud ICE	PISUB		✓	✓
30	Sublimation of GRAUPEL	PGSUB			✓
31	Sublimation of SNOW	PSSUB		✓	✓
32	Riming of cloud ICE	PIIACW			✓

Table 4.2: Significant microphysical processes involved in the Warm Rain, Simple Ice and GSFC schemes and their abbreviations

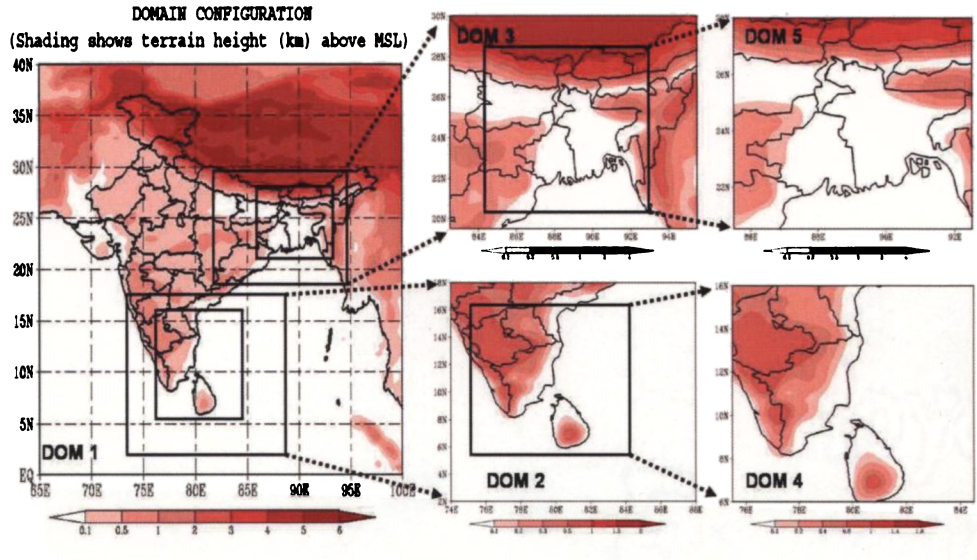


Figure 4.2: Domain configuration for the experiments

The prognostic equation for RNW (Q_R) in simple ice scheme can be expressed as,

$$\frac{\partial Q_R}{\partial t} = -P_S + P_{RAUT} + P_{RACW} + P_{RCCW} + P_{SCNI} - P_{REVP} \quad (4.3)$$

The prognostic equation for the RNW (Q_R) in GSFC scheme can be written as,

$$\begin{aligned} \frac{\partial Q_R}{\partial t} = & -P_S + P_{RAUT} + P_{RACW} + P_{RCCW} + P_{RCSN} + P_{IMLT} + P_{GMLT} + \\ & P_{SNLT} - P_{RCRW} - P_{SIACR} - P_{GFZR} - P_{REVP} \end{aligned} \quad (4.4)$$

Where P_S is the surface rain rate.

4.4 Thunderstorm on 06 May 2007 : Case I

4.4.1 Simulated radar reflectivity

The algorithm for the calculation of radar reflectivity from model data uses empirical equations that relate radar reflectivity to the modeled fields of cloud and rain water (hydromete-

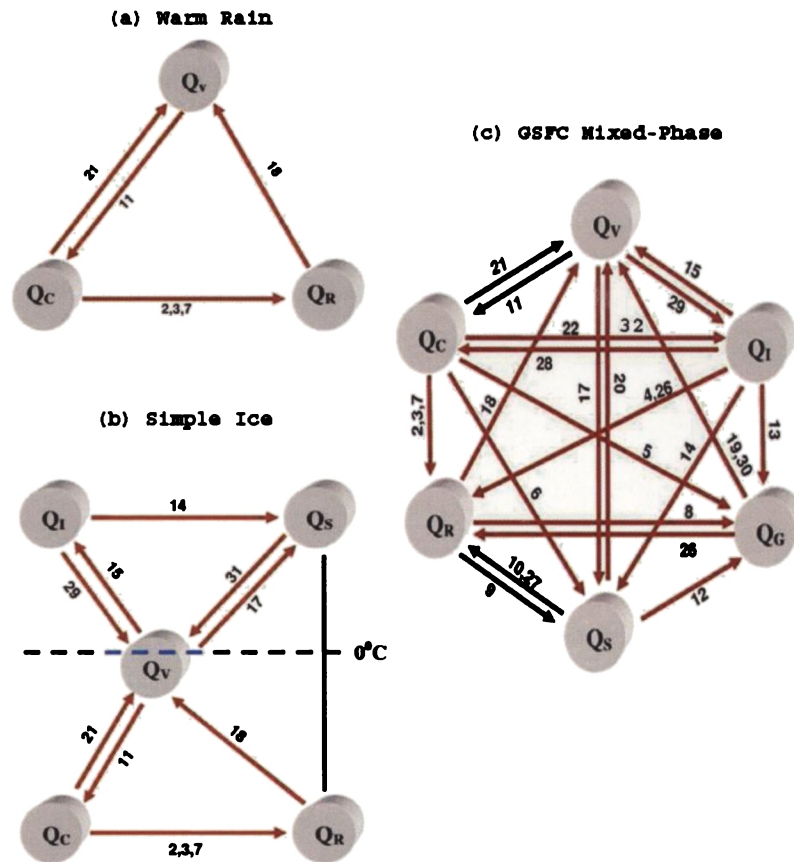


Figure 4.3: Schematic picture of microphysical processes involved in the three microphysical schemes

ors) (*Tao and Simpson, 1984a; McCumber et al., 1991*). These modeled values represent the grid-element mean values of cloud particles/hydrometeors obtained directly from the MM5 simulations with bulk parameterizations. The upper, middle and lower panel of Figure 4.4, 4.5 and 4.6 shows the simulated low level radar reflectivity from the MM5-WR, MM5-SI and MM5-GSFC experiments respectively. All the three experiments show the southeastward propagation of the cloud clusters. The reflectivity field predicted by the MM5-WR is found to be underestimated, while those from MM5-SI experiments overestimated. The MM5-GSFC experiment produced more realistic picture of the radar reflectivity. The spa-

tial structure of the reflectivity field simulated by the MM5-GSFC experiment is more or less similar to the observed reflectivity structure from DWR. This analysis clearly evidenced the impact of microphysical schemes in deriving the reflectivity from model fields.

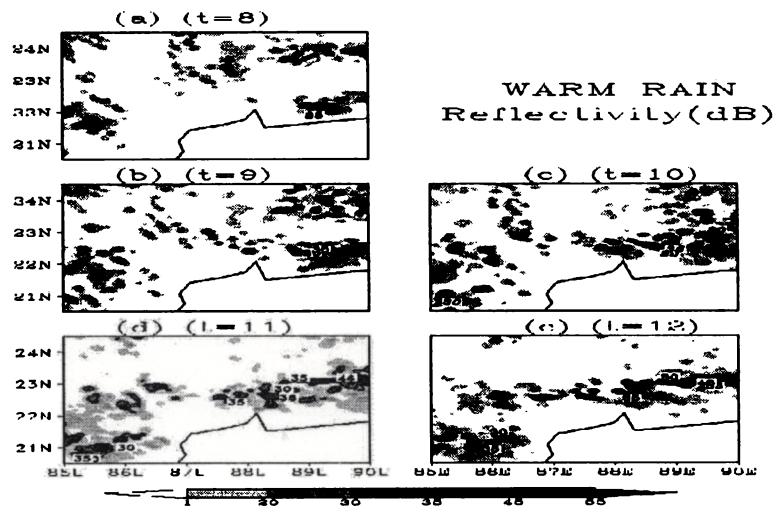


Figure 4.4: Simulated radar reflectivity (dBZ) from MM5-WR

4.4.2 Hydrometeor structure and vertical velocity

Figure 4.7 shows the latitudinal cross-section of CLW mgm^{-3} , RNW mgm^{-3} and total hydrometeors mgm^{-3} at 0900, 1000 and 1100 UTC of 6 May 2007. The left, center and right panels presents the cloud hydrometeor structure from MM5-WR, MM5-SI and MM5-GSFC experiment. As MM5-WR experiment do not consider any ice phase processes, the condensation of water vapor leads to more CLW even in the middle troposphere. The CLW exhibits similar distribution below 4 km for both MM5-WR and MM5-SI experiments. As simple ice scheme treats CLW above 0°C isotherms as cloud ice, the MM5-SI produced no CLW above 5 km. The MM5-GSFC experiment also shows maximum CLW at 4 km.

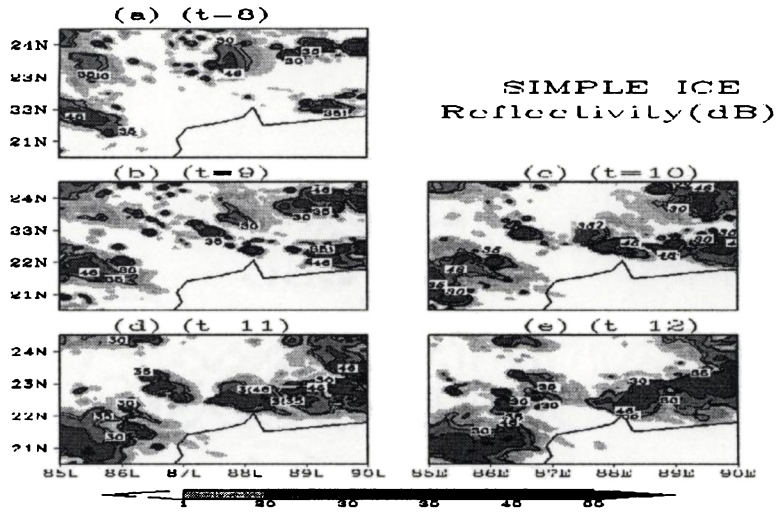


Figure 4.5: Simulated radar reflectivity (dBZ) from MM5-SI

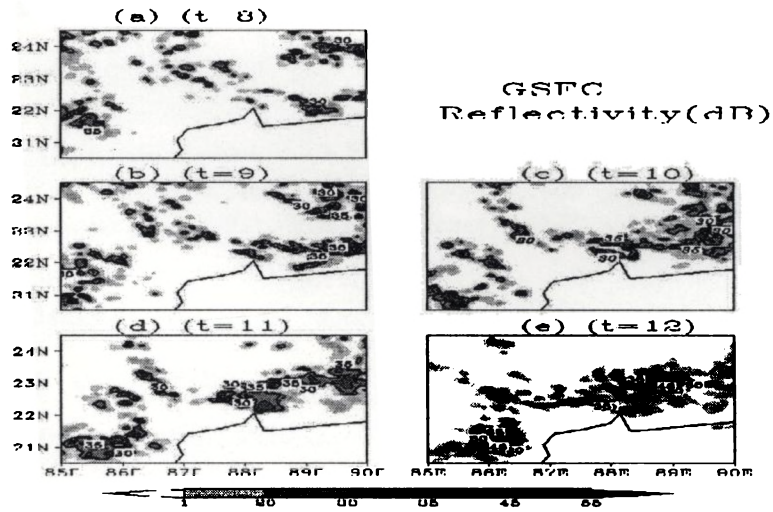


Figure 4.6: Simulated radar reflectivity (dBZ) from MM5-GSFC

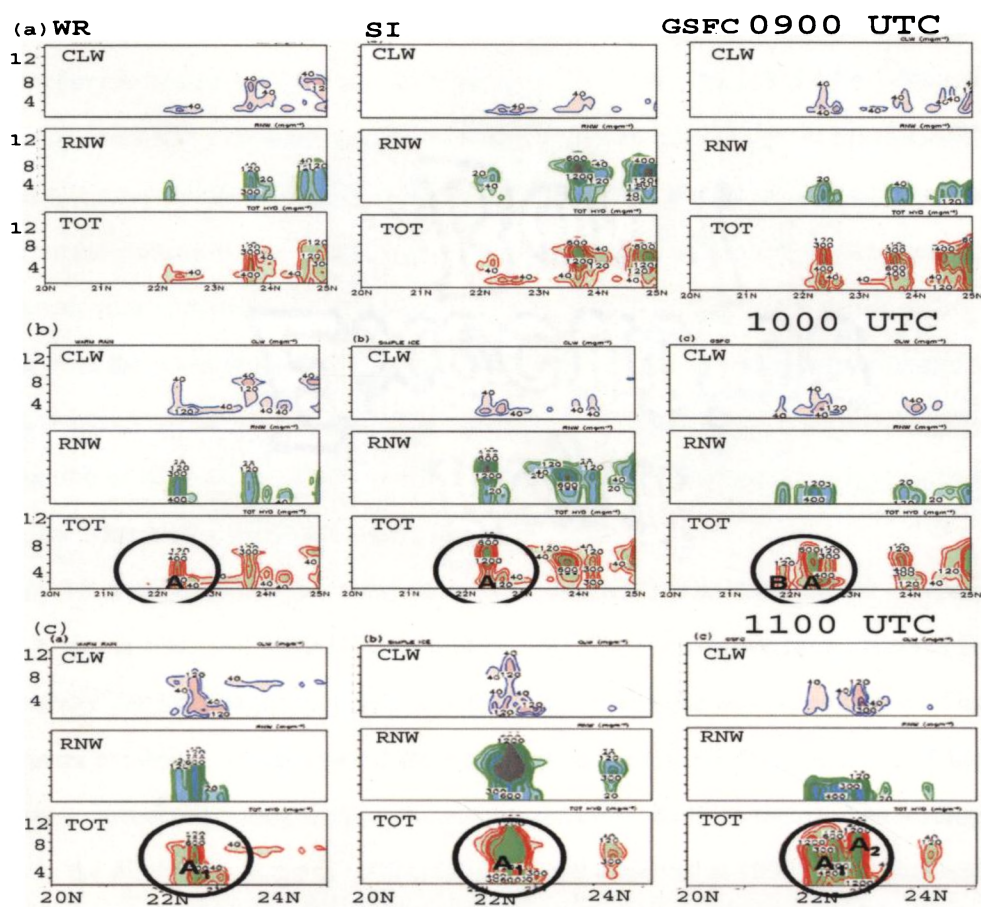


Figure 4.7: Latitudinal section of CLW (mgm^{-3}), RNW (mgm^{-3}) and total hydrometeor (mgm^{-3}) from MM5-WR (left panel), MM5-SI (middle panel), and MM5-GSFC (right panel) experiments at (a) 0900, (b) 1000 and (c) 1100 UTC on 6 May 2007

Unlike the MM5-SI experiment, MM5-GSFC produce little CLW above 4 km which is mainly due to ice conversion processes.

As warm rain processes predicts only liquid phase, the RNW is mainly produced from the autoconversion of CLW to RNW, accretion of CLW by RNW and collection of CLW by RNW and the RNW mostly dissipated through evaporation and rainout. The vertical distribution of RNW from MM5-WR experiment extends upto 10 km with a maximum near 3 km. The simple ice scheme treats CLW above 0°C isotherm as cloud ice without adding ad-

ditional memory. Ice can be converted to snow above the melting level and the total precipitation category is treated as RNW to reduce the memory space. The MM5-SI experiment shows maximum RNW near 8 km and its distribution extends upto 11 km. In MM5-GSFC experiment, the microphysical processes involving RNW other than that described in warm rain scheme are melting of snow, collection of snow by rain and melting of ice and graupel. Raindrops are mostly confined in the lower levels (below 0°C isotherms), which is mainly produced from the autoconversion of CLW to RNW and melting of ice, snow and graupel. Since CLW is very small (see upper panel), the second process contributes significantly to the production of RNW in the lower levels. The MM5-GSFC experiment mostly predicts RNW below 5 km with a maximum near 2 km.

Figure 4.8 a and b shows the radar reflectivity, MAX(Z) from the Kolkata Doppler Weather Radar at 1000 and 1030 UTC of 6 May 2007. Two convective cells observed in the reflectivity pattern, the primary cell is denoted as *A*, and the second cell as *B*. The cloud system exhibits a southeastward movement as is the typical characteristics of the *Nor'Wester*s observed during the pre-monsoon season over Kolkata region. The leading cell *B* is in the dissipating stage at 1000 UTC and is not observed at 1030 UTC. The total hydrometeor structure from MM5-WR and MM5-SI experiments predicts only the primary cell *A*, whereas MM5-GSFC experiment simulates both cells *A* and *B*. As seen from the radar images, the cell *B* extends to 6 km and the cell *A* reaches upto 10 km. The MM5-GSFC experiment also captures the vertical extent of both the cells.

As seen from the radar reflectivity, at 1030 UTC, the convection cell *B* dissipated and the cell *A* split into two cells named *A*₁ and *A*₂. The total hydrometeor structure from MM5-GSFC experiment also captures the storm splitting processes very well (see figure 4.7), whereas MM5-WR and MM5-SI experiments do not simulate the storm splitting. Both MM5-WR and MM5-SI experiments simulate only single cell near the radar site. Hence MM5-GSFC experiment captures observable characteristics of the MCS characteristics for

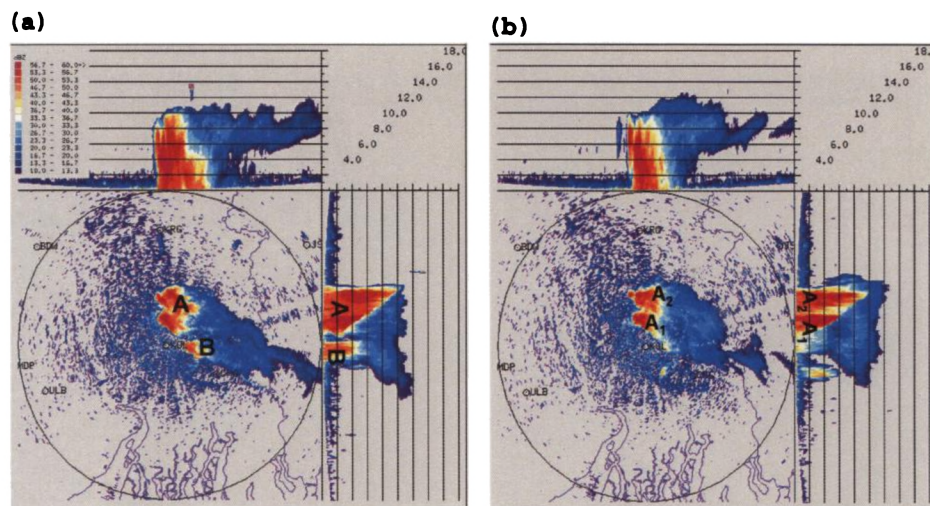


Figure 4.8: Radar reflectivity, MAX (Z) from Kolkata Doppler radar at (a) 10:00 and (b) 10:30 UTC on 6 May 2007

example propagation, structure and storm dynamics such as storm splitting processes.

4.5 Mesoscale Convective System : Case II

Figure 4.9 a, b, c and d shows the three hourly accumulated rainfall from TRMM observations, MM5-WR, MM5-SI and MM5-GSFC experiments respectively. As evidenced from the TRMM observations the rainbands shows a southeastward propagation. All the three sensitivity experiments do show similar propagation of the rainbands. The TRMM observations show more than 2 cm rainfall during the six hours. The MM5-WR experiment predicts relatively small amount of rainfall. However, the MM5-SI and MM5-GSFC experiments shows similar organization and intensity of rainbands. The propagation characteristics and the areal coverage of the rain patches simulated by MM5-GSFC experiment shows good agreement with the TRMM observations. Without ice phase latent heating/cooling processes (depositional warming and sublimative cooling), the MM5-WR experiment pro-

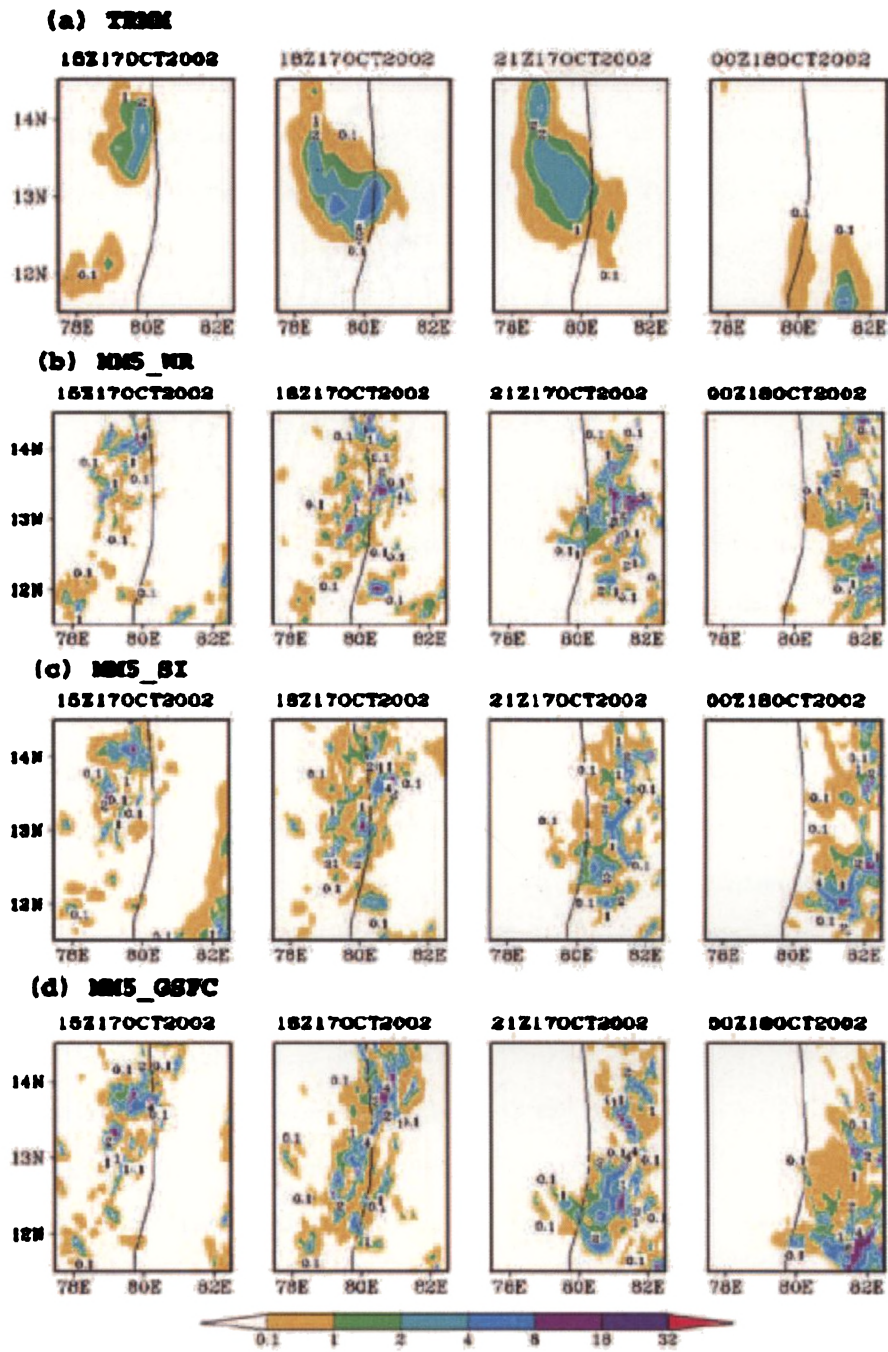


Figure 4.9: 3-hourly accumulated rainfall from (a) TRMM-3B42, (b) MM5-WR, (c) MM5-SI and (d) MM5-GSFC in mmhr^{-1}

duced weakest storms in the composite reflectivity field (not shown) and rainfall is underestimated. Other two experiments produced more intense cloud structure in the reflectivity field and rainfall. The MM5-GSFC experiment generated more solid precipitation particles at upper levels that results in more surface rainfall through melting of snow flakes and graupel. The rainbands predicted by MM5-GSFC experiment propagates southeastwards faster than that seen in TRMM observations.

4.5.1 Hydrometeor structure

The figure 4.10 shows simulated hydrometeor structure. The upper, middle and lower panels shows the hydrometeors at 1300, 1500 and 1700 UTC of 17 October 2002. The distribution of CLW and RNW shows similar structure as discussed for the previous case. The MM5-GSFC scheme simulates more CLW and RNW in the lower levels as compared to other two experiments. In this section, vertical distribution of total hydrometeor has been discussed in detail. The total hydrometeor structure from all the three experiments shows multi-cell structure of the deep convection. The MM5-GSFC experiment simulates more realistic picture of the vertical structure of the cloud system. The observational analysis of the supercell storm case considered here shows large vertical development and overshooting convection in the form of oscillating updrafts and downdrafts as discussed in the chapter 3. The MM5-GSFC experiment does produce the overshooting convection and convective outflow below the tropopause level and the anvil structure of the cloud system. More detailed discussion on the penetrating or overshooting updrafts and the generation of gravity waves has been presented in the chapter 6. Three dimensional structure of the cloud clusters depicted in figure 4.11 shows that MM5-WR and MM5-SI scheme produce more RNW and is distributed upto 10 km in the vertical, while MM5-GSFC experiment produce less RNW and is mostly confined in the lower troposphere. This study indicates that the simulations of the structure and precipitation features of the MCS are highly sensitive to the microphysical

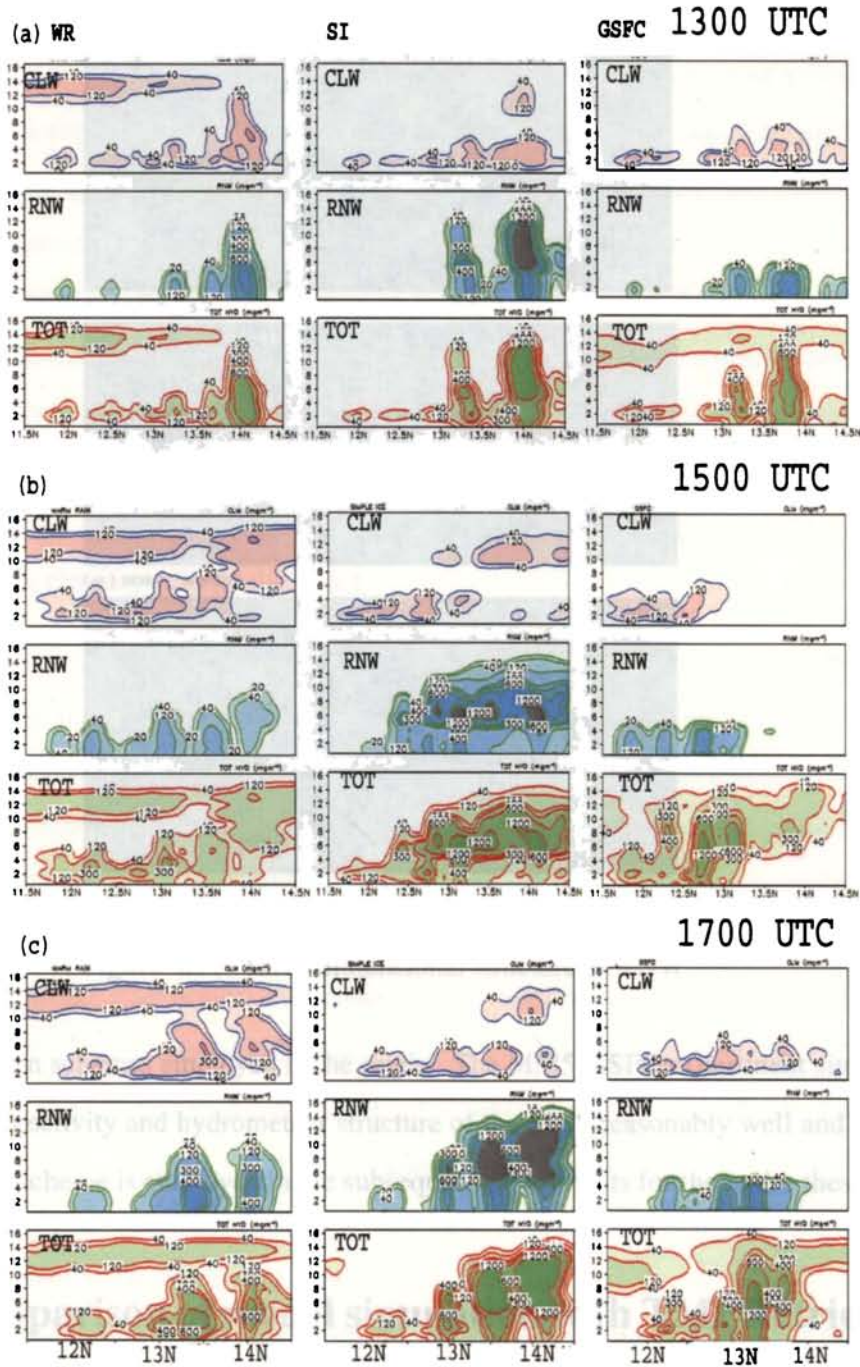


Figure 4.10: Latitudinal section of CLW (mgm^{-3}), RNW (mgm^{-3}) and total hydrometeor (mgm^{-3}) from MM5-WR (left panel), MM5-SI (middle panel), and MM5-GSFC (right panel) experiments at (a) 1300, (b) 1500 and (c) 1700 UTC on 17 October 2002

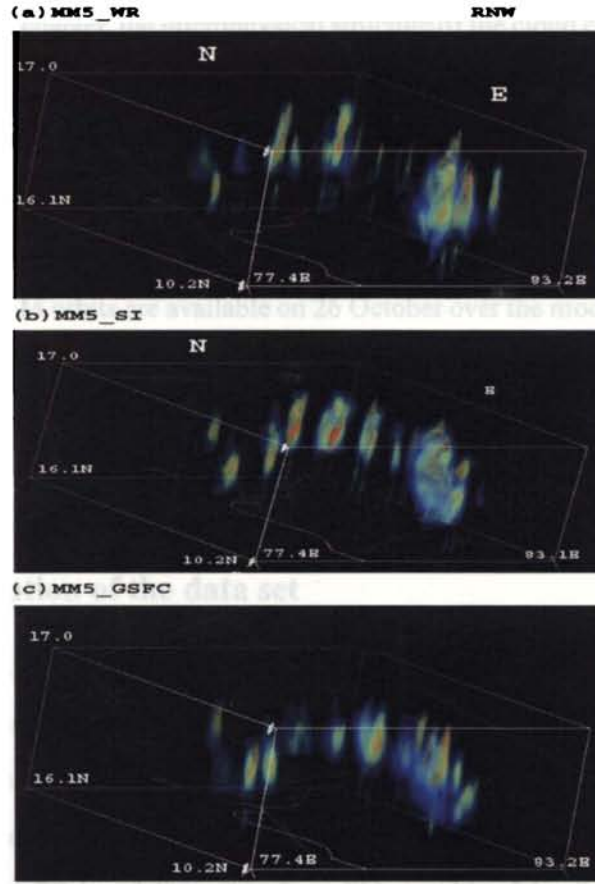


Figure 4.11: Three dimensional structure of RNW

parameterization schemes employed in the model. The MM5-GSFC experiment simulates the rainfall, reflectivity and hydrometeor structure of the MCS reasonably well and GSFC microphysical scheme is employed in the subsequent experiments for the entire thesis.

4.6 Comparison of model simulation with TMI Retrievals

Space-based observations of Tropical Cloud Clusters (TCC) offer great promise for improved understanding and quantitative estimation of rainfall and cloud microphysical struc-

ture. In the present chapter, the microphysical structure of the cloud clusters associated with the TCC has been investigated using the cloud resolving scale configuration of a mesoscale model and the results are compared with the hydrometeor profiles from TMI retrievals. The comparison between the model simulation and TRMM observations has been carried out for the nearest time at which satellite pass is over the model domain (*Abhilash et al.*, 2007c). Two TRMM orbits are available on 26 October over the model domain, which corresponds to the initial and mature phases of the storm. The hydrometeor profiles and radar reflectivity structure of the storm during the initial and mature phases of the storm have been analyzed and the results are discussed in the following sections.

4.6.1 Description of the data set

TRMM Precipitation Radar (PR) is the first radar designed to operate from space for rainfall monitoring. Its operating frequency is 13.5 GHz corresponding to 4.3 km footprint and 250 m vertical resolution with cross-track scanning. Even though it has a narrow swath of 250 km and suffers from same uncertainties for rainfall estimation as do the ground-based radars, the TRMM-PR has delivered an incredible wealth of detailed rain structure information. TRMM microwave imager (TMI) is a passive multi-channel dual-polarized microwave radiometer. TMI utilizes nine channels with operating frequencies of 10.65 GHz, 19.35 GHz, 21.3 GHz (vertical polarization only), 37 GHz and 85.5 GHz. The TMI instrument will provide data related to rainfall rates over oceans, but less reliable data over land, where non-homogeneous surface emissions makes the interpretation difficult. The TMI combined with data from PR, Visible and Infrared Scanner (VIRS) can also be used for deriving precipitation profiles (*Kummerow et al.*, 2000).

The objective of TMI Level 2A Hydrometeor Profile Product (2A12) algorithm is to construct the vertical distribution of vapor, and microphysical parameters pixel by pixel basis. This is accomplished by comparing the measured brightness temperatures in all nine

channels to pre-calculated brightness temperatures corresponding to cloud model profiles. The output from Goddard Cumulus Ensemble (GCE) model (*Tao and Simpson, 1984b*) is used as input into radiative transfer models, from which surface rainfall and crude vertical profiles of hydrometeors would be extracted from a set of satellite-observed brightness temperatures. Of course these retrievals were sensitive to the profiles of large ice and their parameterized properties. Over water the lower frequency channels responds well to the presence of liquid water because of its strong microwave emission over weak emission from ocean surface. However, high microwave emission from land renders the lower frequency channels of little use. Instead, scattering of higher frequency microwave radiation by ice reduces brightness temperatures. Retrievals over land must rely more on the less-direct relationship between column-integrated ice contents and surface rainfall, complicated further by the fact that the size and density of the ice affect the amount of scattering.

The objective of the TRMM and Other-GPI Calibration Rainfall Product (3B42) is to provide a precipitation estimate in the TRMM region that has the (nearly-zero) bias of the TRMM combined instrument precipitation estimate and the dense sampling of the geosynchronous IR imagery. The 3B42 composed of two algorithms, which are (1) to produce monthly IR calibration parameters, and (2) to calibrate the merged IR precipitation data to produce the daily adjusted merged-IR precipitation and RMS precipitation error estimate. At 13.8 GHz, the PR reflectivity profile suffers from significant attenuation in the lowest levels, both in convective and stratiform precipitation. The objective of TRMM Product Level 2A Precipitation Radar (PR) Rainfall Rate and Profile (2A25) is to correct for the rain attenuation in measured radar reflectivity and to estimate the instantaneous three-dimensional distribution of rain from the TRMM Precipitation Radar (PR) data. The estimates of attenuation-corrected radar reflectivity factor and rainfall rate are given at each resolution cell (4 km x 4 km x 250 m) of the PR. More details of the data sets can be found from [http : //disc.gsfc.nasa.gov/data/datapool/TRMM_DP/01_Data_Products](http://disc.gsfc.nasa.gov/data/datapool/TRMM_DP/01_Data_Products)

and National Space Development Agency of Japan (*NASDA*, 1999).

4.6.2 Overview of the synoptic condition

Tropical cloud clusters formed on 26 October 2005 has been selected for the present study. According to the daily weather reports from India Meteorological Department (IMD), an area of convection had persisted almost 740 km east of Chennai (13.0°N, 80.2°E), India and was associated with a well-defined Low Level Circulation Center (LLCC). The disturbance was located under low to moderate vertical shear with a good westerly outflow channel. The maximum winds at the time were estimated as 10-12 ms^{-1} . The TRMM pass at 1153 UTC on 26 October revealed consolidating deep convection over LLCC and signified the potential for further development and reaches depression stage at 1800 UTC on the same day. The tropical storm at this time was located a little less than 370 km east-southeast of Chennai. The system continued moving westward towards Indian coast as it gradually increased in organization. The storm intensified further and reached deep depression stage at 1000 UTC on 27 October and the center was located only about 100 km southeast of Chennai. The storm turned northwards and made landfall near Ongole (15.2°N, 80.3°E), India around 1200 UTC on 28 October and the maximum winds estimated in the range 15-18 ms^{-1} .

4.6.3 Experiment design

The synoptic setting of the case considered in the present study is such that the evolution of the convection is strongly controlled by the environmental dynamics rather than thermodynamics. The predictability of the features will expected to be better in such situations. The smaller scale structure of the cloud clusters can be modeled even when only meso- scale and synoptic scale information is available for model initialization (*Zhang and Fritsch*, 1988). The National Center for Environmental Prediction-Final (NCEP/FNL) global analysis ($1^\circ \times$

1° horizontal resolution) available at 6-hr intervals interpolated to model grid has been used as initial and boundary condition for simulation experiment MM5-GSFC. Two-way nesting is employed with a horizontal resolution of 27 km for the coarse outer grid, 9 km for the inner fine grid with 27 vertical levels.

We use both cumulus parameterization and explicit microphysics in both the domains. *Cram et al.* (1992) carried out several sensitivity tests with cumulus parameterization and grid-scale microphysical process. They found that simulations of the squall line with both cumulus parameterization and explicit microphysics with a 20 km grid spacing compared well with the observed squall-line movement. On smaller grid spacing on the order of 10 km, parameterization is needed due to the lack of observations on such a smaller scale. Microphysical processes play a major role in the development of mesoscale organization of the cloud clusters. Using 25 km grid spacing with fully explicit treatment of clouds produce too much rain and too intense mesowind in a MCC case. Fully explicit approach allows a broad spectrum of interactions among the convective scale and large scales. For a grid spacing less than 2-3 km, the fully explicit approach is superior to the parameterized approaches. For grid spacing between 3-25 km, it remains uncertain that a general solution exists. When grid scale forcing is large and convective instability is small or moderate, the fully explicit approach is sufficient. In such case, the grid scale forcing quickly produces saturation, and the vertical distribution of the heating by the explicit approach differs only slightly from that in nature. The explicit approach fails at these intermediate grids because the resolution is insufficient to realistically model cloud initiation and sub-grid scale transports (*Molinari and Dudek*, 1992).

The model physics used in the present study include Grell scheme for Cumulus parameterization (*Grell et al.*, 1994), boundary layer parameterization of *Hong and Pan* (1996) as used in the Medium Range Forecast (MRF) model, explicit treatment of cloud hydrometeors is based on Goddard Space Flight Centers (GSFC) microphysical scheme (*Tao et al.*,

1987a; Tao and Simpson, 1984b). Cloud radiation interaction is allowed between explicit cloud and clear air.

4.6.4 Hydrometeor structure during the initial phase

Figure 4.12(a) and (b) shows the rainfall derived from TMI and instantaneous rainfall from MM5-GSFC. We considered two boxes A and B (marked as rectangles in figure 4.12) corresponding to rainfall rate greater than 2 mmhr^{-1} covers a horizontal area of nearly $200 \text{ km} \times 200 \text{ km}$. The organization of the rainbands simulated by the model shows good agreement with that derived from TMI. For box A, both the model and TMI shows rainfall rate greater than 10 mmhr^{-1} . For box B (mostly over Sri Lanka), the simulated rainfall is greater than 5 mmhr^{-1} while the rainfall estimated from TMI is about 2 mmhr^{-1} . This may be due to the fact that, the box B mostly covers land area (more than 75%) and the TMI shows less performance of rain estimation over land.

Figure 4.13 and figure 4.14 present longitude-height cross-section of the microphysical parameters centered over the latitudes 11.2°N and 9.1°N in box A and box B, respectively of figure 4.12. The figure clearly shows the mesoscale organization of cloud clusters. Box A marked well organized MCC with three distinct cloud systems. While, box B shows the occurrence of a MCS with a single maximum in microphysical parameters with a stratiform region in the western sector of the box (see figure 4.14). Figure 4.13 (a), (c), (e) and (g) shows the vertical profile of CLW, RNW, ICE and SNOW from the TMI retrieval. Figure 4.13 (b), (d), (f) and (h) shows hydrometeor profiles from MM5-GSFC. The model simulated higher magnitudes of microphysical variables compared to those retrieved from the TMI. The model simulated CLW (fig 4.13(b)) extends up to a height of 8 km and peaks near 4 km signifies the presence of supercooled water, which is in good agreement with TMI retrievals (fig 4.13(a)). Model simulated large quantities of RNW (fig 4.13(d)) below 6 km, with a peak near 3 km and distribution is similar to TMI retrievals (fig 4.13(c)).

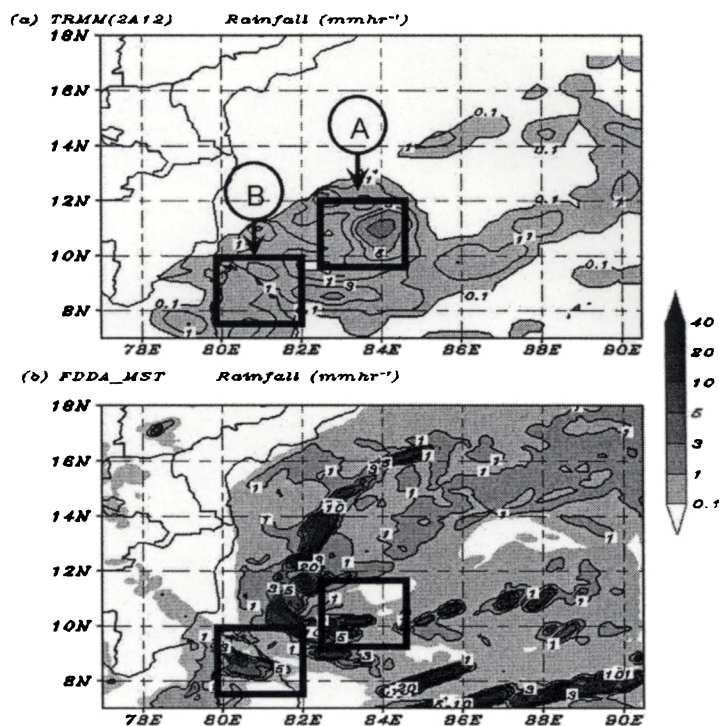


Figure 4.12: Instantaneous rainfall rate (mmhr^{-1}) from (a) TMI and (b) MM5-GSFC during the initial phase of the storm

The ice content simulated from MM5-GSFC (fig 4.13(f)) is ten times higher than TMI retrieval (fig 4.13(e)). For box A, the simulated ice content extends up to a height of 14 km with a peak near 12 km. Unlike the vertical distribution of ice from model simulation, the ice content retrieved from TMI is mostly distributed between 7 and 18 km with peak near 12 km. This is attributed to the higher vertical resolution of the MM5 model above 10 km as compared to TMI, which has poor resolution of 4 km above 10 km. The model simulates the vertical fine scale structure of the ice content. The vertical distribution of snow content from the model simulation (fig 4.13 (h)) shows good agreement with the observations (fig. 4.13 (g)). Both the simulated and TMI profiles shows peak near 8 km. The magnitude of the snow content simulated from the model reaches 300 mgm^{-3} and that retrieved from

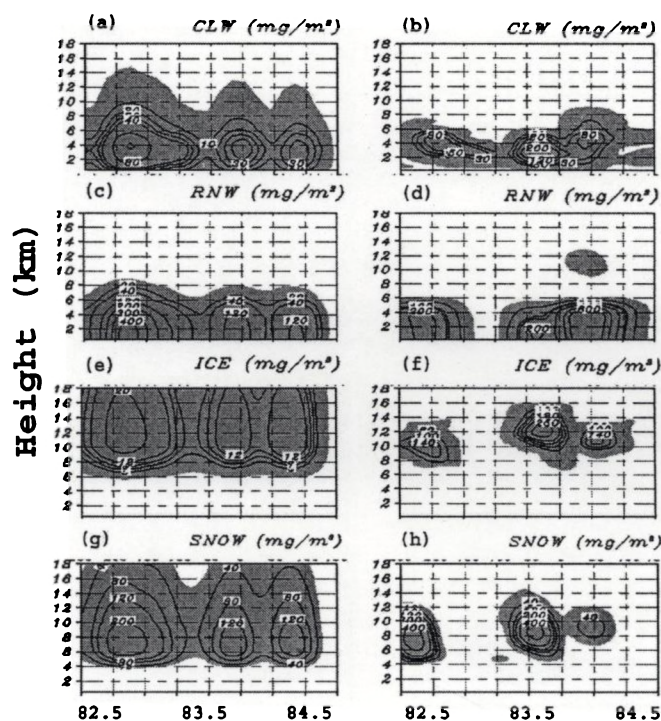


Figure 4.13: Longitude-height section of hydrometeors, CLW (mgm^{-3}), RNW (mgm^{-3}), ICE (mgm^{-3}), and SNOW (mgm^{-3}) from TMI (left panel) and MM5-GSFC (right panel) during the initial phase of the storm for box A

TMI is about 120 mgm^{-3} .

Figure 4.14 is same as figure 4.13 but for box B. Unlike the distribution of clouds in box A, box B does not show the occurrence of individual clouds. Evidently, box B shows a supercell organization of cloud cluster. Two cells of high CLW are seen in box B. Elongated region of RNW implies stratiform precipitation in the western sector of the box B. As evident from the distribution of ice, stratiform anvil region is also present in box B.

Figure 4.15 (a) to (d) shows the box averaged vertical profiles of the CLW, RNW, ICE and SNOW respectively for box A. As seen from the figure 4.15(a), the CLW content simulated by the model shows a peak near 3 km, whereas those retrieved from TMI shows the maximum CLW at a slightly higher altitude. A noticeable feature of figure 4.15(a) is

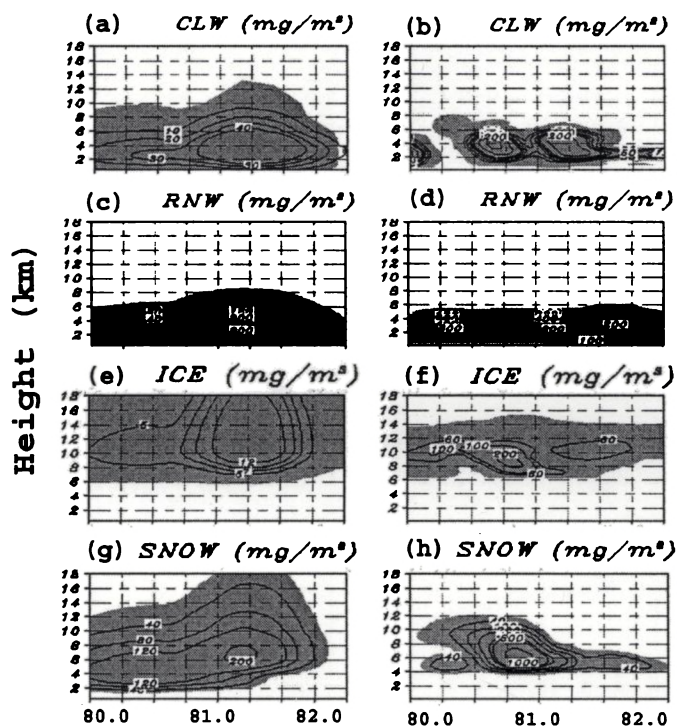


Figure 4.14: Same as figure 4.13, but for box B

that, the model produces a maximum CLW content of 55 mgm^{-3} compared to 35 mgm^{-3} retrieved from TMI. The simulated CLW extends up to a height of 8 km, while that observed from TMI shows the presence of CLW up to a height near 10 km. The RNW simulated by the model and retrieved from TMI shows a peak immediately below 2 km (figure 4.15(b)). The RNW simulated from the model extends up to 6 km, while that retrieved from TMI extends up to 8 km. Model generates more RNW compared to TMI observations.

Figure 4.15(c) shows the vertical distribution of ice for box A. Both the model simulation and TMI show peak in ice content near 10 km. The ice content retrieved from TMI is one order of magnitude less compared to other microphysical parameters. It is evident that the GSFC scheme generates much more ice in the upper troposphere than TMI retrievals.

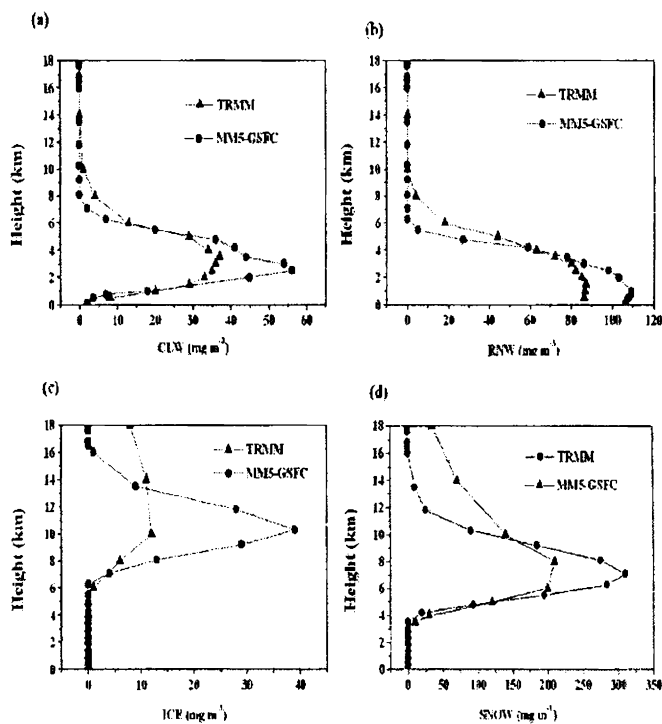


Figure 4.15: Box-averaged vertical profiles of hydrometeors, (a) CLW (mgm^{-3}), (b) RNW (mgm^{-3}), (c) ICE (mgm^{-3}), (d) SNOW (mgm^{-3}) from TMI (solid line) and MM5-GSFC (dashed line) for box A

The ice content from the model simulation reaches a maximum values of 40 mgm^{-3} while those retrieved from the TMI is less than 20 mgm^{-3} . Nevertheless, the retrieved ice content from TMI is less, which produce a deep layer of ice and extends up to 18 km. The simulated ice content from the GSFC scheme extends up to 16 km. The presence of ice in the upper troposphere suggests that GSFC scheme tends to produce optically thicker clouds and TMI retrieval illustrates the presence of physically deeper clouds. The vertical distribution of snow is presented in figure 4.15(d). The box averaged profile of snow content exhibits substantial difference between the GSFC scheme and TMI retrievals. The model generates maximum snow content near 7 km, while TMI profile peaks at 8 km. Like the distribution of ice content, the model simulates snow content up to 12 km, while that from

the TMI retrieval extends up to 18 km. Obviously the GSFC scheme generates substantially more snow in the middle troposphere and slightly less snow in the upper troposphere. Unlike the GSFC scheme, the TMI profiles shows significant amount of snow in the upper troposphere.

Figure 4.16 is same as figure 4.15 but for box B in fig.4.12(b). The vertical distribution and amount of CLW and ice is similar to those in box B. Unlike box A, the maximum RNW for box B is significantly higher and snow content is considerably less. Both MM5-GSFC and TMI profiles produce regions of cloud liquid water, rain water, cloud ice and precipitable ice with significant amounts of supercooled liquid water.

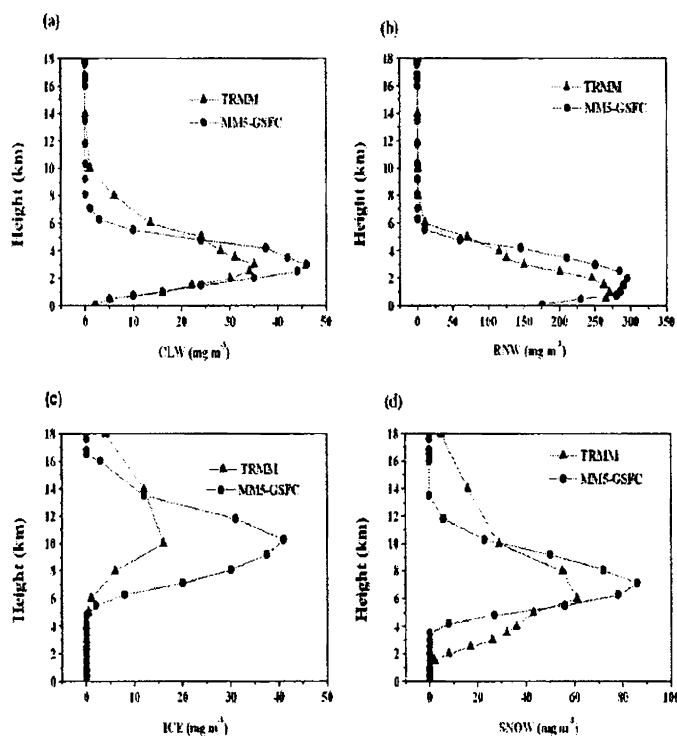


Figure 4.16: Same as figure 4.15, but for box B

4.6.5 Radar reflectivity structure during the initial phase

In this section, measured vertical reflectivity structure from TRMM-PR has been compared with the reflectivity structure simulated by the model. Figure 4.17 (a) and (b) presents the horizontal radar echoes from the TRMM-PR and composite reflectivity from model simulation. Three reflectivity cores of magnitude greater than 20 dBZ are seen in TRMM-PR. The composite reflectivity from the model simulation also predicts the organization and intensity of these three cores of high reflectivity.

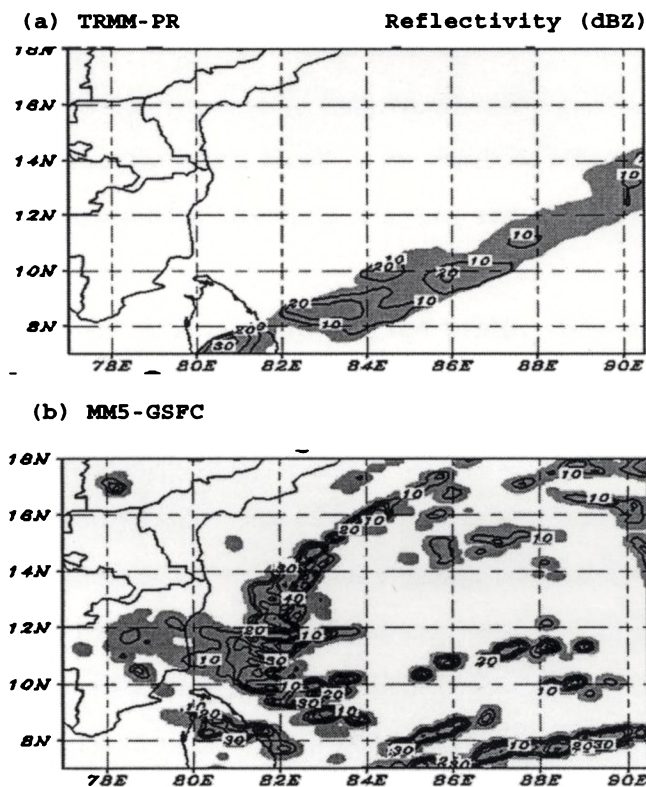


Figure 4.17: (a) Attenuation corrected near surface reflectivity (dBZ) from TRMM-PR and (b) composite reflectivity (dBZ) from MM5-GSFC during the initial phase of the storm.

Vertical cross section of reflectivity from TRMM-PR and MM5-GSFC has also been analyzed to examine the performance of the model to simulate the vertical reflectivity struc-

ture of the storm. Due to narrow swath of TRMM-PR (250 km) compared to the large swath of TMI (875 km), the vertical cross-section of the radar reflectivity structure for box A has been considered here. Figure 4.18 (a) and (b) shows the vertical cross section of reflectivity structure observed by TRMM-PR and those simulated from MM5-GSFC centered over the latitude 10.1°N . The reflectivity fields from PR shows two distinct cells of reflectivity values greater than 30 dBZ up to a height of 8 km. Three individual cells are present in MM5-GSFC profile with an intense cell of reflectivity values greater than 30 dBZ at 40 km west of the center of the storm and two secondary maxima of reflectivity greater than 10 dBZ on both side of the storm center. This third cell to the west of the storm center is absent in the PR reflectivity. The cloud top from PR reflectivity profiles are 2-3 km deeper than those simulated from the model. However, the simulated echo fields from the model is weaker than PR echoes and the structure is compared well with the PR echo pattern.

4.6.6 Hydrometeor structure during the mature phase

Figure 4.19 is same as figure 4.12, but during the mature phase of the storm. Like for the initial phase, we considered two boxes C and D (marked as rectangles) corresponding to rainfall rate greater than 10 mmhr^{-1} and covers a horizontal area of nearly $200 \times 200 \text{ km}$. Obviously, rainfall rate during the mature phase is greater than that during the initial phase of the storm (see fig. 4.12). For box C and D, the organization of the rainbands simulated by the model shows good agreement with that derived from TMI. The maximum rainfall predicted by the model is 20 mmhr^{-1} whereas that retrieved from TMI shows a maximum of 10 mmhr^{-1} . A noticeable feature from fig. 4.19 is the generation of strong precipitation bands over the southeast boundary of the domain, which is absent in the TRMM observations.

Figure 4.20 is same as figure 4.13 but for box C and centered over 13.7°N latitude. The figure clearly shows an intense cloud system over the western sector and a less intense

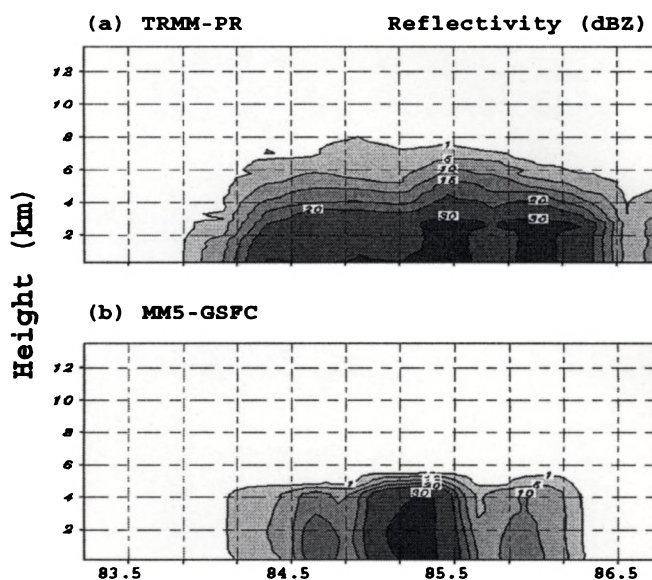


Figure 4.18: Longitude-height section of radar reflectivity (dBZ) from (a) TRMM-PR and (b) MM5-GSFC during the initial phase of the storm.

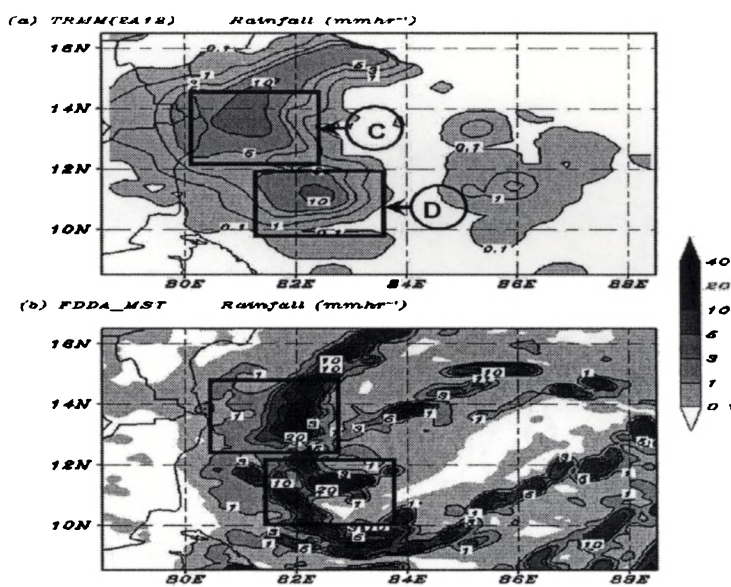


Figure 4.19: Same as figure 4.12, but for during the mature phase of the storm.

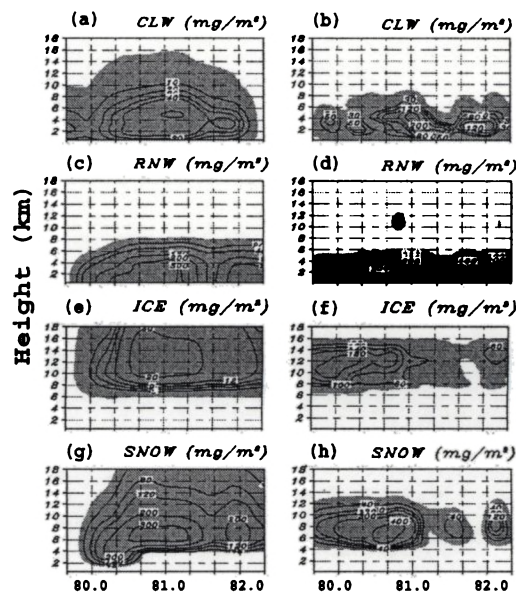


Figure 4.20: Same as figure 4.13, but for box C during the mature phase of the storm.

cloud over the eastern sector of the box C. The vertical distribution of the microphysical parameters is similar to those in box A (see fig. 4.13) with model producing higher amount of hydrometeorological species compared to TMI retrievals. The vertical distribution of CLW and RNW for box C clearly shows the convective region, transition region and trailing stratiform region. Significant amount of ice in the upper troposphere distributed over a larger horizontal extent shows the evidence of anvil shape of clouds during the mature phase of the storm. Unlike for box A, noticeable difference is observed in the vertical distribution of snow content from TMI. Over the western sector of box C, the TMI retrieval shows significant amount of snow field below 4 km, whereas the snow field from MM5-GSFC is generally confined between 4 and 12 km. Figure 4.21 is same as figure 4.13 but for box D and centered over 11.2°N latitude. Unlike the distribution of clouds in box C, box D does not shows well marked individual clouds. Evidently, box D shows a supercell organization of cloud cluster. As evident from the distribution of ice, stratiform anvil region

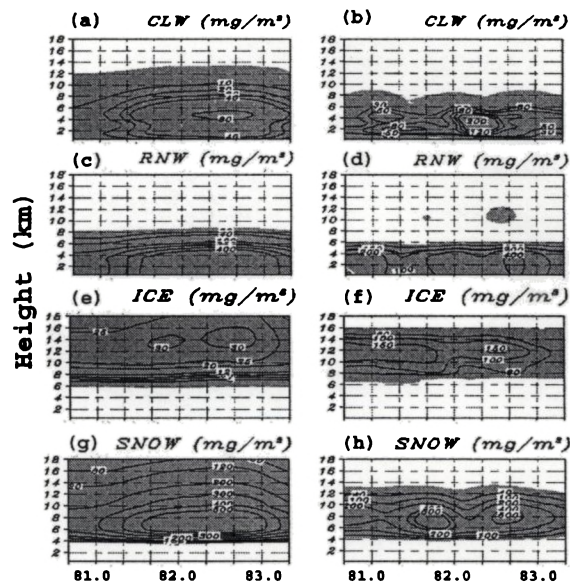


Figure 4.21: Same as figure 4.13, but for box D during the mature phase of the storm.

is also present in box D. Like the distribution of ice, the snow content also distributed over a large horizontal extent.

Figure 4.22 is same as figure 4.15, but for box C. As seen from the figure 4.15 (a) the CLW content from both TMI and MM5-GSFC shows a primary peak just above 2 km and a secondary peak above 4 km. Significant amount of CLW is found above the melting level. The double maximum in the vertical distribution of the CLW shows the evidence of multilayered clouds in box C. The vertical distribution of RNW, ice and snow are identical to that for box A. The box averaged vertical profile of hydrometeors for box D (figure 4.23) shows similar distribution as that for box C. During mature phase of the storm, the hydrometeor content retrieved from TMI and MM5-GSFC is roughly double the magnitude of that during the initial phase of the storm.

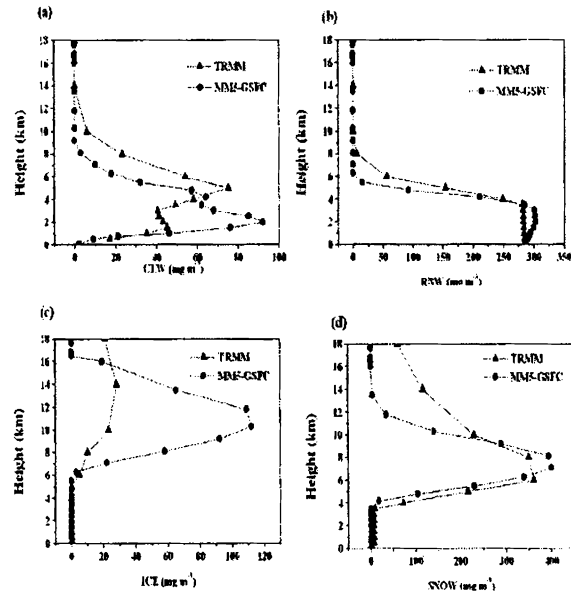


Figure 4.22: Same as figure 4.15, but for box C

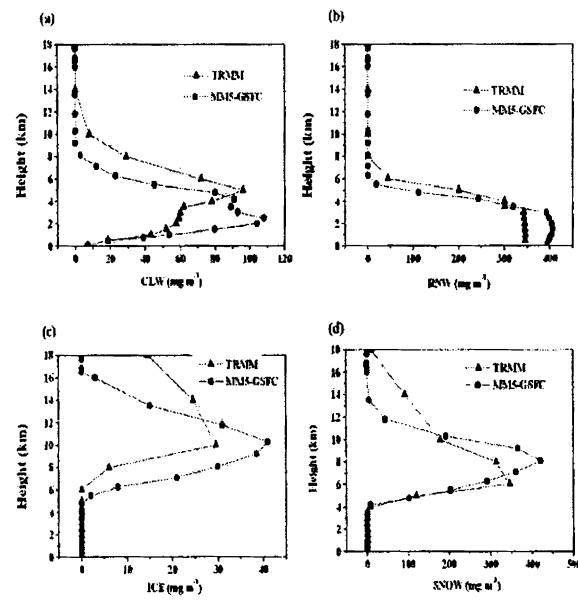


Figure 4.23: Same as figure 4.15, but for box D

4.6.7 Radar reflectivity structure during the mature phase

In this section, measured near surface and vertical reflectivity structure from TRMM-PR has been compared with the reflectivity structure simulated by the model. Figure 4.24 (a) and (b) presents the horizontal radar echoes from TRMM-PR and composite reflectivity from model simulation. As seen from the figure 4.24, TRMM-PR and MM5-GSFC shows reflectivity cores of values greater than 35 dBZ. The TRMM-PR shows maximum reflectivity over northeast of Chennai, while that simulated from MM5-GSFC produce maximum reflectivity cores east of Chennai. Figure 4.25 (a) and (b) presents the vertical cross-section

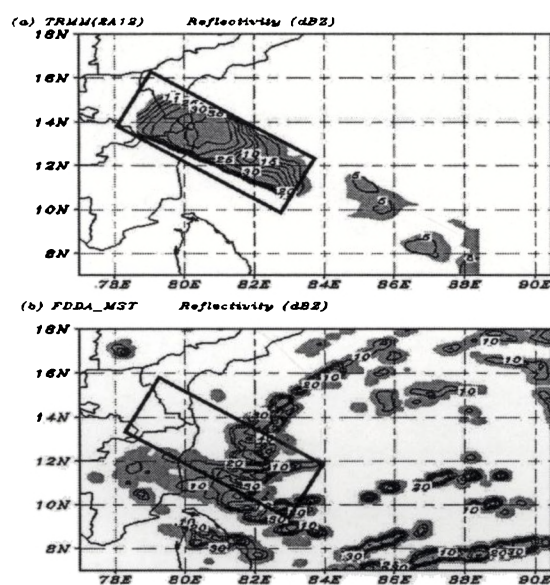


Figure 4.24: Same as figure 4.17, but during the mature phase of the storm.

of radar reflectivity from TRMM-PR and MM5-GSFC during the mature phase of the storm. The longitude-height section has been taken along 12.0 N °latitude. Both TRMM-PR and MM5-GSFC shows strong reflectivity core of magnitude greater than 30 dBZ over the western sector of the domain. However, the simulated reflectivity form MM5-GSFC is shifted to east, the intensity is as good as TRMM-PR.

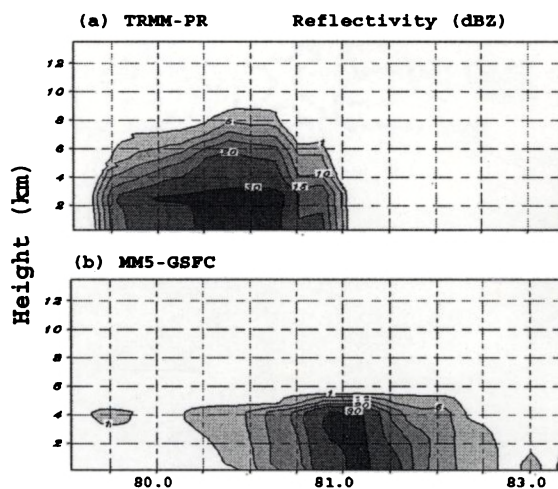


Figure 4.25: Same as figure 4.18, but during the mature phase of the storm.

4.6.8 Accumulated rainfall

Figure 4.26 (a) and (b) shows 24 hr accumulated rainfall from TRMM observations and from MM5-GSFC valid at 0000 UTC of 27 October. Predicted rainfall from the MM5-GSFC shows well organized circular band of rainfall. The TRMM do show the similar organization of the rainbands. The MM5-GSFC overestimated the rainfall over the entire domain. Both the MM5-GSFC and TRMM show three general areas of high precipitation with strongest one being located near Chennai. The weaker one is situated in the extreme northeast sector of the domain and the third one close to the extreme southeast boundary of the domain. However, TRMM estimates lesser amount of rainfall over the southeast sector. The more organized structure of the precipitation bands from MM5-GSFC attributed to the higher resolution of the model (9 km) as compared to the coarse resolution of TRMM data (25 km). The 24-hr accumulated rainfall from TRMM and MM5-GSFC valid for 0000 UTC of 28 October, 2005 is shown in figure 4.26 (c) and (d). The TRMM observation shows a strong precipitation band near Chennai with a maximum amount greater than 20 cm.

The MM5-GSFC experiment does predict the same amount of rainfall with heavy rainfall being located to the northeast of Chennai. In general, MM5-GSFC experiment captures the amount and spatial distribution of the rainfall reasonably well.

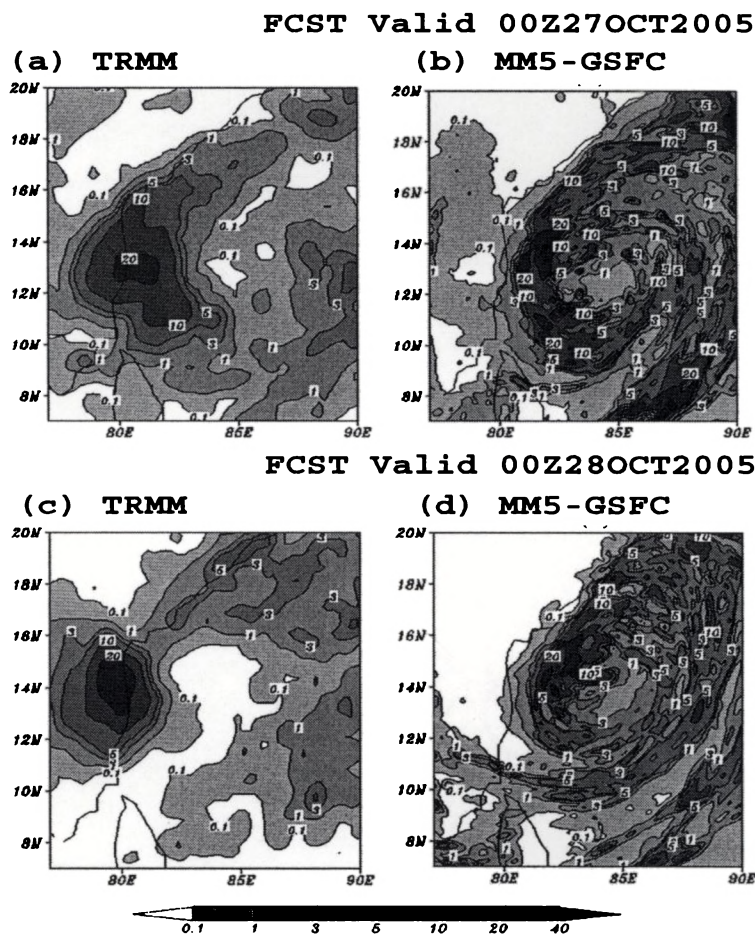


Figure 4.26: 24-hr accumulated rainfall valid at 00:00 UTC on 27th October from (a) TRMM, (b) MM5-GSFC and valid at 00:00 UTC on 28 October 2005 from (c) TRMM and (d) MM5-GSFC

4.7 Summary

Cloud resolving scale configuration of the mesoscale model, MM5 using bulk microphysics parameterization have been used to simulate the evolution and structure of the TMCS. The sensitivity of different microphysical schemes to QPF and hydrometeor structure has been investigated in the chapter. Several numerical experiments have been carried out to study the sensitivity of single moment bulk microphysical schemes such as warm rain, simple ice and GSFC scheme for the simulation and prediction of TMCS. The horizontal and vertical distribution of the cloud hydrometeor fields observed from TMI is compared with those from CRM simulations. The horizontal and vertical reflectivity structure from TRMM-PR has also been compared with model simulations. Further, the 24-hr accumulated rainfall prediction has been verified against the merged rainfall analysis from TRMM 3B42 data sets.

CHAPTER 5

Assimilation of Conventional and Satellite Data for simulating TMCS

5.1 Introduction

The Numerical Weather Prediction (NWP) technique, based on mathematical equations is essentially an Initial value problem. The importance of accurate initial conditions for the success of NWP forecast is well known (*Lewis and Derber, 1985; Talagrand and Courtier, 1987; Rabier et al., 2000; Zupanski et al., 2002*). Obtaining an accurate initial condition is recognized as one of the biggest challenges in NWP. The data assimilation system produces an estimate or analysis of the true atmospheric state at a given time by combining all the information of the atmospheric state in a given time window. The analysis is produced by combining information of observations, previous forecasts (background and first-guess state), their respective errors and laws of physics. The analysis can be used for several purposes including its utilization for initial conditions for a NWP model (initialization),

Observation System Experiment (OSE) to assess the impact of individual components of the existing observations, Observation System Simulation Experiment (OSSE) for predicting the impact of proposed new components of a future observation network, etc.

Rainfall over the Indian subcontinent is predominantly from MCS and it is difficult to produce the operational forecast of these convective systems, mostly because the convective elements within these MCS are relatively small and short-lived. One of the greatest deficiencies in NWP models is their lack of skill in predicting the clouds and precipitation in the early portion of their forecast period because of the *spin-up* problem. Hence predicting rainfall amounts in the regions of convective activity is an important and challenging task. Thunderstorms often produce copious amount of rainfall for a short period. Numerical models currently in operational centers may fail to predict the rainfall amounts with great accuracy. Some models underpredict the rainfall amounts but overpredict the spatial coverage, while some mesoscale models overpredict the rainfall amount and shows large bias (*Junker et al.*, 1989; *Hoke et al.*, 1989; *Black*, 1994; *Olson et al.*, 1995).

During convective events, Quantitative Precipitation Forecasts (QPF) performing poorly throughout the entire globe and are generally not skillful beyond 3 h (*Fritsch and Carbone*, 2004). Many of the difficulty in producing accurate QPF are a result of the coarse resolution, which unable to resolve the mesoscale features (*Kain and Fritsch*, 1992). With the development of modern computing facilities this can be overcome to some extent by increasing the resolution of the model grid. Poor initialization of the mesoscale features that force the convection may result in inaccurate forecasts (*Stensrud and Fritsch*, 1994). Even at higher resolutions, skill scores may not necessarily improve. Spurious small-scale features with unfavorable predictability could negatively affect skill scores at fine resolutions (*Gallus*, 2002). There fore much work is required in this area and more sophisticated method of predicting rainfall needs to be developed. Conventional and Satellite observations provide various information to be assimilated in the mesoscale assimilation system to

improve the initial condition. This chapter discusses the impact of the various conventional and satellite observations for the short range prediction and simulation of the convective systems.

5.2 Brief note on Initialization and Data Assimilation

The purpose of initialization procedure is to prepare grid point data with which the model can integrate forward in time with minimum noise and maximum accuracy of the forecasts of the meteorological scales that the model is designed to simulate. The procedure for eliminating spurious gravity waves before integrating the mathematical equations is referred to as initialization. Some of the initialization techniques are (i) static initialization, (ii) dynamic initialization and (iii) normal mode initialization. The term static initialization refers to a procedure that adjusts the data at a single time level to conform to some dynamical constraints in order to reduce or eliminate the generation of inertial-gravity wave noise. As NWP models inherently possess the mechanism for some adjustments like geostrophic adjustment, the model itself can do the job of initialization. The initialization by integrating the model back and forth in time about the initial state, say time zero is called dynamic initialization. In normal mode initialization, the modes of the model are determined and undesired ones are discarded as noise.

There are two basic approaches to data assimilation, sequential assimilation that only considers observations made in the past until the time of analysis, which is the case of real time assimilation system and non-sequential or retrospective assimilation, where observations from the future can be considered as in the case of reanalysis exercise. Another distinction can be made between methods that are intermittent or continuous in time. In an intermittent method, observations can be processed in small batches, which is technically convenient. In a continuous method, observation batches over longer periods are

considered and the correction to the analyzed state is smooth in time, which is physically more realistic. Hence four basic combinations are (i) sequential-intermittent assimilation, (ii) sequential-continuous assimilation, (iii) non-sequential intermittent assimilation and (iv) non-sequential continuous assimilation. Many assimilation techniques have been developed for meteorology and oceanography. They differ in their numerical costs, their optimality and their suitability for real time data assimilation (Daley, 1991; Lorenc, 1986; Ghil, 1989).

The data that can go into the analysis system comprises the observations, the first guess and the known physical properties of the system. All the pieces of data are important source of information but at the same time we do not trust any of them completely. There are errors in the model and in the observations, hence we can never be sure which one to trust. However, we can look for a strategy that minimizes on average the difference between the analysis and the truth. It is convenient to solve the analysis problem for all components of the model state. We have to reduce the resolution or domain of analysis because of insufficient computer power. In these cases the work space of the analysis is not the model space, but the space allowed for the correction to the background called control variable space.

5.3 Overview of MM5-3DVAR System

The three dimensional variational data assimilation (3-DVAR) system developed for MM5 is flexible enough to allow a variety of research studies apart from its operational utilization. The 3DVAR system developed by Barker *et al.* (2003, 2004) is used for the present assimilation experiments. The basic goal of the 3DVAR system is to produce an optimal estimate of the true atmospheric state at any desired analysis time through iterative solution of a prescribed cost function (Ide *et al.*, 1997). This incremental method reduces compu-

tational expense by minimizing the cost function that has lower resolution than is used by the forecast model. The incremental method is normally an iterative procedure. The cost function is given by,

$$J(x) = J_o + J_b = \frac{1}{2}(x - x_b)^T B^{-1}(x - x_b) + \frac{1}{2}(y - y_o)^T (E + F)^{-1}(y - y_o) \quad (5.1)$$

Where J is called the cost function of the analysis (or misfit or penalty function), J_b is the background term and J_o is the observation term. The variational (VAR) problem can be summarized as the iterative solution of Eq 5.1 to find the analysis state x that minimizes $J(x)$. This solution represents a posteriori maximum likelihood (minimum variance) estimate of the true state of the atmosphere given the two sources of the priori data: the background (previous forecast) x_b and observations y_o (Lorenc, 1986). The fit to individual data points is weighted by estimates of their errors: B, E and F are the background, observation (instrumental) and representivity error covariance matrices respectively. Representivity error is an estimate of inaccuracies introduced in the observation operator H used to transform the gridded analysis x to observation space $y = Hx$. Applications of the 3DVAR system have been reported in real-time analysis and forecasting (Barker *et al.*, 2004).

The 3DVAR system consists of the four components; (i) Background preprocessing, (ii) Observation preprocessing and quality control, (iii) Variational analysis, (iii) Updating the Boundary conditions (Barker *et al.*, 2003, 2004). Figure 5.1 shows the flow chart of MM5-3DVAR system in cold-start and cycling mode. Details of these components are briefly described below.

5.3.1 Background preprocessing

Analysis for a particular initial condition can be done either in cold-start mode or in cycling mode. In cold-start mode standard MM5 preprocessing programs (TERRAIN, REGRID-

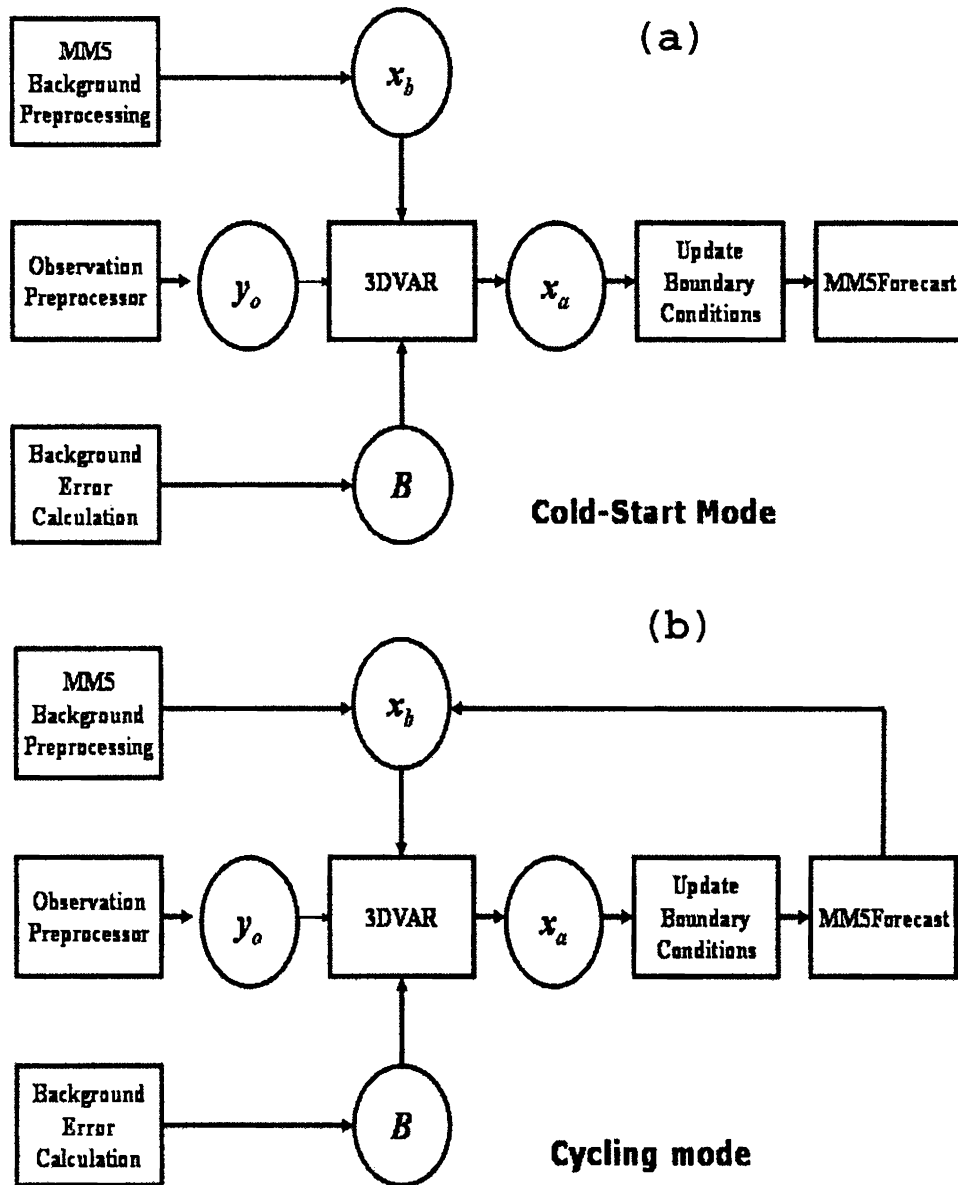


Figure 5.1: Flow chart showing the MM5/WRF 3DVAR system for (a) Cold start and (b) Cycling mode

DER, and INTERPF) may be used to reformat and interpolate forecast fields from a variety of sources to the target MM5 domain. In cycling mode background processing is not required as the background field x_b is supplied by short range forecast of MM5 model over the same domain. Before proceeding to the variational analysis, a background error field of the model is required. In the present study, the background error fields are calculated based on the NMC method (*Parish and Derber, 1992*) as summarized below,

Background error covariances are vital input to any variational analysis scheme. They influence the analysis fit to the observations and completely define the analysis response away from the observations. Background error covariance statistics are used in the MM5-3DVAR cost-function to weight background field. The assimilation system filters those background structures that have high error relative to more accurately known background features and observations. In reality, error in the background field is synoptically dependent. As mentioned earlier the background errors have been calculated using National Meteorological Centers (NMC) method. In this method, background errors are approximated by averaged forecast difference (e.g. month-long series of 24 hr - 12 hr forecasts valid at the same time). Thus the BE covariance matrix (B) is approximated as;

$$B \cong \overline{(T_{12} - T_{24})(T_{12} - T_{24})^T} \quad (5.2)$$

After generating the desired forecast differences, averaged forecast error statistics computation is mainly done through following three stages, (i) Computation of eigenvectors and eigenvalues of vertical background errors, (ii) Calculation of balance regression statistics used to filter balance mass increments, (iii) Calculation of recursive filters and characteristic length-scales.

Generally, before making an attempt to run any assimilation cycle, it is essential to test the BE statistics. With this aim, the old BE statistics was subjected to Pseudo-Single Observation Test (PSOT). It involves the assimilation of a pseudo (or bogus) observation of one of the model variables (u, v, T, p, q) at a single point in the domain. The response

of BE is mainly evaluated in two ways. Firstly, the fit of any observation (O) with analysis (A) or the background (B) is dictated by the background $(\sigma_b)^2$ and observation $(\sigma_o)^2$ error variances according to,

$$(O - A) = \frac{\sigma_o^2}{(\sigma_o)^2 - (\sigma_b)^2} (O - B) \quad (5.3)$$

$$(A - B) = \frac{\sigma_o^2}{(\sigma_o)^2 - (\sigma_b)^2} (O - B) \quad (5.4)$$

Secondly, in addition to setting the relative weight of observation and background in the analysis *via* the above equation, BE also defines the response of the analysis away from the observation location for other variables due to multivariate characteristics of MM5-3DVAR. This is very important especially, in the data sparse region. The PSOT have been performed for different parameters over the Indian region at various vertical levels (*Gupta et al., 2005*). *Abhilash et al. (2007d)* also reported the initial results of the impact of conventional and satellite observations in 3-DVAR system of MM5 for the prediction of rainfall associated with TMCS.

5.3.2 Observation preprocessing and quality control

The MM5-3DVAR has a module, *3DVAR_OBSPROC* for pre-processing and quality control of observations. It packs the observations in a suitable format for ingest into 3DVAR. The main goal of the package is to (i) perform spatial and temporal checks to select the only observations located within the target domain and a specified time-window, then (ii) merge duplicate observations (same location and type), and (iii) choose observations nearest to the analysis time. It estimates and assigns the error for each observation and performs a variety of quality control checks (e.g. check for negative wind speed, spike in wind profile, spike in temperature profile, superadiabatic lapse rate, height above/ below the model lid/ surface etc.). Finally it packs the observations in 3DVAR format.

5.3.3 Variational analysis (VAR)

The VAR problem can be summarized as the iterative solution to the above equation to find the analysis state x that minimizes the cost function $J(x)$. The main features of MM5-3DVAR analysis system are, (i) Incremental formulation of the model-space cost function, (ii) Quasi-Newtonian / Conjugate gradient minimization algorithms, (iii) Analysis increments on unstaggered *Arakawa A* grid, (iv) Analysis performed on the sigma-height levels of MM5, (v) J_b preconditioning *via control variable transform* U defined as $B = UU^T$, (vi) preconditioned control variables are chosen as stream function, velocity potential, unbalanced pressure and specific/relative humidity, (vii) Linearized mass-wind balance (including both geostrophic and cyclostrophic terms) used to define a balanced pressure, (viii) Climatological background error covariance estimated *via* NMC method of averaged forecast differences, (ix) Representation of horizontal components of background error *via* isotropic recursive filters and the vertical component is applied through projection onto climatologically averaged eigenvectors of the vertical error (estimated *via* the NMC-method), (x) Horizontal / vertical errors are non-separable (horizontal scales vary with vertical eigen vector).

Although the variational analysis is frequently described as *optimal*, it is so, subject to a number of assumptions. Firstly, given both imperfect observations and background information as inputs to the assimilation system, the quality of the output analysis depends crucially on the accuracy of the prescribed errors. Secondly, although the variational method allows for the linearized dynamical/physical processes, real errors in the NWP system may be highly nonlinear.

5.3.4 Updation of boundary condition

In order to run MM5 forecast model using 3DVAR analysis as initial conditions, the lateral boundary conditions (originally computed from global model data in INTERPF) is updated

to reflect the modified fields. Only boundary conditions for domain 1 needs updating in MM5 two-way nesting mode as boundary conditions for the inner nests are automatically calculated in MM5.

5.4 Experiment design

Three-dimensional observations are mainly centered on the main synoptic hours (0000, 0600, 1200, 1800 UTC) of the observation. Keeping this in mind, the present assimilation system is designed as a 6-hourly intermittent assimilation scheme, where analysis is performed four times a day i.e. at 0000, 0600, 1200 and 1800 UTC. Global data received through Global Telecommunication System (GTS)/internet is ingested in the system at the analysis time with 3 hours time window. Data over the Indian region (15°S to 55°N and 20°E to 140°E) are separated out from the global data and ingested into the system. Modules have been developed for reading the decoded observation data files from NCMRWFs operational data sets and for packing in *LITTLE-R* format, required for ingesting in 3DVAR observation preprocessor. Only conventional data such as *SYNOP*, *SHIP*, *BUOY*, *AIREP*, *AMDAR*, *TEMP*, *PILOT*, *SATOB* (satellite derived cloud motion vectors) and *SSM/I* are used in the present study. The description of the data set is given in table 5.1. The coverage of *SYNOP*, *TEMP*, *PILOT* and *SSM/I* observations available on one assimilation cycle is shown in figure 5.2.

In the cyclic run, the boundary conditions for MM5 run are taken from global model analysis and 6 hourly forecasts. However, the lateral boundary conditions are updated after each analysis. Subsequently after each analysis, six-hour forecasts are made using MM5 model. The 6-hour forecast of each run (valid for next analysis time) is used as the first guess for the next analysis. Impact of conventional and satellite observations for the QPF, timing, location, areal extent, microphysical structure and propagation characteristics of

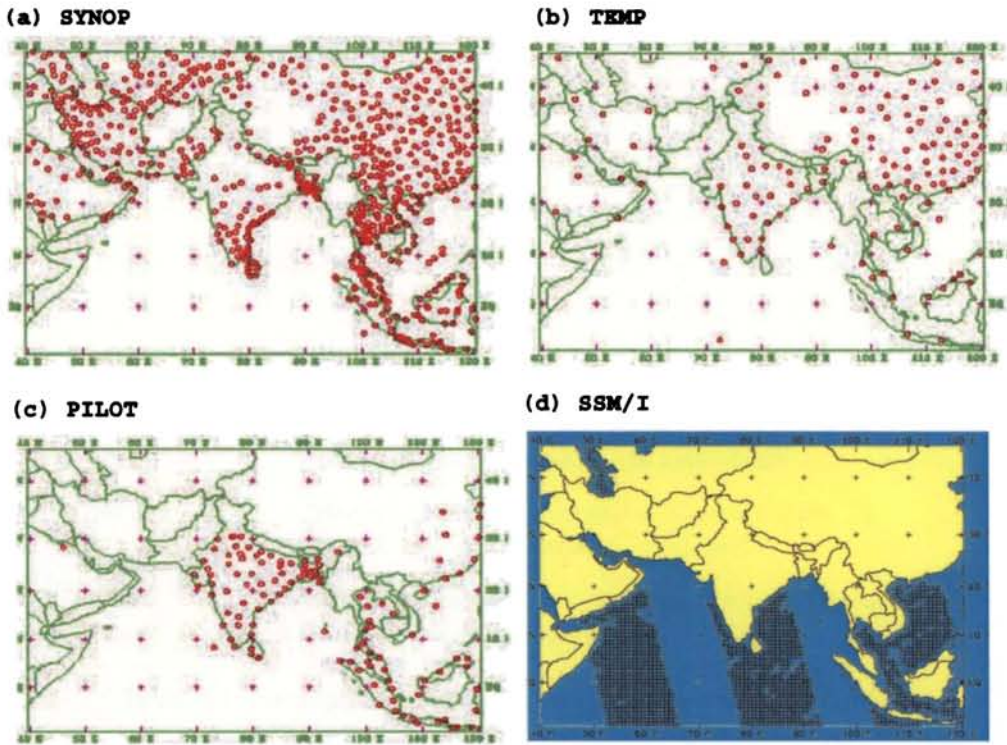


Figure 5.2: Coverage of (a) SYNOP, (b) TEMP, (c) PILOT and (d) SSM/I observations on a typical day used for the assimilation experiments

MCS has been evaluated within this chapter. Keeping this in mind, four convective events over Kolkata with different synoptic settings has been selected.

We use the same domain configuration as described in chapter 4. The model physics include Grell cumulus parameterization (*Grell et al.*, 1994), boundary layer parameterization of *Hong and Pan* (1996) as used in the Medium Range Forecast (MRF) model, explicit treatment of cloud water, rain water, snow, ice and graupel has been performed using GSFC (NASA/Goddard Space Flight Center) scheme (*Tao et al.*, 1987a; *Tao and Simpson*, 1984b), cloud radiation interaction is allowed between explicit cloud and clear air. Keeping all model physics same, two experiments are performed for each case. In the control experiment (MM5-GSFC), the initial and lateral boundary conditions are obtained from

Data	Description
SYNOP	Surface observations from land stations
SHIP	Voluntary observation from sea
BUOY	Drifting and moored buoy observations
TEMP	Upper air profiles of temperature, humidity and wind
PILOT	Wind profiles from optical theodolite
AIREP/AMDAR	Upper level wind and temperature reported by aircrafts
SATOB	Satellite observed cloud motion vectors from INSAT, METEOSAT-6, GMS and GOES
SATEM	Satellite observed wind and total precipitable water from NOAA series of satellites.
SSM/I	Sea surface wind speed and total precipitable water

Table 5.1: Description of data used in the assimilation experiments

the final global analysis of NCEP-FNL at $1.0^\circ \times 1.0^\circ$ resolutions. In the second experiment (MM5-3DVAR), the conventional and non-conventional observations are included in the 6-hr assimilation cycle in which the cold-start is at 0600 UTC of the previous day. Table 5.2 gives the summary of experiments.

Experiment	Initialization and assimilation
MM5-GSFC	Using global analysis of NCEP/FNL without data assimilation
MM5-3DVAR	3DVAR 6-hr assimilation cycle using GTS and Satellite data

Table 5.2: Summary of experiments

5.5 MCS during 05-06 May 2005 : Case I

The radar reflectivity and observed rainfall is used to select the convection events. According to the daily weather report issued by the IMD, the synoptic charts showed a north-south trough extending up to 0.9 km above sea level from northern states to south peninsular India. Maximum temperature was found to be above normal by 2-3°C at many places over the region. Figure 5.3 presents the IR satellite cloud images for 1200 and 1800 UTC on 5 and 6 May 2005. The pictures show scattered convective clouds at many places over the West Bengal and neighborhood during the period. Figure 5.4 (a, b, c and d) presents radar reflectivity, MAX (Z) at 11:48 and 16:48 UTC of 05 May and 11:08 and 14:08 UTC of 06 May 2005. The radar reflectivity pattern clearly shows occurrence of two major cloud bands during the period, which initially formed over northwest of Kolkata and propagated southeastwards.

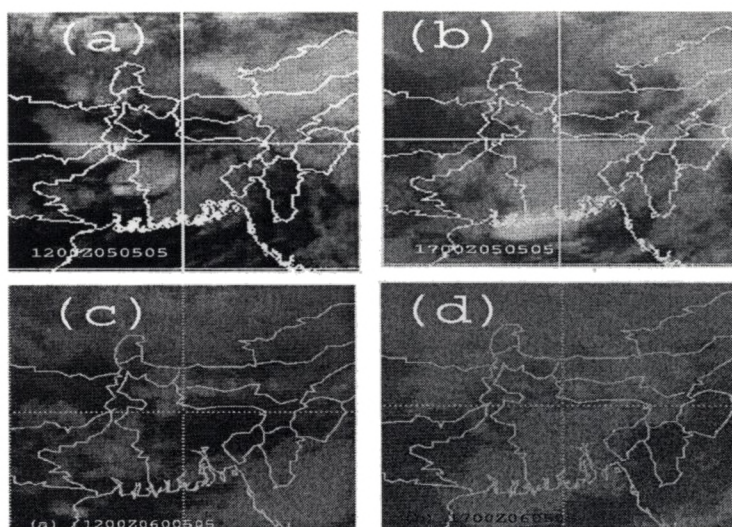


Figure 5.3: Satellite Infra Red images from Kalpana Satellite at (a) 12:00 and (b) 17:00 UTC 5 May, (c) 12:00 and (d) 17:00 UTC 6 May 2005

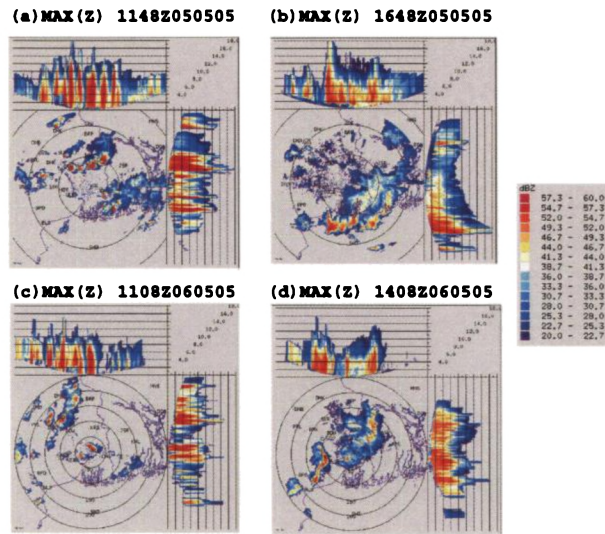


Figure 5.4: Reflectivity MAX (Z) in dBZ at (a) 11:48 UTC and (b) 16:48 UTC of 05 May 2005 and (c) 11:08UTC and (d) 14:08 UTC 06 May 2005

5.5.1 Vorticity

In this section, the wind field such as convergence in terms of vorticity has been analyzed to examine the improvements in the initial condition on assimilating both the conventional and satellite observations. Figure 5.5 (a) and (b) shows the vorticity fields at 0000 UTC 5 May 2005 for the experiments, MM5-GSFC and MM5-3DVAR respectively. The vorticity for the MM5-GSFC experiment is as low as $2 \times 10^{-5} \text{ s}^{-1}$ over the southwest sector of the domain. After assimilating the conventional and satellite data, the initial vorticity fields has been improved well in the second experiment, MM5-3DVAR and shows a maximum value of $10 \times 10^{-5} \text{ s}^{-1}$. This signifies the impact of the conventional and satellite observations in creating localized convergence in the initial condition, which in turn causes development of convective clouds during the early hours of the forecast period.

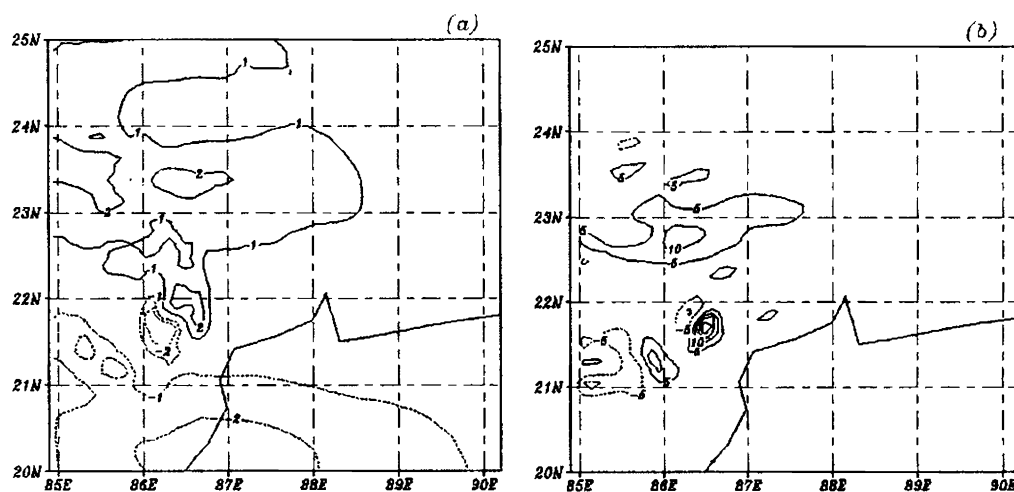


Figure 5.5: Vorticity at 00:00 UTC of 5 May 2005 for (a) MM5-GSFC and (b) MM5-3DVAR experiments

5.5.2 Simulated rainfall

The main purpose of assimilating the high resolution DWR wind data is to improve the heavy rain forecast associated with quasi-stationary MCS. Figure 5.6 shows the 6-hr accumulated rainfall from merged satellite product of TRMM (The details of the 3B42 data set can be found from <http://lake.nascom.nasa.gov/data/dataset/TRMM>). Two rainbands were observed around Kolkata, one over the north and other over southwest of Kolkata during 0600-1800 UTC 5 May. The major rain bands, initially originated from northwest propagated southeastwards during 0600 UTC 5 May and 0000 UTC 6 May, which is a typical characteristic of *Nor'Wester*s (the severe thunderstorms that move from Northwest to Southeast direction over the West Bengal region during the pre-monsoon season). A small patch of rainband is also observed over northwest of Kolkata at 1200 UTC of 6 May, which moved southward and centered around south and southeast of Kolkata at 1800 UTC 6 May. Though the intensity of precipitation was less, this precipitation band moved southeastwards.

Six-hour accumulated rainfall from the three experiments is compared with the observations. Figure 5.7 and 5.8 presents simulated rainfall by the two experiments, namely Control (MM5-GSFC), and assimilation (MM5-3DVAR) respectively. The MM5-GSFC simulation shows 6-8 cm of widespread rainfall between 0600 and 1800 UTC, 6 May and MM5-3DVAR predicts rain bands with less intensity as compared to MM5-GSFC experiment. However, the TRMM does not show much rainfall at these times. The rainfall observed by TRMM may be underestimated as it depends on the pass of the satellite and the rain gauge observations included in its analysis. The observed rainfall amount from TRMM is more during 0600-1800 UTC, 5 May. Both the experiments show the south-eastward propagation of the precipitation bands as observed by TRMM. However, radar reflectivity (see fig. 5.4) does show clouds between 1200-1800 UTC of 6 May. The simulated rainfall from MM5-3DVAR indicates that assimilation of conventional and satellite data has produced rainfall during 1200-1800 UTC of both 5 and 6 May south of Kolkata as seen from TRMM observations and satellite images.

5.6 MCS during 18-19 April 2006 : Case II

Propagation characteristics of the cloud clusters have been discussed in the present section. Figure 5.9 shows DWR reflectivity, MAX (Z) from Kolkata radar during morning and afternoon hours. The observed radar reflectivity shows mesoscale organization of the cloud system. These cloud system propagates southeastwards. The DWR reflectivity shows occurrence of cloud system during morning and early night hours. Figure 5.10 shows simulated composite reflectivity from MM5-GSFC and MM5-3DVAR experiments. The observed reflectivity field from DWR (see fig. 5.9) shows that, at 0700 UTC, the main convection band situated over southeast of the radar site. The composite reflectivity field simulated from MM5-GSFC shows more wide spread cloud structure over Kolkata and southeast sector.

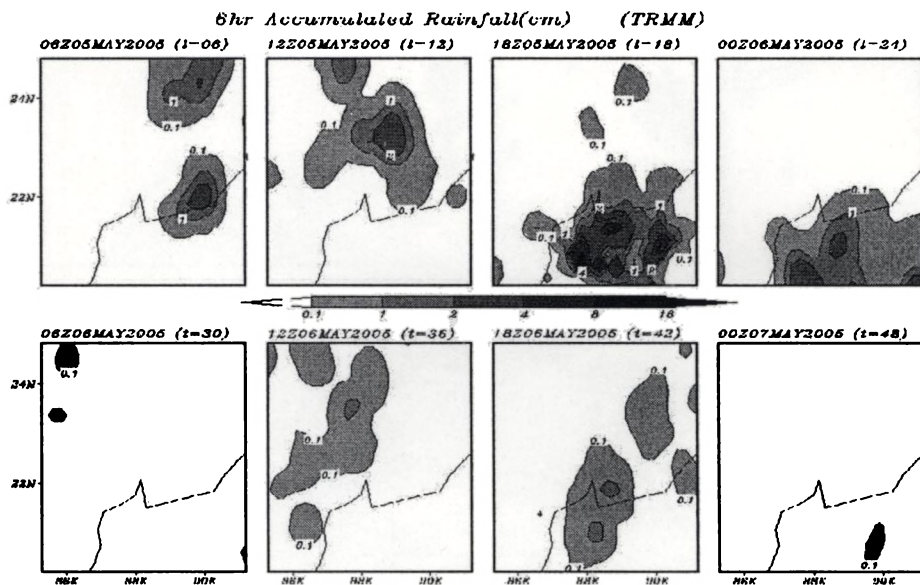


Figure 5.6: Six hourly accumulated precipitation (cm) from TRMM starting from 00:00 UTC, 5 May 2005

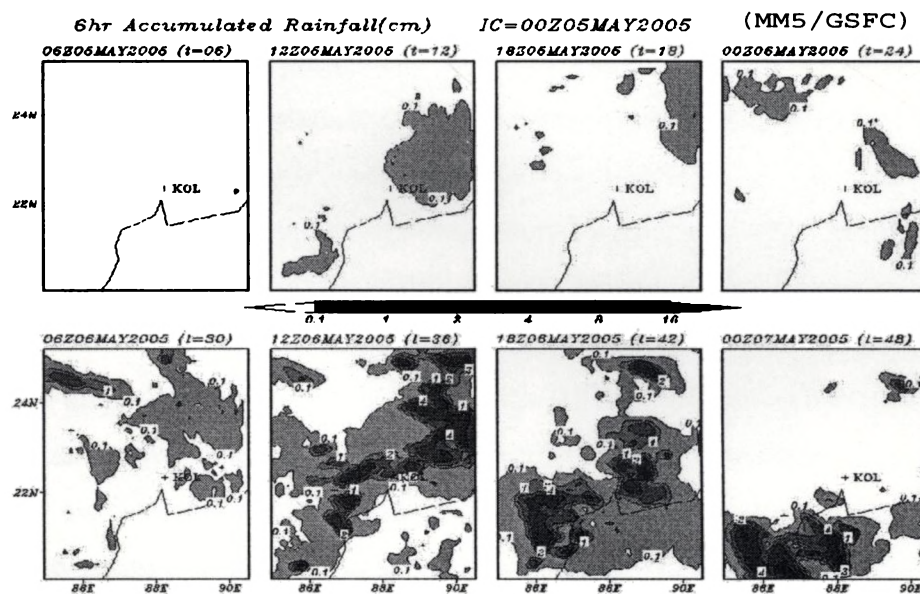


Figure 5.7: Six hourly accumulated precipitation (cm) from MM5-GSFC experiment based on Initial condition of 00:00 UTC, 5 May 2005

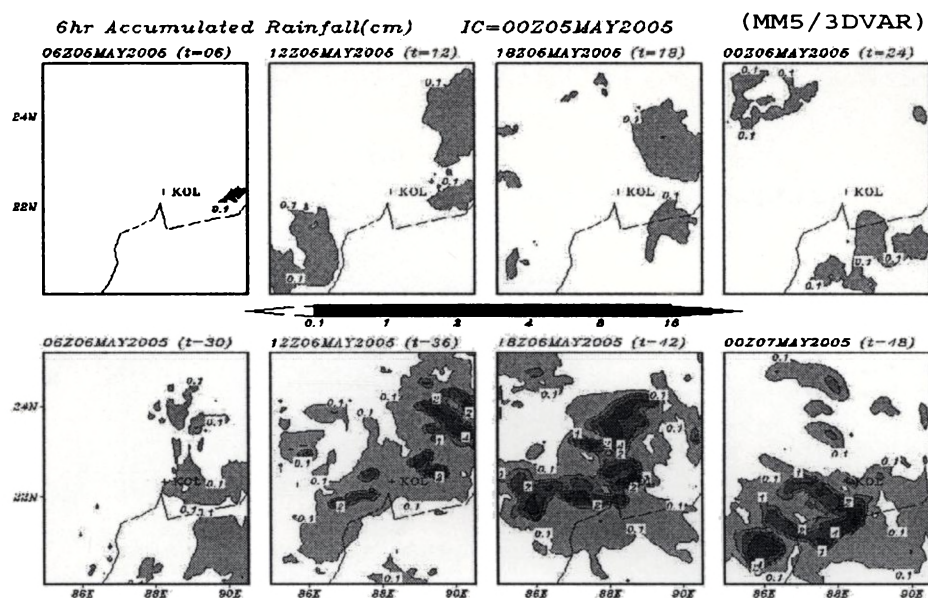


Figure 5.8: Six hourly accumulated precipitation (cm) from MM5-3DVAR experiment based on Initial condition of 00:00 UTC, 5 May 2005

While, MM5-3DVAR simulates clouds east and southeast of the radar site. At 1100 UTC, as evident from the DWR echoes, clouds are in their dissipating stage and located at the extreme southeast sector. Though, both the experiments simulate the clouds over the south-east of the model domain, the organization of the cloud system simulated by MM5-3DVAR is more or less close to the observed reflectivity pattern from DWR. After 1100 UTC, these cloud clusters propagate out of the model domain in the same direction. By this time new cloud system originates at the extreme northwest sector of the model domain. The areal extent of the cloud system simulated by the MM5-3DVAR experiment shows good agreement with the DWR reflectivity. Both the experiment simulates secondary cloud system over the southeast sector of the model domain, whereas which is absent in the observed DWR reflectivity. This analysis put forward the importance of high density conventional, non-conventional mesoscale observations, and satellite observations for the simulation of the organization and propagation characteristics of the tropical cloud clusters.

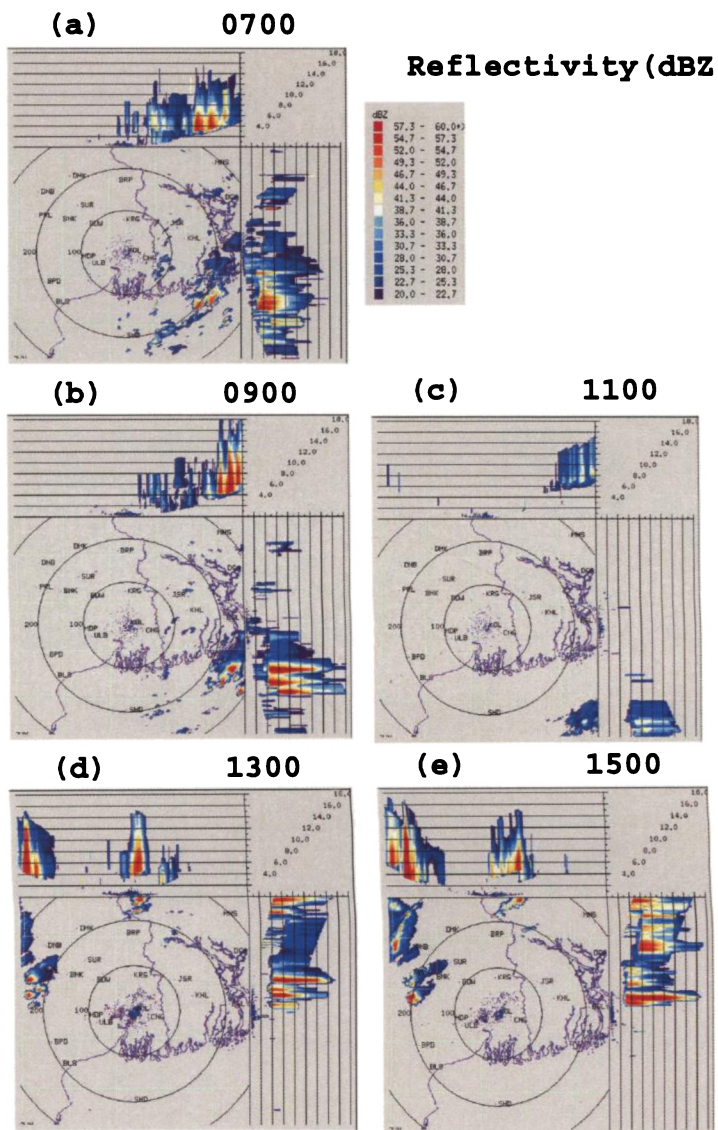


Figure 5.9: Radar reflectivity, MAX (Z) during 07:00 to 15:00 UTC on 18 April 2006

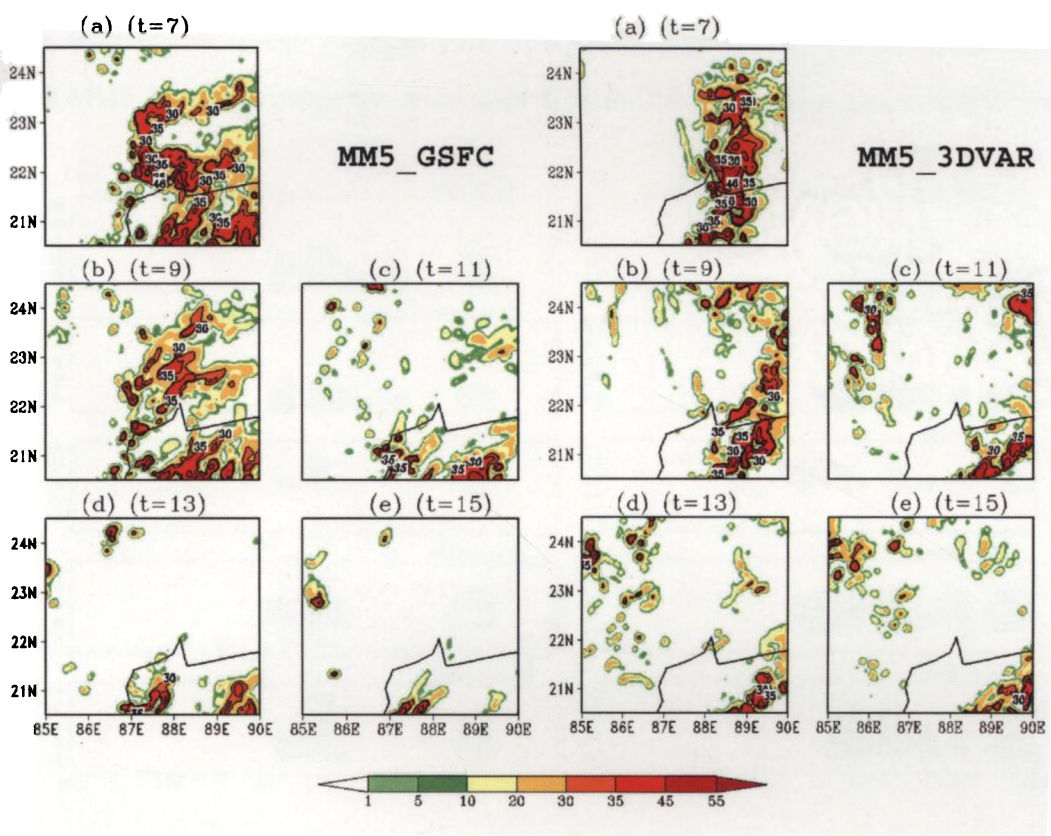


Figure 5.10: Simulated composite reflectivity from the MM5-GSFC and MM5-3DVAR experiments

5.7 MCS during 06-07 May 2007 : Case III

The objective of this section is to discuss the impact of conventional and satellite observations for the simulation of the microphysical structure of an intense cloud system around Kolkata region. The synoptic overview and description of the case considered here has been discussed in the previous chapter. Figure 5.11 (a) and (b) presents the latitudinal section of five hydrometeor species averaged over 1° longitude centered at 88.5°E for MM5-GSFC and MM5-3DVAR experiments. As evident from the DWR imageries (see chapter 4), in-

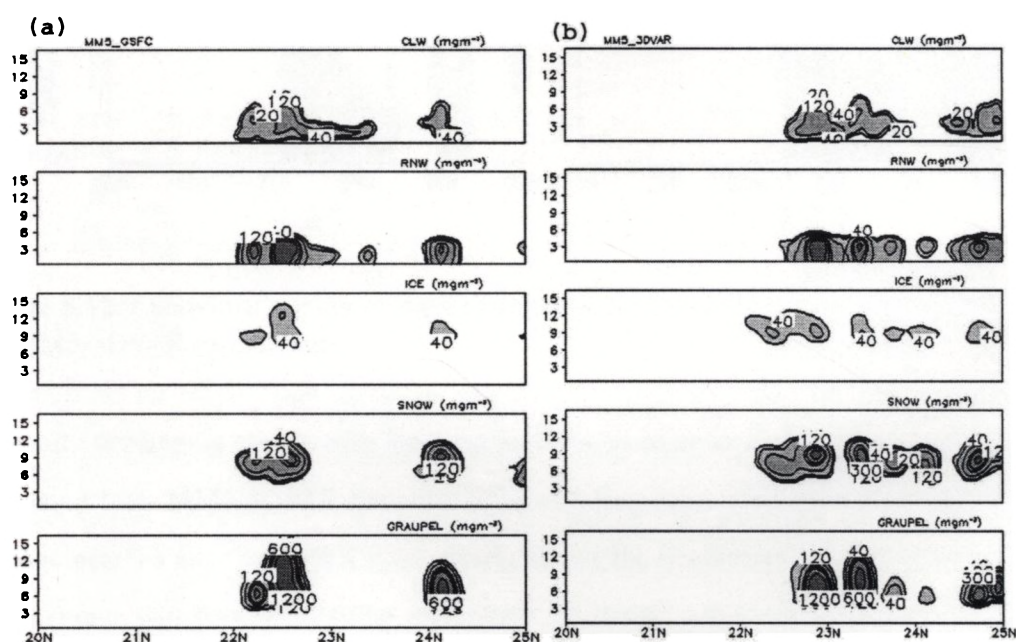


Figure 5.11: Latitudinal section of CLW, RNW, ICE, SNOW and GRAUPEL (mgm^{-3}) for (a) MM5-GSFC and (b) MM5-3DVAR experiments

tense cloud system with large vertical development has been observed north of the radar site. The cloud system simulated by MM5-GSFC experiment is located south of the radar site, whereas MM5-3DVAR simulates cloud north of the radar site. The MM5-3DVAR experiment simulates large amount of hydrometeors as compared to MM5-GSFC. Figure 5.12

(a) and (b) shows the latitudinal section of total hydrometeor from MM5-GSFC and MM5-3DVAR experiments. The DWR echo (see chapter 4) shows that the cloud top reaches near 12 km. The total hydrometeor content from MM5-GSFC experiment produced more

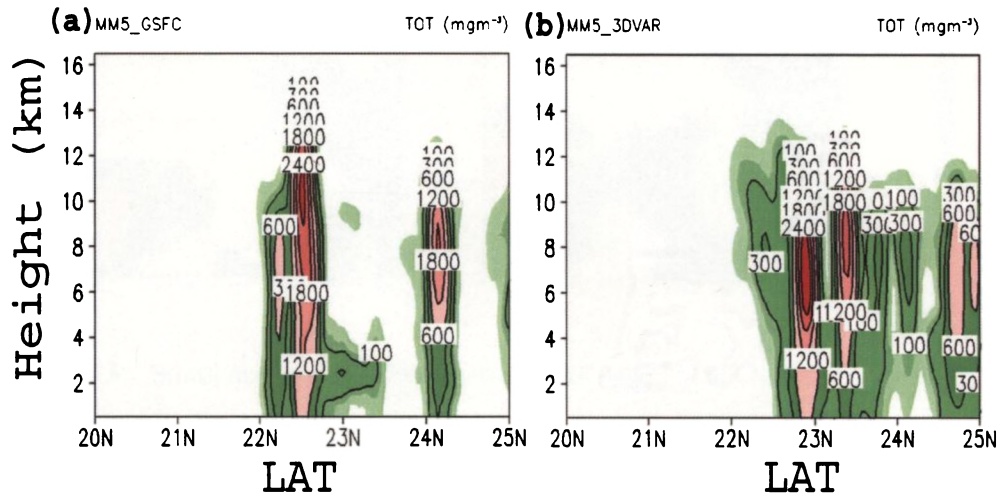


Figure 5.12: Latitudinal section of Total hydrometeors (mgm^{-3}) for (a) MM5-GSFC and (b) MM5-3DVAR experiments

vertically developing clouds with their top reaching as high as 15 km. The cloud system simulated from MM5-3DVAR experiments shows less vertical extent and the cloud top reaches near 14 km. The DWR echo clearly shows the southeastward movement of the cloud system with forward flanking anvil cloud. The total hydrometeor structure simulated by MM5-3DVAR does show anvil clouds, which extends southwards to a considerable distance. The assimilation of the conventional and satellite observations significantly improves the simulation of the vertical structure and organization of the cloud system reasonably well as compared to the control run without data assimilation. Figure 5.13 shows the simulated CAPE (Jkg^{-1}) for the MM5-GSFC and MM5-3DVAR experiments. It is evident that MM5-3DVAR experiment produce more CAPE ($> 3500 \text{ Jkg}^{-1}$) over the southwest sector of the model domain as compared to MM5-GSFC experiment.

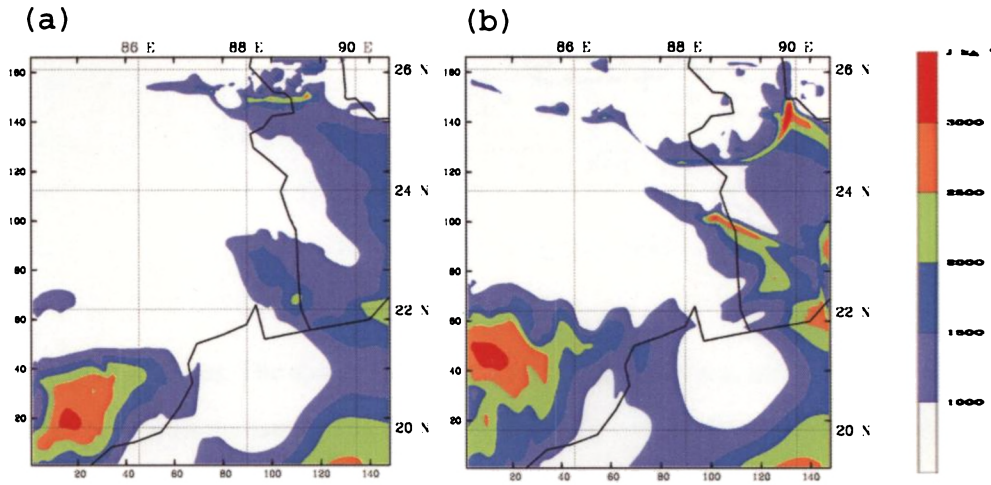


Figure 5.13: Simulated CAPE (Jkg^{-1}) from (a) MM5-GSFC and (b) MM5-3DVAR experiments

5.8 Forecast verification

The model forecast of precipitation has been verified by calculating the equitable threat scores (ETS) for all the three cases considered for the present study. The purpose of equitable threat score is to assess the skill of a model in placing its forecast of an event, say precipitation above a given threshold. The equitable threat score emphasize skill in forecasting the occurrence of the event more than they do the skill in forecasting the non-occurrence of the event. The ETS can be calculated based on the two-dimensional contingency table. For categorical forecast having two possible outcome (Yes or No), the following (2x2) contingency table can be defined (5.3).

The ETS is commonly used for the verification of deterministic forecast of rare events (e.g. precipitation amount above a large threshold). In term of raw cell counts, it is defined as (Schaefer, 1990),

$$ETS = \frac{a - a_r}{a - a_r + b + c} \quad (5.5)$$

where $a_r = \frac{(a+b)(a+c)}{n}$ is the number of hits expected for forecasts independent of obser-

		OBSERVED		
		YES	NO	TOT
FORECAST	YES	a	b	a+b
	NO	c	d	c+d
	TOT	a+c	b+d	a+b+c+d

Table 5.3: Contingency table

variations (pure chance). The appearance of n in the expression for a_r means that the equitable threat score (unlike the threat score) depends explicitly on the number of correct rejections, d .

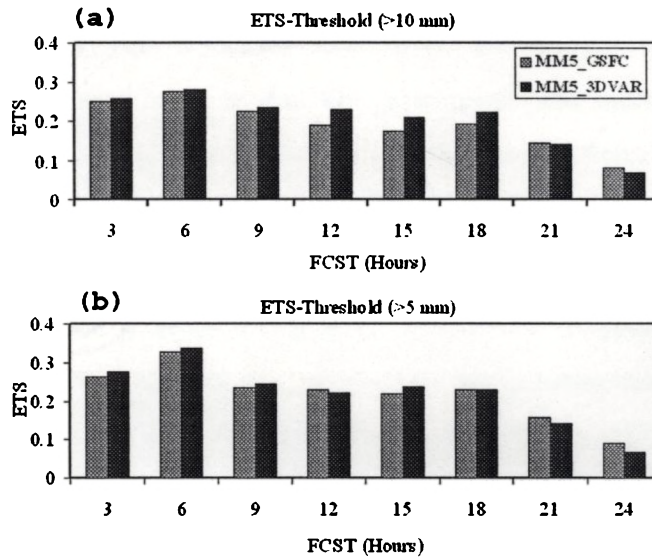


Figure 5.14: Equitable threat scores with a threshold of (a) 10 mm and (b) 5 mm for MM5-GSFC and MM5-3DVAR experiments

The ETS of precipitation forecast has been calculated using 3-hr accumulated precipitation from merged rainfall analysis of TRMM and other satellites (3B42). The predicted rainfall from model is gridded to .25° and values of a, b, c, and d are determined from TRMM observations. The figure 5.14 (a) and (b) presents the 3-hr rainfall verification of

		OBSERVED		
		YES	NO	TOT
FORECAST	YES	a	b	a+b
	NO	c	d	c+d
	TOT	a+c	b+d	a+b+c+d

Table 5.3: Contingency table

variations (pure chance). The appearance of n in the expression for a_r means that the equitable threat score (unlike the threat score) depends explicitly on the number of correct rejections, d .

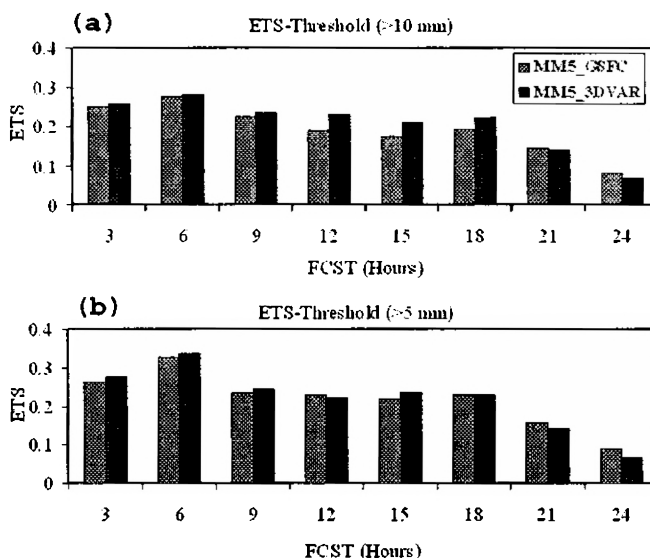


Figure 5.14: Equitable threat scores with a threshold of (a) 10 mm and (b) 5 mm for MM5-GSFC and MM5-3DVAR experiments

The ETS of precipitation forecast has been calculated using 3-hr accumulated precipitation from merged rainfall analysis of TRMM and other satellites (3B42). The predicted rainfall from model is gridded to .25° and values of a, b, c, and d are determined from TRMM observations. The figure 5.14 (a) and (b) presents the 3-hr rainfall verification of

the ETS averaged for the three cases with thresholds of 10 mm and 5 mm respectively. The result shows that, upto 18 hours, the assimilation experiment produces better skill in predicting the rainfall for both thresholds. But the MM5-3DVAR experiment shows more skill score for large thresholds (> 10 mm). This suggests that the assimilation of conventional and satellite observations significantly improves the prediction of intense rainfall associated with TMCS.

5.9 Summary

The impact of conventional and non-conventional data sets received through GTS/internet has been investigated. The variational assimilation scheme, 3DVAR developed for MM5/WRF has been used in the assimilation experiments. The model runs with triple nested domains at 30, 10 and 5 km resolutions with the same configuration as used in the previous chapter. Keeping all model physics same, two experiments have been performed for each case. In the first experiment, the model initial and boundary conditions have been obtained from the global analysis of NCEP/FNL at $1.0^\circ \times 1.0^\circ$ resolutions. In the second experiment, model initial condition has improved by incorporating the conventional and non-conventional data sets in the 6-hr assimilation cycle. Four assimilation cycles have been performed in the second experiment before the model is being run in free forecast mode. The simulated reflectivity and hydrometeor structure has been analyzed and compared with the DWR observations. Forecast verification of rainfall has been carried out by calculating the equitable threat scores.

CHAPTER 6

Signatures of Gravity Waves Associated with Convection

6.1 Introduction

Vertically propagating gravity waves are known to have a profound effect on the structure and circulation of the atmosphere. One of the important issues on gravity waves is the energy sources and generation mechanisms. Deep convection has been recognized as a source of gravity waves (*Gossard and Hooke, 1975*). The atmospheric waves grow in amplitude during their upward propagation into the middle atmosphere. Energy and momentum is transported both horizontally and vertically by these waves. The waves dissipate through various instability processes and deposit the momentum to the background winds thus playing key role to maintain the dynamical structure of the tropical atmosphere.

The gravity waves generated due to convection processes may also be called convection waves (*Dhaka et al., 2001*). *Tsuda et al. (1999)* showed that gravity wave activity is max-

imum over equatorial regions where deep convection is active, thus strongly suggesting their convective origin (*Pfister et al.*, 1993). Convectively generated gravity wave events are tropospheric gravity waves with horizontal wavelengths and periods typically in the range, 10-200 km and 6 min - 2.0 hours, respectively.

Convectively generated gravity waves are one of the major uncertainties in the momentum budget of the stratosphere. The forcing mechanisms responsible for generating vertically propagating waves in convective clouds are not well understood. *Clark et al.* (1986) proposed that oscillating updrafts and downdrafts vertically displace the isentropes at the base of a stable layer. For example, the stratosphere, producing vertically propagating gravity waves in a manner similar to that of a mechanical oscillator in a stratified fluid. The frequency of waves generated in this fashion is specified by the frequency of the oscillator, or in the case of convection, by the frequency of convective updrafts and downdrafts. Squall line simulations by *Fovell et al.* (1992), *Alexander and Pfister* (1995), and *Lane et al.* (2001) showed evidence for this type of wave generation.

Thermal forcing by latent heat release within the convective storm is also been recognized as the main gravity wave forcing. Through a number of numerical experiments, *Salby and Garcia* (1987) showed that the dominant tropospheric vertical wavelength of waves generated by a thermal forcing is approximately equal to twice the vertical extent of heating. For a fixed frequency and horizontal scale, the vertical wavelength varies inversely with the buoyancy frequency. Since the buoyancy frequency in the stratosphere is approximately double that in the troposphere, the vertical wavelength of stratospheric waves predicted by this mechanism should be equal to the vertical extent of the tropospheric heating.

Another mechanism responsible for wave generation is the obstacle effect. In this mechanism (also known as the moving or transient mountain effect), the convective element acts as a barrier to the background flow, producing upstream propagating waves in a manner similar to flow over a mountain (*Pfister et al.*, 1993). Since the convective element oscil-

lates in time and may move relative to the ground, the generated waves are not stationary relative to the ground as in the case of mountain waves, but propagate horizontally, primarily opposite to the wind direction. A detailed study of gravity waves observed over the tropical Indian Ocean confirms this type of wave generation (*Alexander and Vincent, 2000*).

The temporal and spatial variability of vertically propagating convectively generated gravity waves is poorly understood because all of the currently available observational techniques have serious limitations in either time or space. Radar observations have high time resolution, but are limited to only a few locations on the globe (*Sato, 1992, 1993*). Radiosondes have good spatial coverage over land areas, but poor time resolution, and can only be used to indirectly deduce the characteristics of short vertical wavelength gravity waves (*Allen and Vincent, 1995; Vincent and Alexander, 2000*). Satellite radiance data has been used to map the global distribution of gravity wave variances at several levels in the stratosphere by *Wu and Waters (1996)*. However, their method is only capable of resolving very long vertical wavelength gravity waves, and must be used with great caution in deduction of regional and seasonal variations in wave sources (*Alexander, 1998; McLandress et al., 2000*). Aircraft campaigns provide the highest horizontal resolution observations of wave activity; however, they provide little information on the vertical structure of waves and are limited to small areas (*Pfister et al., 1993; Alexander and Pfister, 1995; Alexander et al., 2000*). All of the above observational methods have linked substantial gravity wave activity to convection, however none of them provides adequate information to parameterize the full spectrum of convectively generated waves and their sources.

The VHF clear air Doppler radars provide wind velocities with fine time and height resolutions, which enable us to investigate detailed structures of small-scale gravity waves in a wide range of frequency and vertical wave number spectra. Recent observations using VHF radar and aircraft measurements have shown some evidence of gravity waves coupled with deep convection resulting in the generation of gravity waves (*Fritts and Nastrom,*

1992; Sato, 1993; Sato *et al.*, 1995; Karoly *et al.*, 1996; Shibagaki *et al.*, 2000; Dhaka *et al.*, 2001).

Cram *et al.* (1992) analyzed a squall line simulated by the Colorado State University Regional Atmospheric Modeling System (RAMS) that was associated with a gravity wave of mesoscale dimension. Case studies by Pokrandt *et al.* (1993, 1994) reported generation of mesoscale gravity wave event with lengths of about 200 km and a phase speed of 50 ms^{-1} using University of Wisconsin Nonhydrostatic Modeling System associated with convection (grid resolvable). They hypothesized that the waves began as the rising branch of a Sawyer-Eliassen circulation. Studies by Schneider (1990) and Mawitz and Toth (1993) found evidences of convection and shear as source mechanism for mesoscale gravity wave event.

Observational and model experiments by Powers and Reed (1993) have investigated a mesoscale gravity wave event and found the three most prominent waves with wavelength of 100-160 km, phase speed of 30 ms^{-1} and double amplitudes of upto 7 hPa. While an effective wave duct was found, evidence of convection suggested that wave CISK (conditional instability of second kind) could have contributed to the wave maintenance and amplification. The modeling results indicated convective processes as both the model and actual wave genesis mechanism, although shearing instability remained a possibility. The analysis also showed that elevated convection traveling with the model waves represented a continual forcing mechanism and convection as a maintenance/reinforcement mechanism for the observed wave event.

Alexander and Pfister (1995) carried out non-linear, two-dimensional numerical simulations of midlatitude squall line to study vertically propagating waves generated by deep convection. The model includes more vertical levels in the stratosphere with enough vertical resolution to characterize the wave motion at these altitudes. The spectral analysis of the wave fields points to specific forcing mechanism active in the model. They found that for a

given forcing mechanism, the response of gravity waves is governed by three properties of the storm; viz. (1) the depth of the diabatic heating layer, (2) the oscillation frequency of the main updrafts, (3) the storm propagation speed. The depth of heating largely determines the vertical wavenumber of the wave response. The oscillation frequency of the central updraft of the storm determines the intrinsic frequency of the waves forced by mechanical pumping mechanism.

Powers (1997) carried out several numerical experiments to determine the sensitivity of mesoscale gravity wave simulation to model configuration and physics. He found that wave generation and maintenance are insensitive to upper boundary condition. The wave production and structure are also insensitive to vertical resolution. He also carried out several sensitivity experiments to determine the sensitivity of moist process in the simulated wave event. The results show that latent heat is important in the wave development. Sensitivity of different initialization techniques has been analyzed by *Errico and Bates (1998)*. In the normal mode initialization, which balances the initial mass and wind fields to remove the unrealistic gravity wave noise was tested and found to have no significant impact on mesoscale gravity wave simulation. The data were initialized by running the model for a 12-hr period, with hour 12 forecast becoming first guess field for the sensitivity test runs.

Understanding the wave forcing mechanisms active in convection, as well as the properties of the storm and atmosphere that control the wave characteristics, are crucial steps toward developing a parameterization of their global effects on the middle atmosphere. This chapter discusses the observable features of gravity waves associated with the passage of a TMCS. The present chapter also examines the three-dimensional model simulations of the organization and characteristics of TMCS. *Dhaka et al. (2002)* and *Kumar (2006)* have carried out observational investigation of the cases considered here and found evidence of clouds coupled with convection. A discussion on the relationship between the nature of the forcing mechanism during system lifecycle and fundamental properties of the storm

has also been included. Analysis has been carried out to study the characteristics of the atmosphere that support gravity wave generation and propagation.

6.2 TMCS on 21 June 2000

The detailed descriptions of the synoptic condition and the experiment design have been given chapter 3. Some results obtained by the preliminary analysis of the data have already been reported by *Dhaka et al. (2002)* and *Abhilash and Mohankumar (2004)*. The continuous observations for a period of 5-6 hours starting from 19:23 to 01:23 hrs local time (LT) during 21-22 June 2000 have been used for the present study. Strong vertical wind fluctuations with short periods of several tens of minutes were also reported in the earlier studies. There are several remaining but important issues on the small-scale disturbances associated with convection have to be investigated with the aid of such data of high quality. Spectral structures of the disturbances in relation to the intensity of the convective activity can be investigated in detail.

6.2.1 Vertical velocity disturbance

Figure 6.1 shows the time-height variation of vertical wind field during 19:23 to 01:23 hrs local time during 21-22 June 2000. To remove small scale wind perturbations having vertical wavelength less than 1 km, the vertical wind components were averaged for 900 m. In order to smooth the profile, a three point running mean has been performed on the time scale. The vertical wind fluctuates from - 6 to + 8 ms^{-1} in the middle and upper troposphere and - 3 to +3 ms^{-1} over the rest of the troposphere and lower stratosphere for a period of nearly 2 hrs. (See chapter 3). These large fluctuations in the vertical wind of amplitudes 5-6 ms^{-1} are observed only during cumulus and mature phase of the storm (different phases of the storm life cycle has been discussed in chapter 3). After that, it fluctuates from -2 to + 2

ms^{-1} in the troposphere and lower stratosphere. Based on these vertical wind disturbances we classified the entire period into *convection active* (period of large fluctuations in the vertical wind, between 19:40 and 21:40) and *convection quiet* periods (period of small fluctuations, between 22:00 and 23:50).

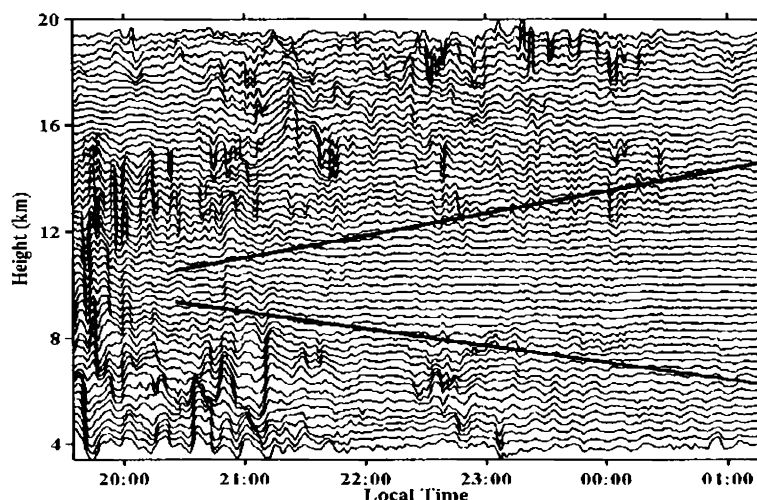


Figure 6.1: Time series of vertical velocity in the troposphere and lower stratosphere during 19:35 on 21 June to 01:20 UTC on 22 June 2000

A temporal discontinuity in the wind disturbances is found after convection-active period. Similar velocity fluctuations have been reported by *Sato* (1993) during the passage of a typhoon. During the convection active periods, the disturbance having strong upward motion is observed in the middle and upper troposphere. This may be due to the release of latent heat in the middle troposphere (*Ley and Peltire, 1981*). A quasi-sinusoidal oscillation in the vertical wind is seen in the lower and upper troposphere. After the initial disturbance in the middle troposphere during the cumulus phase of the storm, amplitude of oscillation becomes very low (between the straight lines in figure 6.1), generally between 8.5 and 11.5 km. The heating may be distributed over a depth of 4 - 6 km in the lower and middle troposphere (humidity and temperature observations not available over the radar site).

6.2.2 Spectral characteristics of the wind disturbance

In order to study the wind fluctuations in the Upper Troposphere and Lower Stratosphere (UT/LS) in more detail, power spectra of vertical winds were computed from the time series. The perturbations of the respective winds are estimated by subtracting the mean values from each instantaneous values. This perturbation in vertical wind is subjected to Fourier analysis to obtain dominant modes of the waves at each range bin. Vertical velocity at a time interval of 35 seconds (δt) for a period of 149.34 min ($T = N\delta t, N = 256$) are used to estimate the time period and amplitude of oscillations. The multi height normalized power spectra in the UT/LS region is shown in figure 6.2 gives an overall picture of the oscillations in vertical velocity. The vertical coherence of the spectrum is clearly seen in the figure 6.2. The spectral analysis sufficiently characterizes the spectral properties of the waves to

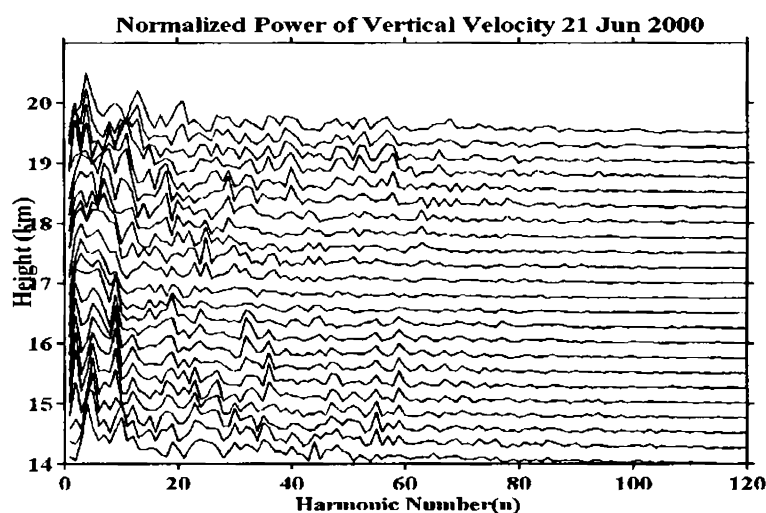


Figure 6.2: Multi-height normalized spectrum of vertical velocity perturbation in the UT/LS region

define their frequencies and vertical wavelength. Spectral analysis shows two dominant modes of oscillations at about 26-30 min and 13-15 min. The most prominent spectral peak is near 13-15 min, which corresponds to most evident wave like oscillations observed in

the time series of vertical velocity. This period is above the local buoyancy (Brunt-Vaisala) frequency and hence the observed oscillations are most likely due to penetrative convection (Curry and Murthy, 1974). The overshooting convection or the oscillating nature of updrafts and downdrafts near the tropopause during the mature phase of the storm has been discussed in chapter 3.

6.2.3 Amplitude-height profile

Figure 6.3 shows the amplitude-height profiles of two dominant modes of oscillations. Both modes of oscillations show the primary peak in the UT/LS region at about 16.5 km and a secondary peak in the troposphere at 8 km on 21 June 2000. The primary minimum is found in the lower troposphere at about 5 km and secondary minima near 9 km. The amplitude of oscillation of the 15 min mode is slightly higher than that of 28 min mode. The signature of wave like oscillations in the UT/LS region is due to oscillating updrafts and downdrafts associated with penetrative convection. This also brings out the role of penetrative convection on tropopause weakening process and associated Stratosphere Troposphere Exchange (STE).

6.2.4 Wavelet analysis of the vertical wind

The time series of a perturbation in vertical velocity consists of several non-interacting waves and turbulence. Small amplitude waves and waves of short duration can be overlooked by spectral calculations. A short period wave may sporadically appear for short durations over a few hours time. However, in a spectrum analysis the wave may appear to have a much longer period. Wavelet technique can be useful in analyzing spectrum of gravity waves consists of two or three frequencies with short duration. Windowing process is the basis of wavelet transforms (WT). By varying the time window, more frequencies are introduced into the spectrum. Repeated passes through the time series with increasing

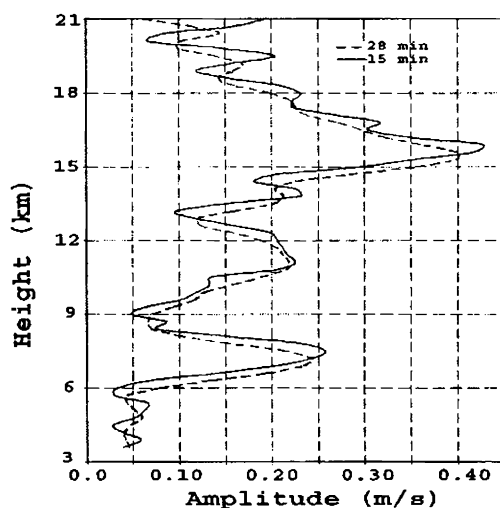


Figure 6.3: Amplitude-height profiles of the two dominant modes of oscillation

window size results in the decomposition of the time series into time-frequency space. By decomposing a time series into time-frequency space, one is able to determine both the dominant modes of variability and their variability in time. The basis of WT is the mother wavelet and the dilation time scale. The Morlet wavelet used in the present analysis is defined as the product of a complex wave and a Gaussian envelop.

$$\phi_0(\eta) = \pi^{-\frac{1}{4}} e^{i\omega_0\eta} e^{-\frac{1}{2}\eta^2} \quad (6.1)$$

Where, ϕ_0 is the wavelet value at non-dimensional time η , ω_0 is the wave number. The scaled wave is then,

$$\phi \left[\frac{(n' - n)\partial t}{s} \right] = \left[\left[\frac{\partial t}{s} \right]^{1/2} \phi_0 \left(\frac{(n' - n)\partial t}{s} \right) \right] \quad (6.2)$$

Where, s is the dilation parameter, used to change the scale, the factor $s^{-1/2}$ is a normalization to keep the total energy of the scaled wavelet constant (*Torrence and Compo, 1998*). The wavelet function behaves much more like a filtering function in band pass filter.

To determine the significance level of the spectrum an appropriate background spectrum is chosen as follows,

$$P = \frac{[1 - \alpha^2]}{[1 + \alpha^2 - 2\cos\left(\frac{2\pi k}{N}\right)]} \quad (6.3)$$

Where, $k = 0, 1, \dots, \frac{n}{2}$ is the frequency index and α is lag-1 auto-correlation.

The null hypothesis is defined for the wavelet power spectrum as follows. It is assumed that the time series has a mean power spectrum, possibly given by the above equation. If a peak in the wavelet power spectrum is significantly above this background spectrum, then it can be assumed to be true feature with a certain percent confidence of 90% or 95%.

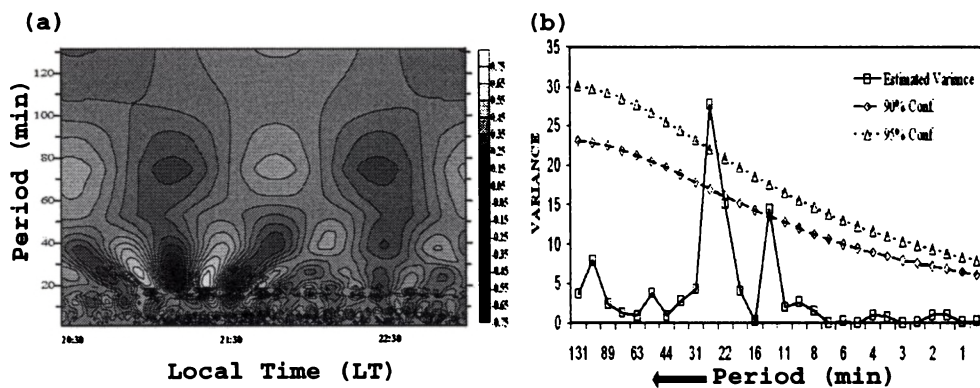


Figure 6.4: (a) Wavelet analysis of the vertical velocity in the lower stratosphere. Local time in ordinate and periods in abscissa. (b) Significance test carried out for the wavelet spectrum

Wavelet analysis of vertical velocity in the lower stratosphere is shown in figure 6.4 (a). Two dominant modes of oscillation with periods around 24-30 min and 11-15 min are present during the observation period. These two dominant modes are determined by carrying out the significance test. The 24-30 min mode is 95% significant, whereas, the 11-15 min mode shows 90% significance (fig. 6.4 (b)). The 15 min mode is prominent in the spectral analysis, whereas 24-30 min mode is significant in wavelet analysis. Wavelet analysis clearly shows that, 15 min wave is present till 21:45 hrs LT (during the convection active

period). As discussed earlier the spectral analysis overlooked at these higher frequency of short duration. Obviously, the 24-30 min wave exists during the entire observation period.

6.2.5 Cloud resolving scale simulation

To support the observational evidence of short period oscillations, simulation experiment of the same case has been performed using cloud resolving scale configuration of MM5 model. The details of the modeling system is given in chapter 4. The model configuration include triple nested domain with 45, 15 and 5-km horizontal resolution and 47 σ levels. The synoptic setting of the case considered in the present study is such that the evolution of the convection is strongly controlled by the environmental dynamics rather than thermodynamics. The predictability of the features will expect to be better in such situations (*Zhang and Fritsch, 1988*).

We use cumulus parameterization only in the outer domains and fully explicit approach in the innermost domain. The model physics used in the present study include Grell scheme for cumulus parameterization (*Grell et al., 1994*), boundary layer parameterization of *Hong and Pan (1996)* as used in the Medium Range Forecast (MRF) model, explicit treatment of cloud hydrometeors is based on Goddard Space Flight Centers (GSFC) microphysical scheme (*Tao et al., 1987a; Tao and Simpson, 1984b*).

The National Center for Environmental Prediction-Final (NCEP/FNL) global analysis ($1^\circ \times 1^\circ$ horizontal resolution) available at 6-hr intervals interpolated to model grid has been used as initial and boundary condition for simulation experiment (MM5-GSFC). The initial condition is further improved by incorporating the upper air data obtained from India Meteorological Department (IMD) along with wind observations from Indian Mesosphere Stratosphere Troposphere (MST) radar through 12 hr analysis nudging. Observations are continuously assimilated into the model during a pre-forecast period (say, $t = -12$ hr to $t = 0$ hr), after which the nudging is turned off. The model is then integrated in a purely prog-

nostic (free forecast) mode. In the pre-forecast period, nudging experiment starts at 0000 UTC of 21 June 2000. After 12 hr analysis nudging (from 0000 UTC 21 to 1200 UTC 21 June 2000), the model is integrated for 12 hr in free-forecast mode.

6.2.6 Simulated reflectivity

As evident from the observational analysis of the convective event, at the time of the TMCS passage over the radar site, the main convection band is in its developing or cumulus stage. Figure 6.5 (a) through (c) shows model simulated composite reflectivity at one hour intervals. The model efficiently simulates the organized multicell structure and northward

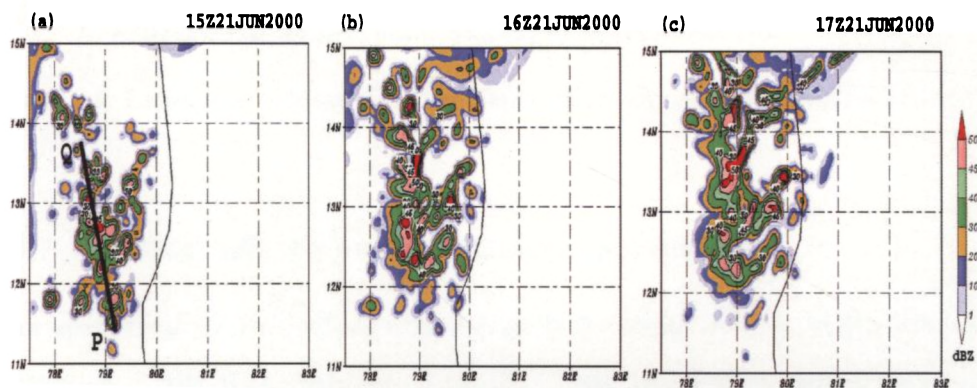


Figure 6.5: Simulated composite reflectivity in dBZ at (a) 15:00 (b) 16:00 and (c) 17:00 UTC on 21 June 2000

propagation of the TMCS. During the genesis stage at 15:00 UTC 21 June 2000, the main convective cell is south of the radar location (fig 6.5(a)). One hour later at 16:00 UTC of the same day, the convection cells are well organized and main convective cell is exactly over the radar site (fig 6.5(b)). At this time the convective system reaches its mature phase. Later on the convective system propagated northwards and the main convective cell is situated north of the radar site (fig 6.5 (c)). Figure 6.6 shows the latitude-height section of simulated radar reflectivity along the longitude - latitude strip covering line PQ (marked in figure 6.5(a)). The convective region, transition region, stratiform region and the secondary

convective region is also marked in the figure 6.6. The radar reflectivity structure shows the leading convection region, transition region and stratiform regions associated with TMCS.

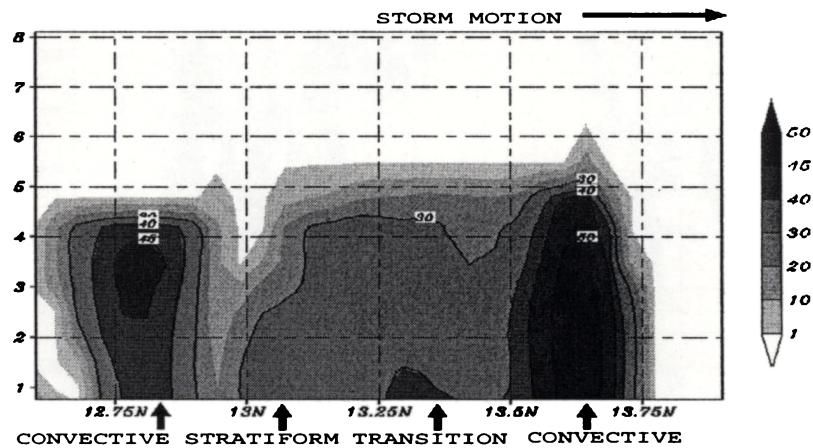


Figure 6.6: Latitudinal section of the simulated reflectivity at 16:30 UTC on 21 June 2000

6.2.7 Vertical velocity and penetrative convection

Time-space cross section analysis is used to study the height variation of the vertical wind fluctuations at selected heights viz., 3, 6, 10, 13 and 16 km at 15 min intervals. Figure 6.7 (a) through (e) shows the time-space evolution of vertical velocity along the latitude section at 3, 6, 10, 13 and 16 km, respectively. Between 1300-1400 UTC of the simulation experiment, convective cells with upward velocity of $1-2 \text{ ms}^{-1}$ located extreme south of the model domain at 3 km level. As upward velocity is seen during the period, this is marked as the genesis stage of the TMCS. During 1430-1600 UTC, three well organized upward motion bands A, B1 and B2 with core velocity greater than 2 ms^{-1} developed just north of the radar site. During the period, a well organized downward motion band is sandwiched between the upward motion bands A and B1. This stage is marked as the initial or developing stage of the TMCS. Between 1600-1730 UTC, the cells B1 and B2 merged to form a strong upward motion band marked as B. During the period, the upward motion

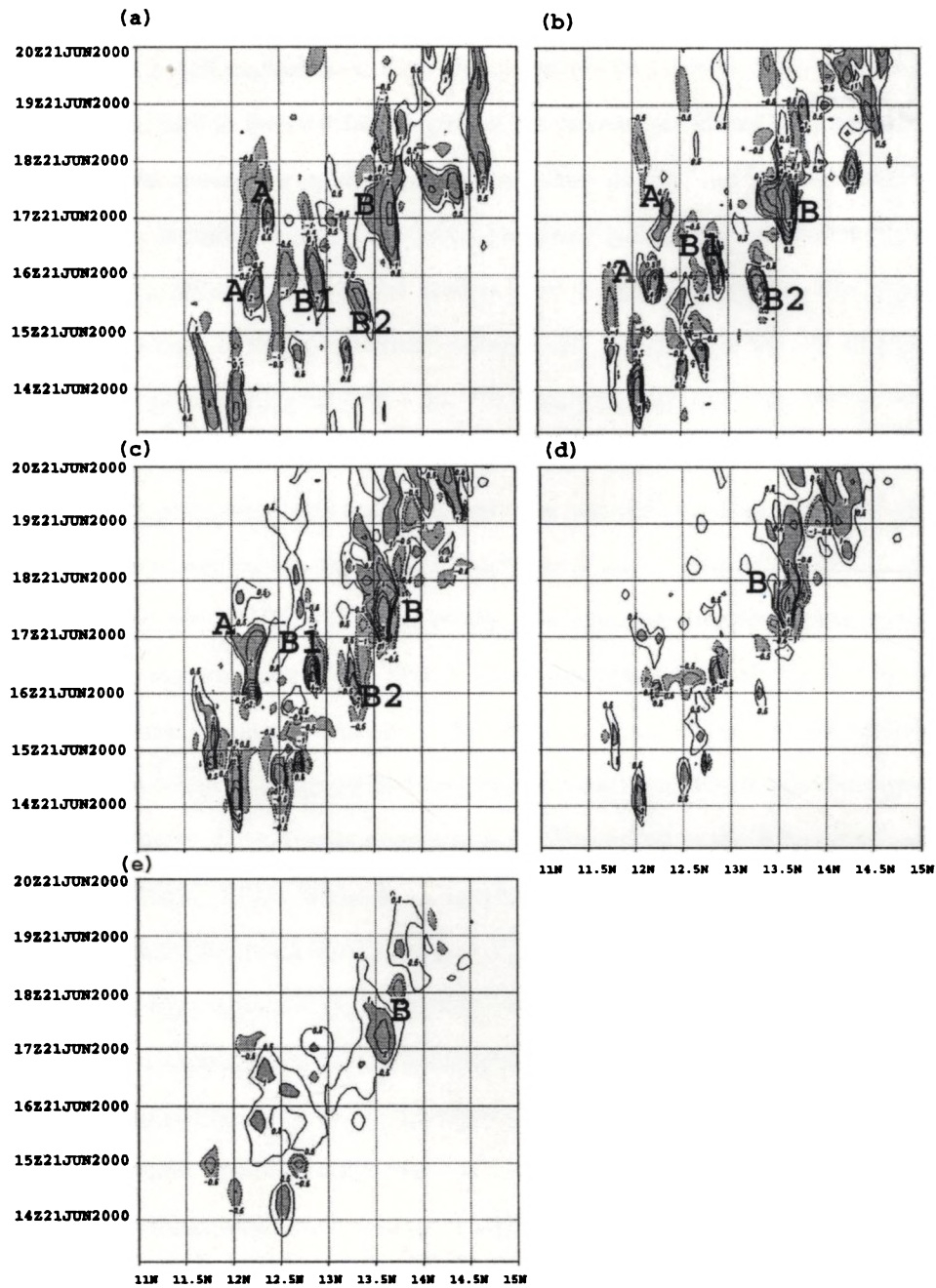


Figure 6.7: Time-space evolution of vertical velocity in ms^{-1} at (a) 3 km, (b) 6 km, (c) 10 km, (d) 13 km and (e) 16 km levels. Solid contours shows upward motion and dashed contours represents downward motion

band exhibits large areal coverage and strong vertical velocity greater than 3 ms^{-1} . The cell A subsist while, a well marked downward motion band with velocity -2 ms^{-1} surrounds it. This region is marked as the stratiform region of the convection. Hence the co-existence of the stratiform and convective region signifies the mature stage of the TMCS, which is well supported by the latitude-height section of the simulated reflectivity depicted in figure 6.6.

Similar organization of the vertical motion band is seen upto 10 km. The maximum vertical velocity core of magnitude greater than 8 ms^{-1} found at 6 km. At 10 km level, vertical velocity cores of magnitude $6-8 \text{ ms}^{-1}$ is found near the radar site. This is in agreement with the VHF radar observations that the maximum velocity of $6-8 \text{ ms}^{-1}$ observed in the middle troposphere. At 13 km level, only the convection cell marked as B exhibits significant upward motion of magnitude greater than 4 ms^{-1} . The cell B subsist upto 16 km. As observed by the VHF radar, the model well simulates the penetrative convection cells during the mature phase of the TMCS. The cloud resolving scale model simulations able to capture the kinematic structure of the storm in terms of the vertical velocity disturbance in the middle troposphere and the penetrative convection. Studies by Lane *et al.* (2001) also considered a vertically oriented convective updraft as the dominant wave forcing term. He pointed out that the source location is variable in space and time but is related to the development of individual convective cell. The largest amplitude waves are generated when the cloud top reaches the upper troposphere. The CSRM simulations also well captures the observational evidence of the overshooting convection and oscillating updraft and downdraft motions. Figure 6.8 shows the simulated thermodynamic profiles at the radar site. The thermodynamic profile is conducive for moist convection with large CAPE value of 2300 Jkg^{-1} and the equilibrium level is near 100 hPa. Hence the simulated thermodynamic diagram also support the overshooting convection.

The response of the evolution of vertical velocity to the hydrometeors has been examined by taking time series analysis of the integrated cloud water (ICLW), integrated rain

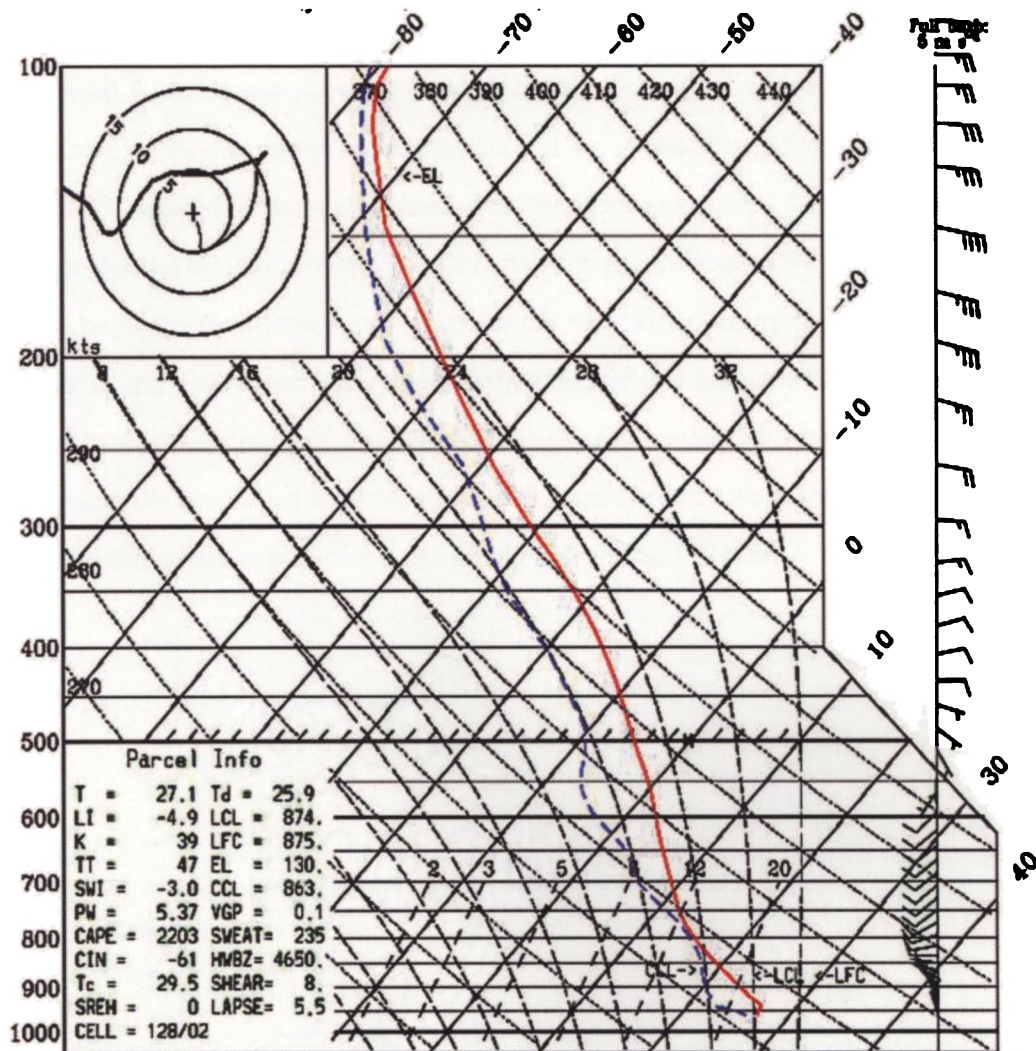


Figure 6.8: Simulated thermodynamic profile at the radar site

water (IRNW) and vertical velocity at 500 hPa (W_{500}). The time series is taken over the radar site (13.5°N, 79.2°E) since; the TMCS is exactly over the radar site during the mature phase of the storm. Figure 6.9 presents the time series of the ICLW, IRNW and W_{500} averaged over 2°X 2° latitude-longitude grids. During the initial hours of the simulation, downward motion present over the radar site till 1500 UTC and this may be due to the convective outflow from the cloud clusters that are in the dissipating stage. During 1530-1800 UTC upward velocity dominates over the radar site. Large ICLW during the period suggest that the updraft is due to the latent heat release associated with condensation. Later hours, large downward velocity exists over the radar site. During the period, large IRNW present over the radar site. This suggests the effect of precipitation loading on downdrafts. Hence the hydrometeor structure significantly affects the vertical velocity evolution during the system life cycle. In a large amplitude mesoscale gravity wave simulation, *Jewett et al.* (2003) found negative correlation of vertical velocity and IRNW.

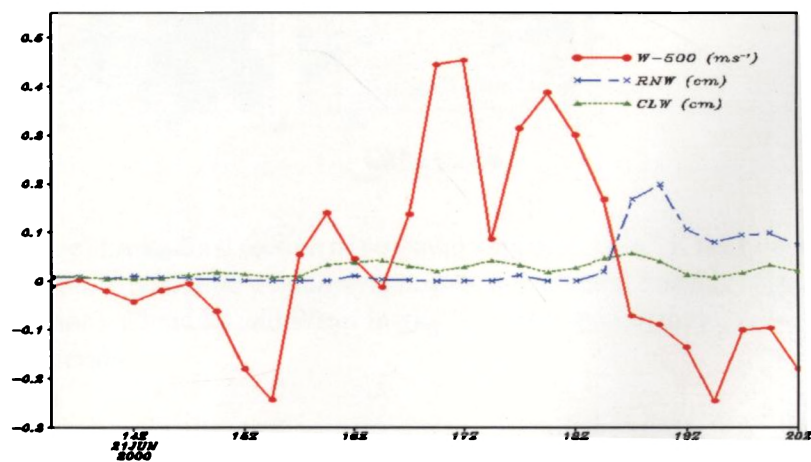


Figure 6.9: Time series of Integrated Cloud Liquid Water (ICLW) in cm (green line), Integrated Rain Water (IRNW) in cm (blue line) and vertical velocity at 500 hPa in ms^{-1} (red line)

6.2.8 Cloud liquid water and system evolution

Figure 6.10 (a)-(e) shows the latitude-height section of the cloud liquid water, vertical velocity and potential temperature at one hour intervals. At 1500 UTC, on 21 June 2000,

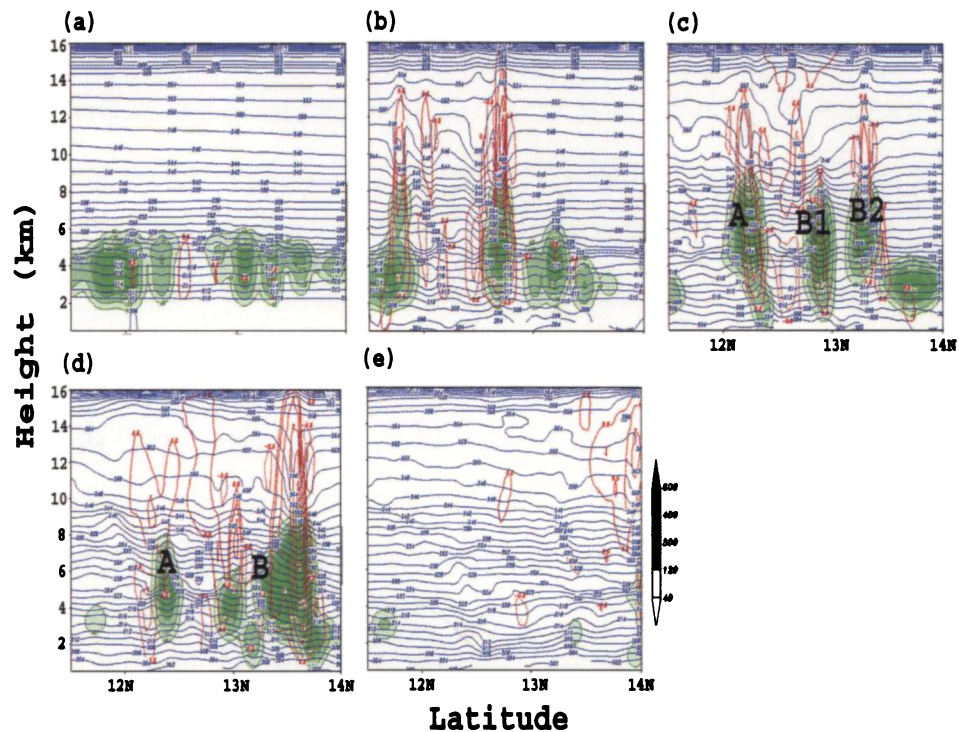


Figure 6.10: (a-e) Latitudinal section of potential temperature in $^{\circ}\text{K}$ (blue contours), Vertical Velocity in ms^{-1} (red solid contours represents upward and dashed contours represents downward motion), Cloud Liquid Water in gkg^{-1} (green shades) during 14:00-18:00 UTC at one hour intervals

the main convection band is south of the radar site. During the time, upward motion exists in the lower troposphere. After one hour (1600 UTC), three well organized convection bands exist just south of the radar site. Maximum vertical velocities of values greater than 4 ms^{-1} is associated with CLW. The three cell structure and organized vertical velocity keep going on till 1700 UTC. As described in the previous section, during the mature phase of the storm, convective cells B1 and B2 merged together to form a large convective

area marked as B. Obviously figure 6.10 (d) supports merging process and penetrative convection at 1800 UTC on 21 June 2000. The northern cells B1 and B2 with considerable cloud liquid water content during 1600-1700 UTC merged to form a large cell at 1800 UTC. During the initial phase at 1500 UTC, wave-like structure in the potential temperature field is trivial. As time progresses, adequate condensation in terms of cloud liquid water grounds vertical velocity disturbance and the wavelike feature in potential temperature are noted. Wave-like structure is quite prominent during 1600-1900 UTC with maximum amplitude of perturbation during the mature phase of the storm at 1800 UTC.

6.3 Supercell storm on 17 October 2002

The detailed descriptions of the case and experiment design have been presented in chapter 3. Studies by *Uccellini and Koch (1987)* found that, mesoscale gravity waves can be generated by or modulate organized convection. It is not apparent from the present data that, whether the convection is induced by the waves or the wave is initiated by convection. Although the wave observed during the time when there is extensive convective activity occurred in the experimental area, the data available are inadequate for a detailed examination of the relationship between the wave and convection on a direct observational basis *Abhilash et al. (2006b)*.

6.3.1 Vertical wind disturbance

Figure 6.11 shows the time-height variation of vertical wind field during 20:30:00 to 00:40:00 hrs LT during 17 - 18 October 2002. To filter out small scale wind perturbations having vertical wavelength less than 1 km, the vertical wind components were averaged for 600 m. In order to smooth the profile, a three point running mean has been performed on the time scale. A quasi-sinusoidal oscillation in the vertical wind is seen in the upper

troposphere and lower stratosphere. After the initial disturbance in the middle troposphere during the cumulus phase of the storm, amplitude of oscillation becomes very low in the lower and middle troposphere. The oscillatory nature of the vertical wind is noted in the UT/LS region. As seen in the figure, updraft-downdraft couplets presents in this region. The updrafts ascends to heights exceeding (overshooting) the parcel equilibrium level, beyond which rising air quickly becomes negatively buoyant. Very strong downward force from negative buoyancy then leads to downdrafts that are negatively buoyant only in the upper levels. These initial overshooting downdrafts similarly overshoot their level of neutral buoyancy leading to subsequent decaying buoyancy oscillations and so, the penetrative or overshooting convection can be regarded as the possible gravity wave forcing in the UT/LS region. During the mature phase of the storm, the maximum updraft speed of 14 ms^{-1} is found between 12-14 km (see chapter 3).

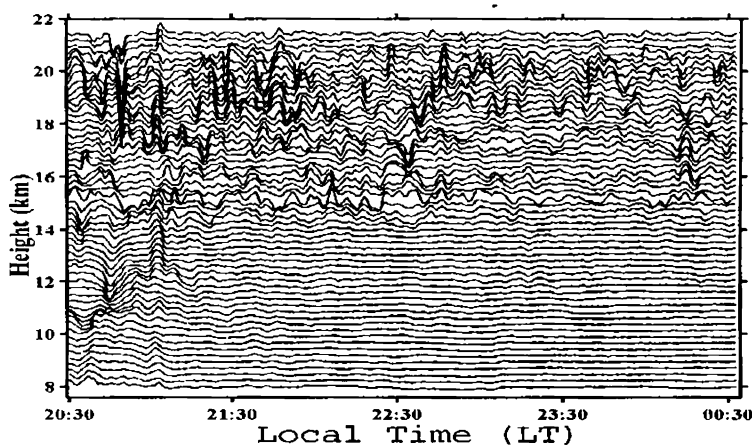


Figure 6.11: Time series of vertical velocity in troposphere and lower stratosphere during 20:30 17 October to 00:45 UTC on 18 October 2002

6.3.2 Spectral characteristics of the observed wave event

In order to study the wind fluctuations in the Upper Troposphere and Lower Stratosphere (UT/LS) in more detail, perturbation in vertical wind is subjected to Fourier analysis to obtain dominant modes of the waves at each range bin. The multi height normalized power spectra in the UT/LS region (not shown) shows distinct peaks at about 28-32 min, 13-15 min and 6-8 min. We can therefore assume that high frequency waves are the dominant part of the observed turbulence and wind disturbance. Figure 6.12 shows the averaged power spectral density of the vertical velocity in the UT/LS region. This spectrum of vertical

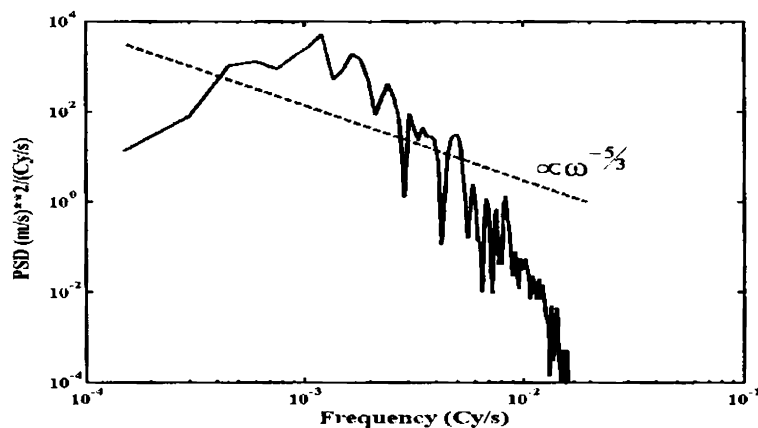


Figure 6.12: Averaged power spectral density in the UT/LS region

velocity displays the dominance of high-frequency waves of period between ~ 8 min and 30 min with power falling steeply below 6 min following a power law proportional to $\omega^{-5/3}$, where ω is the intrinsic frequency. This result is in accord with *Fovell et al.* (1992) that the mechanical pumping/forcing mechanism due to oscillating updrafts and downdrafts impinging on the tropopause as the mechanism for generating high-frequency waves in supercell storms. The higher frequency waves of periodicity 8 - 10 min are just above the local buoyancy (Brunt-Vaisala) frequency and hence the observed oscillations are most

likely due to penetrative convection (Curry and Murthy, 1974).

6.3.3 Wavelet analysis of the vertical wind

Wavelet analysis of vertical velocity in the lower stratosphere is shown in figure 6.13 (a). Three dominant modes of oscillation with periods around 24-30 min, 11-15 min and 7-8 min are present during the observation period. These three dominant modes are determined by carrying out the significance test and is presented in the figure 6.13 (b). Only 24-30

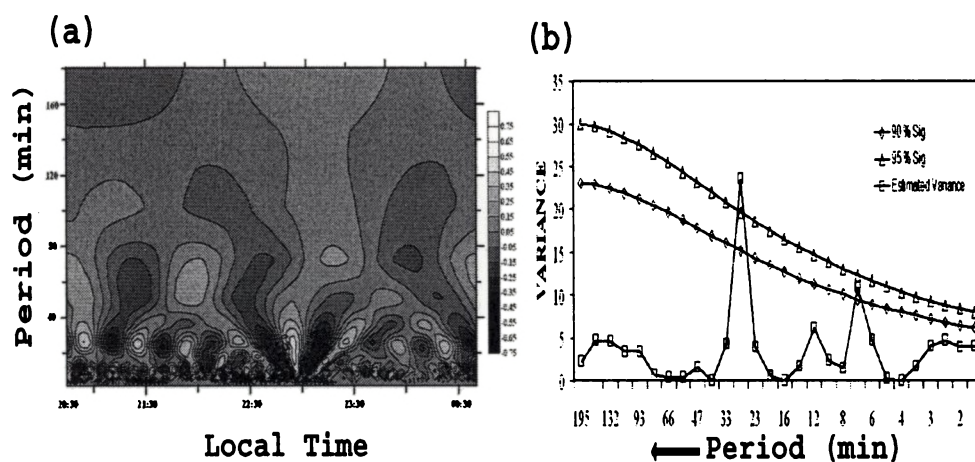


Figure 6.13: (a) Wavelet analysis of the vertical velocity in the lower stratosphere. Local time in ordinate and periods in abscissa. (b) Significance test carried out for the wavelet spectrum

min mode is 95% significant and is present during the entire observation period. The 11-15 min and 7-8 min modes are prominent in the spectral analysis, whereas 24-30 min mode is significant in wavelet analysis. Wavelet analysis clearly shows that, 11-15 min and 7-8 min modes present during the active periods of convection. Though a peak is observed at 11-15 min, which is less significant compared to other two modes. As discussed earlier the spectral analysis overlooked at these higher frequency of short duration. Obviously, the 24-

30 min wave exists during the entire observation period. The occurrence of high frequency modes advocates the evidence of penetrative convection or oscillating updraft downdraft couplets in the UT/LS region as possible source of gravity waves.

6.3.4 Cloud resolving scale simulation

The reflectivity calculated from the model derived hydrometeor fields such as cloud and rain water is presented in figure 6.14 (a). The composite reflectivity at 17:00:00 UTC shows the supercell characteristics of the structure. The reflectivity field shows hook echo characteristics. The vertical section of the reflectivity filed presented in figure 6.14 (b) do shows the Bounded Weak Echo Region (BWER) with overhanging precipitation structure at the forward flank of the storm.

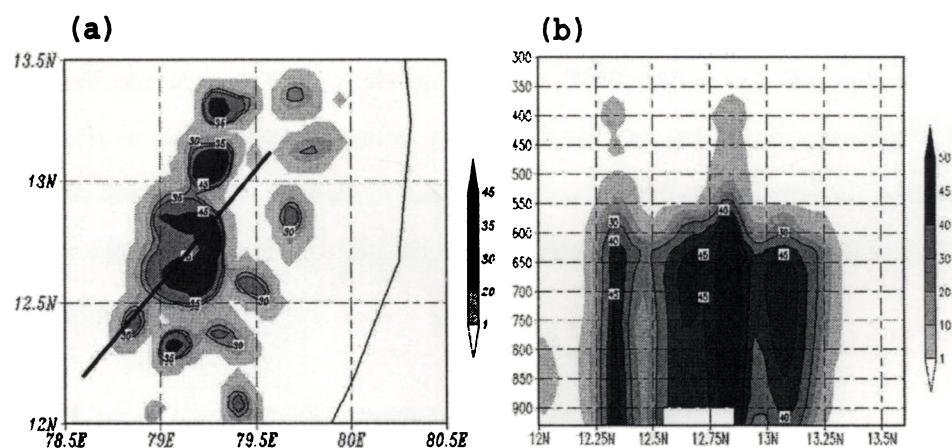


Figure 6.14: (a) Simulated composite reflectivity in dBZ and (b) Latitudinal cross-section of simulated radar reflectivity averaged along 1° longitude strip centered at 79°E valid at 17:00 UTC of 17 October, 2002

6.3.5 Penetrative convection

Time-space cross section analysis is used to study the height variation of the vertical wind fluctuations at selected heights viz., 3, 6, 10, 13 and 16 km at 15 min intervals. Figure 6.15 (a)-(e) shows the time-space evolution of vertical velocity along the latitude section at 3, 6, 10, 13 and 16 km, respectively. Between 15:00:00 and 16:00:00 UTC of the simulation experiment, three upward motion bands present in the model domain at 3 km. During the period, two downward bands are embedded within these updrafts. The upward motion bands are separated by less than 5 km, which suggests that the multicell structures of the upward motion bands are the part of a supercell storm. The co-existence of the updrafts and downdrafts signals the rotating updrafts or mesocyclone behavior of the convective cells associated with a supercell storm. Identical vertical velocity structure is seen upto 16 km. After 16:30:00 UTC, the storm begins to dissipate as downdrafts dominate in the lower levels and weak updrafts in the upper levels. The maximum updraft speed of 16-18 ms^{-1} is seen in the middle troposphere at about 10 km, this is in good agreement with the VHF radar observations of the same storm. The presence of updrafts and downdrafts just below the tropopause at 16 km suggests the oscillatory nature of the vertical velocity and penetrative convection.

6.3.6 Cloud liquid water and system evolution

Figure 6.16 (a)-(h) shows the latitude-height section of the cloud liquid water, vertical velocity and potential temperature at one hour intervals. At 15:00:00 UTC, on 17 October 2002, the main convection band is south of the radar-site. Three convection cells marked as A, B1 and B2 exist south of the radar site. During the time, upward motion exists in the lower troposphere. The tri-cellular structure persists till 16:00:00 UTC. Maximum vertical velocities of values greater than 4 ms^{-1} is associated with CLW. After 16:30:00 UTC, the northern cells are merged together to form a large cell marked as B. The two cell

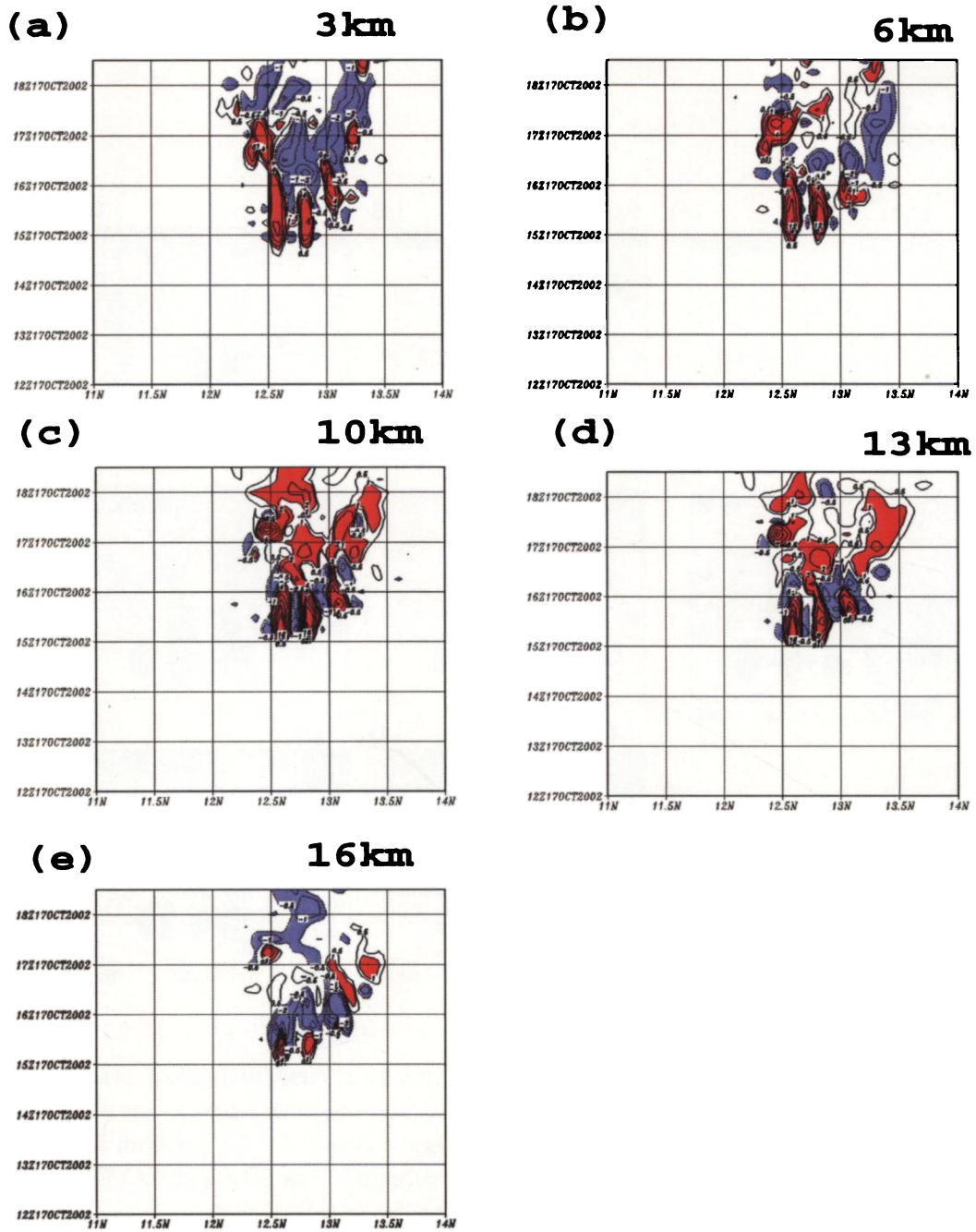


Figure 6.15: Time-space evolution of vertical velocity in ms^{-1} at (a) 3 km, (b) 6 km, (c) 10 km, (d) 13 km and (e) 16 km levels. Red shades represent upward and blue shades represent downward motion

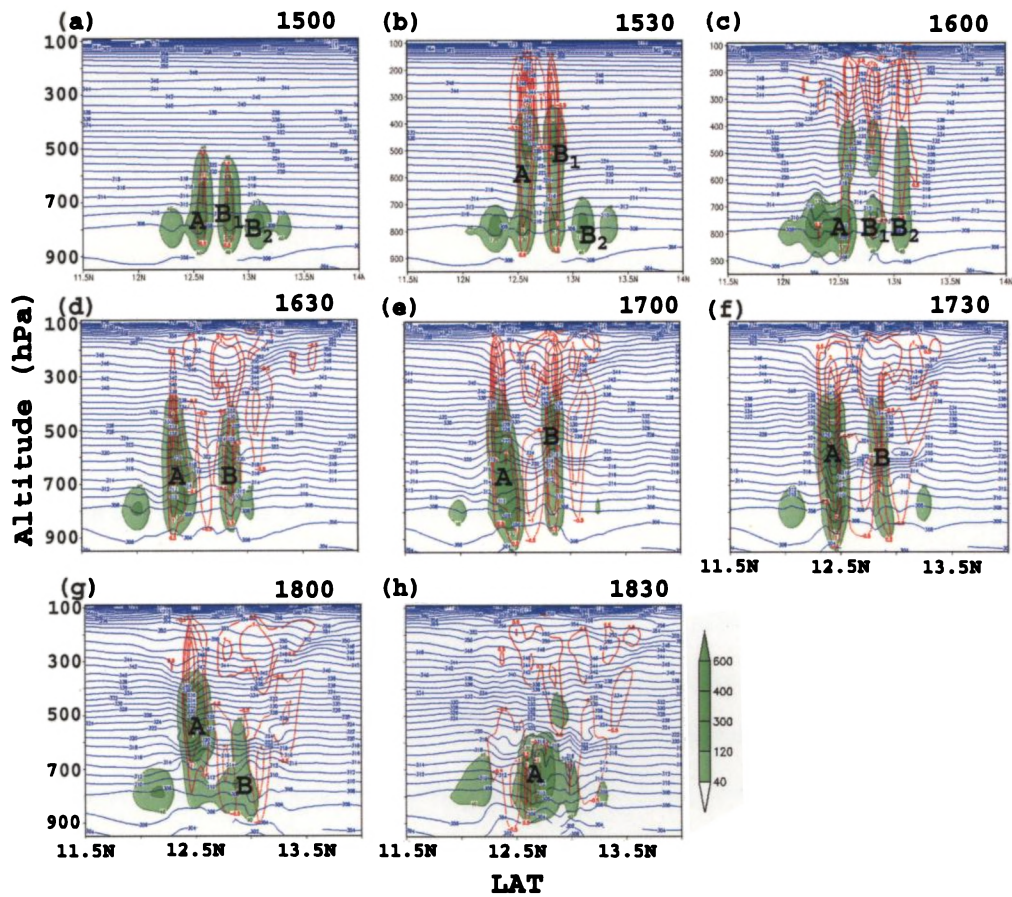


Figure 6.16: Latitudinal section of potential temperature in $^{\circ}\text{K}$ (blue contours), Vertical Velocity in ms^{-1} (red solid contours represents upward and dashed contours represents downward motion), Cloud Liquid Water in gkg^{-1} (green shades) during 15:00 to 18:30 UTC on 17 October 2002 at 30 min intervals

structure and organized vertical velocity keep going on till 17:30:00 UTC. Obviously figure 6.16 (e) supports penetrative convection and oscillatory updraft-downdraft structure near the tropopause at 17:00:00 UTC on 17 October 2002. The northern cells B1 and B2 with considerable cloud liquid water content during 16:00:00-17:00:00 UTC merged to form a large cell at 18:00:00 UTC. During the initial phase at 15:00:00 UTC, wave-like structure in the potential temperature field is trivial. As time progresses, adequate condensation in terms of cloud liquid water grounds vertical velocity disturbance and the wavelike feature in potential temperature field is also noteworthy. Wave-like structure is quite prominent during 16:00:00-19:00:00 UTC with maximum amplitude of perturbation during the mature phase of the storm at 18:00:00 UTC.

6.3.7 Condensational heat and propagation characteristics

The response of gravity waves to the condensational heat and associated wind disturbance is presented in this section. Figure 6.17 (a)-(e) shows the cross-section of condensational heat, vertical velocity and potential temperature along the SW-NE (along the line AB in figure 6.17 (a)) direction. Above 0°C isotherms level (near the melting layer), latent heat is produced by freezing and below it latent heat due to condensation has been considered. The yellow shade represents the condensational heat. Upward motion of magnitude greater than 3 ms⁻¹ is plotted as solid red contours and downward motion with magnitude less than 1.5 ms⁻¹ is plotted as dashed blue contours. During the developing phase, at 15:00:00 UTC, the condensational heat is mainly confined in the lower troposphere and latent heat due to condensation is considered as major source. The three cell structure of the supercell storm during the initial or cumulus stages (discussed in the previous sections) also emerge in the condensational heat. During 16:00:00-17:00:00 UTC, the condensational heat mainly distributed in the middle troposphere and suggest that both condensation and freezing significantly contributing to the condensational heat. Obviously, the cloud merging process

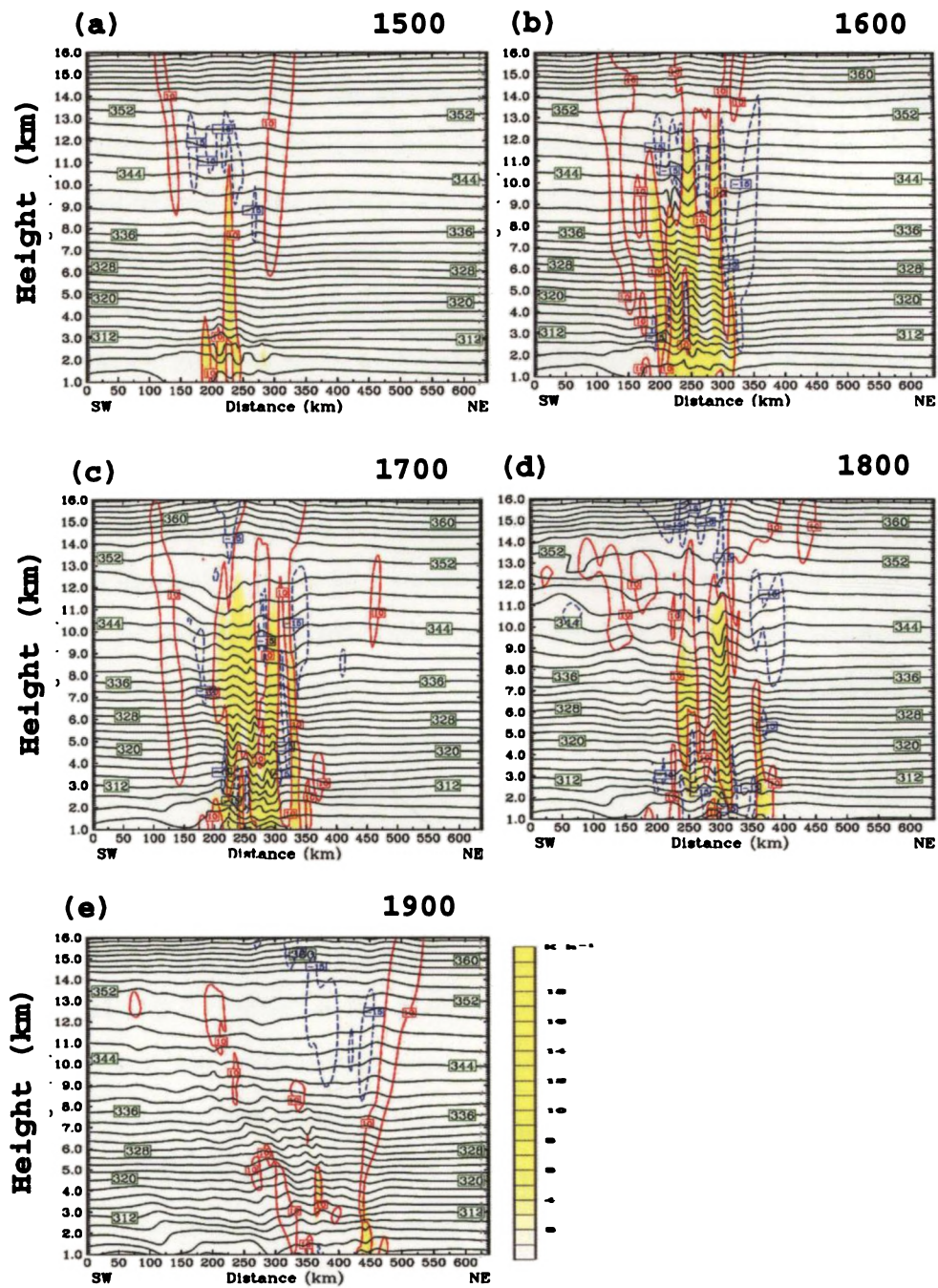


Figure 6.17: (a-e) Cross section of potential temperature in $^{\circ}\text{K}$ (green contours) along line AB (in figure 6.14 a), Condensational Heat in Khr^{-1} (yellow shades), upward velocity greater than 3 ms^{-1} (red solid contour) and downward velocity less than 1.5 ms^{-1} (red dashed contour)

during the mature phase of the storm is also noticeable in the condensational heat field.

During the developing and mature stages, the wave-like structure in the potential temperature field (green contours) is confined in the lower troposphere (see fig 6.17 (a)). This suggests that thermal forcing due to latent heat release as the possible source mechanism for the generation of gravity waves during this period (Abhilash *et al.*, 2006a). Observations of Larsen *et al.* (1982) and Sato (1993) supports the connection between long vertical wavelengths and deep convective heating. During 16:00:00-18:00:00 UTC, wave structure is produced throughout the troposphere. During this period, both updraft-downdraft couplets of relatively same magnitude in the middle and upper troposphere may be considered as the source of gravity waves. Both condensational heat and vertical wind disturbances reaching as high as tropopause level contributes to the gravity wave forcing. Uccellini and Koch (1987) well documented multiple wave genesis and maintenance mechanism as large-amplitude mesoscale gravity wave event. The oscillatory nature of the updraft-downdrafts near the tropopause level might have contributed to the wave forcing and maintenance during the dissipating stage between 18:00:00 and 19:00:00 UTC of 17 October, 2002 (Abhilash *et al.*, 2006a,b).

Figure 6.18 shows the vertical profiles of the condensational heat over the radar site during the three stages of the system life cycle. During the initial or cumulus stage, condensational heat is confined in the lower troposphere and which is associated with the release of latent heat due to condensation. The condensational heat peaks near 2 km. Maximum condensational heat is found during the mature phase of the storm. During this phase, condensational heat is distributed over a depth of 6 km between 3 and 9 km with a peak near 5km. In this period, both latent heat release of condensation and freezing significantly contributed to the condensational heat. During the dissipating stage, condensational heat is confined in the middle and upper troposphere between 6 and 13 km. In the dissipating phase, latent heat release due to freezing is important.

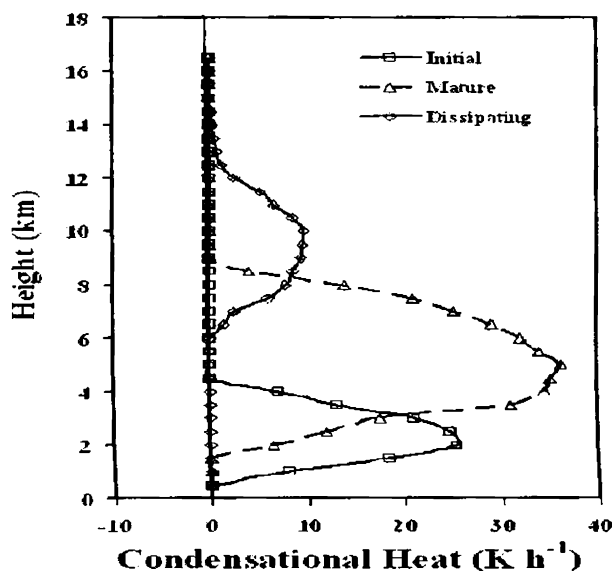


Figure 6.18: Vertical profiles of condensational heat in Khr^{-1} during the initial, mature and dissipating stages of the TMCS

6.3.8 Spectral characteristics of the simulated wave event

To characterize the spectral properties of the waves produced in the simulation, spectral analysis has been carried out on the vertical velocity field. Frequency spectra are computed at each spatial position for a period of 4 hours of the simulation time with 5 min intervals, thereby resolving waves with period between 10 min and 4 h. The spectra then averaged in zonal and in vertical (above 10 km). The averaging reduces the uncertainty in the resulting spectral estimates (*Alexander and Pfister, 1995*). The averaged power spectral density versus intrinsic frequency, ω is shown in figure 6.19 (a). A line proportional to $\omega^{-5/3}$ is plotted in the same coordinate for reference. This spectrum of vertical velocity shows dominance of high frequency waves with periods between 15 min to 1 h. The power drops at periods less than 10 min.

Horizontal wavenumber spectra are computed at each altitude and each time over 560 km in zonal direction, resolving the horizontal wavelength between 10 and 560 km. Figure

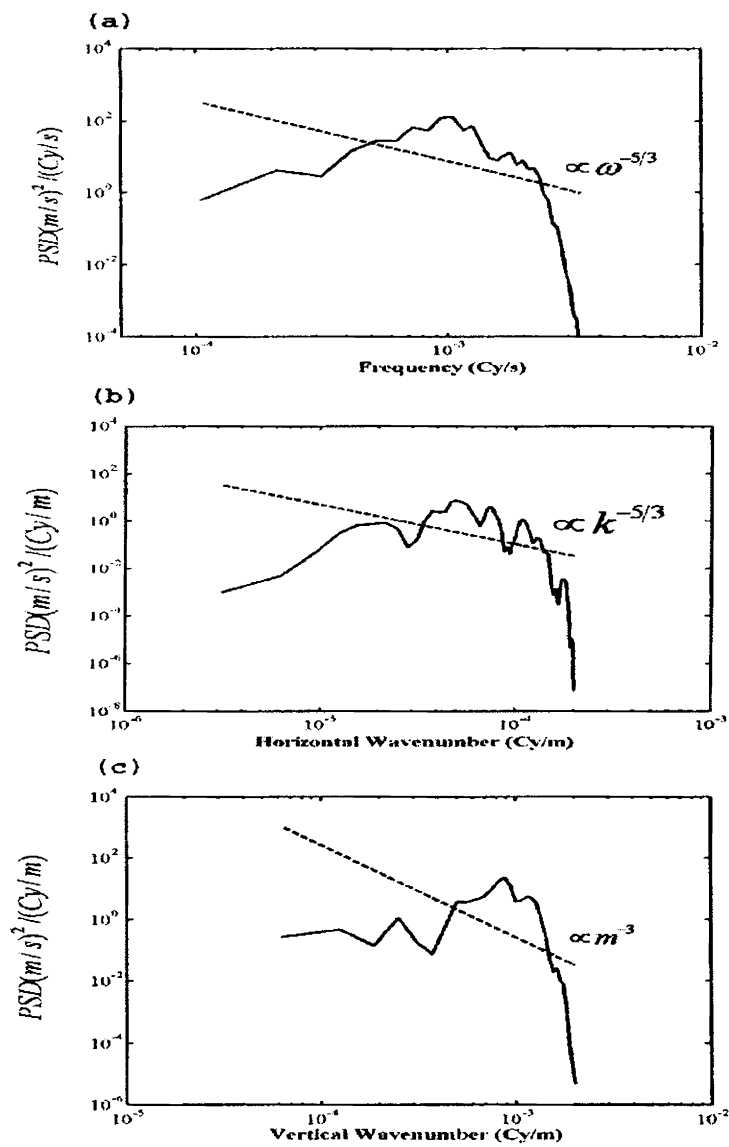


Figure 6.19: Power spectrum of vertical wind field as a function of (a) Frequency (b) Horizontal wavenumber and (c) Vertical wavenumber

6.19 (b) shows the zonally averaged power spectra of vertical velocity as a function of horizontal wavenumber, k . The spectrum shows a dominance of waves with horizontal scales between 10 and 60 km. A line proportional to $k^{-5/3}$ is plotted for reference. Similar studies from aircraft measurements by *Jasperson et al.* (1990) also follow the $k^{-5/3}$ power law over a range of wavelength from 3 to 200 km. Two dimensional modeling studies of *Alexander and Pfister* (1995) reported the dominance of ~ 10 to 100 km waves in their squall line simulation. Likewise spectrum discussed here also display an absence of power at longer ($> 80km$) and shorter ($< 9km$) wavelength end of the spectrum.

The vertical wavenumber spectra are computed at each time, t and each horizontal grid point over the 1-20 km altitude, thus resolving vertical wavelengths of 2.0 and 19 km. The PSD of the vertical wind in the troposphere as a function of vertical wavenumber, m is shown in figure 6.19 (c). The spectrum shows dominant scale of 1-4 km, with power falling off steeply at larger wavenumber. The another peak is observed between 8-9 km. Observational studies by *Dhaka et al.* (2002) reported that waves with shorter vertical wavelength are possibly forced by oscillating updrafts below the tropopause. Similar simulation studies by *Alexander and Pfister* (1995) suggested that the dominance of long vertical wavelengths is excited by thermal forcing due to the release of latent heat. The longer vertical wavelengths are not well resolved in this simulations, because of the limited depth of the model vertical levels. The spectral peaks at longer and shorter vertical wavelength region proposed that both penetrating updrafts/oscillating updrafts impinging on the tropopause and thermal forcing mechanisms are responsible for the generation and maintenance of the gravity waves.

6.4 Summary

The high resolution (both time and height) VHF radar observations have been used in the present study to examine several features of small scale wind disturbances associated with a supercell storm. An attempt has been made to investigate the response of tropical convection on the generation of gravity waves. The data is inadequate to describe all the relation between these internal waves and convection. Several observable characteristics of the convectively generated waves have been outlined. Observations of the vertical velocity by VHF wind-profiling Doppler radar reveals the signatures of gravity waves associated with convection and that closely resembles convection waves reported from the earlier observational and modeling results. The results from the present study are subjected to the limitation of the temperature and humidity observations to calculate the convective heating and moistening. Cloud resolving scale simulations of the observed wave event has been carried out and the role of thermal forcing due the release of latent heat associated with condensation and oscillating updrafts have been discussed.

CHAPTER 7

Impact of DWR Observations in the Simulation of TMCS

7.1 Background and Motivation

The prediction of timing, location, organization and structure of the TMCS especially over tropics is recognized as one of the biggest challenges in mesoscale modeling. Obtaining an accurate initial state is important in the accurate model prediction of these TMCS. Doppler radar observation is an important data source for mesoscale and microscale weather analysis and forecasting. Radar data assimilation could be promising for short range numerical weather prediction. Despite the importance of the DWR data for use in warning the heavy rainfall associated with the convective systems, there remains no effort to include analyzed Doppler radar data in the assimilation cycle of the operational weather prediction models in India (*Das et al.*, 2006). The present chapter reports the results from the first attempt in utilizing India Meteorological Department (IMD) Doppler radar data into a numerical

model for prediction of mesoscale convective complexes (*Das et al.*, 2006; *Abhilash et al.*, 2007a,b).

There are two major objectives of this chapter; one is to understand the impact of the radar wind data on the prediction of precipitation associated with TMCS and the other is to comprehend the detailed thermodynamic and microphysical structure of the convective system. Preliminary results from the radar reflectivity assimilation have also been included in this chapter.

7.2 Single Doppler Velocity Retrieval Method

Radial velocity measurements from single-site radar can be used to obtain wind profiles under the assumption of a linear wind model. In this method, the wind in the vicinity of the radar is expressed as;

$$U(x, y, z) = u_0 + x \frac{\partial u}{\partial x} + y \frac{\partial u}{\partial y} + (z - z_0) \frac{\partial u}{\partial z} \quad (7.1)$$

and likewise for $V(x, y, z)$ and $W(x, y, z)$. Using this linear wind field, the radial wind can be calculated as a function of range, azimuth and elevation. For a uniform wind field this results in:

$$V_r = V_h \cos \theta \cos(\phi - \phi_0) - V_f \sin \theta \quad (7.2)$$

where V_h and ϕ_0 are the horizontal wind speed and direction respectively, ϕ is the azimuth angle, θ is the antenna elevation angle and V_f is the fall velocity of the particle. The horizontal wind field retrieved by this method is also called Uniform Wind Technique (UWT). The wind field derived by UWT technique is valid at constant or small elevation angle close to the radar site whether it is during precipitation or clear weather, but in uniform wind condition.

When Doppler radar data is displayed at constant range and elevation θ , the radial wind is a function of azimuth ϕ will have the form of sine wave. The wind speed and direction

can be determined from the amplitude and phase of the sine, respectively. This technique is called Velocity-Azimuth Display (VAD) and it was introduced by *Lhermitte and Atlas* (1961) and *Browning and Wexler* (1968).

Nowadays, Doppler radars are recording volume scans of reflectivity and radial wind data as a function of range, azimuth and elevation. Different VADs from volume scans as a function height, and a wind profile at the radar site can thus be obtained.

Instead of processing for each height, a single VAD or a series of VADs, one can also process all available volume data in a certain height layer at once. This method is known as Volume Velocity Processing (VVP) technique which has been introduced by *Waldteufel and Corbin* (1979). Using equation 7.2 of the linear wind model, the radial wind can be calculated for all points within a layer centered at height; z_0 via multi-dimensional and multi-parameter linear fit, the parameters of the linear wind can be extracted.

The algorithm developed by *Person and Anderson* (1987) has been used to retrieve horizontal wind fields from measured Doppler velocity. The radial velocity can be expressed as;

$$V_{r\phi} = u_{r\phi}\sin\phi + v_{r\phi}\cos\phi \quad (7.3)$$

where $u_{r\phi}$ and $v_{r\phi}$ are the U and V components of the horizontal wind vector at range (r) and azimuth ϕ . The U and V components of the horizontal wind are estimated using least square regression technique to minimize the function $\sum_{\phi}[u_{r\phi}\sin\phi + v_{r\phi}\cos\phi - V_{r\phi}]^2$ or each elevation range r . The regression is performed for each cell (any value from 4 to 100 km/cell) defined in the resolution of the grid. Details of this technique are available in *Rao et al.* (2004).

The verification of the VAD winds against radiosonde winds and wind from a NWP model is reported by *Anderson* (1998). In this study, the availability and accuracy of the VAD winds of Swedish radar have been investigated. The availability of VAD winds is about 80% at 925 hPa, and it drops to about 15% at 400 hPa. The vector difference be-

tween the VAD winds and the radiosonde winds has an average magnitude of about 2 ms^{-1} . Rao *et al.* (2004) have compared the horizontal wind fields obtained from the DWR with Rawinsonde and Pilot balloon observations and found good agreement between them. Further, they found that these wind fields compared well with synoptic and upper air observations in cyclonic situation of 12 Nov 2002 cyclonic storm over the Bay of Bengal. Das *et al.* (2006) also verified the retrieved wind fields with Pilot balloon observations and wind analysis from NCMRWF T80 model interpolated to a mesoscale domain. Figure 7.1(a) presents the wind field retrieved from DWR Kolkata at a height of 1.0 km at 00:00 UTC 5 May 2005 and, figure 7.1 (b) shows the wind analysis at 900 hPa obtained from the MM5 domain valid at the same time. The retrieved wind from DWR shows good agreement with the model wind analysis.

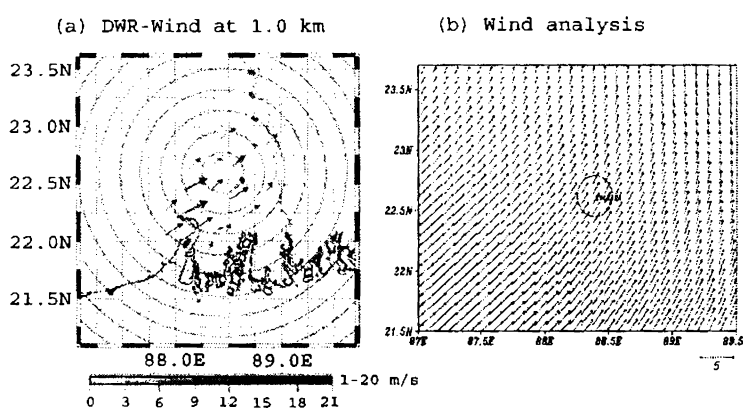


Figure 7.1: (a) Wind field retrieved from DWR at 1.0 km (b) Wind analysis at 900 hPa interpolated to MM5 domain at 00:00 UTC 5 May 2005

7.3 Assimilation of Doppler Radar Wind Data

Heavy rainfall occurs frequently over the Indian peninsula during pre monsoon, monsoon and post-monsoon season associated with TMCS. The radar reflectivity and rainfall obser-

Case	Location	Date
1	Kolkata	6 May 2005
2	Kolkata	22 May 2005
3	Kolkata	7 June 2005
4	Chennai	30 April 2005
5	Chennai	1 May 2005
6	Chennai	2 May 2005
7	Chennai	3 May 2005

Table 7.1: Cases selected for the assimilation experiment

vations are used to select the convection days. In order to investigate the detailed structure of convection and thunderstorms and utility of DWR observations in a mesoscale model, three cases around Kolkata and four cases around Chennai have been selected for the present study. The seven cases are listed in Table 7.1. Accumulated rainfall amount from the simulations are compared with TRMM observations. The results are examined further in two aspects; *viz.* (1) organization and propagation of precipitation bands associated with TMCS and (2) simulated structure of near surface radar reflectivity. For brevity detailed analysis for a single case has been presented in this chapter.

7.3.1 Synoptic overview

Mesoscale convective cloud clusters over Kolkata region during 06:00 UTC of 5 May and 18:00 UTC of 6 May 2005 are selected in the present study. The radar reflectivity and observed rainfall is used to select the convection days. The synoptic charts showed a north-south trough extending up to 0.9 km above sea level from northern states to south peninsular India. Maximum temperature was found to be above normal by 2-3°C at many places over the region. Thunderstorms were reported over Gangetic West Bengal and Sub-Himalayan West Bengal during 5-7 May 2005. Jalpaiguri, Cooch Behar and Malda reported 1 cm

rainfall each on 5 May. Kolkata (Alipore) reported 5 cm and Kolkata (Dum Dum) reported 2 cm on 6 May.

Figure 7.2 presents the IR satellite cloud images for 12:00 and 18:00 UTC on 5 and 6 May 2005. The pictures show scattered convective clouds at many places over the West

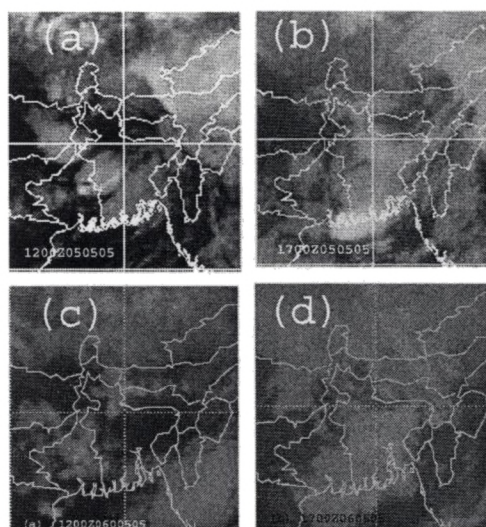


Figure 7.2: Satellite Infra Red images from Kalpana Satellite at (a) 12:00 and (b) 17:00 UTC 5 May, (c) 12:00 and (d) 17:00 UTC 6 May 2005

Bengal and neighborhood during the period. Figure 7.3 shows the radar reflectivity MAX (Z) at 11:48 UTC and 16:48 UTC of 05 May and 11:08 and 14:08 UTC of 06 May 2005. The radar reflectivity pattern clearly shows occurrence of two major cloud bands during the period, which initially formed over northwest of Kolkata and propagated southeastwards.

7.3.2 Experiment design

Figure 7.4 shows the domain configuration for the MM5 experiments. Two-way nesting is employed with a horizontal resolution of 30 km for the coarse outer grid (4.6-38.7°N, 65.3-99.0°E) and 10 km for the inner fine grid (19.5-25.2°N, 85.2-93.5°E). The location of the Kolkata radar site is marked as circle and its maximum range is 250 km. The model

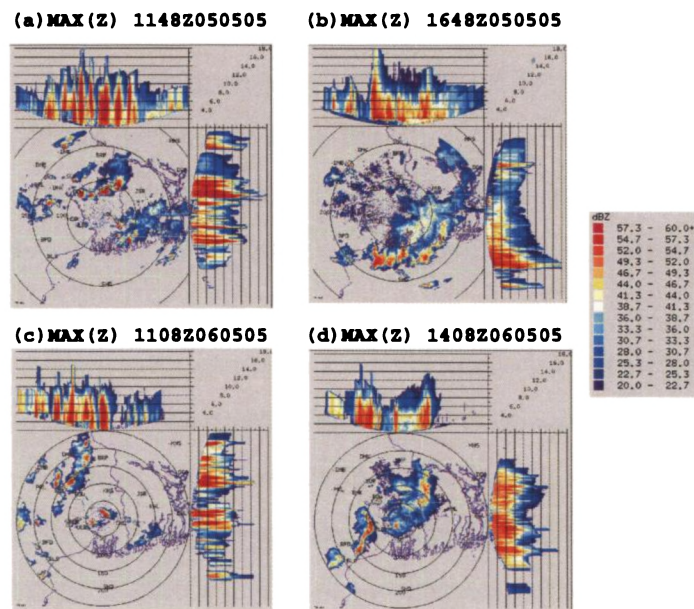


Figure 7.3: Reflectivity MAX (Z) in dBZ at (a) 11:48 UTC (b) 16:48 UTC 05 May 2005 and (c) 11:08 UTC (d) 14:08 UTC 06 May 2005

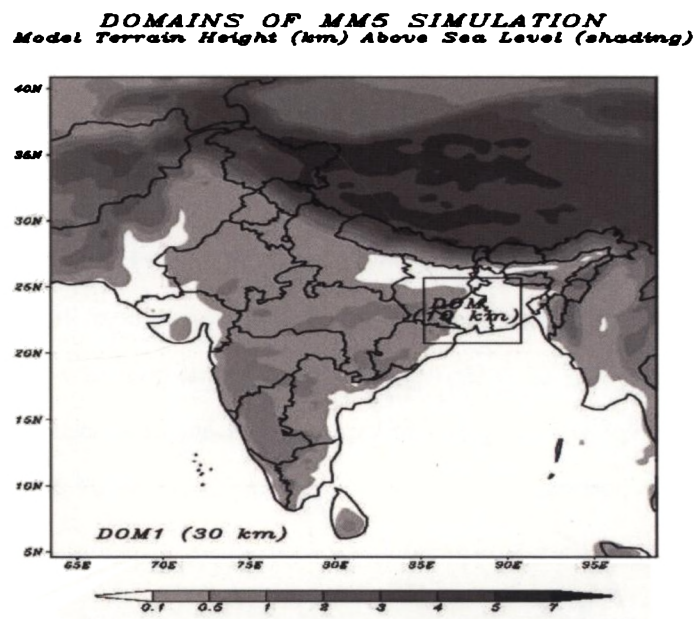


Figure 7.4: Domain configuration for MM5-3DVAR experiments

physics include Grell scheme for Cumulus parameterization (Grell *et al.*, 1994), boundary layer parameterization of Hong and Pan (1996) as used in the Medium Range Forecast (MRF) model, explicit treatment of cloud water, rain water, snow, ice and graupel based on GSFC (NASA/Goddard Space Flight Center) microphysical scheme (Tao *et al.*, 1987a; Tao and Simpson, 1984b). Cloud radiation interaction is allowed between explicit cloud and clear air.

To assess the impact of assimilating the DWR wind data into MM5 3DVAR system on the prediction of mesoscale convective events, three experiments were carried out. The initial and lateral boundary conditions obtained from the global analysis of National Center for Medium Range Weather Forecasting (NCOMRWF) global model (T80-resolution) are used to initialize the first (CTRL/GSFC) experiment. The offline experiments have been carried out using 3DVAR data assimilation system of MM5. In the second experiment (3DVAR/NoDWR), Global data received through Global Telecommunication System (GTS)/ Internet is ingested in the system at the analysis time with ± 3 -hr time window. In the 6-hr assimilation cycle, cold-start is at 06:00 UTC of 4th May 2005 so that four cycles are used to initialize the model. Modules have been developed for reading the decoded observed data from NCOMRWFs operational data sets and for packing in *LITTLE_R* format, required for ingesting in 3DVAR observation preprocessor. In this six-hour 3DVAR update cycle, the 6-hour forecast from the previous cycle serves as the background for the next cycle. The third experiment (3DVAR/DWR) is same as the second experiment, except that the horizontal wind derived from the DWR is used along with other conventional and non-conventional data in the assimilation system. Summary of the experiments are presented in Table 7.2. Figure 7.5 shows the overview of the experiment design for radar data assimilation.

Experiment	Initialization and assimilation
CTRL-GSFC	Using global analysis of NCEP/FNL without data assimilation
3DVAR-NoDWR	3DVAR 6-hr assimilation cycle using GTS and Satellite data
3DVAR-DWR	3DVAR 6-hr assimilation cycle using GTS and DWR data

Table 7.2: Summary of experiments

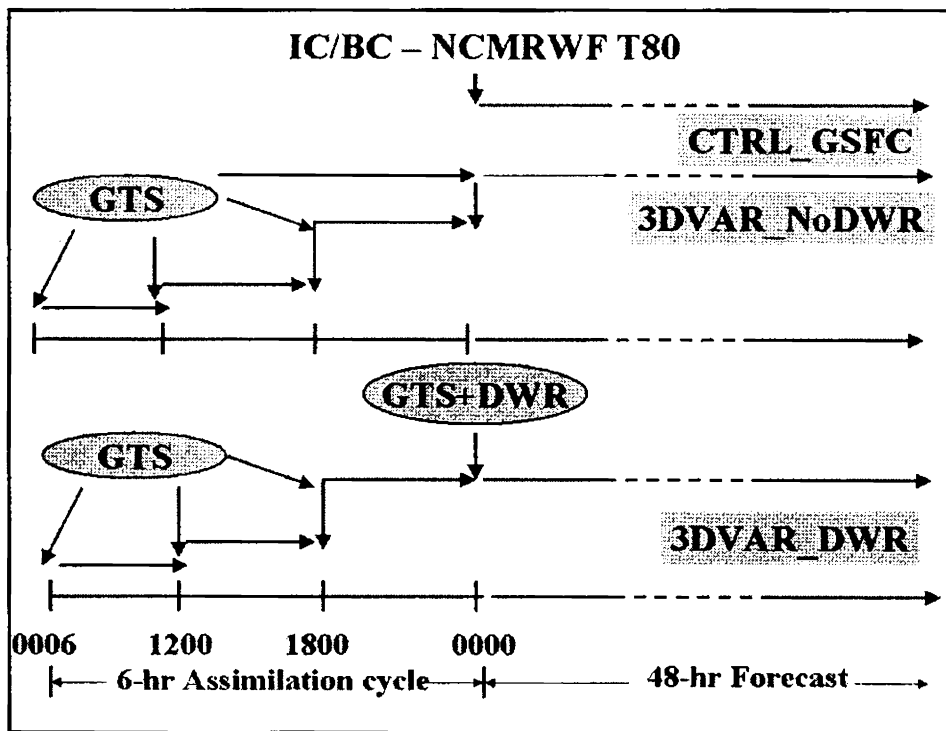


Figure 7.5: Experiment design for radar data assimilation

7.3.3 Vorticity

In this section, the wind field such as convergence in terms of vorticity has been analyzed to examine the improvements in the initial condition on assimilating both the conventional and DWR wind observations. Figure 7.6 (a), (b) and (c) shows the vorticity fields at 00:00 UTC 5 May 2005 (initial condition for the first case) for the experiments, CTRL-GSFC, 3DVAR-NoDWR and 3DVAR-DWR respectively. The vorticity for the CTRL-GSFC ex-

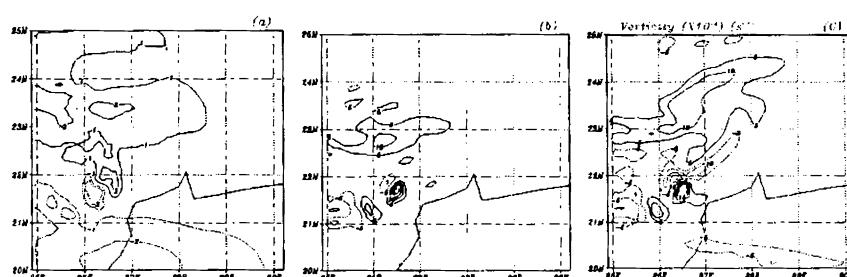


Figure 7.6: Vorticity at 00:00 UTC of 5 May 2005 for the (a) CTRL-GSFC , (b) 3DVAR-NoDWR and (c) 3DVAR-DWR experiments

periment is as low as $2 \times 10^{-5} s^{-1}$ over the southwest sector of the domain. After assimilating the conventional data, the initial vorticity fields has been improved well in the second experiment (3DVAR-NoDWR) and shows a maximum value of $10 \times 10^{-5} s^{-1}$. After incorporating the DWR wind filed to assimilation system (3DVAR-DWR), the vorticity field has increased to a maximum value of $15 \times 10^{-5} s^{-1}$. This analysis signifies the impact of the DWR wind observations in creating localized convergence in the initial condition, which in turn causes development of convective clouds during the early hours of the forecast period. For brevity the vorticity analysis has been carried out only for the first case.

7.3.4 Simulated rainfall

The main purpose of assimilating the high resolution DWR wind data is to improve the heavy rain forecast associated with quasi-stationary MCS. Figure 7.7 shows the 6-hr ac-

cumulated rainfall from merged satellite product of TRMM. Two rainbands were observed around Kolkata, one over the north and the other over the southeast of Kolkata during 06:00-18:00 UTC on 5 May. The major rain bands, initially originated from northwest propagate southeastwards during 06:00 UTC of 5 May and 00:00 UTC of 6 May, which is a typical characteristic of Nor'westers. A small patch of rainband is also observed over northwest Kolkata at 12:00 UTC on 6 May, which moved southward and centered around south and southeast of Kolkata at 18:00 UTC on 6 May. Though the intensity of precipitation is less, this precipitation band also shows a southeastward movement.

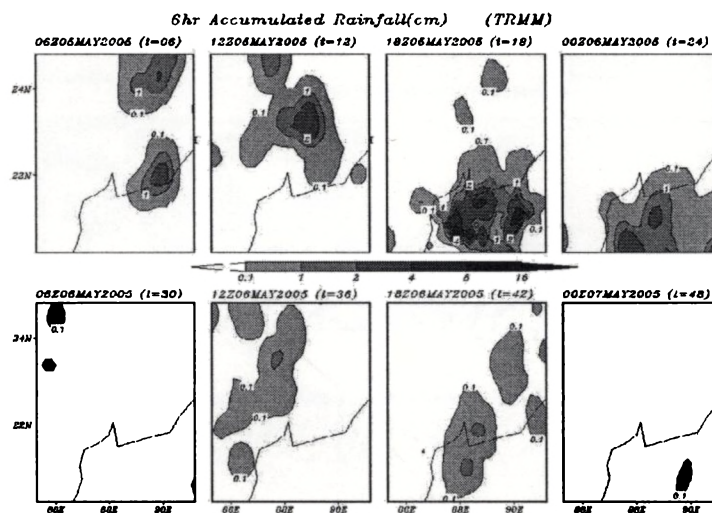


Figure 7.7: Six hourly accumulated precipitation (cm) from TRMM during 05-06 May 2005

Figure 7.8, 7.9, 7.10 presents simulated rainfall by the three experiments, namely CTRL-GSFC, 3DVAR-NoDWR and 3DVAR-DWR respectively. The CTRL-GSFC simulation shows 6-8 cm of widespread rainfall between 06:00-18:00 UTC of 6 May and 3DVAR-NoDWR predicts the similar association of rain bands with intensity slightly reduced compared to CTRL-GSFC experiment, but the TRMM does not show much rainfall at these times. The rainfall observed by TRMM may be underestimated as it depends on

the pass of the satellite and the raingauge observations included in its analysis (*Das et al.*, 2006). The observed rainfall amount from TRMM is more during 06:00-18:00 UTC of 5 May. Both the experiments show southeastward propagation of the precipitation bands as observed by TRMM. However, the Kalpana satellite cloud images (see fig. 7.2) and radar reflectivity (see fig. 7.3) does show clouds between 12:00-18:00 UTC of 6 May.

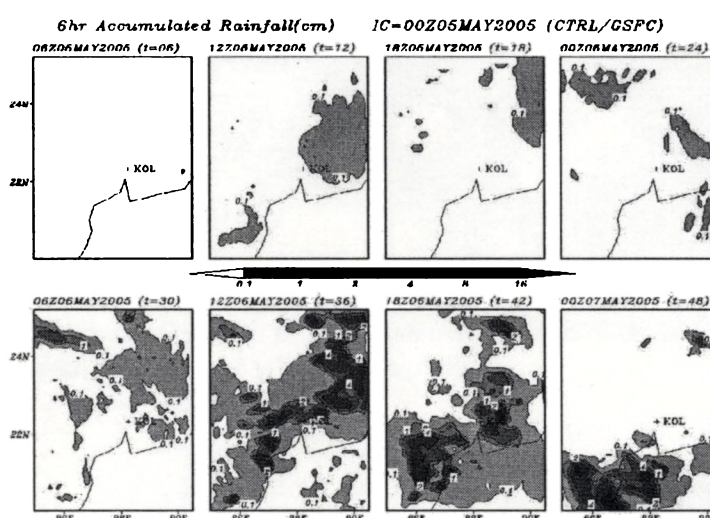


Figure 7.8: Six hourly accumulated precipitation (cm) from CTRL-GSFC experiment based on initial condition of 00:00 UTC, 05 May 2005

The simulated rainfall from 3DVAR-DWR indicates that assimilation of DWR data has produced rainfall during 12:00-18:00 UTC of both 5 and 6 May, south of Kolkata as seen from TRMM observations and satellite images. The CTRL-GSFC experiment overestimates the rainfall. While, overall rainfall from 3DVAR-NoDWR is reduced as compared to the control simulation and further reduced in the 3DVAR-DWR experiment, making it closer to observations. The aerial extent of the precipitation band is also reduced in the 3DVAR-DWR experiment. Both the CTRL-GSFC and 3DVAR-NoDWR experiment predicted widespread rainfall over the entire domain and is overestimated on 6 May 2005. An important result from the 3DVAR-DWR experiment is the prediction of the rain bands on

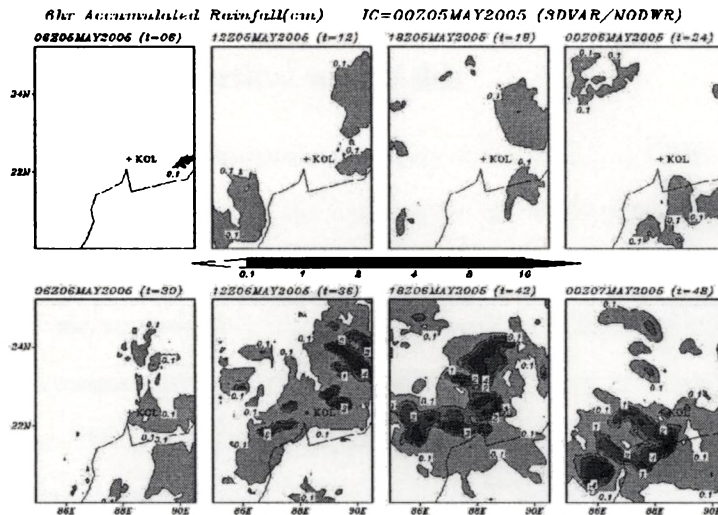


Figure 7.9: Six hourly accumulated precipitation (cm) from 3DVAR-NoDWR experiment based on initial condition of 00:00 UTC, 05 May 2005

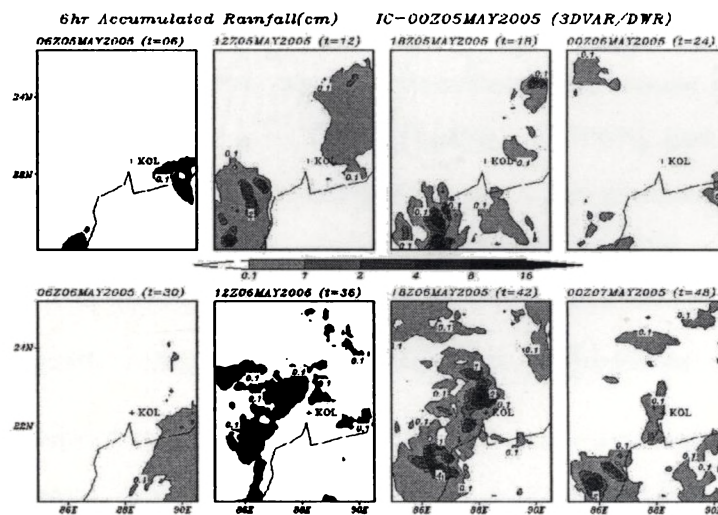


Figure 7.10: Six hourly accumulated precipitation (cm) from 3DVAR-DWR experiment based on initial condition of 00:00 UTC, 05 May 2005

both the days and the generation of new rain band northeast of Kolkata on 5 May 2005.

7.3.5 Horizontal and vertical wind fields

In this section we examine the horizontal and vertical wind fields at 18:00 UTC on 6 May 2005. Figure 7.11 (a) and (b) shows the horizontal wind vectors and vertical velocity of the three experiments at 850 and 700 hPa respectively. Southwesterly winds are present south of Kolkata and northwesterly winds are seen north of Kolkata at 850 hPa. Both the assimilation experiments produced strong winds at 850 hPa as compared to the CTRL-GSFC experiment. The maximum vertical velocity is also found near the region where the horizontal wind convergence occurs. The 3DVAR-DWR experiment predicts two positive vertical velocity cores (solid circles) and a negative core (dashed circle) in between at 850 hPa, while scattered positive regions are simulated by other two experiments. The 700 hPa horizontal wind is nearly westerly to northwesterly. The horizontal wind speed at 700 hPa is reduced in the assimilation experiments, while the CTRL-GSFC predicted strong winds at this level. At 700-hPa level, 3DVAR-DWR experiment simulated three positive cores (solid circle) of vertical velocity whereas other two experiments show similar vertical velocity structure as at 850 hPa. The three upward motion bands are 50-100 km apart. The maximum vertical velocity of each band reaches more than 50 cm s^{-1} . This analysis also confirms the evidence of elevated convection and is well simulated by 3DVAR-DWR experiment.

7.3.6 Composite reflectivity and integrated liquid water

Figure 7.12 (a) shows the simulated composite radar reflectivity (shading) and surface pressure (dotted contours) of the three experiments valid at 18:00 UTC on 6 May 2005. The model-derived echoes from the CTRL-GSFC experiment are distributed over a large area with maximum reflectivity of more than 50 dBZ over Kolkata region, while that from the 3DVAR-NoDWR experiment shows two individual maxima in radar reflectivity over and

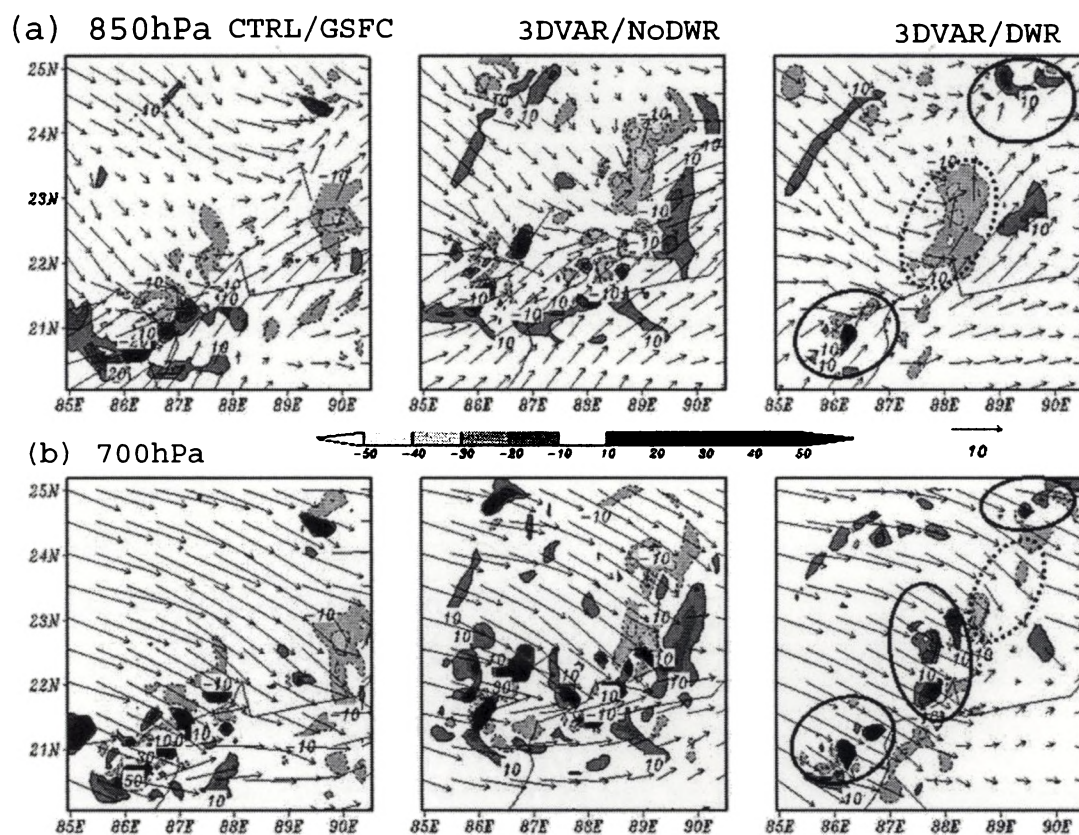


Figure 7.11: Horizontal velocity vector and vertical velocity in cms^{-1} (shading) at (a) 850 hPa and (b) 700 hPa valid for 18:00 UTC 06 May 2005

west of Kolkata. The 3DVAR-DWR experiment simulates radar echoes extending from the southwest to north east of Kolkata with three distinct maxima of reflectivities (> 50 dBZ) one over Kolkata, the second one over southwest and third over northeast of Kolkata. The radar reflectivity predicted by the 3DVAR-DWR experiment is almost close to observed low-level (elevation angle of 0.5 degree) radar reflectivity from the DWR (see fig. 7.3). The main result from this analysis is that the intensity, location and organization of MCS are better simulated by the 3DVAR-DWR experiment. Though the simulated reflectivity does not match exactly with observations in terms of location, their magnitudes are of same order and range from 10-50 dBZ. The integrated cloud water represents the vertically integrated cloud water given as the depth of the water substance over the area of the grid cell in millimeters (mm) contained within the entire MM5 grid column from surface to the model top. Figure 7.12 (b) shows the vertically integrated liquid water (shading) and potential temperature (dotted contours). All the three experiments simulated the vertically integrated liquid water (VIL) reasonably well during 12:00-18:00 UTC of 6 May 2005. However, the 3DVAR-DWR experiment produced better VIL at 12:00 UTC on 5 May 2005 corresponding to the rainfall observed by TRMM and radar reflectivity.

7.3.7 Hydrometeor fields

The physics options of the simulation experiments are able to predict the hydrometeor species like mixing ratios of cloud liquid water, rainwater, ice, snow and graupel. Figure 7.13 shows the latitude-height section of the sum of these five species, called total cloud hydrometeor (TCH) averaged over 87-89°E and centered around 88°E valid at 18:00 UTC of 6 May 2005 for the three experiments. The TCH simulated by 3DVAR-DWR experiment clearly shows evidence of three individual convective cloud bands and such profiles are not available from DWR for comparison. An interesting feature observed in Figure. 7.13 is that, the hydrometeor structure shows a strong precipitating convection over south

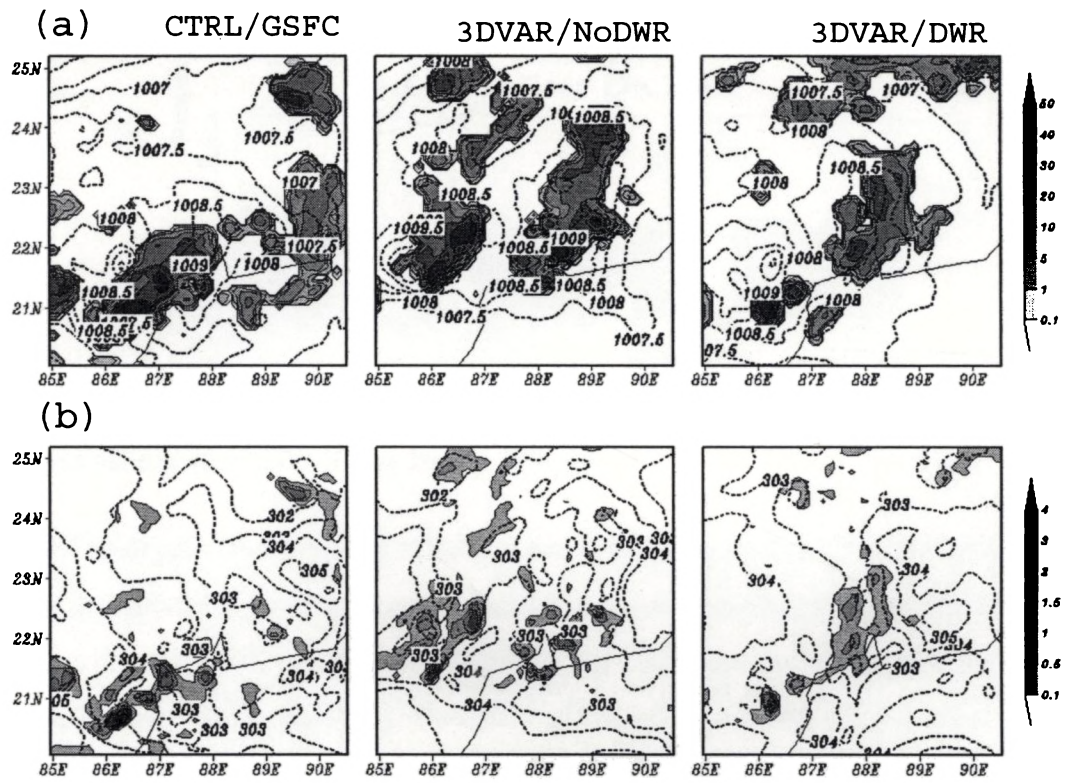


Figure 7.12: Simulated a) Composite reflectivity in dBZ (shading) and surface pressure (dotted contours at 3 hPa intervals) b) vertically integrated liquid water (VIL) in mm and potential temperature (dotted contours at 3°K intervals) from the three experiments valid at 18:00 UTC 06 May 2005 based on initial condition at 00:00UTC 05 May 2005

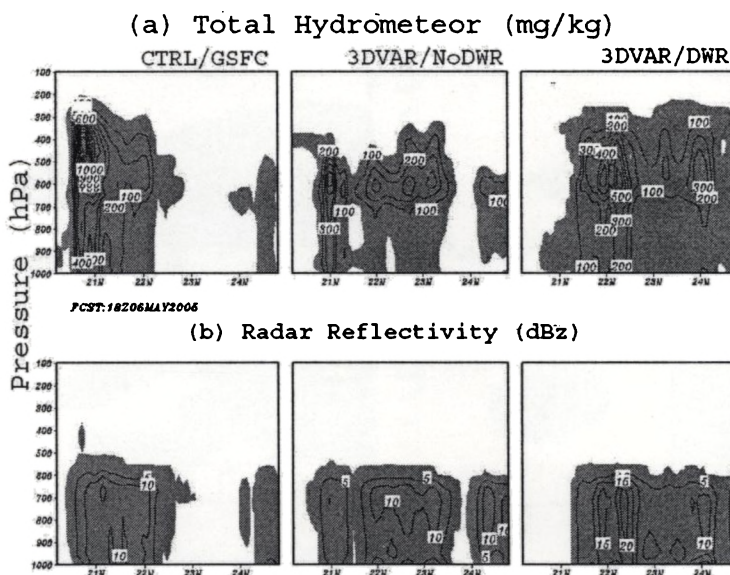


Figure 7.13: Latitudinal cross-section of (a) total cloud hydrometeor (mgkg^{-1}) and (b) radar reflectivity averaged along 2° longitude strip centered at 88.0°E for the three experiments valid at 18:00UTC 06May 2005

and a small patch over northeast of Kolkata and is well supported by TRMM observations. The 3DVAR-DWR experiment also simulated a non-precipitating patch over Kolkata and MAX (Z) from DWR showing the evidence of this central cell, but no precipitation bands were observed from TRMM over the area. The PPI (Z) from DWR does not show strong reflectivity at the surface during the period. This supports the occurrence of elevated convection. The major outcome of this analysis is that both precipitating and non-precipitating convection as well as elevated convection is better simulated by the 3DVAR-DWR experiment as compared to the CTRL-GSFC and 3DVAR-NoDWR. Latitude-height section of radar reflectivity derived from the model also shows similar structure (Figure 7.13 (b)). Time-height section of the cloud water mixing ratio and rainwater mixing ratio is shown in Figure 7.14. The upper, middle and lower panel shows simulated CLW and RNW from CTRL-GSFC, 3DVAR-NoDWR and 3DVAR-DWR experiments. The 3DVAR-DWR ex-

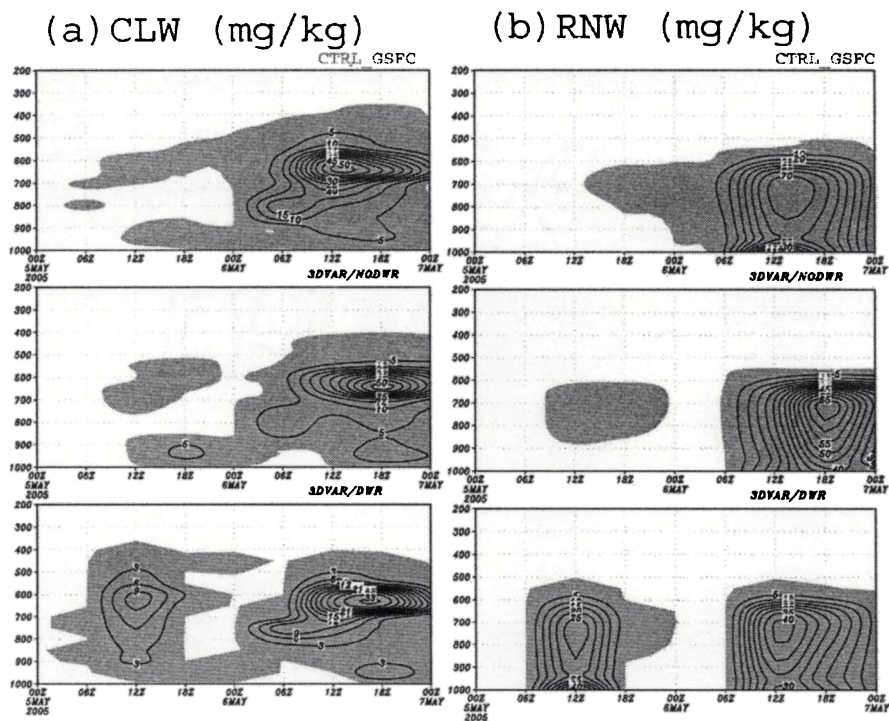


Figure 7.14: Time section of (a) cloud water mixing ratio (mgkg^{-1}) and (b) rain water mixing ratio (mgkg^{-1}) averaged over 2° latitude/longitude around Kolkata for the three experiments based on the initial condition at 00:00UTC 05 May 2005.

periment predicts the occurrence of clouds during 12:00-18:00UTC on both 5 and 6 May, while CTRL-GSFC and 3DVAR-NoDWR predicts the occurrence of convection only on 6 May 2005.

7.3.8 Forecast verification

The model forecast of precipitation has been verified by calculating the ensemble equitable threat scores for all seven cases considered for the present study. The ETS of precipitation forecast has been calculated using 6-hr accumulated precipitation from merged rainfall analysis from TRMM satellite. The figure 7.15 (a) and (b) presents the 6-hr rain-

fall verification of the ETS averaged for the seven cases with thresholds of 10 mm and 20 mm respectively. For 12 hours, the results indicate that the assimilation of Doppler radar

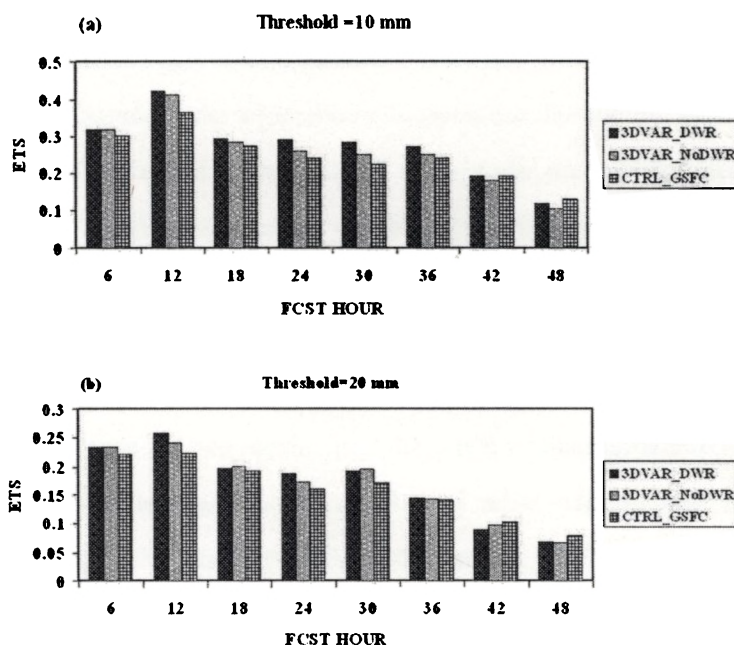


Figure 7.15: Equitable threat scores with a threshold of (a) 10 mm and (b) 20 mm for the three experiments

data has a positive impact on the short range rainfall forecast. Significant improvements in the precipitation forecast appeared in the first 12-hr forecast period. The ETS score decreases after 12-hr forecast and remains more or less constant till 36-hr and thereafter ETS decreases considerably. The 3DVAR experiments produce higher scores as compared to the CTRL-GSFC experiments. The difference between the two assimilation experiments 3DVAR-DWR and 3DVAR-NoDWR are statistically less significant for both the precipitation thresholds. It may be kept in mind that the DWR wind fields are available in only one of the four assimilation cycles.

This chapter presents the results of the first attempt in utilizing IMD Doppler radar data into a numerical model for the prediction of rainfall associated with mesoscale convective

systems. The main purpose of assimilating the DWR wind data is to improve wind field such as convergence in the initial condition for the prediction of intense convective events. The 3DVAR-NoDWR and 3DVAR-DWR experiment predicts the intensity and organization of rainbands convincingly well. The results from this study shows positive impact of the assimilation of Doppler radar wind observations on the short range QPF. However, ETS from the 3DVAR-DWR and 3DVAR-NoDWR experiments are less significant and reveals the need to directly assimilate the reflectivity data in the regional assimilation system.

7.4 Assimilation of Radar Reflectivity and Radial velocity

As an extension to the promising results from the DWR wind assimilation, we made an attempt to assimilate the Doppler radar reflectivity and radial velocity in the 3DVAR system of Weather Research and Forecast (WRF) model and the results are presented in the following section. The present WRF-3DVAR system has the capability to assimilate Doppler radial velocity (*Xiao et al.*, 2005) and reflectivity data (*Xiao and Sun*, 2006).

7.4.1 Brief description of the WRF modeling system

The development of the Weather Research and Forecasting (WRF) modeling system is a multi institutional effort intended to provide a next generation mesoscale and forecast model and data assimilation system that will advance both the understanding and prediction of mesoscale weather systems. The WRF Software Framework (WSF) provides the infrastructure that accommodates multiple dynamic solvers, physics packages that plug into the solvers through a standard physics interface, programs for initialization and the WRF variational data assimilation (WRF-Var) system. The Advanced Research WRF (ARW) and the Non-hydrostatic Mesoscale Model WRF (NMM) are the two main dynamic solvers of the WRF modeling system. While there are important differences regarding certain aspects of

each subset(for example, the vertical coordinate and time integration scheme), both share a similar frame work for their physics and software packages.

The preprocessor, WRFSI(WRF Standard Initialization) is used primarily for real-data simulations and which defines the simulation domains, interpolating terrestrial data (such as terrain, landuse and soil type) to the simulation domain and de gridding and interpolating meteorological data to the simulation domain and to model vertical co-ordinate. The WRF-Var program is optional but can be used to ingest observations into the interpolated analysis created by WRFSI. It can also be used to update WRF models initial conditions when WRF model is run in cyclic mode. The ARW Solver is the key component of the modeling system, which is composed of several initialization programs for idealized, and real-data simulations, and numerical integration program. It also includes a program to do one-way nesting. More details of the modeling system including the ARW solver, model physics, WRF-Var system and WRF software framework can be found from *Wang et al. (2004)*.

...

7.5 Overview of WRF-3DVAR system

The WRF-Var system has been adapted from MM5-3DVAR (*Barker et al., 2004*) and is encompassed within ARW. Like the MM5-3DVAR system discussed in chapter 5, the WRF-3DVAR system mainly consists of the following four components: (a) Background Pre-processing, (b) Observation Pre-processing and quality control, (c) Variational Analysis and (d) Updation of Boundary Conditions (*Barker et al., 2004*).

Analysis for a particular initial condition can be done either in cold start mode or in a cycling mode. In cold-starting mode, standard WRF preprocessing programs (GRIBPREP, HINTERP, and VINTERP) may be used to reformat and interpolate forecast fields from a variety of sources to the target WRF domain. In cycling mode, background processing is not required as the background filed is supplied by short-range forecast of WRF model

over the same domain.

The configuration of WRF/MM5 3DVAR system is based on the multivariate incremental formulation. The preconditioned control variables used in the present study are stream function, velocity potential, unbalanced pressure and total water mixing ratio. The background error statistics for the WRF domain can be carried out *via* NMC method (*Parish and Derber, 1992*). The major development of Doppler radar data assimilation in WRF-3DVAR system is the inclusion of the analyses (increments) for vertical velocity and cloud water and rain water mixing ratios (*Xiao et al., 2005*).

7.5.1 Vertical velocity increments

Richardson's equation (*Richardson, 1922*) can be linearized by writing each variable in terms of a basic state (overline) plus a small increment (prime) gives:

$$\begin{aligned} \gamma \bar{p} \frac{\partial w'}{\partial z} = & -\gamma \bar{p}' \frac{\partial \bar{w}}{\partial z} - \gamma \bar{p} \nabla \cdot \vec{v}'_h - \gamma \bar{p}' \nabla \cdot \vec{v}_h - \vec{v}'_h \cdot \nabla p' - \\ & \vec{v}'_h \cdot \nabla \bar{p} + g \int_z^\infty \nabla \cdot (\bar{\rho} \vec{v}'_h) dz + g \int_z^\infty \nabla \cdot (\rho' \vec{v}_h) dz \end{aligned} \quad (7.4)$$

where w is the vertical velocity, \vec{v}_h is the vector of horizontal wind, γ is the ratio of specific heat capacity at constant pressure and volume, p is the pressure, ρ is the density, z is height.

The linear and adjoint of Richardson's equation are incorporated into the 3DVAR system, which serves as a bridge between the 3DVAR analysis and the the vertical velocity component of the Doppler radial velocity observations (*Xiao et al., 2005*).

7.5.2 Partitioning of the moisture and water hydrometeor increments

Because, the total water mixing ratio q_t is used as control variable, partitioning of moisture and water hydrometeor increments is necessary in the 3DVAR system. A sophisticated microphysical processes would be necessary to do the partitioning. However, development

of adjoint scheme for such process is not trivial. In this study, a simple warm rain processes is introduced into MM5/WRF 3DVAR system. The tangent linear and its adjoint of the scheme are developed and incorporated into the 3DVAR-system. Although the control variable is q_t ; the q_v , q_c and q_r increments are produced through the partitioning procedure during the 3DVAR analysis. The warm rain parameterization builds a relation among rainwater, cloud water, moisture and temperature. When rainwater information (from reflectivity) enters into the minimization iteration procedure, the forward warm rain process and its backward adjoint distribute this information to the increments of other variables. Once the 3DVAR system produces the q_c and q_r increments, the assimilation of reflectivity is straight forward (Xiao and Sun, 2006).

7.5.3 The observation operators for radial velocity and reflectivity

The observation operator for Doppler radial velocity is,

$$V_r = u \frac{(x - x_i)}{r_i} + v \frac{(y - y_i)}{r_i} + (w - V_T) \frac{(z - z_i)}{r_i} \quad (7.5)$$

where (u , v , and w) are the wind components, (x , y , and z) are the radar location, (x_i , y_i and z_i) are the location of the radar observation, r_i is the distance between the radar and the observation and V_T is the terminal velocity. Following the equation of the Sun and Crook (1998),

$$V_T = 5.40 a q_r^{0.125} \quad (7.6)$$

The quantity, a is a correction factor defined by

$$a = \left(\frac{p_0}{\bar{p}} \right)^{0.4} \quad (7.7)$$

where \bar{p} is the base state pressure p_0 is the surface pressure

The observation operator for doppler radar reflectivity is (Sun and Crook, 1997),

$$Z = 43.1 + 17.5 \log(\rho q_r) \quad (7.8)$$

Where Z is the reflectivity in units of dBZ and q_r is the rain water mixing ratio

7.6 Synopsis of the cyclonic event Ogni

Originating from the southeast Bay of Bengal, the system reaches the deep depression stage by 12:00 UTC, 28 October and IMD upgraded it to cyclonic storm status at 12:00 UTC, 29 October and assigned the name Ogni. Cyclonic storm Ogni moved in a northward direction along the longitude under the steering flow associated with the environmental wind. It reached its maximum intensity by 20:00 UTC on 29 October with maximum surface wind (MSW) of 25 ms^{-1} . Ogni continues to move northwards and made landfall near Bapatla, Andhra Pradesh at around 07:30 UTC on 30 October 2006. Before it made landfall, IMD downgraded the system to deep depression with a MSW of 15 ms^{-1} .

7.6.1 Experiment design

The National Center for Environmental Prediction (NCEP), Final Analysis (FNL) with $1.0^\circ \times 1.0^\circ$ horizontal resolution interpolated to the model domain has been used as initial and boundary condition for model integration. To assess the impact of the Doppler radial velocity and reflectivity observations in the prediction and simulation of mesoscale features associated with tropical cyclone, two experiments were carried out. We use single domain with horizontal grid spacing of 30 km. In the control experiment WRF-NoDWR the conventional and non-conventional observations from GTS have been used in the 6-hr assimilation cycle of the 3DVAR system with cold start at 12:00 UTC on 27 October 2006. In the second experiment WRF-NoDWR, along with the GTS data, Doppler radar radial velocity and reflectivity data from Sriharikota Doppler weather radar has been used in the assimilation cycle of the 3DVAR experiment. Three assimilation cycles have been run in

the pre-forecast mode and model has been initialized at 00:00 UTC on 28 October 2006 and integrated for 60 hours.

7.6.2 Mean sea level pressure

Figure 7.16 illustrates the sea level pressure (SLP) simulated by the two experiments at 24-hr interval. The figure 7.16 (a) shows SLP forecast for the WRF-NoDWR experiment valid at 12:00 UTC, 28 October. Storm is centered around 10.5°N , 80.5°E with a minimum SLP of 1006.1 hPa. The figure 7.16 (b) is same as 7.16 (a), but for WRF-DWR experiment. The WRF-DWR experiment predicts a minimum SLP of 1004.3 hPa and the storm is located near 11.0°N , 80.5°E . The observed storm center from IMD report is 11.7°N , 79.9°E . Figure 7.16 (c), and (d) shows 36-hr forecast of minimum SLP valid for 12:00 UTC, 29 October for the WRF-NoDWR and WRF-DWR experiments, respectively. The WRF-NoDWR predicts a minimum SLP of 1000.7 hPa, whereas the WRF-DWR predicts a minimum SLP of 998.1 hPa. The position of the storm from the WRF-NoDWR experiment is around 13.5°N , 80.0°E , while the storm center predicted by the WRF-DWR experiment is near 14.2°N , 80.2°E and is close to the observed storm center (15.2°N , 80.4°E). Fig 7.16 (e) and (f) shows minimum SLP valid at 12:00 UTC, 30 October 2006 for the WRF-NoDWR and WRF-DWR experiment respectively. The minimum SLP predicted by the WRF-NoDWR experiment is 1004.1 hPa, while that from the WRF-DWR experiment is 1002.6 hPa. The cyclone is centered near 14.0°N , 79.4°E in the WRF-NoDWR and near 14.8°N , 79.7°E in WRF-DWR. The storm centre predicted by WRF-DWR experiment is close to the observed storm center (16.0°N , 79.8°E). The observed minimum sea level pressure is 982 hPa, whereas predicted minimum sea level pressure from WRF-NoDWR is 1000.7 hPa and that from WRF-DWR experiment is 998.1 hPa.

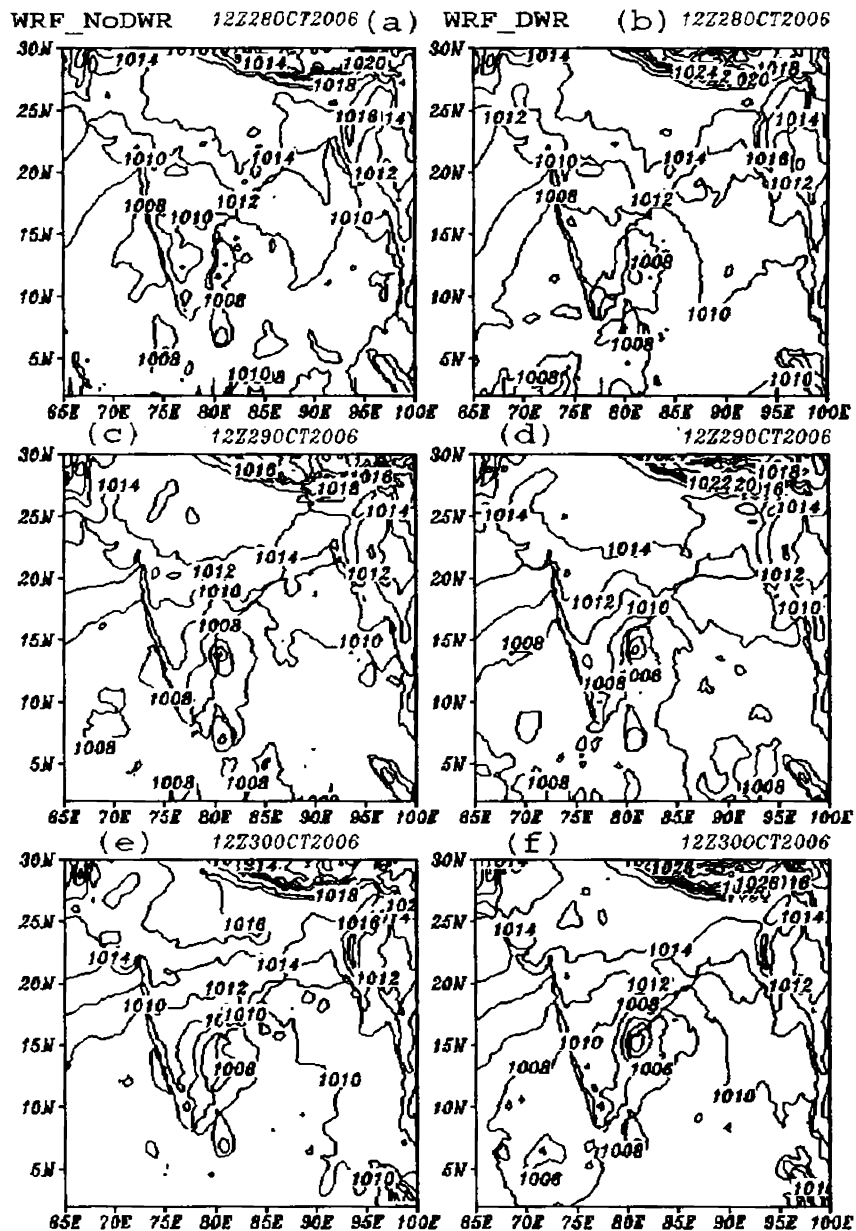


Figure 7.16: Mean sea level pressure simulated by the WRF-NoDWR experiment (left panel) and WRF-DWR experiment (right panel), valid at 12:00 UTC 28 October (top panel), 12:00 UTC, 29 October (middle panel) and 12:00 UTC, 30 October 2006 (lower panel).

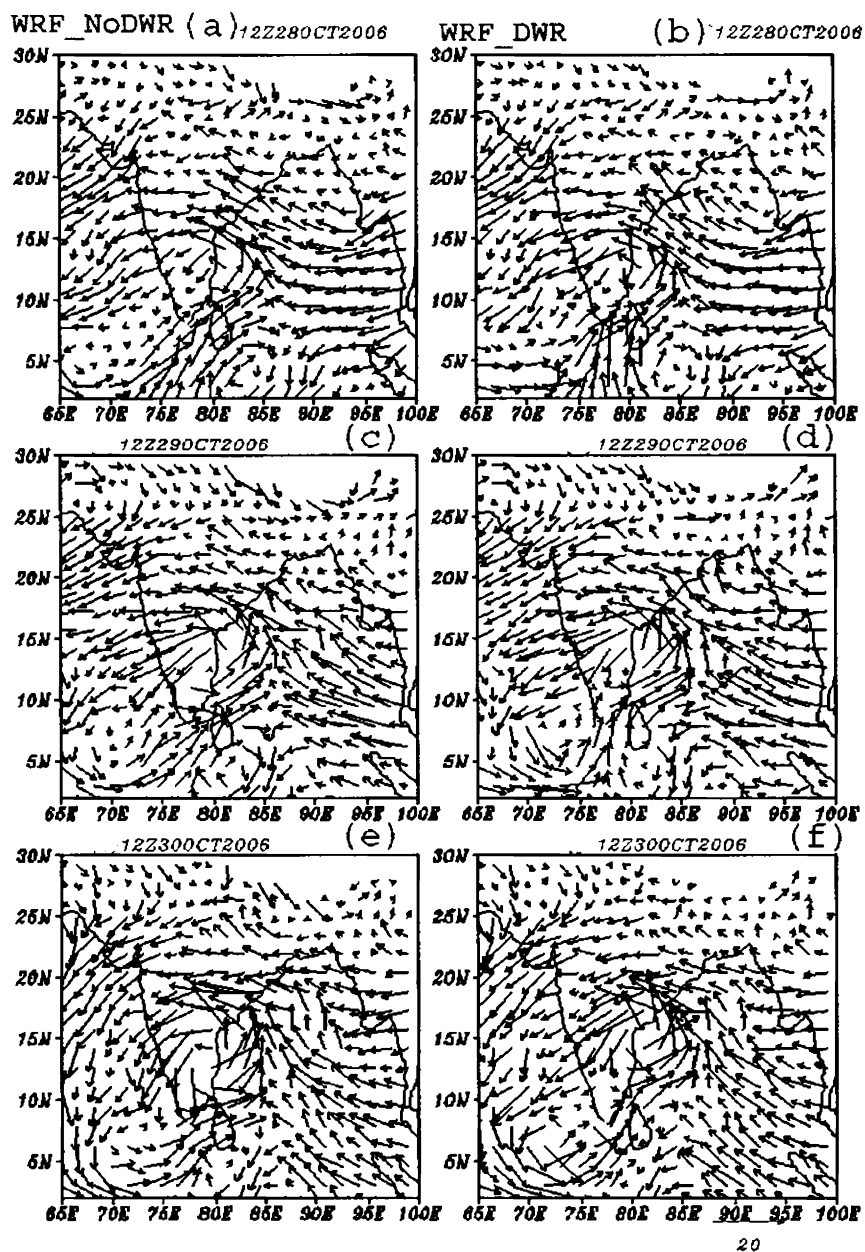


Figure 7.17: Horizontal wind vectors at 850 hPa simulated by the WRF-NoDWR experiment (left panel) and WRF-DWR experiment (right panel), valid at 12:00 UTC, 28 October (top panel), 12:00 UTC, 29 October (middle panel) and 12:00 UTC, 30 October 2006 (lower panel)

7.6.3 Horizontal wind

Figure 7.17 (a) and (b) show the 12-hr forecast of vector wind at 850 hPa valid at 12:00 UTC, 28 October 2006 for the WRF-NoDWR and WRF-DWR experiments, respectively. The circulation pattern is characterized by strong southeasterly wind north of the cyclone center and southwesterlies prevailed over south of the cyclone center. Although the circulation pattern is similar in the two experiments, the WRF-DWR experiment predicts stronger wind as compared to the WRF-NoDWR experiment. Figure 7.17 (c) and (d) show 36-hr forecast of wind vector valid at 12:00 UTC 29 October for the WRF-NoDWR and WRF-DWR experiments, respectively. Strong wind is found in the northeast and southeast sector of the cyclone center. The wind speed is more or less comparable in magnitude for the two experiments. Figures 7.17 (e) and (f) present 60-hr forecast of the vector wind valid at 12:00 UTC on 30 October 2006. The wind speed and circulation pattern is found to be decreased in both the experiments and new circulation pattern developed in the Arabian Sea. This analysis suggests that the assimilation of Doppler radial velocity and reflectivity produce stronger circulation pattern. Figure 7.18 shows time series of the maximum wind

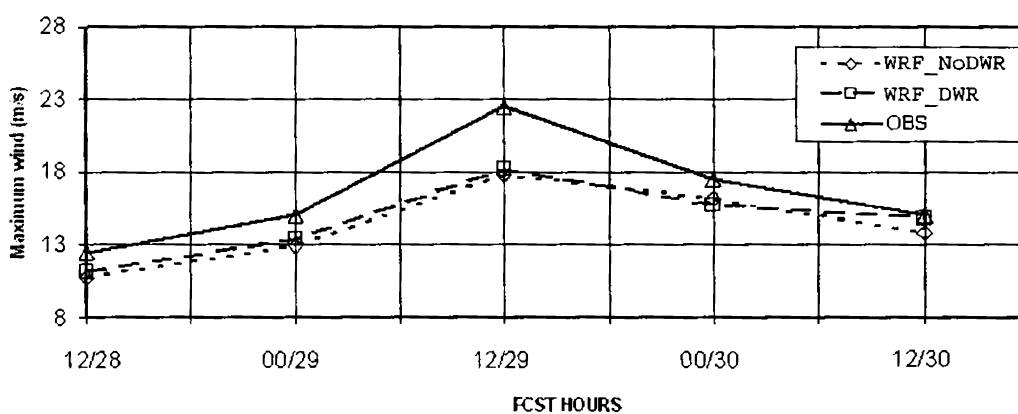


Figure 7.18: Time series of (at 12-hr intervals) of Maximum wind (ms^{-1}) for the WRF-NoDWR, WRF-DWR and from Observed / Estimated

speed. The observed wind speed increases from 12.5 ms^{-1} at 12:00 UTC 28 October to a maximum value of 22.5 ms^{-1} at 12:00 UTC on 29 October and thereafter decreases and reaches 13.5 ms^{-1} at 12:00 UTC, 30 October 2006. The WRF experiment do show the similar time evolution but the intensity is underestimated. The maximum wind speed predicted by WRF-NoDWR experiment is 17.8 ms^{-1} and WRF-DWR experiment shows a maximum wind speed of 18.2 ms^{-1} at 12:00 UTC on 29 October 2006.

7.6.4 Rainfall

Figure 7.19 (a) and (b) presents 24-hr accumulated precipitation valid at 00:00 UTC, 29 October 2006 and 00:00 UTC, 30 October 2006. The left, middle and right panel presents the simulated precipitation from WRF-NoDWR, WRF-DWR and observed rainfall from TRMM satellite respectively. On both days, WRF-NoDWR experiment predicts extensive rainfall over the ocean. The rainfall simulated from the WRF-DWR experiment is mostly distributed near the coast. The TRMM observations show main precipitation band along the coast of Andhra Pradesh and Tamilnadu and secondary precipitation band off the southwest coast. The TRMM observation shows more than 16 cm rainfall. The rainfall predicted from WRF-DWR do shows the rainfall amount greater than 16 cm, while the rainfall predicted from WRF-NoDWR experiment is greater than 32 cm and is overestimated. Nevertheless, both WRF-NoDWR and WRF-DWR experiments produce more widespread rainfall over the ocean, the rainfall amount and distribution from WRF-DWR experiment is more or less closer to that observed from TRMM.

7.6.5 Mesoscale organization of clouds

Figure 7.20 (a) and (b) present the total hydrometeor structure from WRF-NoDWR and WRF-DWR experiments during the mature phase of the cyclone near 18:00 UTC on 29 October 2006. The figure clearly shows the cloud structure during the mature phase of

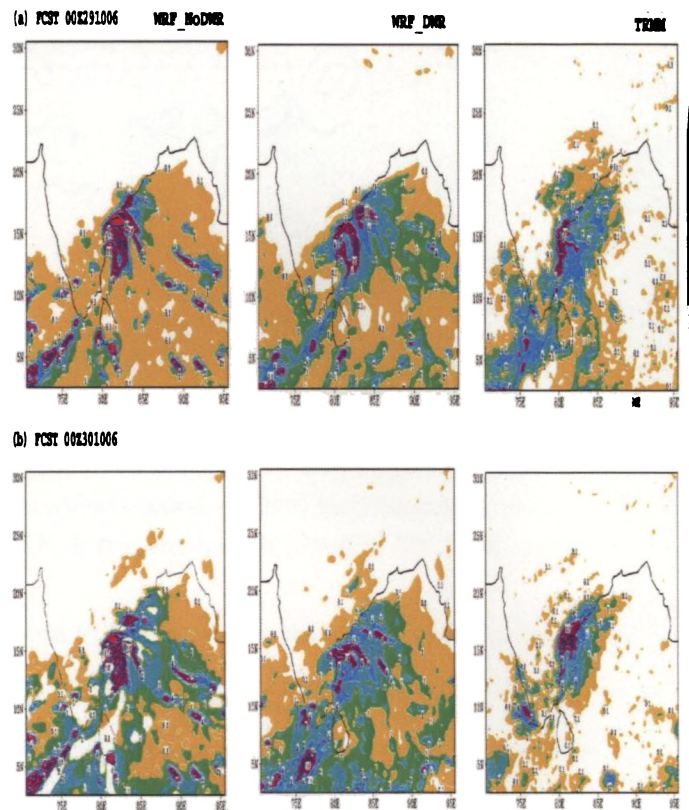


Figure 7.19: 24 -hr accumulated rainfall from forecast valid at (a) 00:00 UTC 29 October and (b) 00:00 UTC 30 October 2006. Left, middle and right panel shows the simulated rainfall from WRF-NoDWR, WRF-DWR and TRMM observations

the storm. The cloud structure simulated by the WRF experiment at a coarse resolution of 30 km does not resolve the eye structure of the cyclonic storm during the mature phase. However, the WRF-DWR experiment shows evidence of eye wall with the storm center at 15.0°N , while that simulated by WRF-NoDWR experiment is centered over 14.2°N . The observed storm center at this time is around 15.5°N . As seen from the figure 7.20, WRF-DWR experiment well simulates the anvil shape of the cloud structure, with large horizontal coverage. Compared to WRF-NoDWR experiment, WRF-DWR experiment captures the vertical extent of the clouds reasonably well.

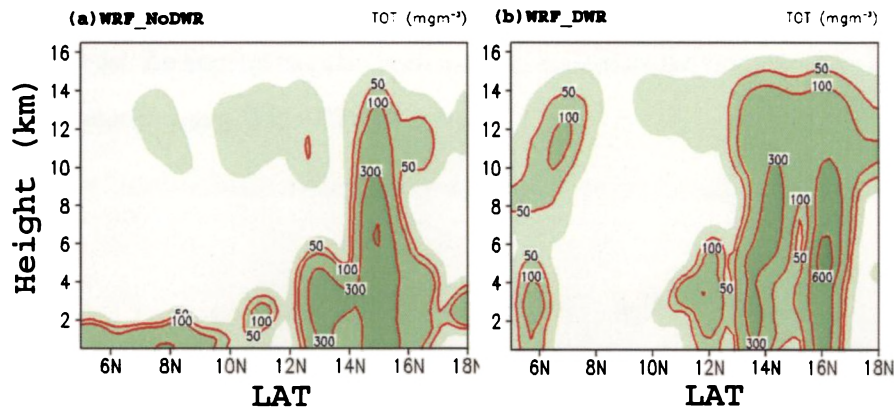


Figure 7.20: Latitudinal section of Total Hydrometeor (mgm^{-3}) from (a) WRF-NoDWR and (b) WRF-DWR during the mature phase of the storm

The results from the assimilation of Doppler radial velocity and reflectivity show improvements in the prediction and simulation of mesoscale features of the cyclonic storm. However, the assimilation experiment shows little skill in rainfall forecast, the WRF-DWR experiment could able simulate the mesoscale cloud structure including, signatures of wall cloud and anvil shape reasonably well. The results presented in this section is preliminary and more detailed analysis have to be carried in future.

7.7 Summary

This chapter focuses on the impact of Doppler Weather Radar (DWR) and other conventional and non-conventional data in simulating the intense convective events over Chennai and Kolkata. Three strong convective events each over Chennai and Kolkata have been considered for the present study. The model forecast of precipitation has been verified by calculating the ensemble equitable threat scores for all seven cases considered for the present study. The ETS of precipitation forecast has been calculated using 6-hr accumulated precipitation from merged rainfall analysis from TRMM satellite. For 12 hours, the results

indicate that the assimilation of Doppler radar data has a positive impact on the short range rainfall forecast. An attempt has also been made to assimilate the Doppler radar reflectivity and radial velocity using WRF-3DVAR system.

CHAPTER 8

Conclusion and Recommendations

The main purpose of the Ph.D thesis is to improve the state of knowledge and understanding of the physical structure of the TMCS and its short range prediction. The present study principally addresses the fine structure, dynamics and microphysics of severe convective storms. Major outcome of the thesis is summarized in the following sections.

8.1 Radar Observations of TMCS

As scattering mechanism depends on operating frequency or wavelength of the probing radar, the thesis discusses the radar observations of the convection and clouds at three frequency bands (VHF, L band UHF and S band DWR). The scanning Doppler weather radars provide good horizontal spatial coverage, whereas the vertically pointing wind profilers provide a higher temporal and vertical spatial resolution view of the atmosphere. In the present study, individual observations of the internal structure of the clouds and con-

vection using VHF (53 MHz) and UHF (1357.5 MHz) radars at Gadanki (13.2 °N, 79.5 °E) and DWR (2.8 GHz) at Chennai (13.0 °N, 80.1 °E) have been reported.

The thesis makes use of the capability of clear air VHF radar to measure the fine scale vertical structure of the convective systems passing over the radar site. Since, convection is much more evident in the vertical wind component, the vertical beam data have been used to explore the vertical structure of the storm. The time-height intensity variation of radar reflectivity and vertical velocity together with the duration and separation of updraft cores with vertical velocity greater than 3 ms^{-1} have been used to identify the storm type and to classify characteristic regions of the storm. Detailed dynamical, thermodynamical and microphysical processes associated with a TMCS with multicell characteristics, a supercell storm and a weak evolving multicell with supercell characteristics have been reported in the thesis.

The multicell organization of the clouds associated with the TMCS consists of four distinct regions viz initial (convective), mature, transition zone and stratiform region. Convective precipitation dominates early in the system life cycle, while stratiform precipitation in final stage of the system. The average height profiles of the vertical velocity have been obtained for the four regions. Distinct vertical velocity and reflectivity structure is unique for each region. Characteristics of each region is summarized as follows,

(i) Genesis (cumulus) region is characterized by growth of high reflectivity cores from the lower troposphere to the middle and upper troposphere. The mean vertical motion is upward in the troposphere with a peak near 10 km. Maximum updraft is observed during the genesis stage of the system.

(ii) Mature region of the system lifecycle is clearly seen when WER detected. Peak upward motion was found near 12km while vertical motion is downward in the lower troposphere. The penetrating updraft and weakening of tropopause in the mature region reveal the occurrence of overshooting convection.

iii) Transition region is characterized by diminishing structure of reflectivity and layered structure near tropopause moving back to the stable atmospheric condition. Intense downdraft is present in the lower and middle troposphere with local pockets of updrafts.

(iv) Stratiform region is marked by only weak vertical motion and weakening of echoes. Convective downdrafts are present in the middle and lower troposphere. An important feature in the stratiform region is the occurrence of double ERZ or BB structure, one near 5 km and another near 3.5 km.

In the case of supercell storm, observation starts at the mature phase of the storm. The vertical profiles of average vertical velocity are also obtained for the mature and dissipating phases of the storm. The characteristic features of each phase are as follows,

(i) Mature phase is characterized by the growth of high reflectivity cores from the lower troposphere to the middle and upper troposphere. The mean vertical motion is upward in the troposphere with a peak near 10 km. A WER is also observed during the mature phase of the system.

(ii) Dissipating phase is characterized by diminishing structure of reflectivity. This phase is marked by relatively small vertical velocity. Intense downdraft is present in the lower and middle troposphere with local pockets of updrafts in the upper troposphere.

The variance in the atmospheric refractive index explains the occurrence of the ERZ and WER and the associated dynamical and microphysical processes. The WER can be explained using the cloud base and lateral entrainment processes. The observed WER is not found at the level of maximum updraft velocity, instead found in the height range, 4-6 km where strong gradient of vertical velocity exists. The observed structure of ERZ is due to the combined effect of melting, evaporation, entrainment and precipitation drag. The analysis shows that both dynamical and microphysical processes contribute to the occurrence of ERZ or BB. Hence the observed ERZ and WER can be produced by both dynamical and microphysical processes.

The radar reflectivity structure and Doppler vertical velocity during precipitating convection has also been investigated using the UHF wind profilers. The time height variation of radar reflectivity is used to classify the convective, transition and stratiform regions of convection. Bright band structure near the melting level is explained using the vertical profiles of hydrometeor reflectivity and Doppler vertical velocity. The BB layer and BBH is determined from these profiles. Both the dynamical and microphysical processes such as the precipitation drag, melting, evaporation, droplet break up and aggregation, droplet size and inertia effect can be used to explain the observed structure of the BB and associated processes.

The radar features can be used to understand the processes associated with both convection and cloud. The main limitation of this analysis is the lack of thermodynamic observation to support the kinematic storm analysis. The results clearly indicate the potential of VHF radar to observe the fine structure of TMCS, but there is a need for simultaneous wind, temperature and humidity measurements.

8.2 CSRM Simulations

With the advances in computer technology, mesoscale models are being run on grid spacing less than 5 km. These CSRM treat cloud and convection explicitly and QPF and other cloud related parameters depend entirely on microphysical parameterization. The sensitivity of bulk microphysical schemes such as warm rain, simple ice and GSFC schemes to the initiation, evolution, duration, areal extent and structure of the TMCS has also been investigated and found that the structure and QPF is sensitive to microphysical processes. The GSFC microphysical scheme with five hydrometeor species well simulates the observed structure of the TMCS. The horizontal and vertical distributions of the cloud hydrometeor fields from CSRM simulations are compared with those observed from TRMM. Substan-

tial difference is noticed in the amounts of cloud microphysical parameters. The present study shows that the amount of hydrometeorological fields retrieved from TMI is significantly lesser than those simulated by the model. Spatial distribution of Cloud Liquid Water (CLW) and Rain Water (RNW) from TMI and model simulations well corresponds with each other. The TRMM-PR captures most of the detailed structure and intensity of the cloud system reasonably well. This type of analysis offers a pathway to identify the uncertainties in space-based rainfall estimation and validation of microphysical schemes in mesoscale models.

The high resolution (both time and height) VHF radar observations have been used in the present study to examine several features of small scale wind disturbances associated with a TMCS. The spectral and wavelet analysis has been carried out on the vertical wind perturbations to find out the dominant modes of oscillations in the UT/LS region. Vertical wind disturbances having short periods of 8-30 min is distributed in the troposphere. As simultaneous temperature and humidity observations are not available at the radar location, CSRM simulations were carried out to understand different forcing mechanisms for the generation and maintenance of gravity waves such as, oscillating updrafts-downdrafts and thermal forcing due to the release of latent heat associated with condensation.

The model performed well in simulating the observed structure of the storm. The northward propagation and the penetrative convection in terms of large upward motion near the tropopause level were well captured in the model simulations. The kinematic structure of the storm very much depends on the moist processes in the model. Large upward velocity is found during the period when maximum ICLW in the model domain and the large downward motion is associated with maximum IRNW. Strong association of the condensational heat release to the vertical velocity disturbance and hence the model wave development is noteworthy. Despite the fact that, heating is the primary source of the vertical wind disturbance in the middle troposphere and associated wave generation, multiple mechanisms such

as thermal forcing due to condensational heat and oscillatory nature of updraft-downdraft pairs reaching as high as tropopause level is considered as the gravity wave maintenance and amplification. The spectral characteristics of the simulated waves suggest that both thermal forcing and penetrative updrafts are contributing energy to the gravity waves. Isolating the role of thermal forcing and oscillating updrafts is difficult, if both the processes are important.

8.3 Mesoscale Data Assimilation

Increased resolution alone is insufficient to produce accurate QPF. In addition to the problems with the parameterization schemes, the lack of sufficient mesoscale details in the initial data can significantly contribute errors in QPF. The thesis also put forward the importance of high density conventional, non-conventional mesoscale observations, and satellite observations for the simulation of the organization and propagation characteristics of the tropical cloud clusters. The model predictions of rainfall has been compared with the observed rainfall from TRMM and equitable threat score has been calculated by considering all the cases and found that the assimilation experiments show better skill during the first 12-18 hours and thereafter scores decreases.

The first attempt in utilizing IMD Doppler radar data into a numerical model for the prediction of rainfall associated with mesoscale convective systems and to forecast the thunderstorm evolution and structure has been included in the thesis. The model forecast of precipitation has been verified by calculating the ensemble equitable threat scores for all seven cases considered for the present study. For 12 hours, the results indicate that the assimilation of Doppler radar data has a positive impact on the short range rainfall forecast. Significant improvements in the precipitation forecast appeared in the first 12-hr forecast period. The ETS score decreases after 12-hr forecast and remains more or less constant till

36-hr and there after ETS decreases considerably. The 3DVAR experiments produce higher scores as compared to the CTRL-GSFC experiments. The difference between the two assimilation experiments 3DVAR-DWR and 3DVAR-NoDWR are statistically less significant for both the precipitation thresholds. It may be kept in mind that the DWR wind fields are available in only one of the four assimilation cycles. As an extension to the promising results from the DWR wind assimilation, the preliminary results from Doppler radar reflectivity and radial velocity data in the 3DVAR system of Weather Research and Forecast (WRF) model has also been included in the thesis.

8.4 Future scope

The thesis put forward the importance of the mesoscale data analysis and assimilation. The structure and dynamics of the Tropical cloud clusters over Indian region is not well understood. The observational cases discussed in the thesis are limited to the temperature and humidity observations. We propose a mesoscale observational network along with all the available Doppler radars and other conventional and non-conventional observations. Simultaneous observations with DWR, VHF and UHF radars of the same cloud system will provide new insight into the dynamics and microphysics of the clouds. More cases have to be studied in detail to obtain climatology of the storm type passing over tropical Indian region. These observational data sets provide wide variety of information to be assimilated to the mesoscale data assimilation system and can be used to force CSRM.

The gravity wave generation and stratosphere troposphere exchange (STE) processes associated with convection gained a great deal of attention to modern science and meteorologist. Round the clock observations using VHF and UHF radars along with supplementary data sets like DWR, satellite, GPS/Radiosondes, meteorological rockets and aircraft observations is needed to explore the role of convection and associated energetics in detail.

In future field campaigns like STORM and PROWNOM, in addition to the mesoscale observations, high resolution observations should be needed to improve our understanding of cloud system at microphysical level and prediction of TMCS. As IMD is upgrading conventional cyclone detecting S-band radar network with Doppler capability, these data sets along with the high resolution observations collecting during STORM and PROWNOM field campaigns can be used to improve the initial condition for the short range prediction of convective systems in real time.

REFERENCES

- Abhilash, S. and Mohankumar, K., Prominent features of the gravity waves generated by tropical convection detected by VHF Doppler radar: A case study, in *Proceedings of 14th International Conference on Clouds and Precipitation*, ICCP, Bologna, Italy, 2004.
- Abhilash, S. and Mohankumar, K., Vertical structure and evolution of a Supercell storm: Observations using VHF radar, *International Journal of Remote Sensing*, **Accepted**, 2007.
- Abhilash, S., Mohankumar, K., Das, S. S., Anandan, V. K., and Rao, D. N., Gravity waves associated with a supercell storm. Part II: Assimilation of vhf radar data and cloud resolving scale simulations, in *Proceedings of MST-11*, NARL, Gadanki, Tirupati, India, 2006a.
- Abhilash, S., Mohankumar, K., Kumar, K. K., Anandan, V. K., and Rao, D. N., Gravity waves associated with a supercell storm. Part I: Observations, in *Proceedings of MST-11*, NARL, Gadanki, Tirupati, India, 2006b.
- Abhilash, S., Das, S., Kalsi, S. R., Gupta, M. D., Mohankumar, K., George, J. P., Banarjee, S. K., Thampi, S. B., and Pradhan, D., Assimilation of Doppler radar wind observations for the prediction of rainfall associated with mesoscale convective systems, *Journal of Earth System Science*, **116(3)**, 275–304, 2007a.
- Abhilash, S., Das, S., Kalsi, S. R., Gupta, M. D., Mohankumar, K., George, J. P., Banarjee, S. K., Thampi, S. B., and Pradhan, D., Impact of Doppler radar wind observations in simulating the intensity and propagation of rainbands associated with mesoscale convective complexes using MM5-3DVAR system, *J. Pure and Appl. Geophysics*, **164(8-9)**, 1491–1509, 2007b.
- Abhilash, S., Mohankumar, K., and Das, S., Microphysical structure associated with tropical cloud clusters simulated using a mesoscale model and comparison with TRMM observations, *International Journal of Remote Sensing*, **In Press**, 2007c.

- Abhilash, S., Mohankumar, K., George, J. P., Das, S., and Bohra, A. K., Assimilation of conventional and satellite observations for the short range prediction of convective systems, in *METOC-07*, Indian Navy, Southern Naval Command, Cochin, 2007d.
- Alexander, M. J., Interpretations of observed climatological patterns in stratospheric gravity wave variance, *J. Geophys. Res.*, **103(D8)**, 8627–8640, 1998.
- Alexander, M. J. and Pfister, L., Gravity wave momentum flux in the lower stratosphere over convection, *Geophys. Res. Lett.*, **22**, 2029–2032, 1995.
- Alexander, M. J. and Vincent, R. A., Gravity waves in the tropical lower stratosphere: A model study of seasonal and interannual variability, *J. Geophys. Res.*, **105(D14)**, 983–993, 2000.
- Alexander, M. J., Beres, J. H., and Pfister, L., Tropical stratospheric gravity wave activity and relationships to clouds, *J. Geophys. Res.*, **105(D17)**, 299–309, 2000.
- Allen, S. J. and Vincent, R. A., Gravity wave activity in the lower atmosphere: Seasonal and latitudinal variations, *J. Geophys. Res.*, **100(D1)**, 1327–1350, 1995.
- Anandan, V. K., *The Atmospheric Data Processor, Technical and User Reference Manual*, National MST Radar Facility, Department of Space, Govt. of India, Gadanki-517112, AP, India, 1996.
- Anderson, T., VAD winds from C band Ericsson Doppler weather radars, *Meteor. Zeitschrift*, **7**, 309–319, 1998.
- Arakawa, A. and Schubert, W. H., Interaction of cumulus cloud ensemble with large scale environment, Part I, *J. Atmos. Sci.*, **31**, 674–701, 1974.
- Asnani, G. C., Tornadoes-A review, *Vayu Mandal*, **15**, 97–133, 1985.
- Atlas, D., Hardy, K. R., and Joss, J., Radar reflectivity of storms containing spongy hail, *J. Geophys. Res.*, **69**, 1955–1964, 1964.
- Atlas, D. C., Ulbrich, C. W., Marks, F. D., Amitai, E., and Williams, C. R., Systematic variation of drop size and radar-rain fall relations, *J. Geophys. Res.*, **104**, 6155–6169, 1999.
- Balsley, B. B. and Gage, K. S., The MST radar technique: Potential for middle atmospheric studies, *Pure Appl. Geophys.*, **118**, 452–493, 1980.
- Barker, D. M., Huang, W., Guo, Y. R., and Bourgeois, A., A three dimensional variational (3DVAR) data assimilation system for use with MM5, in *NACR Technical Note*, vol. **68p**, NCAR, TN-453+STR, 2003.
- Barker, D. M., Huang, W., Guo, Y. R., and Xiao, A three dimensional variational (3DVAR) data assimilation system with MM5: Implementation and initial results, *Mon. Weather Rev.*, **132**, 897–914, 2004.
- Barnes, G. and Garstang, M., Subcloud layer energetics of precipitating convection, *Mon. Weather Rev.*, **110**, 102–117, 1982.

- Battan, L. J., *Radar observations of the atmosphere*, University of Chicago press., Chicago, 1973.
- Bean, B. R. and Dutton, E. J., *Radar Meteorology*, Dover Publications, New York., 1964.
- Betts, A. K., Greenhouse warming and the tropical water budget, *Bull. Am. Meteorol. Soc.*, **71**, 1464–1465, 1990.
- Bhattacharya, P. K. and Banerjee, S. K., Pre-monsoon tornadoes over West Bengal during April 1977, *Vayu Mandal*, **10**, 14–18, 1980.
- Biggerstaff, M. I., Kinematics and microphysics of the transition zone of the 10-11 June 1985 squall line, *J. Atmos. Sci.*, **50**, 3091–3110, 1993.
- Biswas, B. and Gupta, K., Heights of CB clouds around Kolkata airport-diurnal and seasonal variations, *Mausam*, **40**, 169–174, 1989.
- Biswas, B. and Gupta, K., Radar echo pattern during the onset of southwest monsoon over Gangetic West Bengal, *Mausam*, **43**, 439–444, 1992.
- Black, T. L., The new NMC mesoscale Eta model: Description and forecast examples, *Weather forecasting*, **9**, 265–278, 1994.
- Bluestein, H. B., Pazmany, A. L., Galloway, J. C., and McIntosh, R. E., Studies of the structure of severe convective storms using a mobile 3 mm wavelength Doppler radar., *Bull. Am. Meteorol. Soc.*, **76**, 2155–2167, 1995.
- Browning, K. A., The structure and mechanism of hailstorms. Hail: A review of hail science and hail suppression, in *Meteorological Monograph*, vol. **16**, pp. 1–17, Am. Met. Soc., 1977.
- Browning, K. A. and Ludlam, F. H., Radar analysis of a hailstorm., in *Dep. Meteorol.*, vol. **5**, Imperial College, London., 1960.
- Browning, K. A. and Ludlam, F. H., Airflow in convective storms., *Q. J. R. Meteorol. Soc.*, **88**, 117–135, 1962.
- Browning, K. A. and Wexler, R., The determination of kinematic properties of a wind field using Doppler radar, *J. Appl. Met.*, **7**, 105–113, 1968.
- Burgess, D. and Ray, P. S., Principles of radar: Mesoscale meteorology and forecasting, in *Mesoscale meteorology Ed. By P. S. Ray*, pp. 85–117, American Meteorological Society, Boston, 1986.
- Burrows, D., An operational algorithm for the identification and location of a bright band from radar volume data, in *Conference on Radar Meteorology*, vol. **37**, Amer. Meteor. Soc., Munich, Germany, 2001.
- Byres, H. R. and Braham, R. R., The Thunderstorms., in *U. S. Weather Bur.*, Washington, D. C., 1949.
- Carter, D. A., Ecklund, W. L., McAfee, J. R., Gage, K. S., Keenan, T., and Manton, M., Results from the first year of observations using the Darwin VHF wind profiler, in *25th*

- Int. Conf. on Radar Meteorology*, vol. **288-291**, American Meteorological Society, Paris, France, 1991.
- Chaboureau, J. P., Cammas, J. P., Duraon, J., Sitnikov, N. M., and Voessing, H. J., A numerical study of tropical cross-tropopause transport by convective overshoots, *Atmospheric Chemistry and Physics*, **7**, 1731–1740, 2007.
- Chisholm, A. J. and Renick, J. H., The kinematic structure of multicell and supercell Alberta hailstorms. Alberta hail studies, in *Meteorological Monograph*, vol. **Rep. No. 722**, Research Council of Alberta Hail Studies, 1972.
- Choudhari, S. and Chattopadhyay, S., Genesis of severe local storms-A genetic algorithm approach, *Science and Culture*, **69**, 331–335, 2003.
- Chu, Y. H. and Lin, C. H., The severe depletion of turbulent echo power in association with precipitation observed by using Chung-Li VHF radar, *Radio Sci.*, **29**, 1311–1320, 1994.
- Churchil, D. D. and Houze, R. A., Development and structure of winter monsoon cloud clusters on 10 December 1978, *J. Atmos. Sci.*, **41**, 931–960, 1984.
- Clark, T. L., Hauf, T., and Kuettner, J. P., Convectively forced internal gravity waves: Results from two-dimensional numerical experiments, *Q. J. R. Meteorol. Soc.*, **112(474)**, 899–925, 1986.
- Cornford, S. G. and Spavins, C. S., Some measurements of cumulonimbus tops in the pre-monsoon season in northeast India, *Meteorological Magazine*, **102**, 314–332, 1973.
- Cotton, W. R., Numerical simulation of precipitation development in supercooled cumuli, Part I, *Mon. Weather Rev.*, **100**, 757–763, 1972.
- Cotton, W. R., Cloud models: Their evolution and future challenges, in *Meteorological Monograph Series*, vol. **29(51)**, Amer. Meteor. Soc., 2003.
- Cotton, W. R. and Anthes, R. A., *Storm and cloud dynamics*, Academic Press, Inc, 1989.
- Cotton, W. R., George, R. L., and Knupp, K. R., An intense, Quasi-Steady Thunderstorm over Mountainous terrain. Part I: Evolution of the storm initiating mesoscale circulation, *J. Atmos. Sci.*, **39**, 328–342, 1982.
- Cram, M., Pielke, R. A., and Cotton, W. R., Numerical simulation and analysis of a pre-frontal squall line. Part II: Propagation of the squall line as an internal gravity wave, *J. Atmos. Sci.*, **49**, 209–225, 1992.
- Currier, P. E., Avery, S. K., Balsley, B. B., Gage, K. S., and Ecklund, W. L., Combined use of 50 MHz and 915 MHz wind profilers in the estimation of raindrop size distributions, *Geophys. Res. Lett.*, **119**, 1017–1020, 1992.
- Curry, M. J. and Murthy, R. C., Thunderstorm generated gravity waves, *J. Atmos. Sci.*, **31**, 1402–1408, 1974.
- Daley, R., *Atmospheric Data Analysis*, Cambridge Atmospheric and Space Science Series,

- Cambridge University Press, 1991.
- Das, S., Kalsi, S. R., Abhilash, S., Gupta, M. D., George, J. P., Banerjee, S. K., Thampi, S. B., Pradhan, D., and Mohankumar, K., Assimilation of Doppler weather radar wind in a mesoscale model and their impact on simulation of thunderstorms and severe weather systems, in *Report no. NMRF/RR/01/2006*, vol. **01/06**, NCMRWF, Noida, 2006.
- De, A. C., Movement of pre-monsoon squall-lines over Gangetic West Bengal as observed by radar at dum dum airport, *Ind. J. Met. Geophys.*, **14**, 37–51, 1963.
- De, A. C. and Sen, S. N., A radar study of pre-monsoon thunderstorms (NorWesters) over Gangetic West Bengal, *Ind. J. Met. Geophys.*, **12**, 51–62, 1961.
- Dhaka, S. K., Choudhary, R. K., Malik, S., Shibagaki, Y., Yamanaka, M. D., and Fukao, S., Indian MST radar observations of gravity wave activities associated with tropical convection, *J. Atmos. Terr. Phys.*, **63**, 1631–1642, 2001.
- Dhaka, S. K., Choudhary, R. K., Malik, S., Shibagaki, Y., Yamanaka, M. D., and Fukao, S., Observable signatures of a convectively generated wave field over the tropics using indian MST radar at Gadanki, *Geophys. Res. Lett.*, **29**, 1872–1880, 2002.
- Doswell, C. A., Severe convective storms, in *Meteorological Monograph Series*, vol. **28(50)**, Amer. Meteor. Soc., 2002.
- Doviak, R. J. and Zrnic, D. S., Doppler radar and weather observations, in *Second edition*, Academic Press, Inc, 1991.
- Dudhia, J., A non-hydrostatic version of penn state NCAR mesoscale model: Validation tests and simulation of an Atlantic cyclone and cold front, *Mon. Weather Rev.*, **121**, 1493–1513, 1993.
- Dudhia, J. and Moncrieff, M. W., A numerical simulation of quasi-stationary tropical convection bands., *Q. J. R. Meteorol. Soc.*, **113**, 929–967, 1987.
- Ebert, E., Damrath, U., Wergen, W., and Baldwin, M., The WGNE assessment of short-term quantitative precipitation forecasts, *Bull. Am. Meteorol. Soc.*, **84**, 481–492, 2003.
- Ecklund, W. L., Gage, K. S., and Williams, C. R., Tropical precipitation studies using a 915 MHz wind profiler, *Radio Sci.*, **30**, 1055–1064, 1995.
- Emmanuel, K. A., Overview and definition of mesoscale meteorology, in *Mesoscale Meteorology and Forecasting*, pp. 1–17, Amer. Meteor. Soc., P. S. Ray, Ed., 1986.
- Engelbart, D., Steinhagen, H., Grsdorf, U., Lippmann, J., and J. Neisser, A 1290 MHz profiler with RASS for monitoring wind and temperature in the boundary layer, *Beitr. Phys. Atmosph.*, **69**, 63–80, 1996.
- Errico, R. M. and Bates, G. T., Implicit normal mode initialization of the PSU/NCAR mesoscale model, in *NCAR Tech. Note*, vol. **TN-312+1A**, Available from UCAR Communications, Boulder CO 80307, 1998.

- Evans, J. V., Theory and practice of ionosphere study by Thomson scatter radar, in *Proc.*, vol. 57, IEEE, 1975.
- Fabry, F. and Zawadski, I., Long-term radar observations of the melting layer of precipitation and their interpretation, *J. Atmos. Sci.*, **52**, 838–851, 1995.
- Farley, D. T., Overview of on-line data processing for MST radar, in *Handbook for MAP*, pp. 262–267, SCOSTEP Secretariat, University of Illinois, Urbana, Ill, 1984.
- Foote, G. B., A study of hail growth utilizing observed storm condition., *J. Clim.Appl.Meteorol.*, **23**, 84–101, 1984.
- Foote, G. B. and Wade, C. G., Case study of hailstorms in Colorado. Part I: Radar echo structure and evolution., *J. Atmos. Sci.*, **39**, 2828–2846, 1982.
- Fovell, R., Durran, D., and Holten, J. R., Numerical simulation of convectively generated stratospheric gravity waves, *J. Atmos. Sci.*, **49**, 1427–1442, 1992.
- Friend, A. W., Theory and practice of tropospheric sounding by radar, in *Proc.*, vol. 37, Inst., Radio Engg., 1949.
- Fritsch, J. M., Cumulus dynamics: Local compensating subsidence and its implications for cumulus parameterizations, *J. Pure and Appl. Geophysics*, **13**, 851–867, 1975.
- Fritsch, J. M. and Carbone, R. E., Improving quantitative precipitation forecast in warm season: A USWRP research and development strategy, *Bull. Am. Meteorol. Soc.*, **85**, 955–965, 2004.
- Fritsch, J. M. and Chapell, C. F., Numerical prediction of convectively driven mesoscale pressure systems. Part I: Convective parameterization, *J. Atmos. Sci.*, **37**, 1722–1735, 1980.
- Fritts, D. C. and Nastrom, G. D., Sources of mesoscale variability of gravity waves. Part II: Frontal, convective and jet stream excitation, *J. Atmos. Sci.*, **49**, 111–127, 1992.
- Fujitha, T. T., *Analytical mesometeorology: A review, Severe Local Storms*, vol. 27, Amer. Meteor. Soc., 1963.
- Fujitha, T. T., *Overshooting thunderheads observed from ATS and Learjet*, Satellite Mesometeorol. Res, Dep. Geophys. Sci., 1974.
- Fujitha, T. T., Tornadoes and downbursts in the context of generalized planetary scales, *J. Atmos. Sci.*, **38**, 1511–1534, 1981.
- Fukao, S., Yamanaka, M. D., Ao, N., Hocking, W. K., Sato, T., Yamamoto, M., Nakamura, T., Tsuda, T., and Kato, S., Seasonal variability of vertical eddy diffusivity in the middle atmosphere 1. Three-year observations by the middle and upper atmosphere radar, *J. Geophys. Res.*, **99**, 18,973–18,987, 1994.
- Gage, K. S. and Balsley, B. B., Doppler radar probing of the clear atmosphere, *Radio Sci.*, **15**, 243–257, 1978.
- Gage, K. S. and Balsley, B. B., On the scattering and reflection mechanisms contributing to

- clear air radar echoes from the troposphere, stratosphere and mesosphere, *Radio Sci.*, **17**, 153–164, 1980.
- Gage, K. S., Williams, C. R., and Ecklund, W. L., UHF wind profilers: A new tool for diagnosing tropical convective cloud systems, *Bull. Am. Meteorol. Soc.*, **75**, 2289–2294, 1979.
- Gallus, W. A., Impact of verification grid box size on warm season QPF skill measures, *Weather and Forecasting*, **17**, 1296–1302, 2002.
- Gambheer, A. V. and Bhatt, G. S., Life cycle characteristics of deep cloud systems over the indian region using INSAT-1B pixel data, *Mon. Weather Rev.*, **128**, 4071–4083, 2000.
- Gambheer, A. V. and Bhatt, G. S., Diurnal variation of deep cloud systems over the indian region using INSAT-1B pixel data, *Meteorol. and Atmos. phys.*, **78**, 215–225, 2001.
- Ghil, M., Meteorological data assimilation for Oceanographers Part II: Description and theoretical frame work, *Dyn. Of Atmos. Oceans*, **13**, 171–218, 1989.
- Glickman, T. S., Glossary of meteorology, in 2nd Ed., vol. , Amer. Meteor. Soc., 2000.
- Golder, R. N., Banerjee, S. K., and Debnath, G. C., Tornado in India and neighbourhood, in *Pre-published scientific report*, vol. **No.2/2001**, India Meteorological Deptment, Regional Met. Centre, Kolkata, 2001.
- Gossard, E. E. and Hooke, W. H., *Waves in the atmosphere*, Elsevier, Inc, 1975.
- Gossard, E. E., Wolfe, D. E., Moran, K. P., Paulus, R. A., Andreson, K. D., and Rogers, L. T., Measurement of clear-air gradients and turbulence properties with radar wind profilers, *J. Atmos. Ocean. Technol.*, **15**, 321–342, 1986.
- Grabowski, W. W., Xiaoqing, W., and Moncrieff, M. W., Cloud Resolving Modeling of Tropical Cloud systems during Phase II of GATE. Part I: Two-dimensional experiments, *J. Atmos. Sci.*, **53(24)**, 3684–3709, 1996.
- Green, J. L., Wingler, R. H., Warnock, J. H., I. Clark, W., Gage, K. S., and Vanzandt, T. E., Observations of the enhanced reflectivity associated with convective clouds, in *Conference on radar meteorology*, pp. 88–93, American Meteorological Society, Atlanta, USA, 1986.
- Grell, G. A., Prognostic evaluation of assumptions used by cumulus parameterizations, *Mon. Weather Rev.*, **121**, 764–787, 1993.
- Grell, G. A., Dudhia, J., and Stauffer, D. R., A description of the 5 th generation Penn State/NCAR mesoscale model (MM5), in *NCAR technical note*, vol. **TN-398**, NCAR, 1994.
- Gupta, H. N. and Ghosh, S. K., North Delhi tornado of 17 March 1978, *Mausam*, **31**, 93–100, 1980.
- Gupta, M. D., George, J. P., and Das, S., Performance of MM5-3DVAR system over Indian sub-continent, in *Proc. International Conf. on MONEX and its legacy*, vol. , NCMRWF-IMS, Delhi, 2005.

- Hadi, T. W., Tropical sea-breeze circulation and related atmospheric phenomena observed with l-band boundary layer radar in Indonesia, *J. Meteorol. Soc. Japan*, **78**, 123–140, 2000.
- Harrison, E. F., Minnis, P., Barkstorm, B. R., Ramanathan, V., Cess, R. D., and Gibson, G. G., Seasonal variation of cloud radiative forcing derived from the Earth Radiation Budget Experiment, *J. Geophys. Res.*, **95**, 18 687–18 703, 1990.
- Hashiguchi, H., Fukao, S., Tsuda, T., Yamanaka, M. D., Harijono, S. W. B., and Wiryosumarto, An overview of the planetary boundary layer observations over Equatorial Indonesia with an L-band clear-air Doppler radar, *Beitr. Phys. Atmosph.*, **69**, 13–25, 1996.
- Hilderbrand, P. H. and Sekhon, R. S., Objective determination of the noise level in Doppler spectrum, *J. Appl. Met.*, **13**, 808–811, 1974.
- Hoke, J. E., Phillips, N. A., DiMego, G. J., Tuccillo, J. J., and Sela, J., The regional analysis and forecast system of the National Meteorological Center, *Weather forecasting*, **4**, 323–334, 1989.
- Holland, G. J., McBride, J. L., Smith, R. K., Jasper, D., and Keenan, T. D., The BMRC Australian Monsoon Experiment: AMEX, *Bull. Am. Meteorol. Soc.*, **67**, 1466–1472, 1986.
- Hong, S. Y. and Pan, H. L., Nonlocal boundary layer vertical diffusion in a medium-range forecast model, *Mon. Weather Rev.*, **124**, 2322–2339, 1996.
- Houze, R., Structure and dynamics of a tropical squall line system observed during GATE, *Mon. Weather Rev.*, **105**, 1540–1567, 1977.
- Houze, R. A., Structure of atmospheric precipitation systems-A global survey., *Radio Sci.*, **16**, 671–689, 1981.
- Houze, R. A., *Cloud Dynamics*, Academic Press, Inc, 1993.
- Houze, R. A., Stratiform precipitation in regions of convection: A meteorological paradox?, *Bull. Am. Meteorol. Soc.*, **78**, 2179–2196, 1997.
- Houze, R. A., Geotis, S. G., Marks, F. D., and West, A. K., Winter monsoon convection in the vicinity of North Borneo. part I: Structure and time variation of the clouds and precipitation., *Mon. Weather Rev.*, **125**, 1418–1432, 1981.
- Houze, R. A., Smull, B. F., and Dodge, P., Mesoscale organization of springtime rainstorms in Oklahoma, *Mon. Weather Rev.*, **118**, 613–654, 1990.
- Ide, K., Courtier, P., GHil, M., and Lorenc, A. C., Unified notation for data assimilation: Operational, sequential and variational, *J. Met. Soc. Japan.*, **75**, 181–189, 1997.
- Jasperson, W. H., Nastrom, G. D., and Fritts, D. C., Further study of terrain effects on the mesoscale spectrum of atmospheric motions, *J. Atmos. Sci.*, **47**, 979–987, 1990.
- Jayanti, N., Narayana, V., and Balasubramanian, V., A climatological study of the heights

- of radar cloud tops, *Mausam*, **40**, 169–174, 1980.
- Jewett, B. F., Ramamurthy, M. K., and Rauber, R. M., Origin, evolution, and finescale structure of the St. Valentine's Day mesoscale gravity wave observed during STORM-FEST. Part III: Gravity wave genesis and the role of evaporation, *Mon. Weather Rev.*, **131**, 617–633, 2003.
- Johnson, R. H. and Nicholls, M., A composite analysis of the boundary layer accompanying a tropical squall line, *Mon. Weather Rev.*, **111**, 308–319, 1983.
- Johnson, R. H., Miner, B. D., and Ciesielski, P. E., Circulations between mesoscale convective systems along a cold front, *Mon. Weather Rev.*, **123**, 585–599, 1995.
- Joseph, P. V., Raipal, D. K., and Deka, S. N., Andhi, the convective dust-storm of northwest India, *Mausam*, **31**, 432–441, 1980.
- Junker, N. W., Hoke, J. E., and Grumm, R. H., Performance of NMC regional models, *Weather forecasting*, **4**, 368–390, 1989.
- Kain, J. S. and Fritsch, J. M., The role of convective trigger function in numerical forecasts of mesoscale convective systems, *Meteorol. and Atmos. phys.*, **49**, 93–106, 1992.
- Karoly, D. J., Roff, G. L., and Reeder, M. J., Gravity wave activity associated with tropical convection detected in TOGA COARE sounding data, *Geophys. Res. Lett.*, **23**, 261–264, 1996.
- Kessler, E., On the distribution and continuity of water substance in Atmospheric circulation, in *Meteorological Monograph Series*, vol. **10**, Amer. Meteor. Soc., 1969.
- Klemp, J. B. and Wilhelmson, R. B., Simulations of right moving supercell storms, *J. Atmos. Sci.*, **35**, 1097–1110, 1978.
- Knupp, K. R. and Cotton, W. R., An intense, quasi-steady thunderstorm over mountainous terrain. Part II: Doppler radar observations of the storm morphological structure., *J. Atmos. Sci.*, **39**, 343–358, 1982.
- Kulshrestha, S. M. and Jain, P. S., Radar climatology of Delhi and neighbourhood: convective cells of the hot weather season, *Ind. J. Met. Geophys.*, **16**, 85–97, 1965.
- Kumar, A., A climatological study of thunderstorms at Lucknow airport, *Mausam*, **43**, 441–444, 1992.
- Kumar, K. K., VHF radar observations of convectively generated gravity waves: Some new insights, *Geophys. Res. Lett.*, **33**, 1342–1345, 2006.
- Kumar, K. K., Jain, A. R., and Rao, D. N., VHF/UHF radar observations of tropical mesoscale convective systems over southern India., *Annals Geophysicae.*, **23**, 1673–1683, 2005.
- Kummerow, C., Simpson, J., and Co-authors, The status of tropical rainfall measuring mission (TRMM) after two years in orbit, *J. Appl. Met.*, **39**, 1965–1982, 2000.
- Kundu, M. M. and De, A. C., Radar study of pre-monsoon thunderstorms at Agartala aero-

- drome, *Ind. J. Met. Geophys.*, **20**, 56–62, 1969.
- Laing, A. G. and Fritsch, J. M., The global population of mesoscale convective complexes, *Q. J. R. Meteorol. Soc.*, **123**, 389–405, 1997.
- Lane, T. P., Reeder, M. J., and Clark, T. L., Numerical modeling of gravity wave generation by deep tropical convection, *J. Atmos. Sci.*, **58**, 1249–1274, 2001.
- Larsen, M. F. and Rottger, J., Observations of thunderstorm reflectivities and Doppler velocities measured at VHF and UHF, *J. Atmos. Ocean. Technol.*, **4**, 151–159, 1987.
- Larsen, M. F., Swartz, W. E., and Woodman, R. F., Gravity-wave generation by thunderstorms observed with a vertically pointing 430 MHz radar, *Geophys. Res. Lett.*, **9**, 571–574, 1982.
- Leary, C. A. and Houze, R. A., The structure and evolution of convection in a tropical cloud cluster, *J. Atmos. Sci.*, **36**, 437–457, 1979.
- Lemon, L. R., Updraft identification with radar, in *19th conf. on severe local storms*, vol. **40**, American Meteorological Society, Minneapolis, mn, 1998.
- Lemon, M. A. and Zipser, E. J., Cmandal umulonimbus vertical velocity events in GATE, Part I: Diameter, Intensity and Mass flux, *J. Atmos. Sci.*, **37**, 2444–2457, 1980.
- Lewis, J. M. and Derber, J. C., The use of adjoint equations to solve a variational adjustment problem with adjective constraints, *Tellus*, **27**, 309–322, 1985.
- Ley, B. E. and Peltire, W. R., Propagating mesoscale cloud bands, *J. Atmos. Sci.*, **38**, 1206–1219, 1981.
- Lhermitte, R. M. and Atlas, D., Precipitation motion by pulse Doppler radar, in *9th conference on Radar Meteorology*, Amer. Meteorol. Soc., Kansas City, 1961.
- Lin, C. and Arakawa, A., The macroscopic Entrainment processes of simulated cumulus ensemble. Part II: Testing the entraining-plume model, *J. Atmos. Sci.*, **54(8)**, 1044–1053, 1997.
- Lin, Y. L., Farley, R. D., and Orville, H. D., Bulk parameterization of snow field in a cloud model, *J. Clim. Appl. Meteorol.*, **22**, 1065–1092, 1983.
- Lindzen, R. S., Some coolness concerning global warming, *Bull. Am. Meteorol. Soc.*, **71**, 288–299, 1990.
- Liu, C., Moncrieff, M. W., and Grabowski, W. W., Explicit and parameterization relations of convective cloud systems in TOGA-COARE, *Mon. Weather Rev.*, **129(7)**, 1689–1703, 2001.
- Lorenc, A., Analysis methods for numerical weather prediction, *Q. J. R. Meteorol. Soc.*, **112**, 1177–1194, 1986.
- Maddox, R. A., Mesoscale convective complexes., *Bull. Am. Meteorol. Soc.*, **61**, 1374–1387, 1980.
- Mandal, G. S., Characteristics of some recent north Indian tornadoes, *Vayu Mandal*, **13**,

- 74–80, 1983.
- Mapes, B. E., The large-scale part of mesoscale convective system circulations: A linear vertical spectral band model, *J. Met. Soc. Japan.*, **76**, 29–55, 1998.
- Marshall, J. S. and Palmer, W. M., The distribution of raindrops with size, *J. Meteor.*, **5**, 165–166, 1948.
- Martner, B. E., Wuertz, D. B., Stankov, B. B., Strauch, R. G., Westwater, E. R., Gage, K. S., Ecklund, W. L., Martin, C. L., and Dabberdt, W. F., An evaluation of Wind profiler, RASS and Microwave Radiometer performance, *Bull. Am. Meteorol. Soc.*, **74**, 599–613, 1993.
- Marwitz, J. D., The structure and motion of severe hailstorms. Part I: Supercell storms., *J. Appl. Met.*, **11**, 189–201, 1972.
- Mawitz, J. D. and Toth, J., A case study of heavy snowfall in Oklahoma, *Mon. Weather Rev.*, **121**, 648–660, 1993.
- McAnelly, R. L. and Cotton, W. R., The precipitation life cycle of mesoscale convective complexes, *Mon. Weather Rev.*, **117**, 784–808, 1989.
- McBride, J. L. and Gray, W. M., Mass divergence in tropical weather systems. Part I: Diurnal variations., *Q. J. R. Meteorol. Soc.*, **106**, 501–516, 1980.
- McCumber, M., Tao, W.-K., Simpson, J., Penc, R., and Soong, S.-T., Comparison of ice-phase microphysical parameterization schemes using numerical simulations of tropical convection, *J. Appl. Met.*, **30**, 985–1004, 1991.
- McLandress, C., Alexander, M. J., and Wu, D. L., Microwave limb sounder observations of gravity waves in the stratosphere: A climatology and interpretation, *J. Geophys. Res.*, **105(D9)**, 947–967, 2000.
- Miller, L. J., Tuttle, J. D., and Knight, C. K., Airflow and hail growth in a severe northern high plains supercell, *J. Atmos. Sci.*, **45**, 736–762, 1988.
- Molinari, J. and Dudek, M., Parameterization of convective precipitation in mesoscale numerical models: A critical review, *Mon. Weather Rev.*, **120**, 326–344, 1992.
- Moller, A. R., Doswell, C. A., and Przybylinski, R., High-precipitation supercells: A conceptual model and documentation, in *16th conf. on severe local storms*, American Meteorological Society, Kananaskis park, AB, 1990.
- Moncrieff, M. W., Krueger, S. K., Gregory, Redelpserger, Luc, J., and Tao, W. K., GEWEX cloud system study (GCSS) working group 4: Precipitating convective cloud systems, *Bull. Am. Meteorol. Soc.*, **78(5)**, 831–836, 1997.
- Mukherjee, A. K. and Bhattacharya, P. K., The Diamond Harbour tornado, *Ind. J. Met. Geophys.*, **23**, 227–230, 1972.
- Narayan, V. and Krishnamurthy, G., A radar study of pre-monsoon thunderstorms over Bombay airport, *Ind. J. Met. Geophys.*, **16**, 645–657, 1966.

- NASDA, TRMM PR algorithm instruction manual v1.0, in *Communications Research Laboratory*, vol. 52, available from Communications Research Laboratory, 4-2-1 Nukui-Kitamachi, Tokyo 184, Japan, 1999.
- Nesbitt, S. W., Zipser, E. J., and Cecil, D. J., A census of precipitation features in the tropics using TRMM: Radar, ice scattering, and ice observations, *J. Clim.*, **13**, 4087–4106, 2000.
- Newton, C. W., Dynamics of severe convective storms, in *Meteorological Monograph*, vol. 7, Severe Local storms, Am. Met. Soc., 1963.
- Nizamudin, S., hail occurrences in India, *Weather*, **48**, 90–92, 1993.
- Ogura, Y., *A review of numerical modeling research on small-scale convection in the atmosphere*, Severe Local Storms, Meteor. Monogr., No. 27., 65-76, Amer. Meteor. Soc, 1963.
- Ogura, Y. and Takahashi, T., The development of warm rain in a cumulus model, *J. Atmos. Sci.*, **30**, 262–277, 1973.
- Olson, D. A., Junker, N. W., and Korty, B., Evaluation of 33 years of quantitative precipitation forecasting at the NMS, *Weather forecasting*, **10**, 498–511, 1995.
- Ooyama, K. V., Conceptual evolution of the theory and modeling of the tropical cyclone, *J. Met. Soc. Japan.*, **60**, 369–380, 1982.
- Orlanski, I., A rational subdivision of scales for atmospheric processes, *Bull. Am. Meteorol. Soc.*, **56**, 527–534, 1975.
- Orville, H. D. and Kopp, F. J., Numerical simulation of the life history of a hailstorm, *J. Atmos. Sci.*, **34**, 1596–1618, 1977.
- Ottersten, H., Atmospheric structure and radar backscattering in clear air, *Radio Sci.*, **4**, 1179–1193, 1969.
- Parish, D. F. and Derber, J. C., The national meteorological centers spectral statistical interpolation analysis system, *Mon. Weather Rev.*, **120**, 1747–1763, 1992.
- Person, P. O. and Anderson, T., A real time system: Automatic wind field interpretation of Doppler radar wind components, in *Proc. Symp. Mesoscale Analysis and Forecasting*, vol. SP282, European Space Agency, Vancouver, 1987.
- Pfister, L., Alexander, J. M., and Coauthors, Gravity waves generated by a tropical cyclone during the STEP tropical field program: A case study, *J. Geophys. Res.*, **98**, 8611–8638, 1993.
- Pokrandt, P. J., Tripoli, G. J., and Houghton, D. D., Numerical investigation of the dynamical coupling between an observed meso- γ scale wave disturbance and an intense middle latitude cyclone, in *Ninth Conf. on Atmospheric and Oceanic Waves and Stability*, vol. 25-28, Amer. Meteor. Soc., San Antonio. TX, 1993.
- Pokrandt, P. J., Tripoli, G. J., and Houghton, D. D., A numerical investigation of the de-

- velopment mechanisms of the mesoscale waves of 15 December 1987, in *Preprints, Int. Symp. On the Life Cycles of Extratropical Cyclones*, vol. III, University of Bergen Geophysical Institute, Bergen, Norway, 1994.
- Powers, J. G., Numerical model simulation of a mesoscale gravity wave event: Sensitivity tests and spectral analysis, *Mon. Weather Rev.*, **124**, 1838–1869, 1997.
- Powers, J. G. and Reed, R. J., Numerical simulation of the large-amplitude mesoscale gravity-wave event of 1987 in the central United States, *Mon. Weather Rev.*, **121**, 2285–2308, 1993.
- Probert-Jones, J. R., Meteorological use of pulse Doppler radar., *Nature*, **186**, 271–273, 1960.
- Rabier, F. H., Jarvinen, E., Klinker, E., Mahfouf, J. ., and Simmons, A., The ECMWF operational implementation of four-dimensional variational assimilation. Part. I: Experimental results with simplified physics, *Q. J. R. Meteorol. Soc.*, **126**, 1143–1170, 2000.
- Raghavan, S., Sivaramakrishnan, T. R., and Ramaswamy, V., Radar study of convective clouds around Madras during MONEX, in *National symposium on early results of MONEX-79 experiment*, March 1981, New Delhi, 1981.
- Ramanathan, V. and Collins, W., Thermodynamic regulation of ocean warming by cirrus clouds deduced from the 1987 ElNino, *Nature*, **351**, 27–32, 1991.
- Rao, P. B., Radar for atmospheric sciences: MF/HF and MST radars, *Indian J. Radio and Space Phy.*, **19**, 326–342, 1990.
- Rao, P. B., Jain, A. R., Balamuralidhar, P., Damle, S. H., and Viswanathan, G., Indian MST radar I. System description and sample vector wind measurements in ST mode, *Radio Sci.*, **30**, 1125–1138, 1995.
- Rao, R. P., Sundaram, S. K., Thampi, S. B., Suresh, R., and Gupta, J. P., An overview of first Doppler weather radar inducted in the cyclone detection network of India Meteorological Department, *Mausam*, **55**, 155–176, 2004.
- Rao, T. N., Rao, D. N., and Raghavan, S., Tropical precipitating systems observed with Indian MST Radar, *Radio Sci.*, **34**, 1125–1139, 1999.
- Rasmussen, E. N., Straka, J., Gilmore, J. M., and Davies-Jones, R., A preliminary survey of rear-flank descending reflectivity cores in supercell storms, *Weather forecasting, In Press*, 2007.
- Reddy, K. K., Kozu, K. T., Nakamura, K., Jain, A. R., Anandan, V. K., Rao, P. B., Rao, R. R., and Viswanathan, G., Lower atmospheric wind profiler at Gadanki, tropical India: Initial results, *Meteorol. Z.*, **10**, 457–466, 2001.
- Redelsperger, J. L. and Lafore, J. P., A three dimensional simulation of a Tropical Squall line: Convective Organization and Thermodynamic vertical transport, *J. Atmos. Sci.*, **45**, 1334–1356, 1988.

- Richardson, L. F., *Weather Prediction by Numerical Process*, Cambridge University Press, London, 1922.
- Riddle, A. C., Parameterization of spectrum, in *Handbook for MAP*, edited by S. A. Bowhill and B. Edwards, pp. 546–547, SCOSTEP Secretariat, University of Illinois, Ill., 1983.
- Robinson, F. J. and Sherwood, S. C., Modeling the impact of convective entrainment on the tropical tropopause, *J. Atmos. Sci.*, **63**, 1013–1027, 2006.
- Rogers, R. R., Ecklund, W. L., Carter, D. A., Gage, K. S., and Ethier, S. A., Research Applications of a boundary-layer wind profiler, *Bull. Am. Meteorol. Soc.*, **74**, 567–580, 1993.
- Röttger, J. and Liu, C. H., Partial reflection and scattering of VHF radar signal from the clear air atmosphere, *Geophys. Res. Lett.*, **5**, 357–360, 1978.
- Rutledge, S. A., Williams, E. R., and Keenan, T. D., The Down Under Doppler and Electricity Experiment (DUNDEE): Overview and preliminary results, *Bull. Am. Meteorol. Soc.*, **73**, 3–16, 1992.
- Salby, M. L. and Garcia, R. R., Transient response to localized episodic heating in the tropics. Part I: Excitation and short-time near-field behavior, *J. Atmos. Sci.*, **44**, 458–498, 1987.
- Sarkar, B. K., Tole, P. B., and Agarwal, A., Feeder network for the Indian MST, in *Handbook for MAP*, p. 472, SCOSTEP Secretariat, University of Illinois, Urbana, Ill, 1988.
- Sato, K., Vertical wind disturbances in the afternoon of mid-summer revealed by the MU-radar, *Geophys. Res. Lett.*, **19**, 1943–1946, 1992.
- Sato, K., Small-scale wind disturbances observed by the MU radar during the passage of typhoon Kelly, *J. Atmos. Sci.*, **50**, 518–537, 1993.
- Sato, K., Hashiguchi, H., and Fukao, S., Gravity waves and turbulence associated with cumulus convection observed with the UHF/VHF clear-air Doppler radars, *J. Geophys. Res.*, **100**, 7111–7119, 1995.
- Sato, T., Radar principles, in *Handbook for MAP*, edited by S. Fukao, pp. 19–53, SCOSTEP Secretariat, University of Illinois, Urbana, Ill, 1989.
- Schaefer, J. T., The critical success index as an indicator of warning skill, *Weather forecasting*, **5**, 570–575, 1990.
- Schneider, R. S., Large-amplitude mesoscale wave disturbances within the intense Midwest extratropical cyclone of 15 December 1987, *Weather forecasting*, **5**, 533–558, 1990.
- Shibagaki, Y., Yamnaka, M. D., Shimizu, S., Uyeda, H., Watanabe, A., Maekawa, Y., and Fukao, S., Meso- β to γ scale wind circulations associated with precipitating clouds near Baiu front observed by the MU and meteorological radars, *J. Met. Soc. Japan.*, **12**, 69–91, 2000.
- Smull, B. F. and Houze, R. A., Dual-Doppler radar analysis of a midlatitude squall line

- with a trailing region of stratiform rain, *J. Atmos. Sci.*, **44**, 2128–2148, 1987.
- Srinivasan, V., Ramamurthy, K., and Nene, Y. R., Summer Norwesters and Andhi and large scale convective activity over peninsula and central parts of the country, in *Forecasting Manual Part 3*, India Meteorological Department, India, 1973.
- Steiner, M., Houze, R. A., and Yuter, S. E., Climatological characterization of three dimensional storm structure from operational radar and rainguage data, *J. Appl. Met.*, **34**, 1978–2007, 1995.
- Stensrud, D. J. and Fritsch, J. M., Mesoscale convective systems in a weakly forced large scale environment: Part:III Numerical simulations and implications for operational forecsat, *Mon. Weather Rev.*, **112**, 2084–2104, 1994.
- Sun, J. and Crook, N. A., Dynamical and microphysical retrievals from doppler radar observations using a cloud model and its adjoint Part I: Model development and simulated data experiments, *J. Atmos. Sci.*, **54**, 1642–1661, 1997.
- Sun, J. and Crook, N. A., Dynamical and microphysical retrievals from Doppler radar observations using a cloud model and its adjoint Part II: Retrieval experiments of an observed Florida convective storm, *J. Atmos. Sci.*, **55**, 835–852, 1998.
- Talagrand, O. and Courtier, P., Variational assimilation of meteorological observations with adjoint velocity equation. Part I: Theory, *Q. J. R. Meteorol. Soc.*, **113**, 1313–1330, 1987.
- Tao, W. K. and Simpson, J., Cloud Interactions and merging: Numerical Simulations, *J. Atmos. Sci.*, **41**, 2901–2917, 1984a.
- Tao, W. K. and Simpson, J., The Goddard Cumulus Ensemble Model. Part I: Model description, *Terr. Atmos. Oceanic Sci.*, **4**, 35–72, 1984b.
- Tao, W. K., Simpson, J., and McCumber, M., An ice-water saturation adjustment, *Mon. Weather Rev.*, **117**, 231–235, 1987a.
- Tao, W. K., Simpson, J., and Soon, S. T., Statistical properties of a cloud ensemble: A numerical study, *J. Atmos. Sci.*, **44**, 3175–3187, 1987b.
- Tao, W. K., Simpson, J., Sui, C. H., Zhou, B., Lau, K. M., and Moncrieff, M. W., Equilibrium states simulated by Cloud-Resolving Models, *J. Atmos. Sci.*, **56(17)**, 3128–3139, 1999.
- Tokay, A., Tropical rainfall associated with convective and stratiform clouds: Intercomparison of disdrometer and profiler measurements, *J. Appl. Met.*, **38**, 302–320, 1999.
- Torrence, C. and Compo, P., A practical guide to wavelet analysis, *Bull. Am. Meteorol. Soc.*, **791**, 61–78, 1998.
- Tsuda, T., Nashida, M., Rocken, C., and Ware, R. H., A global distribution of gravity wave activity in the stratosphere, in *SPARC Newsl*, vol. **13**, SPARC, 1999.
- Uccellini, L. W. and Koch, S. E., The synoptic setting and possible energy sources for

- mesoscale wave disturbances, *Mon. Weather Rev.*, **115**, 721–729, 1987.
- Vasiloff, S. V., Brandes, E. A., and Davies-Jones, R. P., An investigation of the transition from multicell to supercell storms., *J. Clim. Appl. Meteorol.*, **25**, 1022–1036, 1986.
- Vincent, R. A. and Alexander, M. J., Gravity-waves in the tropical lower stratosphere: An observational study of seasonal and interannual variability, *J. Geophys. Res.*, **105(D14)**, 971–982, 2000.
- Waldteufel, P. and Corbin, H., On the analysis of single Doppler radar data, *J. Appl. Met.*, **18**, 532–542, 1979.
- Wang, P. K., Moisture plumes above thunderstorm anvils and their contributions to cross-tropopause transport of water vapor in midlatitudes, *J. Geophys. Res.*, **108**, 4194–4203, 2003.
- Wang, W., Barker, D., Bruyere, C., Dhudia, J., Gill, D., and Michalakes, J., WRF version 2 modeling system users guide, in *WRF Documentation*, vol. , MMM division of NCAR, Boulder, 2004.
- Webster, P. J., Response of the tropical atmosphere to local steady forcing, *Mon. Weather Rev.*, **100**, 518–540, 1972.
- Webster, P. J. and Houze, R. A., The Equatorial Mesoscale Experiment (EMEX): An overview, *Bull. Am. Meteorol. Soc.*, **72**, 1481–1505, 1991.
- Webster, P. J. and Lukas, R., TOGA CORE: The Coupled Ocean-Atmosphere Response Experiment, *Bull. Am. Meteorol. Soc.*, **73**, 1377–1416, 1992.
- Webster, P. J. and Stephens, G. L., Tropical upper-tropospheric extended cloud: Influences from winter MONEX, *J. Atmos. Sci.*, **37**, 1521–1541, 1984.
- Weisman, M. L. and Klemp, J. B., The structure and classification of numerically simulated convective storms in directionally varying wind shears., *Mon. Weather Rev.*, **112**, 2479–2498, 1984.
- White, A. B., Fairall, C. W., Frisch, A. S., Orr, B. W., and Snider, J. B., Recent radar measurements of turbulence and microphysical parameters in marine boundary layer clouds, *Atmos. Res.*, **40**, 177–221, 1996.
- White, A. B., Gattas, D. J., Strem, E. T., Ralph, F. M., and Neiman, P. J., An automated bright band height detection algorithm for use with Doppler radar spectral moments, *J. Atmos. Ocean. Technol.*, **19**, 687–697, 2002.
- Williams, C. R., Ecklund, W. L., and Gage, K. S., Classification of precipitating clouds in the tropics using 915 MHz wind profilers, *J. Atmos. Ocean. Technol.*, **12**, 996–1012, 1995.
- Williams, C. R., Kruger, A., Gage, K. S., Tokay, A., Cifelli, R., Krajewski, W. F., and Kummerow, C., Comparison of simultaneous rain drop size distribution estimated from two surface disdrometer and a UHF profiler, *Geophys. Res. Lett.*, **27**, 1763–1766, 2000.

- Woodman, R. F., Spectral moment estimation in MST radar, *Radio Sci.*, **20**, 1185–1195, 1985.
- Wu, D. L. and Waters, J. W., Satellite observations of atmospheric variances: A possible indication of gravity waves, *Geophys. Res. Lett.*, **23**, 2631–2634, 1996.
- Wu, W., Xiaoqing, W., Grabowski, W. W., and Moncrieff, M. W., Long-term behavior of cloud system in TOGA-COARE and their interactions with radiative and surface processes, Part I: Two-dimensional modeling study, *J. Atmos. Sci.*, **55(17)**, 2693–2714, 1999.
- Xiao, Q. and Sun, J., Multiple radar data assimilation and short range QPF of a squall line observed during IHOP 2002, in *Second international symposium on QPF and Hydrology*, vol. 4, Colorado, Boulder, 2006.
- Xiao, Q., Kuo, Y. H., Sun, J., Lee, W. C., Lim, E., Guo, Y. R., and Barker, D., Assimilation of Doppler radar observations with a regional assimilation system: Impact of Doppler radar velocities and reflectivity on the forecast of QPF of heavy rainfall case, *J. Appl. Met.*, **44**, 768–788, 2005.
- Xu, K. M. and Randall, D. A., Explicit Simulation of Cumulus Ensembles with the GATE Phase III Data: Comparison with observations, *J. Atmos. Sci.*, **53(24)**, 3710–3736, 1996.
- Yeung, K. K., Use of wind profiler in severe weather monitoring, *Meteorol. Zeitschrift*, **7**, 326–331, 1998.
- Zhang, D. L. and Fritsch, J. M., Numerical sensitivity experiments of varying model physics on the structure, evolution and dynamics of the mesoscale convective systems, *J. Atmos. Sci.*, **45**, 261–293, 1988.
- Zupanski, M., Zupanski, D., Parrish, D., Rogers, E., and DiMego, G., Four-dimensional variational data assimilation for the Blizzard of 2000, *Mon. Weather Rev.*, **130**, 1967–1988, 2002.

List of Publications

- 1 **S. Abhilash.**, Someshwar Das., S. R. Kalsi.,Munmun Dasgupta., K. Mohankumar., John P. George., S. K. Banarjee., S. B. Thampi and D. Pradhan, Assimilation of Doppler Radar Wind Observations for the Prediction of Rainfall Associated with Mesoscale Convective Systems, *Journal of Earth System Science*, **116-3**, 275-304, 2007.
- 2 **S. Abhilash.**, Someshwar Das., S. R. Kalsi.,Munmun Dasgupta., K. Mohankumar., John P. George., S. K. Banarjee., S. B. Thampi and D. Pradhan, Impact of Doppler radar Wind Observations in simulating the Intensity and Propagation of Rainbands Associated with Mesoscale Convective Complexes using MM5-3DVAR System, *Journal of Pure and Applied Geophysics*, **164-9**, 1491-1509, 2007.
- 3 **S. Abhilash.**, K. Mohankumar and Someshwar Das, Microphysical Structure associated with Tropical Cloud Clusters simulated using a mesoscale model and comparison with TRMM observations, *International Journal of Remote Sensing*, **In press**, 2007.
- 4 **S. Abhilash.**, and K. Mohankumar, Vertical Structure and Evolution of a Supercell Storm: Observations Using VHF Radar, *International Journal of Remote Sensing*, **Accepted**, 2007.
- 5 **S. Abhilash.**, K. Mohankumar, S. Shankar Das and K. Kishore Kumar, VHF Radar Observations of the Evolution and Structure of Tropical Mesoscale Convective Systems, *Meteorology and Atmospheric Physics*, **Review**, 2007.
- 6 **S. Abhilash.**, K. Mohankumar and Preveen Kumar D, Vertical Wind Disturbance in the Troposphere and Signatures of Gravity Waves Associated with Tropical

- Mesoscale Convective Systems. Part I: Observations, *Earth planet and space science (Japan)-special issue of CPEA*, **Review**, 2007.
- 7 **S. Abhilash.**, K. Mohankumar, K. Kishore Kumar, V. K. Anandan, and D. N. Rao, Gravity Waves Associated with a Supercell Storm. Part I: Observations, *Anales Geophys.-special issue of MST-11*, **Submitted**, 2007.
- 8 **S. Abhilash.**, K. Mohankumar, S. S. Das, V. K. Anandan, and D. N. Rao, Gravity Waves Associated with a Supercell Storm. Part II: Assimilation of VHF Radar Data and Cloud Resolving Scale Simulations, *Anales Geophys.-special issue of MST-11*, **Submitted**, 2007.
- 9 **S. Abhilash.**, and K. Mohankumar, UHF radar Observations of the precipitating convection associated with the passage of a Tropical Mesoscale Convective System, *Journal of Solar and Terrestrial Physics*, **Submitted**, 2007.

PAPERS PRESENTED IN INTERNATIONAL CONFERENCES

10. **S. Abhilash**, K. Mohankumar., and G. Mrudula., VHF Radar observations on prominent features of Gravity waves and Weakening of Tropopause associated with Tropical Convection . *(Paper presented in SPARC 3rd general assembly, held during 1-7 August 2004 at Victoria (BC), Canada.)*
11. K. Mohankumar., G. Mrudula., and **S. Abhilash**., Observations of Gravity wave activity associated with Indian Summer Monsoon. *(Presented at AGU Chapman Conference on Gravity Wave Processes and Parameterization, During 10-14 January, 2004 at Hawaii, USA)*
12. G. Mrudula., K. Mohankumar., and **S. Abhilash**., Observation of Gravity waves Activity during the passage of Tropical Cyclone over India. *(Presented at AGU Chapman Conference on Gravity Wave Processes and Parameterization, During 10-14 January, 2004 at Hawaii, USA)*
13. **S. Abhilash** and K. Mohankumar., Prominent features of the Gravity Waves generated by Tropical Convection detected by VHF Doppler Radar: A case study. *(Proceedings of 14th International Conference on Clouds and Precipitation Bologna, Italy, 18-23 July 2004)*
14. **S. Abhilash**., Someshwar Das., Munmun Dasgupta., John P. George., S. R. Kalsi., S. K. Banarjee and K. Mohankumar., Impact of Doppler Weather Radar wind observations for the Prediction of the Organization and Structure of Mesoscale Convective Systems. *(Presented in International Conference on Mesoscale Processes in Atmosphere and Ocean at Indian Institute of Technology (IIT), Delhi, during 10-14 February, 2006.)*
15. **S. Abhilash**., and K. Mohankumar., Assimilation of the VHF radar data in Simulating the Structure of the observed Gravity Wave Event Associated with Tropical Convection. *(Presented at International CPEA Symposium, Kyoto University, Japan held during 20-23 March 2007)*
16. **S. Abhilash** and K. Mohankumar., Observational and modeling studies on Tropical Mesoscale convective systems., *(Presented at 4th Kyoto University International summer school on Active Geosphere at Institute of Bandung, Indonesia during 22nd July to 4th August 2007)*

T451



PAPERS PRESENTED IN NATIONAL SEMINARS

17. **S. Abhilash**, K. Mohankumar., G. Mrudula., Someshwar Das., V. K. Anandan. and D. Narayana Rao, Assimilation of MST Radar wind observations for the Prediction of the Track and Intensity of Tropical Cyclone over Bay of Bengal. (*Presented at National Atmospheric Research Laboratories during Sixth User's Scientist workshop on MST Radar applications, Tirupati, India June 2006.*)

18. **S. Abhilash** and K. Mohankumar., Assimilation of Satellite Derived parameters for the Short Range Prediction of Mesoscale Convective Systems and Validation of Microphysical Schemes in Mesoscale Models. (*Presented in the First National Workshop on Megha-Tropiques, IISc, Bangalore, July 2006*)

SCIENTIFIC REPORT.

Das Someshwar., Kalsi, S.R., **Abhilash, S.**, Das Gupta, M., George, J.P., Banerjee, S.K., Thampi, S.B., Pradhan, D., and Mohankumar, K., Assimilation of Doppler Weather Radar Wind in a Mesoscale Model and their Impact on Simulation of Thunderstorms and Severe Weather Systems. (*Report no. NMRF/RR/01/2006, 120 pages, Published by NCMRWF, A-50, Institutional Area, Sector-62, NOIDA, India 201 307, 2006*)